

QCD PHENOMENOLOGY AT HIGH TEMPERATURES

ROLAND A. SCHNEIDER

QCD PHENOMENOLOGY AT HIGH TEMPERATURES

Roland A. Schneider

Vollständiger Abdruck der von der Fakultät für Physik der Technischen Universität München zur Erlangung des akademischen Grades eines

Doktors der Naturwissenschaften (Dr. rer. nat.)

genehmigten Dissertation.

Vorsitzender: Univ.-Prof. Dr. Stephan Paul

Prüfer der Dissertation:

1. Univ.-Prof. Dr. Wolfram Weise
2. Univ.-Prof. Dr. Andrzej J. Buras

Die Dissertation wurde am 23.9.2002 bei der Technischen Universität München eingereicht und durch die Fakultät für Physik am 27.11.2002 angenommen.

Summary

A phenomenological, thermodynamically consistent quasiparticle model of the quark-gluon plasma is constructed, taking into account information from lattice QCD simulations. Close to the phase transition, confinement is incorporated by a modification of the particle distribution function. The formalism is extended to systems with small quark chemical potential. For the description of ultra-relativistic heavy-ion collisions, a fireball is developed in accord with the quasiparticle model and a multitude of hadronic observables. Low mass dilepton radiation and J/ψ suppression are calculated within a unified framework. Both times, the results are compared with experimental data from the CERN/SPS, and estimates for the RHIC collider are given. Finally, asymptotic freedom at high temperatures is derived using an external field method.

Zusammenfassung

Es wird ein phenomenologisches, thermodynamisch konsistentes Quasiteilchenmodell des Quark-Gluon-Plasmas konstruiert, das Informationen von Gitter-QCD Simulationen beinhaltet. Confinement wird nahe des Phasenübergangs durch eine Modifikation der Teilchenverteilungsfunktion eingebaut. Der Formalismus wird zu Systemen mit kleinem chemischen Potential der Quarks ausgedehnt. Für die Beschreibung von ultrarelativistischen Schwerionenstößen wird ein Feuerball entwickelt, der sich im Einklang mit diesem Quasiteilchenmodell und einer Vielzahl an hadronischen Observablen befindet. Dilepton-Strahlung bei kleinen invarianten Massen und J/ψ Unterdrückung werden innerhalb eines einheitlichen Rahmens berechnet. Beide Male werden die Ergebnisse mit experimentellen Daten von CERN/SPS verglichen und Schätzungen für den RHIC Beschleuniger abgegeben. Schliesslich wird asymptotische Freiheit bei hohen Temperaturen mit der Methode des äusseren Feldes abgeleitet.

Contents

1	Introduction	7
2	QCD at Finite Temperature	13
2.1	QCD at zero temperature	13
2.2	Symmetries and condensates	15
2.3	Thermal field theory	17
2.3.1	Perturbative techniques	19
2.3.2	Hard Thermal Loops	20
2.3.3	Lattice techniques	20
2.4	The QCD phase diagram	22
2.4.1	Orders of magnitude	22
2.4.2	A non-perturbative toy model	24
2.4.3	Order parameters and critical temperature	28
2.4.4	The QCD phase diagram in the $T - \mu$ plane	31
3	Quasiparticle Model of the QGP	35
3.1	Lattice results	35
3.1.1	Pure gauge theory	35
3.1.2	Dynamical quarks	36
3.2	Perturbative results	37
3.3	Gluonic quasiparticles	39
3.3.1	Basic quasiparticle model	39
3.3.2	Thermal masses: Debye vs. Asymptotic	41
3.3.3	Deconfinement and the quasiparticle model	42
3.3.4	Thermal masses close to T_c	44
3.3.5	Results for SU(3) gauge theory	46
3.4	Unquenching the quarks	50
3.4.1	Thermal masses	51
3.4.2	Physical quark masses	53
3.4.3	Comparison with other work	55
3.5	Finite quark chemical potential	56
3.5.1	The equation of state	56
3.5.2	Quark number susceptibilities	59
3.6	Intermediate summary	61
4	Dilepton Rates	63
4.1	Dileptons from a fireball	63
4.2	Calculation of the photon spectral function	64
4.2.1	The quark-gluon phase	64
4.2.2	The hadronic phase	68
4.2.3	After freeze-out contributions	71
4.2.4	Drell-Yan and charm contributions	72
4.3	Fireball model	73

4.3.1	Initial and freeze-out conditions	74
4.3.2	Volume evolution	74
4.3.3	Temperature evolution	76
4.3.4	Chemical composition	78
4.3.5	Variations with beam energies and centralities	79
4.3.6	Discussion of temperature and volume	81
4.4	Dilepton invariant mass spectra	83
4.4.1	SPS data at 40 and 160 AGeV	83
4.4.2	RHIC at $\sqrt{s} = 200$ AGeV	87
4.4.3	Sensitivity to model parameters	90
4.5	Intermediate summary	91
5	J/ψ Suppression	93
5.1	Screening and the J/ψ	93
5.2	Initial conditions	95
5.2.1	Open charm	95
5.2.2	Hidden charm	95
5.3	Thermodynamics of the medium	97
5.4	Charmonium Evolution	98
5.4.1	Kinetic description of dissociation and formation	98
5.4.2	Cross sections for dissociation and formation	100
5.4.3	Results	103
5.5	Intermediate summary	105
6	Screening at Finite Temperature	107
6.1	Thermal screening	107
6.2	The Debye mass on the lattice	108
6.3	The zero temperature case	112
6.4	The temperature-dependent part	114
6.4.1	A first (incomplete) approximation	116
6.4.2	A better approximation	118
6.4.3	Results for QED	118
6.4.4	Results for QCD	119
6.5	The gluonic lowest Landau level	121
6.6	Intermediate summary	123
7	Summary and Conclusions	125
A	Thermal Spectral Functions	131
B	Hard Thermal Loop Self-Energies	133
B.1	Gauge boson HTL self-energies	133
B.2	Fermion HTL self-energies	136
C	Integral Expansions	139
	List of Figures	141
	Bibliography	143
	Acknowledgements	151

Quantum chromodynamics is conceptually simple.
Its realization in nature, however, is usually very
complex. But not always.

FRANK WILCZEK

The truth is rarely pure
and never simple.

OSCAR WILDE

1 Introduction

In recent years, there has been steadily increasing activity aimed at analysing the phase structure of Quantum Chromodynamics (QCD), the theory of strong interactions. This effort has been mainly motivated by the expectation that the place in nature where QCD is *not* staggeringly complicated, as referred to by Frank Wilczek in his quotation, is the realm of very high temperature and extremely high density. The anticipated reduction of complexity is intimately tied to the concept of a running coupling constant in renormalisable quantum field theories. There, the coupling constant g depends on the momentum scale Q a specific process is probed at. Asymptotic freedom, one of the striking properties of non-abelian gauge theories like QCD, implies that g becomes small at large energy and momentum scales, and a perturbative description of the physics in terms of weakly interacting partons is possible. The parton model has subsequently been successfully applied in a number of high-energy processes, most prominently in deep inelastic scattering. On the other side, at low energies $Q \lesssim 1$ GeV the coupling constant is large, and QCD shows what is sometimes called infrared slavery: all quarks and gluons are bound in colourless composite objects, the hadrons. The phenomenon of confinement, the absence of free, observable partons, to date evades a thorough theoretical description due to its highly non-perturbative nature. The interactions of hadrons are described within effective theories that capture parts of the initial QCD dynamics and symmetries. However, there is no feasible first-principles approach based on the fundamental constituents, at least not for the lightest quarks, that leads us to “understand” the confinement mechanism.

Consider heating up a system that consists of hadrons: the temperature T will ultimately constitute the only relevant energy scale, hence the coupling

$$g(T) \sim \frac{1}{(11N_c - 2N_f) \log(T^2/\Lambda_{\text{QCD}}^2)} \quad (1.1)$$

will become small. We should then be able to treat the hot system in terms of a gas of weakly interacting partons, instead of a multitude of strongly reacting hadronic resonances. The same will hold if the system is extremely densely compressed. The momenta of the particles at the Fermi surface are typically large, of the order of the chemical potential μ , and $g \sim 1/\log(\mu)$ becomes small, again, which was first realised by Collins and Perry [1] almost 30 years ago. Consequently, there will be a transition from the cold, dilute hadronic world to a hot, dense *quark-gluon plasma* (QGP). This new state of matter is clearly of great interest. First, it simply tells us what ordinary matter looks like under extreme conditions. Second, in observing the response of QCD to the variation of external control parameters like temperature and chemical potential, a more detailed understanding of its non-perturbative properties (confinement, chiral symmetry breaking) and their interdependence may be gained.

The transition can be modelled in a first, crude approximation by a percolation scenario: around a critical temperature T_c the hadrons will start to overlap and form a region where their former constituents can stream almost freely over large distances.

We can estimate that this phase transition happens when the hadrons fill up all available space. For a gas of massless pions, its thermal number density reads

$$n_\pi(T, \mu) = 3 \int \frac{d^3p}{(2\pi)^3} \frac{1}{\exp([p - \mu]/T) - 1} \simeq 0.3 T^3 \text{ for } \mu = 0, \quad (1.2)$$

so the condition for percolation becomes $n_\pi(T_c) \simeq V_\pi^{-1}$. Assuming that the volume occupied by a single pion is $V_\pi = (4\pi/3)r_\pi^3$, we obtain

$$T_c \simeq \frac{1}{r_\pi}.$$

Then with a typical hadronic scale, represented by $r_\pi \simeq 0.7$ fm, $T_c = \mathcal{O}(200 \text{ MeV})^1$. In fact, we expect *two* transitions in QCD that are *a priori* not correlated: the deconfinement process, which leads to the liberation of the internal degrees of freedom of the hadrons, and the restoration of the spontaneously broken chiral symmetry, which is a low-energy phenomenon and responsible for the large 'constituent' quark masses $m_q \sim 300$ MeV. Lattice QCD, the numerical *ab initio* simulation of QCD on a discretised Euclidean space-time lattice, has confirmed that qualitative picture of the QCD phase transition at finite temperature and zero density. Recent advances in computing power and algorithms have yielded results on the equation of state, the critical temperature and many more observables with unprecedented accuracy. As $T_c \approx 10^{12}$ K, the QGP is likely to be encountered in nature only in astrophysical contexts: according to the standard cosmological model, it existed a few microseconds after the Big Bang and may have left traces in the primordial nuclear abundances. Apart from that, there are ongoing discussions whether the core of neutron stars, with baryon densities exceeding 10^{15} g/cm^3 , may possibly be composed of one of various manifestations of deconfinement at high density.

The main reason why the QGP has attracted so much interest over the last years is that it may be created in earth-bound experiments, the ultra-relativistic heavy-ion collisions (URHIC). It is expected that the colliding nuclei deposit so much energy in the collision region that a thermalised system of particles forms which subsequently expands and cools off. If the initial energy density is above the critical $\epsilon_c \sim 1 \text{ GeV/fm}^3$, the medium should be describable in terms of a QGP. First dedicated experiments started at CERN at the SPS, followed by the AGS at BNL where already a c.m. energy of $\sqrt{s} \simeq 5$ AGeV was reached. Subsequently, further experiments have been and are still being conducted at CERN with the fixed-target SPS (c.m. energy up to $\sqrt{s} = 17$ AGeV), and are underway at BNL with the collider RHIC (c.m. energy up to $\sqrt{s} = 200$ AGeV). In the future, collision energies will increase by another order of magnitude at the collider LHC ($\sqrt{s} = 5500$ AGeV) at CERN.

A sketch of the expected phase diagram of QCD is shown in figure 1.1. The $(T, \mu_B = 0)$ axis is reasonably well constrained by lattice results whereas the exact line of the phase transition line for non-vanishing baryonic chemical potential is strongly model-dependent and, consequently, has considerably larger errors. The big dots depict the chemical freeze-out points of the various experiments mentioned above, based on a statistical model: the measured abundances of hadrons (π, p, K, \dots) are fitted by an

¹At zero temperature, but finite baryonic chemical potential, the transition is expected to set in at a density of $\rho = 3 - 10 \rho_0$ (corresponding to $\mu_B = 1 - 1.5 \text{ GeV}$), where $\rho_0 = 0.17 \text{ fm}^{-3}$ is the ordinary nuclear density. At much larger densities, a very rich and complex phase structure has been predicted by a number of perturbative calculations [37], among them colour-flavour locking and colour superconducting phases. These are of no concern for this work, though.

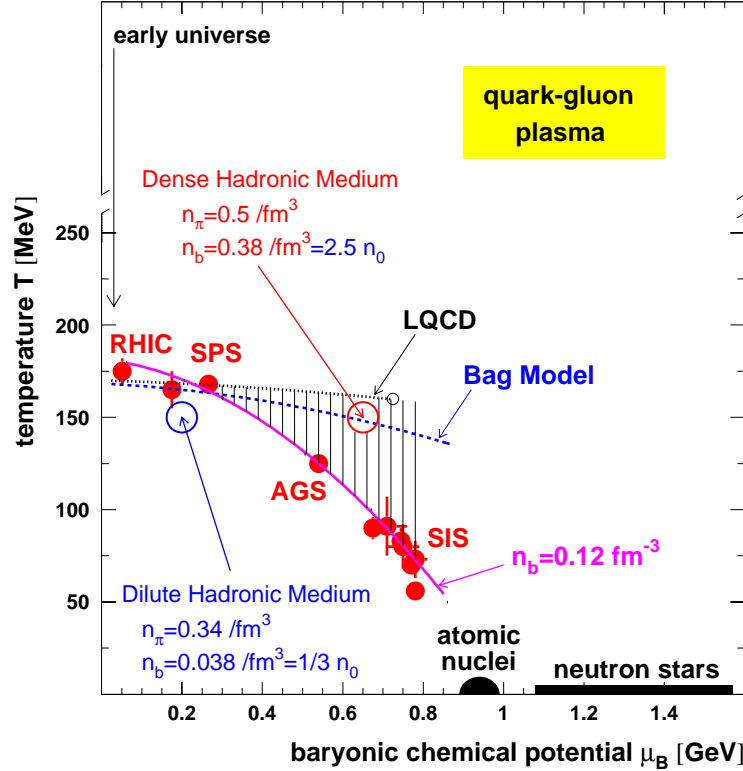


FIGURE 1.1: A sketch of the phase diagram of QCD in the $T - \mu_B$ plane [2]. The dotted line shows the phase transition line as determined from first lattice QCD (LQCD) calculations at finite μ_B [39] that ends in a critical point. The dashed line labels the corresponding line evaluated in a bag model calculation. For further explanations, see text.

ideal gas formula similar to eq.(1.2). The two fit parameters T and μ_B then mark the point of chemical freeze-out (i.e. the point from where on inelastic, particle number changing interactions cease to be efficient in the fireball evolution) in the phase diagram. Apparently, the chemical freeze-out at SPS and RHIC occurs within errors at the phase transition line, indicating (along with other arguments) that the initial energy density is indeed sufficient to create a QGP in experiments.

However, as pointed out so poignantly by Oscar Wilde, the truth is *never* simple. The QGP might very well have been produced, but for us to study its properties, we require it to leave distinct traces in the detectors. Any signature of the QGP is folded with the time evolution (and consequently the evolution of volume, temperature, and baryon density) of the fireball created in a URHIC. Furthermore, this evolution continues after the system runs through the phase transition and thus, any information is mixed with signals from the conventional hadronic phase. The simulation of a heavy-ion collision – multi-particle physics with strong interactions – is in itself a dauntingly complex task. If the system thermalises (and there are good indications for that), a description in terms of averaged thermal properties may be helpful. However, notwithstanding asymptotic freedom, perturbative calculations at finite temperature have failed spec-

tacularly in describing even the most basic features of the QGP (as evaluated on the lattice), let alone calculating signatures with a sufficient accuracy. At the moment, there is no scheme to perform reliable, controllable thermal field theory calculations at reasonable temperatures, only far beyond the Planck scale the existing series start to converge.

An all-embracing description of an URHIC from scratch is therefore clearly out of reach. With that, phenomenology becomes important: heavy-ion physics is a 'data-driven' science. A plethora of models has emerged over the last years that are able to describe isolated pieces of data, at the expense of parametrising parts of the ongoing physics. It is, however, difficult to construct a consistent picture of an URHIC from these different approaches. As an example, we mention ref.[121] where the dilepton data taken at the SPS in Pb(158 AGeV)+Au collisions can be well described when a fireball with initial temperature of 190 MeV is used, whereas ref.[3] needs an initial temperature of 335 MeV in order to fit the direct photon data – within the same experimental setup. That factor of 2 in the temperature translates into roughly an order of magnitude difference in the calculated initial energy density. Clearly, the theoretical uncertainties are much larger than any experimental error bars.

There is therefore not much to be gained from models which dial their parameters to fit a certain piece of data, not regarding that these parameters lead to inconsistent results when a different observable is looked at. On the other hand, experiments and lattice simulations² have accumulated a sufficiently large set of data that eventually allow to constrain models to quite some degree. In the light of these facts, we believe that the time is ripe to adopt a more holistic approach: instead of tailoring a model to every observable, we will explore in a *unified description*, taking into account as much information as is available, to what extent the formation of a QGP can be inferred (with one fundamental assumption, that of local thermal equilibrium) and what its consequences are – that is the main theme of this thesis. We start out with a new description of the medium, a quasiparticle interpretation, with aspects of confinement incorporated, of the QGP for $T \lesssim 3 T_c$, which is the temperature region where current heavy-ion experiments operate. Various lattice data are used to set up the model and test its predictions. Following that, we construct a fireball that is constrained by a multitude of hadronic observables. Its expansion dynamics is largely controlled by the equation of state of the aforementioned quasiparticle model. Having forged this space-time arena, signatures of the QGP can be placed into it. We will have a look at dilepton radiation and J/ψ suppression and compare with experiment, each time consistently modelling the medium above T_c by our quasiparticle model constrained by lattice QCD. It is worth stressing that, in our approach, the fireball evolution is explicitly decoupled from the signatures, it is fixed beforehand and not changed afterwards. The fireball is eliminated as a free parameter since we aim to describe as many observables as possible within a single and tightly constrained framework. In doing so, a small step on the long journey towards a consistent 'standard model' of heavy-ion collisions has hopefully been taken. Last but not least, we close the circle with a more conceptual work and present a simple, yet elegant derivation of asymptotic freedom at high temperatures that has hitherto not been obtainable in a rigorous calculation.

²We frequently adopt the jargon that lattice QCD simulations produce 'data'. At the moment, these are the only reliable sources to assess properties of QCD at high temperature. We will, of course, keep in mind and discuss the inherent limitations of the technique.

In more detail, this thesis is structured as follows:

Since the field of heavy-ion collisions requires a broad knowledge of QCD phenomenology at high temperatures, we present in the second chapter an up-to-date overview of the thermodynamics of QCD, referring mainly to latest lattice data. Within a toy model, a non-perturbative treatment of $\lambda\phi^4$ theory with spontaneous symmetry breaking, we outline the main features of a field theory in the vicinity of a phase transition. We discuss the order parameters of the QCD phase transitions, the critical temperature and its dependence on the number of flavours, bare quark mass and quark chemical potential.

In the third chapter, we construct a novel quasiparticle model of the QGP. First, lattice QCD results of the equation of state (EOS) of pure gauge theory and QCD with a varying number of flavours are discussed, along with a careful assessment of remaining lattice artefacts. Various interpretations of these data have been attempted, most prominently as a gas of massive, non-interacting quark and gluon quasiparticles. We argue that for $T \lesssim 3 T_c$, non-perturbative confinement physics not amenable in an expansion in g starts to become important. Our main new ingredient, as compared to previous work, will be a phenomenological parametrisation of (de)confinement, supplemented by thermal quasiparticle masses compatible with lattice results. The resulting model is tested against a number of lattice data and extended to systems with small quark chemical potential.

We put the quasiparticle formalism to use in two ways in chapter 4: to describe the dynamics of a URHIC, a fireball model reminiscent of hydrodynamics is set up. Assuming isentropic expansion, the EOS of the system will link initial and final states of the collision. The equation of state in the QGP phase for physical values of the quark masses is taken from our quasiparticle setup. This procedure results in a thermodynamically self-consistent description of a fireball evolution which is, for the first time, in accordance with lattice results. We use this fireball in the calculation of dilepton rates. Dileptons (correlated e^+e^- and $\mu^+\mu^-$ pairs) or, equivalently, virtual photons are interesting probes since they do not interact strongly and escape unthermalised from the hot fireball region at all stages of the collision. Therefore, in contrast to hadronic probes which can tell only of the late stages of the fireball expansion (the freeze-out), dileptons also carry information on the early moments of the collision. Whereas in the hadronic phase dileptons predominantly stem from pion and kaon annihilation processes which are enhanced due to the formation of the light vector mesons ρ, ω and ϕ , in the QGP phase they originate mainly from $q\bar{q}$ annihilation processes. If the spectra of the two phases are sufficiently distinct, we might be able to tell the QGP from the ordinary hadronic phase. As it turns out, the dilepton rates are indicative of a possible restoration of chiral symmetry that would imply 'duality' of those spectra. In the region below T_c , we calculate the dependence of the photon spectral function (that enters the dilepton rate) on temperature and baryon density using Vector Meson Dominance combined with Chiral Dynamics. Above T_c , we consistently employ the quasiparticle picture to one-loop order. Folding the spectra with the fireball evolution, we compare the resulting dilepton rates with data taken at the CERES/NA45 experiment from the CERN SPS in Pb(40 AGeV)+Au and Pb(158 AGeV)+Au collisions. We also give estimates for Au+Au collisions with the PHENIX detector setup at RHIC at a c.m. energy of $\sqrt{s} = 200$ AGeV.

For a second signature, we apply the unaltered quasiparticle and fireball models in chapter 5 to the phenomenology of J/ψ suppression. At high temperatures, the gluon density will be so large that the colour interaction between a c and a \bar{c} quark, produced during the initial nuclear impact, is Debye screened. The formation of bound $c\bar{c}$ states ($J/\psi, \psi', \chi_c$) is then aggravated, leading to a suppression of charmonia in heavy-ion collisions. J/ψ suppression hence constitutes an early QGP probe and is considered as a direct signal of the deconfinement transition. We use a kinetic approach to describe the interactions of the J/ψ with the medium that is, above T_c , again modelled by the quasiparticle model. Convolved with the fireball, the resulting suppression pattern is compared with data from the NA50 experiment at the CERN SPS, taken in Pb(158 AGeV)+Pb collisions. RHIC estimates with emphasis on the possibility of colour coalescence are also briefly discussed.

In the sixth chapter, we shift our scope away from experiments towards a more conceptual problem: asymptotic freedom lies at the heart of the QGP, but it has never been explicitly derived at high temperature in a concise manner. We calculate in a transparent fashion perturbatively a running coupling constant in QED and QCD at very high temperatures where the coupling is small, ultimately justifying the phenomenological *ansatz* of Collins and Perry [1] put forward in 1975. Instead of a loop expansion, we evaluate the energy shift of the thermal vacuum to leading order in the coupling constant after applying an external (chromo)magnetic field H , from which we extract an effective, temperature and scale-dependent coupling constant $\alpha_{\text{eff}}(H, T)$ in the limit $H/T^2 \ll 1$, i.e. high temperature and large distances.

The seventh and last chapter summarises our results, concludes and presents an outlook regarding future work.

The appendix lists some general properties of particle spectra at finite temperature. In particular, the perturbative Hard Thermal Loop expressions for quark and gluon propagation in a heat bath are quoted. Finally, some useful expansions of integrals that frequently appear in finite temperature calculations are given.

A note on *conventions*: we use 'God-given' units $\hbar = c = k_B = 1$ throughout. Indices that appear twice in a formula are summed over. Temperature is denoted by T and sometimes by $\beta = 1/T$. A thermal average of an operator \mathcal{O} reads $\langle \mathcal{O} \rangle$, unless there is a possibility of confusion, in which case the T -dependence is explicitly written out as $\langle \mathcal{O} \rangle_\beta$ or $\langle \mathcal{O} \rangle_T$.

2 QCD at Finite Temperature

This chapter introduces QCD and its non-perturbative phenomena. We summarise the basics of thermal field theory, the Hard Thermal Loop calculation scheme and how to “put QCD on the lattice”. The phenomena of phase transitions in a quantum field theory are exemplified using a thermal renormalisation group analysis of $\lambda\phi^4$ theory. Finally we gather what is quantitatively known about the QCD phase transition and its dependences on the external parameters temperature, bare quark mass and quark chemical potential. These results will be extensively referred to in the upcoming chapters.

2.1 QCD at zero temperature

Within our current understanding, the theory of strong interactions is Quantum Chromodynamics (QCD), a non-abelian gauge field theory with the colour gauge group $SU(N_c)$, and $N_c = 3$. The spin-1 gauge boson degrees of freedom, the gluons A_μ^a , are characterised by their colour index a ($a = 1..N_c^2 - 1$) and transform as the adjoint representation of the gauge group. The fermion sector of the theory consists of massive spin- $\frac{1}{2}$ Dirac spinor fields Ψ , the quarks. They belong to the fundamental complex representation of $SU(N_c)$. Each quark carries one of N_c possible colour charges. The dynamics and interactions of these particles are described by the Lagrangian

$$\mathcal{L}_{\text{QCD}} = \mathcal{L}_q + \mathcal{L}_g = \bar{\Psi}(i\gamma_\mu D^\mu - \mathbf{m})\Psi - \frac{1}{4}\mathcal{G}_{\mu\nu}\mathcal{G}^{\mu\nu}, \quad (2.1)$$

which involves the gluonic field-strength tensor

$$\mathcal{G}_{\mu\nu} = (\partial_\mu A_\nu^a - \partial_\nu A_\mu^a + gf^{abc}A_{\mu,b}A_{\nu,c})t_a \quad (2.2)$$

and the gauge covariant derivative

$$D_\mu = \partial_\mu -igt_a A_\mu^a. \quad (2.3)$$

The index $a = 1..8$ is summed over the generators of the $SU(3)$ gauge group $t^a = \lambda^a/2$ that are related to the structure constants of the group by $[t^a, t^b] = if^{abc}t^c$. The strong coupling constant is denoted by g in the following, and $\alpha_s \equiv g^2/(4\pi)$.

Eq.(2.1) is invariant under local gauge transformations $G(x)$

$$\Psi(x) \rightarrow \Psi'(x) = G(x)\Psi(x), \quad \bar{\Psi}(x) \rightarrow \bar{\Psi}'(x) = \bar{\Psi}(x)G^\dagger(x) \quad (2.4)$$

and

$$A_\mu(x) \rightarrow A'_\mu(x) = G(x)A_\mu(x)G^\dagger(x) - \frac{i}{g}G(x)\partial_\mu G^\dagger(x). \quad (2.5)$$

Here, $G(x) = \exp(i\omega_a(x)t^a)$ is a $SU(3)$ rotation matrix in colour space with arbitrary c -functions $\omega_a(x)$.

Among the $N_f = 6$ quark flavours with $m_u, m_d, m_s \approx 4, 7, 150$ MeV and $m_c, m_b, m_t \approx 1.5, 4.5, 170$ GeV, there is a natural separation in sectors of 'light' and 'heavy' quarks. We will mainly consider light quarks in this work: As we work within a temperature range $T \ll m_c$, the influence of heavy quarks on thermodynamics is negligible. With $N_f = 3$ then,

$$\Psi(x) = \begin{pmatrix} u_\alpha(x) \\ d_\alpha(x) \\ s_\alpha(x) \end{pmatrix} \quad (2.6)$$

($\alpha = 1..3$ is a colour index), and the current quark mass matrix in \mathcal{L}_{QCD} becomes

$$\mathbf{m} = \begin{pmatrix} m_u & & \\ & m_d & \\ & & m_s \end{pmatrix}. \quad (2.7)$$

Since QCD is renormalisable, its bare parameters g and m_q depend on the energy scale μ at which the theory is probed. The renormalisation group equation for the running coupling $\alpha_s(\mu)$ reads

$$\mu \frac{d}{d\mu} \alpha_s(\mu) = \beta(\alpha_s) = -\frac{\beta_0}{6\pi} \alpha_s^2 - \frac{\beta_1}{24\pi^2} \alpha_s^3 - \mathcal{O}(\alpha_s^4), \quad (2.8)$$

where

$$\beta_0 = 11N_c - 2N_f \quad \text{and} \quad \beta_1 = 34N_c^2 - \left(10N_c + \frac{3}{N_c}(N_c^2 - 1)\right) N_f. \quad (2.9)$$

Its solution exhibits the famous property of *asymptotic freedom* in QCD:

$$\alpha_s(\mu) = \frac{12\pi}{\beta_0 \log(\mu^2/\Lambda_{\text{QCD}}^2)} - \frac{36\pi\beta_1 \log(\log(\mu^2/\Lambda_{\text{QCD}}^2))}{\beta_0^3 \log^2(\mu^2/\Lambda_{\text{QCD}}^2)} + \mathcal{O}\left(\frac{\log^2(\log \mu)}{\log^3 \mu}\right) \quad (2.10)$$

with $\Lambda_{\text{QCD}} \simeq 0.2 - 0.3$ GeV. Since $N_f < 16$, the coupling constant therefore becomes small at high energies (e.g. $\alpha_s(m_\tau = 1.77 \text{ GeV}) = 0.35$ and $\alpha_s(m_Z = 91 \text{ GeV}) = 0.117$ [4]), thus allowing the perturbative treatment of the interactions between quarks and gluons. As we will elaborate on in chapter 6, asymptotic freedom can be explained semi-classically in terms of a paramagnetic ground state.

In the infrared, the expression for α_s , eq.(2.10), features a Landau pole. Hence, α_s is large at low energies $\lesssim 1$ GeV, and the coloured fundamental quarks and gluons become bound into colourless 'white' hadrons. The phenomenon of the absence of coloured asymptotic states in particle reactions has been baptised *confinement of colour*. Since there are no free quarks observed, the (empty) vacuum of a Fock space is not a suitable ground state anymore to construct a meaningful field theory. Otherwise it would be possible to excite a single, stable quark as an asymptotic state. Comparing experimental upper limits on abundances of free quarks with theoretical expectations in a world without confinement, the discrepancy between these results amounts to a factor of 10^{-15} [5]. This number is unnaturally tiny to be explained in terms of a small parameter. Confinement is then likely to constitute an intrinsic property of the QCD vacuum, not a perturbative phenomenon. Confinement also manifests in the potential between two heavy quarks: the spectra of bound $c\bar{c}$ or $b\bar{b}$ states are well described by the Cornell potential of the form

$$V_{\bar{q}q}(r) = \frac{\bar{\alpha}}{r} + \sigma r, \quad (2.11)$$

i.e. a Coulomb-like $1/r$ term with $\bar{\alpha} \simeq 0.25$ and a linearly rising piece with the string tension $\sqrt{\sigma} \simeq 420$ MeV [4] (see also later figure 5.1). A large separation of the quarks hence would require a very large amount of energy if there were no light quarks present. In the real world, string breaking occurs at a separation of about 1 fm by quark-antiquark production out of the vacuum, and two colour-neutral mesons are formed.

2.2 Symmetries and condensates

In the chiral limit $m_q \rightarrow 0$, the classical QCD Lagrangian shows a wealth of symmetries. After quantisation and regularisation of quantum fluctuations, some of these symmetries are broken. Apart from Poincaré invariance, the classical QCD symmetry group is the direct product of

$$S[\mathcal{L}_{\text{QCD}}]_{cl} = \text{SU}(3)_c \otimes \text{SU}(N_f)_L \otimes \text{SU}(N_f)_R \otimes \text{U}(1)_V \otimes \text{U}(1)_A \otimes \mathcal{C}. \quad (2.12)$$

Invariance under the local colour symmetry $\text{SU}(3)_c$ determines the dynamics of the gauge and quark fields. The global $\text{U}(1)_V$ symmetry enforces baryon number conservation, whereas the axial $\text{U}(1)_A$ symmetry is broken at the quantum level due to the chiral anomaly. It can be connected to the existence of saddle points with finite Euclidean action in the path integral, the instantons.

Since \mathcal{L}_{QCD} in the chiral limit has only a single dimensionless parameter g , the QCD action $S_{cl} = \int d^4x \mathcal{L}_{\text{QCD}}(x)$ is invariant under global scale transformations $\mathcal{C}(\lambda)$ in Minkowski space

$$x_\mu \rightarrow \lambda^{-1} x_\mu, \quad A_\mu^a \rightarrow \lambda A_\mu^a(\lambda x), \quad \Psi \rightarrow \lambda^{\frac{3}{2}} \Psi(\lambda x).$$

The conserved quantity is the dilatation current

$$j_D^\mu = x_\nu T^{\mu\nu}, \quad \partial_\mu j_D^\mu = T^\mu_\mu = 0,$$

where $T^{\mu\nu}$ is the energy-momentum tensor of the theory. Renormalisation introduces a scale Λ_{QCD} to the theory that breaks the conformal symmetry. The divergence of the current j_D^μ becomes

$$\partial_\mu j_D^\mu = \frac{\beta(\alpha_s)}{4\alpha_s} \mathcal{G}_{\mu\nu}^a \mathcal{G}_a^{\mu\nu}$$

with the Gell-Mann-Low beta function of eq.(2.8). To lowest order,

$$\partial_\mu j_D^\mu = -\frac{\beta_0}{24} \mathcal{G}^2, \quad \mathcal{G}^2 = \frac{\alpha_s}{\pi} \mathcal{G}_{\mu\nu}^a \mathcal{G}_a^{\mu\nu}.$$

The scalar vacuum expectation value associated with this broken symmetry is the *gluon condensate*

$$\langle \mathcal{G}^2 \rangle \equiv \langle 0 | \mathcal{G}^2 | 0 \rangle \simeq (1.5 \pm 0.5) \text{ GeV}^3. \quad (2.13)$$

Its numerical value can be extracted from QCD sum rules for charmonium systems [6]. $\langle \mathcal{G}^2 \rangle$ itself is a non-perturbative quantity, as an operator of dimension 4 its dependence on g is non-analytic since $\langle \mathcal{G}^2 \rangle \simeq \exp(-12/[\beta_0 g^2])$.

The low-energy dynamics of hadrons is driven by the *chiral symmetry*. In the limit of vanishing quark masses, \mathcal{L}_{QCD} is invariant under global vector and axialvector rotations in $\text{SU}(3)$ flavour space. Considering this limit is justified as the masses in

(2.7) are small compared to typical hadronic scales of 1 GeV. The flavour components of (2.6) transform for $SU(3)_V$ as

$$\Psi' \rightarrow \exp(i\alpha_i \lambda^i / 2) \Psi$$

and for $SU(3)_A$ as

$$\Psi' \rightarrow \exp(i\gamma_5 \alpha_i \lambda^i / 2) \Psi.$$

When we decompose the quark fields into right- and left-handed chirality components $\Psi_{R,L} = \frac{1}{2}(1 \pm \gamma_5)\Psi$, we obtain a global $SU(3)_L \otimes SU(3)_R$ chiral symmetry in flavour space. The conserved currents are the vector currents

$$j_{V,i}^\mu = \bar{\Psi} \gamma^\mu \frac{\lambda_i}{2} \Psi$$

and the axial vector currents

$$j_{A,i}^\mu = \bar{\Psi} \gamma^\mu \gamma_5 \frac{\lambda_i}{2} \Psi,$$

$i = 1..3$ labelling the flavour. However, there is strong empirical evidence that chiral symmetry is spontaneously broken in the physical vacuum:

- (i) For massless fermions helicity eigenstates are also parity eigenstates. With chiral symmetry unbroken, we would expect degenerate hadronic multiplets of opposite parity (so-called parity doublets) in the meson or baryon spectrum. If we compare the scalar meson octet with the pseudoscalar octet or the axial vector octet with the vector octet, we find substantial mass differences. For example, the mass of the ρ meson ($J^P = 1^-$) with 770 MeV differs considerably from that of its axial partner, the a_1 meson ($J^P = 1^+$) with 1260 MeV.
- (ii) There are eight very light (compared to 1 GeV) bosons ($\pi^\pm, \pi^0, K^\pm, K^0, \bar{K}^0$ and η) that interact weakly at low energies. These particles can be interpreted as *Goldstone bosons* of the spontaneously broken chiral symmetry. The unnaturally large mass of the η' can be traced back to the axial anomaly.

Thus $SU(3)_L \otimes SU(3)_R$ is spontaneously broken down to $SU(3)_V$. The axial symmetry generators do not annihilate the ground state of the theory,

$$\exp(i\gamma_5 \alpha_i \lambda^i / 2) |0\rangle \neq |0\rangle,$$

thus the symmetry is present in the Nambu-Goldstone realisation whereas the vector symmetry is in the Wigner-Weyl realisation with $\exp(i\alpha_i \lambda^i / 2) |0\rangle = |0\rangle$.

Each spontaneously broken global symmetry implies a massless Goldstone boson, so π, K and η acquire their masses of 140-500 MeV only from the explicit symmetry breaking by the finite quark masses (2.7). Another consequence of the Goldstone theorem is that the axial current matrix element between the vacuum and a Goldstone boson is non-vanishing:

$$\langle 0 | j_{A,i}^\mu | \pi_j(p) \rangle = i p^\mu \delta_{ij} f_\pi e^{-ipx}.$$

Considering the $SU(2)$ subgroup ($i=1..3$), π_i denotes the pion field and $f_\pi = 92.4$ MeV the pion decay constant.

In the case of chiral symmetry the *quark condensate* $\langle \bar{q}q \rangle$ acts as an order parameter for the symmetry breaking and can be interpreted as a scalar quark-antiquark pair

condensate in the ground state. It is defined by the short-distance limit of the full quark propagator,

$$\langle \bar{q}q \rangle = - \lim_{y \rightarrow x_+} \text{Tr} \langle 0 | \mathcal{T}[q(x)\bar{q}(y)] | 0 \rangle. \quad (2.14)$$

Here, $q(x)$ is one of the quark fields in (2.6) and $\mathcal{T}[\dots]$ denotes the time-ordered product. Using the Wick theorem,

$$\mathcal{T}[q(x)\bar{q}(y)] = :q(x)\bar{q}(y): + q(x)\widehat{\bar{q}(y)}, \quad (2.15)$$

where $:\dots:$ is the normal-ordering and $\widehat{\dots}$ the contraction of two field operators. Now, the perturbative quark propagator

$$\langle 0 | \mathcal{T}[q(x)\bar{q}(y)] | 0 \rangle = S_F(x-y) = \int \frac{d^4k}{(2\pi)^4} e^{ik(x-y)} \frac{i(\not{k} + m_q)}{k^2 - m_q^2 + i\epsilon}$$

encodes the ultraviolet physics as $y \rightarrow x$, and the normal-ordered terms in eq.(2.15) vanish in perturbation theory at zero temperature. A non-vanishing $\langle \bar{q}q \rangle$ hence stems from long-range, non-perturbative physics. At finite temperature, the ultraviolet behaviour of the theory remains unchanged, but normal-ordered expectation values usually are non-zero. As we will discuss in section 2.4.3, this fact requires a careful interpretation of lattice data on $\langle \bar{q}q \rangle_\beta$ and a re-definition of the order parameter. The condensate can be related to the pion decay constant f_π via the Gell-Mann, Oakes, Renner (GOR) relation [7]

$$m_\pi^2 f_\pi^2 = -\frac{1}{2}(m_u + m_d)\langle \bar{u}u + \bar{d}d \rangle + \mathcal{O}(m_{u,d}^2). \quad (2.16)$$

Taking $m_u = 5$ MeV and $m_d = 7$ MeV yields a value for the quark condensate, $\langle \bar{u}u \rangle = \langle \bar{d}d \rangle \simeq -(250 \text{ MeV})^3$.

2.3 Thermal field theory

The central quantity of a system in thermal equilibrium that incorporates all thermodynamic information is the partition function connected to the statistical density matrix ρ by

$$\mathcal{Z}(T, V) = \text{Tr}[\rho] = \text{Tr}[\exp(-\beta H)] = \sum_n \langle n | e^{-\beta E_n} | n \rangle. \quad (2.17)$$

Here, $\beta = 1/T$, H is the Hamilton operator, and the trace is performed on a complete set of physical eigenstates. The statistical average of an operator \mathcal{O} follows as

$$\langle \mathcal{O} \rangle_\beta \equiv \frac{1}{\mathcal{Z}} \text{Tr}[\rho \mathcal{O}]. \quad (2.18)$$

The thermal excitations of the ground state, the vacuum, are eigenstates of H , that is, particles. Using (2.15) and taking the thermal average $\langle \dots \rangle_\beta$, the free thermal propagator acquires a thermal contribution due to the non-vanishing normal-ordered product of field operators and reads, for the bosonic case,

$$\begin{aligned} \langle \mathcal{T}\phi(x)\phi(x') \rangle_\beta &= \int \frac{d^4k}{(2\pi)^4} e^{-ik(x-x')} D_F(k), \\ D_F(k) &= \frac{i}{k^2 - m^2 + i\epsilon} + 2\pi\delta(k^2 - m^2) f_B(|k^0|), \end{aligned} \quad (2.19)$$

where we have introduced the *Bose-Einstein* particle distribution function

$$f_B(k^0) = \frac{1}{\exp(\beta k^0) - 1}.$$

The second, T -dependent part of the propagator hence describes the propagation of "on-shell" particles from the heat bath with their respective probability of being there with the appropriate (positive) energy $|k^0|$. For fermions, the different sign convention for the time-ordered product of spinor fields has to be taken into account, and we obtain for the free propagator

$$S_F(k) = (\not{k} + m) \cdot \left(\frac{i}{k^2 - m^2 + i\epsilon} - 2\pi\delta(k^2 - m^2)f_D(|k^0|) \right) \quad (2.20)$$

with

$$f_D(k^0) = \frac{1}{\exp(\beta k^0) + 1}, \quad (2.21)$$

the *Fermi-Dirac* distribution function [8, 9].

Consider a scalar field ϕ with a Lagrangian $\mathcal{L}[\phi]$. Since the statistical density operator $\rho = \exp(-\beta H)$ can be regarded as a time evolution operator in imaginary time over the interval $[0, \beta]$, the partition function for $\phi(x)$ can be expressed in terms of a Euclidean path integral

$$\mathcal{Z}(T, V) = \oint \mathcal{D}\phi \exp \left(- \int_0^\beta d\tau \int_V d^3x \mathcal{L}_E[\phi(\tau, \vec{x})] \right), \quad (2.22)$$

with the sum restricted over periodic field configurations $\phi(0, \vec{x}) = \phi(\beta, \vec{x})$. Due to their spinor nature, fermionic fields obey anti-periodic boundary conditions. Field theory at finite temperature is then equivalent to a Euclidean field theory in a four-dimensional space-time with the time component compactified on a ring with circumference $\beta = 1/T$. For an observable represented by the operator $\mathcal{O}[\phi]$ in contact with a heat bath, its expectation value in the canonical ensemble becomes

$$\langle \mathcal{O} \rangle_\beta = \frac{1}{\mathcal{Z}} \oint \mathcal{D}\phi \mathcal{O}[\phi] \exp \left(- \int_0^\beta d\tau \int_V d^3x \mathcal{L}_E[\phi(\tau, \vec{x})] \right). \quad (2.23)$$

The formal similarity of (2.22) with the generating functional $Z[J]$ for vanishing external sources J at zero temperature makes both perturbative (Feynman diagram) and lattice techniques easily adaptable tools to evaluate $\langle \mathcal{O} \rangle_\beta$. The corresponding expression of (2.22) for QCD follows as

$$\mathcal{Z}(T, V, m_0, \mu) = \oint \mathcal{D}A_\mu \mathcal{D}\bar{\Psi} \mathcal{D}\Psi \exp \left(- \int_0^\beta d\tau \int_V d^3x \{ \mathcal{L}_G^E + \mathcal{L}_q^E(m_q) - \mu \Psi^\dagger \Psi \} \right), \quad (2.24)$$

where \mathcal{L}_G^E and \mathcal{L}_q^E are the Euclidean versions of eq.(2.1), and we have introduced an explicit dependence on the additional external parameters, quark chemical potential μ and bare quark mass m_q .

2.3.1 Perturbative techniques

In the imaginary time formalism, the only modifications of the usual Feynman rules at $T = 0$ arise from the (anti)periodic boundary conditions in (2.22) that lead to a discretisation of imaginary (Matsubara) frequencies in momentum space [8, 9]. The loop integrals are replaced by

$$\int \frac{d^4 k}{i(2\pi)^4} \rightarrow \frac{1}{\beta} \sum_{n=-\infty}^{+\infty} \int \frac{d^3 k}{(2\pi)^3},$$

and energy-momentum conserving delta functions become

$$i(2\pi)^4 \delta^{(4)}(k) \rightarrow \beta(2\pi)^3 \delta_{n,0} \delta^{(3)}(\vec{k}).$$

Furthermore, all frequencies are changed to

$$k_0 \rightarrow \frac{2\pi i}{\beta}(n + \zeta), \quad n \in \mathbb{Z} \text{ and } \zeta = \begin{cases} 0 & \text{for bosons,} \\ \frac{1}{2} & \text{for fermions.} \end{cases}$$

Perturbation theory can also be formulated directly in real time where the separation between $T = 0$ and T -dependent contributions is obvious from the beginning. The time integration in (2.23) runs then from $-\infty$ to $+\infty$. However, owing to the different boundary conditions compared to the $T = 0$ case, the field degrees of freedom are doubled, and the propagator acquires a 2×2 matrix structure. There is a second 'ghost' field which has an unphysical complex time component which is, loosely speaking, necessary to return from $t = +\infty$ to $t = -\infty - i\beta$. Of course, only the field with a real time component occurs on the external lines of a propagator. However, the ghost field is essential for a consistent real-time theory. Without it, ill-defined products of δ -functions with the same argument – pinch singularities – would arise in loop calculations.

As a simple example, we calculate the tadpole diagram in massless $\lambda\phi^4$ theory. The T -independent part vanishes in dimensional regularisation. Furthermore, in this specific case it is sufficient to directly integrate over the thermal propagator of eq.(2.19). The result reads

$$\begin{aligned} \Pi(T) &= \frac{\lambda}{2} \int \frac{d^4 k}{(2\pi)^4} f_B(|k^0|) (2\pi) \delta(k^2 - m^2) \\ &= 2 \frac{\lambda}{2} \int \frac{d^3 k}{(2\pi)^3} \frac{1}{2\omega_k} f_B(\omega_k), \end{aligned} \quad (2.25)$$

the 2 in front counting particle and antiparticle alike. For massless particles, the integral can be carried out analytically:

$$\Pi(T) = m_\beta^2 = \frac{\lambda T^2}{4\pi^2} \int_0^\infty dx \frac{x}{e^x - 1} = \frac{\lambda}{24} T^2. \quad (2.26)$$

Since this result is momentum-independent, $\Pi(T)$ can be interpreted as a thermal mass m_β^2 that arises from the continuous interaction of the propagating particle with the heat bath. This is a radiatively generated mass which does not break any chiral symmetries present in the original Lagrangian since finite temperature only induces a mixing of states.

Finally, it is worth noting that finite temperature does not destroy the renormalisability of a theory: renormalisation of the considered theory at zero temperature suffices and no new counter-terms are needed. The heat bath introduces a new scale, T , in the system, but this does not change the ultraviolet behaviour of the considered theory as for $k^2 \gg T^2$, medium effects are unimportant. This is also clear from the fact that the Bose- or Fermi-Dirac functions cut off the momentum integrals at values $k = \mathcal{O}(T)$.

2.3.2 Hard Thermal Loops

In a renormalisable theory with no masses, only one dimensional scale Λ , the renormalisation point, is present. Consider now the calculation of a loop diagram, say, the self-energy Π at external momentum p^μ and $g \ll 1$. At zero temperature, dimensional arguments and Lorentz invariance dictate $\Pi(p) = g^2 p^2 f(p^2/\Lambda^2)$, where $f(x)$ is a dimensionless function, and the self-energy can be resummed in the propagator (as long as $f(x)$ does not blow up) where it modifies the physical mass and the decay width. Switching on the heat bath introduces a second scale, the temperature T . Owing to the on-shell character of thermally propagating particles in a loop, the corresponding loop integrals are dominated by momenta $k \sim T$. Since a thermal self-energy leads to the appearance of a thermal mass term $m_\beta^2 \sim g^2 T^2$, it can only be resummed if $p^2 \gg m_\beta^2$. If p^μ is soft, $p \sim gT$, the correction becomes as large as the inverse bare propagator, and naive perturbation theory breaks down. A resummation of the dominant collective effects from the onset becomes necessary.

The Hard Thermal Loop (HTL) resummation scheme [10, 11] reorganises perturbation theory such that at least the contributions from the HTLs are consistently resummed. It starts with the distinction between hard ($p^\mu \sim T$) and soft ($p^\mu \sim gT$) momenta. Subsequently, the thermal mass is generated by a loop integral where the momentum running inside the loop is hard. Whereas hard external momenta do not require resummation, for soft momenta resummed propagators have to be used to include the collective effects that enter predominantly at these momentum scales. The crucial point is that HTLs do not only exist in scalar theories, but also in gauge theories (see appendix B): the general form of the thermal self-energy is always $m_\beta^2 h(p^0, \vec{p}, T)$, where h is a dimensionless function. Formally, an effective QCD Lagrangian for the soft modes that arises from integrating out all hard modes [8, 12] can be written down:

$$\mathcal{L}_{\text{HTL}} = m_f^2 \int \frac{d\Omega_v}{4\pi} \bar{\Psi} \frac{\not{v}}{v^\nu D_\nu} \Psi - \frac{3}{2} \omega_{\text{pl}}^2 \text{Tr} \int \frac{d\Omega_v}{4\pi} \mathcal{G}^{\mu\alpha} \frac{v_\alpha v^\beta}{(v^\nu D_\nu^{\text{adj}})^2} \mathcal{G}_{\mu\beta}. \quad (2.27)$$

Here, $\omega_{\text{pl}}, m_f \sim gT$ are the bosonic and fermionic plasma frequencies (B.16) and (B.25), respectively, and v^μ is associated with the light-like four-velocity of the hard thermal plasma constituents $p^\mu \sim T v^\mu$. $d\Omega_v$ stands for a spatial average over v . Most importantly, it can be shown that \mathcal{L}_{HTL} is manifestly gauge invariant and gauge independent. The covariant derivative D_μ in the denominators makes the Lagrangian non-local, leading in general to an involved form of the HTL vertices.

2.3.3 Lattice techniques

A complementary way to evaluate \mathcal{Z} is based on lattice techniques. Since large fluctuations in (2.24) are exponentially damped (instead of strongly oscillating in Minkowski space), the numerical evaluation of the path integral is possible within Monte-Carlo techniques. Furthermore, the introduction of a lattice spacing a introduces a cut-off

$1/a$ in momentum space that regularises the continuum-inherent ultraviolet divergences. Space-time is then discretised onto a grid of lattice sites, parametrised by

$$x^\mu = a(n_0, n_1, n_2, n_3)^T, \quad n_i \in \mathbb{N}.$$

The total extent of the lattice is given by the number of spatial (N_σ^3) and temporal lattice sites N_τ . Volume and temperature are related to those by

$$V = (N_\sigma a)^3 \quad \text{and} \quad \beta = \frac{1}{T} = N_\tau a.$$

In order to preserve the underlying gauge symmetry of the QCD Lagrangian (2.1) even in the discretised version, new degrees of freedom are chosen that transform in a simple fashion under $SU(3)$ [13]. For \mathcal{L}_G in (2.1), these are link variables between adjacent lattice sites x and $x + a\hat{\mu}$:

$$U_\mu(x) = \mathcal{P} \exp \left(ig \int_x^{x+a\hat{\mu}} dx'_\mu A^\mu(x') \right).$$

Here, \mathcal{P} denotes path ordering along the integration contour, and $\hat{\mu}$ is a unit vector pointing along a lattice link. Since the link variables transform homogeneously under gauge transformation, $U_\mu(x) \rightarrow G(x)U_\mu(x)G^\dagger(x + a\hat{\mu})$, the simplest gauge-invariant object is a traced closed link around a lattice plaquette

$$\mathcal{U}_{\mu\nu} = \text{Tr}[U_\mu(na)U_\nu(na + \hat{\mu}a)U_\mu^\dagger(na + \hat{\nu}a)U_\nu^\dagger(na)]. \quad (2.28)$$

This expression already yields a discretised approximation of the action since

$$\text{Re } \mathcal{U}_{\mu\nu} = N_c - \frac{N_c g^2 a^4}{2} \mathcal{G}_{\mu\nu} \mathcal{G}^{\mu\nu} + \mathcal{O}(a^6).$$

Summing over all lattice sites and introducing an effective temperature $\bar{\beta}$, the so-called *Wilson action* is then given by

$$S_G^W = \bar{\beta} \sum_{n, 0 \leq \mu < \nu \leq 3} P_{n, \mu\nu} \quad (2.29)$$

with

$$P_{n, \mu\nu} = 1 - \frac{1}{N_c} \text{Re } \mathcal{U}_{\mu\nu} \quad \text{and} \quad \bar{\beta} = \frac{2N_c}{g^2}. \quad (2.30)$$

Since S_G contains no dimensionful parameter, the lattice spacing a enters only by renormalisation group arguments: demanding that physical quantities remain unchanged under a change of a requires $g = g(a)$. For large $\bar{\beta}$,

$$a\Lambda_T \simeq \exp(-\bar{\beta}/\beta_0),$$

where $\beta_0 > 0$ from (2.9). Hence, for $g \rightarrow 0$ also $a \rightarrow 0$, indicating the existence of a sensible continuum limit. The scale parameter Λ_T is a constant of integration and is determined by calculating on the lattice an experimentally measured quantity, usually taken to be the ρ meson mass or the string tension σ . The Wilson action (2.29) is an $\mathcal{O}(a^2)$ approximation to the continuum action. More sophisticated actions exist (tree level improved Symanzik action [14], tadpole improved actions [15]) that eliminate the $\mathcal{O}(a^2 g^0)$ cut-off terms and also take into account interactions, allowing the use of a comparably small lattice extension in temporal direction, i.e. $N_\tau = 4 - 8$.

The incorporation of chirally symmetric fermions on the lattice is difficult because of the antiperiodicity of the fermion fields. Naively taking the difference approximation for the derivative in \mathcal{L}_q , $\partial_\mu \Psi(x) \simeq [\Psi(x + \hat{\mu}) - \Psi(x - \hat{\mu})]/(2a)$, leads to a different particle content of the continuum theory than we have started with. The lattice propagator for a massless fermion has not only a pole at $p = 0$, as expected, but also at the end of the Brillouin zone $p_\mu a = \pi$. For each dimension, the number of particles hence doubles, leading to $2^4 = 16$ fermions in the continuum limit. Recently, formalisms have been developed that both conserve chiral symmetry and avoid the doubling problem simultaneously by introducing an extra fifth dimension [16]. Since the required computing power increases dramatically, first studies with these actions have only been exploratory. The problem can also be circumvented by adding an effective mass term for the unwanted fermion that diverges as $1/a$ [17]. This additional term for the *Wilson fermions*, however, violates chiral symmetry to $\mathcal{O}(a)$, requiring a careful continuum extrapolation of quantities like $\langle \bar{q}q \rangle$. Alternatively, it is possible to keep a continuous subgroup of the chiral symmetry even at finite a by distributing the Dirac spinors over several lattice sites (*staggered* or *Kogut-Susskind fermions*), effectively reducing the number of doubled fermions to $N_f/4$ [18]. The corresponding discretised action reads, after integrating out the staggered fermions,

$$\mathcal{Z}(N_\sigma, N_\tau, T, m_q, \mu) = \int \sum_{n, \mu} d\mathcal{U}_{\mu\nu} (\text{Det} Q^{\text{KS}}(m_q, \mu))^{N_f/4} \exp(-\beta S_G). \quad (2.31)$$

Here, S_G stands for a suitably improved gluonic action, and $Q^{\text{KS}}(m_q, \mu)$ is the staggered fermion matrix and includes all dependence on m_q and μ . Since the number of flavours only appears in the power of the determinant, by analytic continuation it is possible to simulate theories with 2 or 3 flavours with this action.

2.4 The QCD phase diagram

2.4.1 Orders of magnitude

A bosonic massless particle in a weakly interacting heat bath has an average absolute three-momentum

$$\langle k \rangle = \frac{\int d^3k k f_B(k)}{\int d^3k f_B(k)} \approx 2.7 T. \quad (2.32)$$

Furthermore,

$$\sqrt{\langle k^2 \rangle} \approx 3.2 T, \quad (2.33)$$

so the fluctuation becomes

$$\Delta k = \sqrt{\langle k^2 \rangle - \langle k \rangle^2} \approx 1.7 T. \quad (2.34)$$

For fermions, $\langle k \rangle \approx 3.2 T$, $\sqrt{\langle k^2 \rangle} \approx 3.6 T$ and $\Delta k \approx 1.7 T$. Alternatively, one may also argue that at high temperatures only the lowest, non-vanishing Matsubara frequencies dominate the thermal physics (because all higher modes become increasingly suppressed), therefore the relevant scale is

$$\langle k \rangle = 2\pi T \text{ for bosons and } \langle k \rangle = \pi T \text{ for fermions.} \quad (2.35)$$

We will ultimately show in chapter 6 that this is indeed a sensible choice. Assuming that the average squared momentum transfer between particles is of the order k^2 , we may substitute $\mu^2 \sim 10 T^2$ in the running coupling $\alpha_s(\mu)$ of eq.(2.10) to get at leading order

$$\alpha_s(T) = \frac{12\pi}{\beta_0 \log(T^2/\Lambda_T^2)} \text{ with } \Lambda_T \simeq \Lambda_{\text{QCD}}/3 \simeq 100 \text{ MeV.} \quad (2.36)$$

Hence, α_s should become small as $T \gtrsim (2-3)\Lambda_{\text{QCD}} = \mathcal{O}(500 \text{ MeV})$, setting the scale where a perturbative description of the QCD plasma in terms of elementary partons might become reasonable. The colourless hadrons will then release their parton content at some critical temperature $T_c = \mathcal{O}(\Lambda_{\text{QCD}})$. The subsequent increase of the thermally active number of degrees of freedom will reflect in bulk thermodynamical properties such as the pressure: in the chiral ideal gas limit, the ratio of the pressure of a pion gas and a QGP becomes

$$\frac{p_\pi^{\text{id}}}{p_{\text{QGP}}^{\text{id}}} \sim \frac{p(T \rightarrow 0)}{p(T \rightarrow \infty)} = \frac{3}{2(N_c^2 - 1) + 10.5N_f} \simeq \frac{1}{12} \quad (2.37)$$

for a two flavour QGP, and this drastic change is indeed seen in lattice calculations (see chapter 3). We hence expect a confinement/deconfinement phase transition. In addition, low energy phenomena like spontaneous symmetry breaking will be absent at sufficiently high T , so the global chiral symmetry of \mathcal{L}_{QCD} is restored at some stage, accompanied by a vanishing quark condensate. However, since temperature is a new scale in the system, the conformal symmetry remains broken even for $T \gg \Lambda_{\text{QCD}}$, and the gluon condensate stays non-zero at high T , cf. figure 3.7.

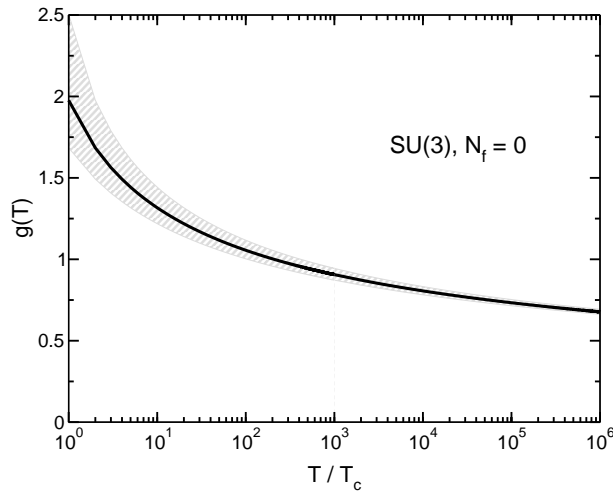


FIGURE 2.1: The one-loop running coupling $g(T)$ as a function of T/T_c in pure SU(3) gauge theory. The hatched band is obtained by varying the renormalisation point μ in (2.10) from $\mu = \pi T$ (upper limit) to $\mu = 4\pi T$ (lower limit). The solid line shows $g(2\pi T)$.

It is, however, important to keep in mind that at finite temperature, not the smallness of α_s is indicative of the validity of perturbative calculations, rather it is $g(T)$. The HTL resummation programme requires $g \ll 1$, not $\alpha_s \ll 1$, for its separation of hard and soft scales in the plasma. Collective 'soft' effects are usually of the order gT (not $\alpha_s T$) and can only be consistently resummed if they are a small correction to the 'hard' physics at a scale T . If g is of order one, there is no distinction between hard and soft modes, and the HTL programme is not applicable. Figure 2.1 shows the one-loop running coupling $g(T) = \sqrt{4\pi\alpha_s(T)}$ from (2.36) as a function of T/T_c in pure SU(3) gauge theory. T_c is taken to be 270 MeV, see eq.(2.51). Even when varying the renormalisation point μ in eq.(2.10) from πT to $4\pi T$, the coupling g is never small for all temperatures of interest, and this does not change when the two-loop result for $\alpha_s(\mu)$ or quark flavours are included. Inserting numbers, $g(T) < 0.5$

for $T > 10^8$ GeV and $g(T) < 0.25$ only for $T > 10^{36}$ GeV, which casts serious doubt on the applicability of perturbative calculations for all temperatures of interest. For comparison, the Planck scale beyond which gravitation will play a dominant role is about 10^{19} GeV. We will discuss perturbative results on the equation of state in section 3.2 and on the Debye screening mass in section 6.2. Comparing these with lattice data, it will turn out that (bare) perturbation theory does indeed a spectacularly bad job, necessitating a more phenomenological description of the QGP.

2.4.2 A non-perturbative toy model

In order to get insight into the thermal behaviour of a quantum field theory with spontaneous symmetry breaking (SSB) at $T = 0$, this section outlines the non-perturbative thermal renormalisation group (TRG) analysis applied to $\lambda\phi^4$ scalar field theory with broken $Z(2)$ symmetry. Although not comparable in complexity with QCD, all the main features of thermal phase transitions can already be studied within the model that henceforth may serve as a reference point. The TRG for scalar fields has been introduced in [19] and subsequently extended to gauge theories [20] and fermions [21]. Applications to the $O(1)$ model [19, 22], the $O(N)$ model [23] and the chiral phase transition [21] have shown that the TRG is suitable to calculate universal and non-universal quantities of phase transitions. More recently, the TRG has also been used to calculate a dynamical quantity, the plasmon damping rate [24, 25]. Here, we want to study the theory for $|T_c - T| \lesssim T_c$ since that temperature region is approximately covered by heavy-ion collisions to date.

In the following, we consider a single real scalar field $\phi(x)$. An extensive discussion of the TRG and the derivation of the flow equation can be found in [19] and [23]; here we will only sketch the basic ideas. In the real-time formulation of thermal field theory, the 2-point Green function separates into a $T = 0$ quantum part and a finite temperature part where a Bose-Einstein distribution function appears, as apparent, e.g., from the 11-component of the thermal matrix propagator, $i\Delta_{11}(k) = D_F(k)$, with D_F as in eq.(2.19). Since the thermal excitations of the vacuum are real particles, the thermal part acts only on the on-shell sector of the theory. Therefore it is possible to distinguish between hard and soft *thermal* modes even in Minkowski space. The TRG introduces a momentum cut-off Λ acting only on the thermal part of the tree-level propagator, by replacing $f_B(|k^0|) \rightarrow f_B(|k^0|)\theta(|\vec{k}| - \Lambda)$, where $\theta(x)$ is the Heaviside step function. The effective action $\Gamma[\phi]$ which generates the full OPI n -point correlation functions, depends now on Λ . It is straightforward to derive a functional differential equation for Γ_Λ that tells us how the cut-off dependent effective action evolves as Λ changes:

$$\Lambda \frac{\partial}{\partial \Lambda} \Gamma_\Lambda[\phi] = \frac{i}{2} \text{tr} \left\{ \Lambda \frac{\partial D_\Lambda^{-1}}{\partial \Lambda} \cdot \left[\frac{\delta^2 \Gamma_\Lambda}{\delta \phi \delta \phi} + D_\Lambda^{-1} \right]^{-1} \right\}. \quad (2.38)$$

Here the trivial kinetic part has been subtracted from Γ_Λ . The trace stands for a sum over the thermal, momentum and possible internal indices, and D_Λ is the real-time matrix propagator of the scalar field, with the cut-off imposed on the thermal part. For $\Lambda \rightarrow \infty$, the thermal contribution to D_Λ is exponentially suppressed, and we recover the full $T = 0$, quantum action, which acts as the boundary condition for (2.38). Lowering Λ corresponds to integrating out thermal modes with a momentum $|\vec{k}| > \Lambda$, and in the limit $\Lambda \rightarrow 0$, the full thermal action is obtained. Renormalisation group flow equations for various Green functions are now simply obtained from (2.38) by taking functional derivatives with respect to ϕ .

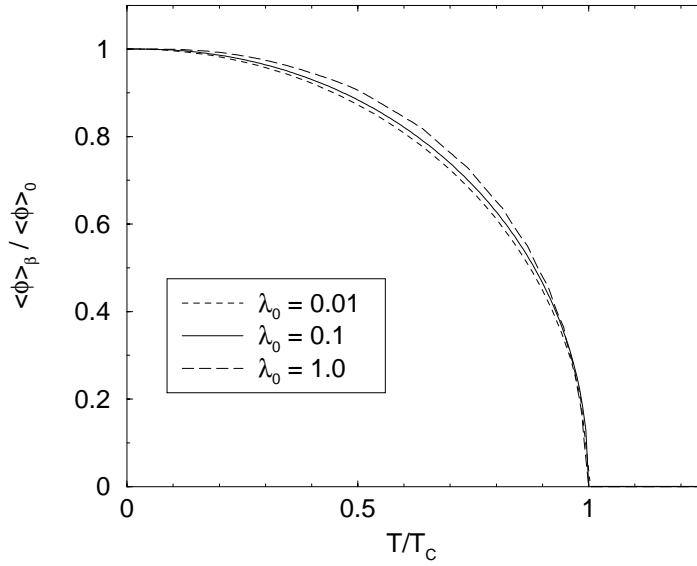


FIGURE 2.2: Ratio of expectation values $v_\beta/v_0 = \langle \phi \rangle_\beta / \langle \phi \rangle_0$ as a function of T/T_c for the couplings $\lambda_0 = 0.01, 0.1$ and 1 . The thermal expectation value v_β is obtained from $V'(v_\beta) = 0$.

The functional integro-differential equation (2.38) is too difficult to solve, so to proceed we perform a derivative expansion of Γ and keep only the first non-trivial term, the effective potential V :

$$\Gamma_\Lambda[\phi] = -V_\Lambda(\phi) \int d^4x.$$

This approximation amounts to neglecting the momentum dependence of the self energy and of the four-point vertex. It can be interpreted as an expansion in the anomalous dimension η which is known to be small ($\eta \approx 0.05$). The second approximation consists in discarding the imaginary part of the self-energy in the full propagator appearing in (2.38). This runs under the 'quasi-particle' approximation and is supposed to be valid as long as λ is small. After some manipulations we end up with the following flow equation:

$$\Lambda \frac{\partial}{\partial \Lambda} V_\Lambda(\phi) = -\frac{\Lambda^3}{2\pi^2\beta} \ln \left(1 - \exp \left\{ -\beta \sqrt{\Lambda^2 + V_\Lambda''(\phi)} \right\} \right) \theta(\Lambda^2 + V_\Lambda''(\phi)). \quad (2.39)$$

Considering V a function of the cut-off Λ and the field ϕ , eq.(2.39) is a non-linear, partial differential equation, with the boundary condition that $V_\infty(\phi)$ is the renormalised effective potential at zero temperature. This equation can be solved numerically. We will be mainly interested in the solutions for the two-point and four-point functions, i.e. the thermal mass and the coupling constant.

Let us describe a phase with spontaneous symmetry breaking by an interaction Lagrangian $\mathcal{L}_{\text{int}} = +\mu^2\phi^2/2 - \lambda\phi^4/24$. For the time being, we do not include $T = 0$ quantum corrections to the effective potential. The Lagrangian $\mathcal{L} = 1/2 (\partial_\mu\phi)(\partial^\mu\phi) + \mathcal{L}_{\text{int}}$ is invariant under a global $Z(2)$ transformation, i.e. $\phi(x) \rightarrow -\phi(x)$, whereas the ground state is not. The parameter that describes the strength of the SSB is therefore the non-vanishing vacuum expectation value of ϕ , $v_0 = \langle 0|\phi|0\rangle = \sqrt{6\mu^2/\lambda}$. Since SSB usually constitutes an infra-red effect, one would expect that the corresponding symmetry

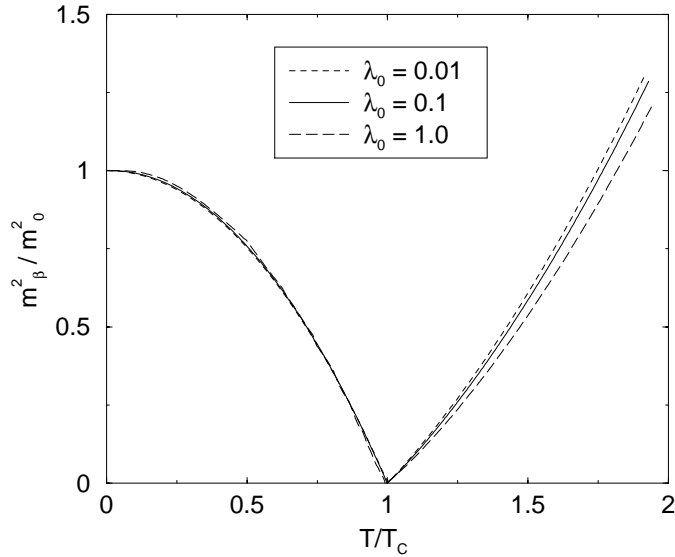


FIGURE 2.3: Ratio of the thermal mass m_β^2 over the zero temperature mass $m_0^2 = 2\mu^2$ as a function of T/T_c for the couplings $\lambda_0 = 0.01, 0.1$ and 1 .

becomes restored at high temperatures $T \gg v_0$, hence a suitable order parameter for the transition from the broken to the unbroken phase is the thermal expectation value of ϕ , $v_\beta = \langle \phi \rangle_\beta$. The critical temperature can be defined as the point where $v_\beta = 0$, and, to one-loop order in perturbation theory, is calculated as $T_c^{(1)} = 2v_0$.

The results of the full TRG calculation for v_β for the couplings $\lambda_0 = 0.01, 0.1$ and 1 are displayed in figure 2.2. The order parameter v_β smoothly approaches zero, as expected for a second order phase transition, and the qualitative shape of the curve remains the same when the coupling strength is increased. Furthermore, to a good accuracy T_c stays equal to $2v_0$ even for large couplings, in accordance with an explicit calculation of $T_c/T_c^{(1)}$ in [23]. Figure 2.3 shows the evolution of the thermal mass for $\mu^2 = 1$ and $\lambda = 0.01, 0.1$ and 1 with increasing temperature on both sides of the phase transition. The mass follows from

$$m_\beta^2 = \left. \frac{\partial^2 V(\phi, \Lambda)}{\partial \phi^2} \right|_{\phi=v_\beta, \Lambda=0}. \quad (2.40)$$

Starting from its zero temperature value $m_0^2 = 2\mu^2$, m_β^2 drops as T grows and reaches zero at T_c . This confirms the divergence of the correlation length $\xi \sim m_\beta^{-1}$ which characterises the spatial exponential decay of correlation functions.

There have been attempts to describe the phase transition in terms of resummed perturbation theory. Since in $\lambda\phi^4$ theory the only HTL is the simple momentum-independent tadpole (2.26), the resummations can even be carried out iteratively, leading to so-called “superdaisy”-resummed perturbation theory. All these techniques, however, fail to reproduce the correct critical behaviour at the second-order phase transition [26] which can be traced back to the fact that they do not take into account the thermal running of the coupling constant, which is a major effect in the vicinity of the phase transition [27, 28, 19]. In order to exhibit the phenomenon of critical

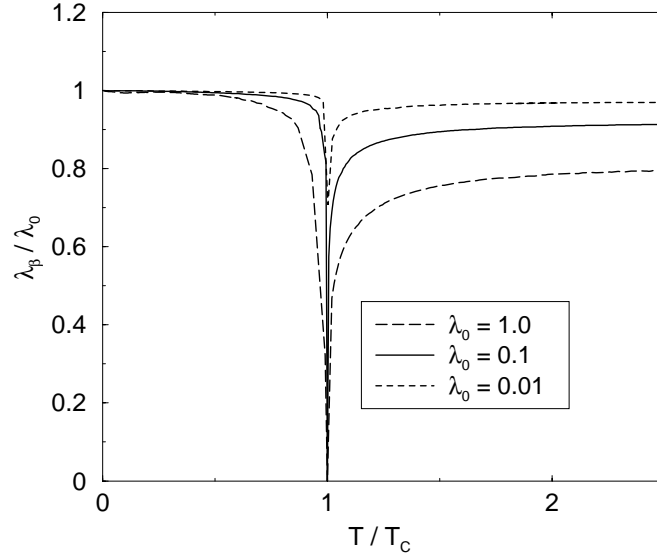


FIGURE 2.4: Ratio of the thermal coupling constant λ_β over λ_0 as a function of T/T_c for the couplings $\lambda_0 = 0.01, 0.1$ and 1 .

slowing down, i.e. the vanishing of the thermal damping rate γ_β as the correlation length grows larger and larger, λ_β has to approach zero as $T \rightarrow T_c$. In figure 2.4, we plot the results of the TRG calculation for

$$\lambda_\beta = \left. \frac{\partial^4 V(\phi, \Lambda)}{\partial \phi^4} \right|_{\phi=v_\beta, \Lambda=0} \quad (2.41)$$

for both phases. The vanishing of the coupling constant is indeed observed at either side of the transition. Since \mathcal{L}_{int} contains a mass scale, the T -dependence of $\lambda(T)$ is non-trivial, although we did not include quantum corrections to the effective potential. In the broken phase, for a small coupling $\lambda_0 = 0.01$ or 0.1 , λ_β stays almost constant at its zero temperature value up to $|T_c - T|/T_c \sim 0.1$, then abruptly drops to zero at T_c . The presence of trilinear couplings in the broken phase seems to suppress the thermal renormalization of the 4-point coupling constant for temperatures not too close to T_c . For a larger coupling $\lambda_0 = 1$, the deviation from the zero temperature value starts earlier, but the most dramatic change happens again near T_c . The behaviour of the coupling constant in the restored symmetric phase is different: λ increases at a slower rate from zero to a value close to the classical λ as the system becomes more and more similar to an initially $Z(2)$ -symmetric system for $T^2 \gg \mu^2$. This is true for both small and large couplings. Note that the behaviour of $\lambda(T)$ close to T_c deviates dramatically from the expected logarithmic running

$$\lambda(T) \sim 1/\log(T),$$

over the range $|T - T_c| < T_c$ it is better parametrised by

$$\lambda(T) \sim |T - T_c|^\gamma, \quad (2.42)$$

where γ is a kind of a critical exponent. The vanishing of λ_β also implies that it takes longer and longer for long wavelength modes to come into equilibrium close to T_c which may have observable consequences in heavy-ion collisions [29].

To summarise: close to the second-order phase transition investigated here, mass and coupling constant deviate significantly from perturbative expectations. As anticipated, both show critical behaviour. The qualitative form of the curves remains the same when the zero temperature coupling strength is increased by two orders of magnitude. When we construct a phenomenological model for the QCD phase transition in chapter 3, we will use these results as a guideline.

2.4.3 Order parameters and critical temperature

As outlined above, a phase transition is frequently associated with the restoration of a spontaneously broken symmetry and hence connected to global symmetries of the Lagrangian. With the QCD Lagrangian (2.1), a concise order parameter can so far only be chosen in the chiral ($\mathbf{m} = 0$) or in the $\mathbf{m} = \infty$ limit. The first one is associated with the chiral symmetry restoration of QCD with N_f massless flavours, restoring the $SU(N_f)_V \otimes SU(N_f)_A$ in (2.12), the second one with the deconfinement transition in a pure Yang-Mills theory. The chiral condensate $\langle \bar{\Psi}\Psi \rangle$ (cf. (2.14)) constitutes a natural order parameter for the chiral phase transition. Analogously to figure 2.2, we expect (in the chiral limit, $\mathbf{m} \rightarrow 0$):

$$\langle \bar{\Psi}\Psi \rangle \begin{cases} \neq 0 & T \text{ small,} \\ = 0 & T \text{ large.} \end{cases}$$

When evaluated on the lattice, $\langle \bar{\Psi}\Psi \rangle$ indeed shows a qualitative change in behaviour when a certain temperature is crossed, as apparent from the right panel of figure 2.5¹. However, care has to be taken in interpreting lattice data when the chiral condensate is evaluated by the derivative of the pressure

$$\langle \bar{\Psi}\Psi \rangle = \frac{\partial p(T, m_q)}{\partial m_q}, \quad (2.43)$$

as done in figure 2.5. Lattice calculations can so far not be performed in the chiral limit, so m_q will always be different from zero in actual simulations. With definition (2.43), $\langle \bar{\Psi}\Psi \rangle$ is then non-vanishing even for an ideal, massive gas of quarks (which corresponds to the infinite temperature limit), because

$$\frac{\partial p^{\text{id}}(T, m_q)}{\partial m_q} \simeq -\frac{2N_c N_f}{\pi^2} m_q T^2 \left(\frac{\pi^2}{12} + \frac{m_q^2}{4T^2} \left[\log\left(\frac{m_q}{\pi T}\right) + 0.0772 \right] + \dots \right)$$

for $m_q/T \ll 1$ and using the expansion formula (C.2)². Since finite quark masses break the chiral symmetry explicitly, they act like an external field in a ferromagnetic spin system and tend to wash out the phase transition, so it is not surprising that the condensate does not vanish. However, a conceptual problem arises from the T^2 -dependence: regardless of how small m_q (and hence the explicit symmetry breaking) is, $\langle \bar{\Psi}\Psi \rangle$ will blow up to arbitrary values at high enough temperatures. This peculiar behaviour does not contain any interaction physics, though, but is purely a remnant of the system's approach to the massive ideal gas. Subtracting that piece enforces that

¹What is actually plotted in the graphs are the dimensionless, positive quantities $|\langle \bar{\Psi}\Psi \rangle|a^3$ and $|\chi_m|a^2$, where a is the lattice spacing. Due to large cut-off effects, the magnitude of these quantities is expected to change by at least a factor of 2 in the continuum limit. Using the relation $1/T = N_\tau a$ ($N_\tau = 4$ in the simulation), a can be converted to temperature. For the mass term, $m_q a = 0.02$ accordingly translates into $m_q/T = 0.08$.

²Equivalently, one may argue that the thermal expectation value of the normal-ordered operator product $\langle : q(x)\bar{q}(y) : \rangle$, as appearing in (2.15), does not vanish even in the absence of interactions.

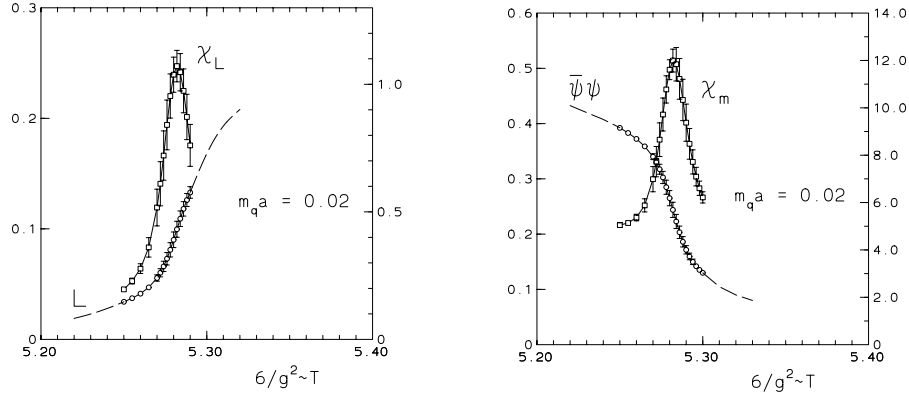


FIGURE 2.5: Left panel: The Polyakov loop expectation value $\langle L \rangle$ and its susceptibility χ_L as a function of $\bar{\beta} = 6/g^2$, a measure for the temperature (see (2.30)). Right panel: The chiral condensate $|\langle\bar{\Psi}\Psi\rangle|/T^3$ and its susceptibility $|\chi_m|/T^2$ for $N_f = 2$. All lattice calculations were performed with a running bare quark mass $m_q = 0.08 T$, corresponding to 14 MeV at T_c . The critical temperature T_c is defined at $\bar{\beta} \simeq 5.28$ [30].

the condensate drops to zero at high enough temperatures, as it should, so a more appropriate definition of the order parameter would be

$$\langle\bar{q}q\rangle = - \lim_{y \rightarrow x_+} \left\{ \text{Tr}\langle 0 | \mathcal{T}[q(x)\bar{q}(y)] | 0 \rangle - \text{Tr}\langle \tilde{0} | \mathcal{T}[q(x)\bar{q}(y)] | \tilde{0} \rangle \right\}. \quad (2.44)$$

Here, $|0\rangle$ stands for the non-trivial, full QCD vacuum and $|\tilde{0}\rangle$ for the empty, perturbative vacuum. Now, for $g \rightarrow 0$, also $\langle\bar{q}q\rangle \rightarrow 0$, even in the presence of quark masses. This subtraction procedure has so far not been applied in the lattice plots of figure 2.5, that is why all quantities have been divided by the appropriate powers of temperature there to make them dimensionless and suppress the inherent increase.

The chiral susceptibility

$$\chi_m = \frac{\partial\langle\bar{\Psi}\Psi\rangle}{\partial m_q} \quad (2.45)$$

exhibits a pronounced peak structure which is commonly used to define a critical chiral temperature T_c^χ . The narrowness of the peak suggests that drastic changes in the condensate structure occur only for $|T - T_c^\chi|/T_c^\chi \lesssim 0.1$, i.e. very close to T_c^χ . Constructing an effective theory for the order parameter, the phase transition is found to be first order for $N_f \geq 3$ [31], which is confirmed by lattice calculations. For two flavours, it is expected that the transition belongs to the $O(4)$ universality class. Available lattice data, however, are not yet decisive on that issue [32].

In the absence of thermally active quarks, owing to the finite temperature boundary conditions there exists a global $Z(N_c) \in \text{SU}(N_c)$ centre symmetry that becomes broken at high T . The order parameter is the gauge invariant Polyakov loop (or Wilson line)

$$\langle L(x) \rangle = \frac{1}{N_c} \text{Tr} \left[\mathcal{P} \exp \left(ig \int_0^\beta d\tau A_0(\tau, x) \right) \right], \quad (2.46)$$

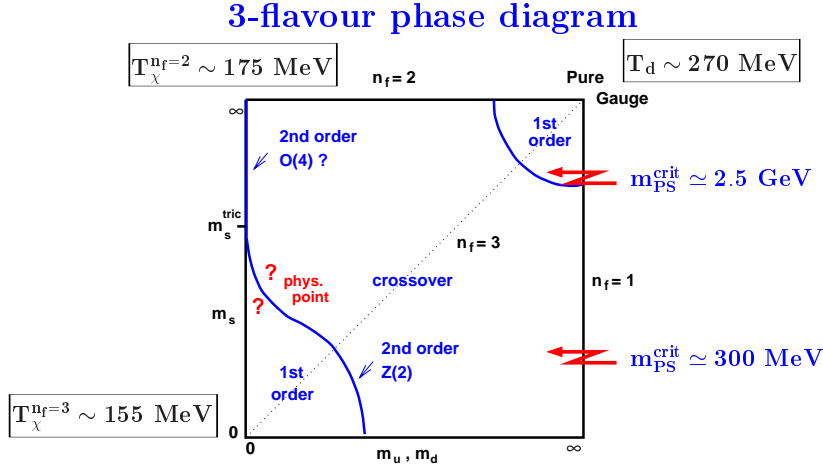


FIGURE 2.6: The finite temperature phase diagram of QCD as a function of the light (m_u, m_d) and heavy (m_s) quark masses [30].

A_0 being the time component of the gauge field A_μ . For a single static quark located at $x = 0$, its excess free energy $F_q - F_0$ for a volume V can be expressed by

$$\langle L \rangle = \frac{1}{V} \int d^3x \langle L(x) \rangle \quad (2.47)$$

via

$$\langle L \rangle = e^{-\beta(F_q(T) - F_0)}. \quad (2.48)$$

In the confined phase, a coloured source cannot be screened if there are no dynamical quarks, hence its free energy is infinite and $\langle L \rangle = 0$. In the deconfined phase, the free energy of a static quark-antiquark pair remains finite as their distance increases which can be interpreted as the absence of the confining string tension σ of eq.(2.11). The Polyakov loop is then related to the heavy quark-antiquark potential $V_{\bar{q}q}(r, T)$ by

$$e^{-\beta V_{\bar{q}q}(r, T)} = \langle L(r) L^\dagger(0) \rangle, \quad (2.49)$$

where r is now the distance between the two heavy quark sources. At large separations $r \rightarrow \infty$, eq.(2.49) approaches the value $|\langle L \rangle|^2$ for two uncorrelated sources. Measuring $V_{\bar{q}q}$ on the lattice, one can read off the behaviour of the order parameter:

$$\langle L \rangle \begin{cases} = 0 & T \text{ small,} \\ \neq 0 & T \text{ large,} \end{cases} \quad (2.50)$$

characteristic for an disorder-order transition. For $N_c = 3$, the effective theory for $\langle L \rangle$ becomes a 3-dimensional spin model with global $Z(3)$ symmetry. From universality arguments it is then expected that the phase transition is first order [33], which is confirmed by lattice calculations. The order parameter $\langle L \rangle$ and its susceptibility $\chi_L = V(\langle L^2 \rangle - \langle L \rangle^2)$ are shown in figure 2.5 (left panel). Again, χ_L is strongly peaked around a temperature T_c^d . For $N_f \neq 0$, $\langle L \rangle$ is not an exact order parameter anymore because $\langle L \rangle > 0$ for all T now, but nevertheless still shows a strong variation around T_c .

Since chiral symmetry breaking and confinement are not *a priori* related phenomena, there is no reason to expect that T_c^x and T_c^d are equal, there might as well be two separate phase transitions. This behaviour is indeed seen in theories similar to QCD, e.g. SU(3) gauge theory with adjoint fermions [34] where $T_c^d < T_c^x$. However, in QCD the transitions are strongly correlated and occur within statistical errors at the same temperature, as can be seen by the peak positions of the corresponding susceptibilities in figure 2.5. From the arguments in section 2.4.1 we expect $T_c = \mathcal{O}(\Lambda_{\text{QCD}})$, which is already in surprising agreement with the lattice result for SU(3) gauge theory:

$$T_c = (271 \pm 2) \text{ MeV}. \quad (2.51)$$

The addition of thermally active flavours lowers T_c because the critical energy density that triggers the phase transition can be reached earlier when more degrees of freedom are present. The necessary extrapolations are at the moment not as well under control as in the pure glue case, therefore the error bars on T_c are larger. The critical temperature in the chiral limit reads [35]

$$T_c = (173 \pm 8) \text{ MeV for } N_f = 2, \quad (2.52)$$

and

$$T_c = (154 \pm 8) \text{ MeV for } N_f = 3. \quad (2.53)$$

The errors are only statistical, it has to be borne in mind that the systematic errors are estimated to be of the same order. For two light and a heavy quark flavour, the transition temperature remains close to the two-flavour value, indicating that the quark mass dependence of T_c is small. A fit of several lattice calculations of T_c at different quark mass values suggests a linear behaviour of the form

$$T_c(m_\pi) = T_c(0) + 0.04(1)m_\pi, \quad (2.54)$$

where m_π stands for the mass of the pseudo-scalar Goldstone particle. The weak m_π -dependence indicates that the transition is not 'pion'-dominated, rather 'resonance'-driven.

Finally, figure 2.6 shows the QCD phase diagram as a function of the light u - and d - and the heavy s -quark mass. The finite quark masses will turn the transition into a rapid cross-over if it is second order in the chiral limit. For a first order transition, the discontinuities may prevail up to a critical pseudo-scalar mass m_{PS}^{crit} and become smoothed out only after that. For three degenerate flavours, that value is about 300 MeV. Intriguingly, the physically relevant point with \mathbf{m} as in eq.(2.7) lies in the vicinity of the border line that separates first order and crossover regions in the phase diagram. Calculations with two light and a strange quark with a mass comparable to T_c indicate [36] that m_s^{crit} is about half the value of m_s , so in the real world the transition is likely to be a smooth crossover.

2.4.4 The QCD phase diagram in the $T - \mu$ plane

A variety of theoretical models [37] suggests that at large μ and finite T , the transition becomes first order (although "large" usually really translates into "asymptotically large": simply replace $g(T)$ by $g(\mu)$). The quantitative mapping of the $T - \mu$ phase diagram can so far only be achieved by lattice calculations – at least in principle. The border line where $T \neq 0$ and $\mu = 0$ is reasonably well understood. At finite μ , however, the status of lattice QCD is not nearly as advanced. The staggered fermion determinant in (2.31) is real for vanishing quark chemical potential, but becomes

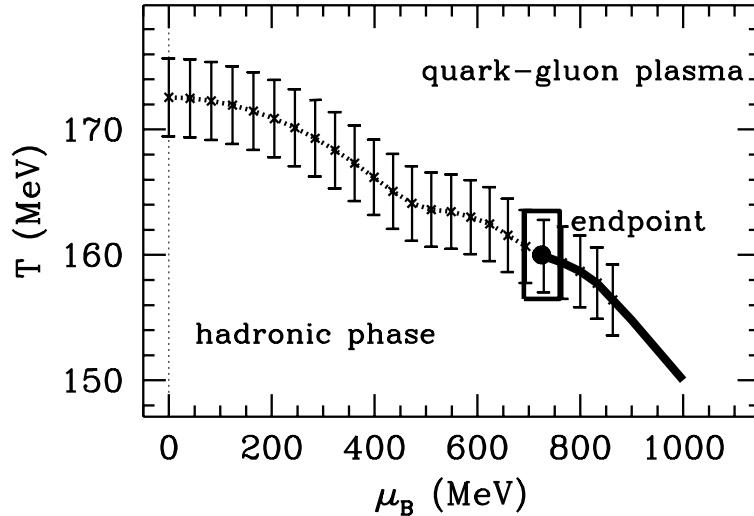


FIGURE 2.7: The $T - \mu$ diagram from the lattice calculation of [39]. Note that $\mu_B \equiv 3\mu$. The critical endpoint is located at $T_E = 160 \pm 4$ MeV and $\mu_E = 242 \pm 12$ MeV. The solid line denotes a first order transition, dashed the crossover. $T_c(\mu = 0)$ is determined within the same calculation as 172 ± 3 MeV.

complex as soon as $\mu \neq 0$. Therefore, the application of importance-sampling methods is no longer feasible, increasing the numerical efforts by several orders of magnitudes. This constitutes the *sign problem* of QCD and prohibits so far an accurate lattice determination of the full $T - \mu$ phase diagram. Fugacity expansions of the grand canonical partition function at finite μ (the Glasgow algorithm [38]) have been studied in detail, however, so far the results show little physical relevance. Only recently, improved methods have been proposed that allow a determination of thermodynamics at reasonably large μ . We briefly dwell on two of them in the following.

In [39], a new reweighting method has been introduced that lifts some of the restrictions of the Glasgow method. The phase diagram for $N_f = 2 + 1$ is shown in figure 2.7 for staggered fermions on lattices $N_\tau \times N_\sigma^3 = 4 \times 8^3$ with a pion mass at least twice as large as the physical value. The calculation finds a critical point $(T_E, \mu_E) = (160 \pm 4 \text{ MeV}, 242 \pm 12 \text{ MeV})$ where the first-order transition that separates hadronic and QGP phases, ends. For smaller T and μ , the transition becomes a crossover. Note that the data are not yet extrapolated to the continuum and physical quark masses and that the present lattice size is comparably small.

A different attempt to explore the phase diagram at least for small μ exploits the fact that derivatives of an observable with respect to μ can be calculated with standard methods at $\mu = 0$. Hence, the phase transition line close to $\mu = 0$ is obtained by Taylor expanding [40]:

$$T_c(\mu) = T_c(0) + \mu \left. \frac{dT_c}{d\mu} \right|_{\mu=0} + \frac{\mu^2}{2} \left. \frac{d^2T_c}{d\mu^2} \right|_{\mu=0} + \dots \quad (2.55)$$

Derivatives with odd powers of μ vanish because of the realness of the partition function, so it is sufficient to calculate only $d^2T_c/d\mu^2(\mu = 0)$ on the lattice. Truncation errors accordingly enter at $\mathcal{O}(\mu^4)$. Assuming that the transition line remains parabolic,

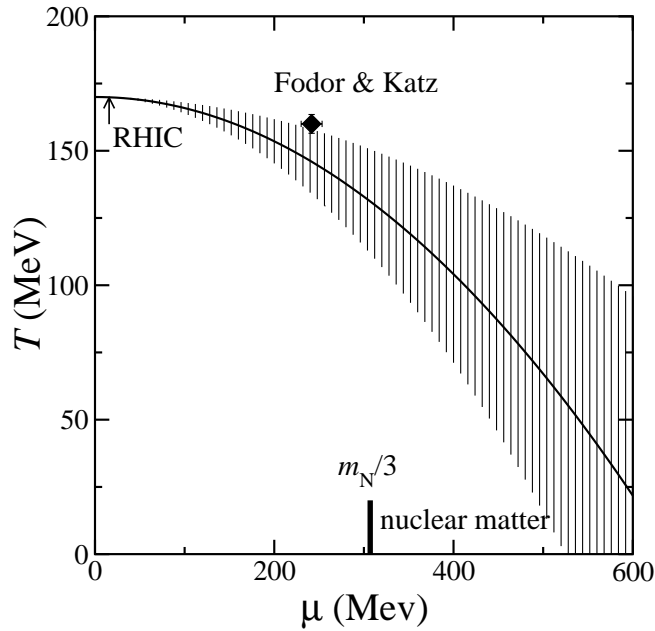


FIGURE 2.8: Sketch of the phase diagram for $N_f = 2$ using the value for $d^2T_c/d\mu^2(\mu = 0)$ [40], calculated on a 4×16^3 lattice with rotationally improved staggered fermions. The diamond shows the end point of the first order phase transition from figure 2.7. The arrow marks the chemical freeze-out point at RHIC Au+Au collisions at $\sqrt{s} = 130$ AGeV [42].

a sketch of the phase diagram for $N_f = 2$ staggered fermions can be drawn, see figure 2.8. Using a similar approach, ref.[43] calculated a Taylor expansion of $T_c(\mu)$ at imaginary chemical potential (thus avoiding the problem of the complex determinant) and analytically continued the corresponding series to real μ . Their results are in agreement with [40] for $\mu_B < \pi T$, the range of applicability of the method. For small values of $\mu/T_c \lesssim 0.5$, the transition behaviour shows no significant deviation from the $\mu = 0$ case. Since the chemical freeze-out at SPS occurs at about $\mu_{f.o.} \simeq 100$ MeV [41] and at RHIC at $\mu_{f.o.} \simeq 15$ MeV [42], neither experiment is expected to come close to the critical point (T_E, μ_E) , and striking phenomenological consequences (like critical opalescence or anomalously large fluctuations) are not supposed to be present.

3 Quasiparticle Model of the QGP

From the arguments of section 2.4.1 we expect that QCD undergoes a transition from a confined hadronic phase to a deconfined partonic phase at a critical temperature of $T_c = \mathcal{O}(\Lambda_{\text{QCD}})$. A central quantity of matter in thermal equilibrium is the Helmholtz free energy

$$F = -T \log \mathcal{Z}(T, V), \quad (3.1)$$

from which the pressure p , energy density ϵ and entropy density s are derived. These entities are central for the description of ultra-relativistic heavy-ion collisions at the CERN SPS and RHIC and have been calculated on the lattice within certain approximations. Various interpretations of these data have been attempted, most prominently as a gas of quark and gluon quasiparticles. Since all microscopic dynamics has been integrated out in the equation of state (EOS), there exists no unique interpretation of the lattice data, and one must resort to additional information in order to further restrict the setup of such models. In a phenomenological framework, quarks and gluons are simply treated as non-interacting, massive quasiparticles [44, 45, 46, 47]. Their thermally generated masses are based on perturbative calculations carried out in the HTL scheme. In this chapter, we extend the quasiparticle approach. We argue that for $T \lesssim 3 T_c$, non-perturbative confinement physics not amenable in an expansion in g becomes important, so our main new ingredient, as compared to previous work, will be a phenomenological parametrisation of (de)confinement, supplemented by thermal quasiparticle masses compatible with lattice results. The resulting model is tested against a number of available lattice data and extended to systems with small quark chemical potential. We also construct the continuum EOS for realistic quark masses (that cannot be simulated on the lattice to date) which will be used in the forthcoming chapters to model the fireball. The main body of this chapter has been published in [48].

3.1 Lattice results

3.1.1 Pure gauge theory

In the limit $\mathbf{m} \rightarrow \infty$, the EOS for SU(3) gauge theory has been extensively numerically studied [49, 50, 51, 52]. Figure 3.1 shows the pressure as a function of T/T_c , calculated with different actions and extrapolated to the continuum limit. Obviously, all curves agree remarkably well, so the necessary approximations seem to be under control. Figure 3.2 then summarises the energy density, the entropy density and the pressure [50], normalised such as to approach the same asymptotic limit. Since the transition is first order, there is a discontinuity in the energy density at T_c , and the hatched band marks the latent heat $\Delta\epsilon \simeq 0.5 - 1 \text{ GeV/fm}^3$.

The pressure below T_c is very small, which is naturally explained by the heavy mass of the bound degrees of freedom, the glue balls. Since already the lightest glue ball state 0^{++} has a mass of about 1.5 GeV at zero temperature [53], the Boltzmann

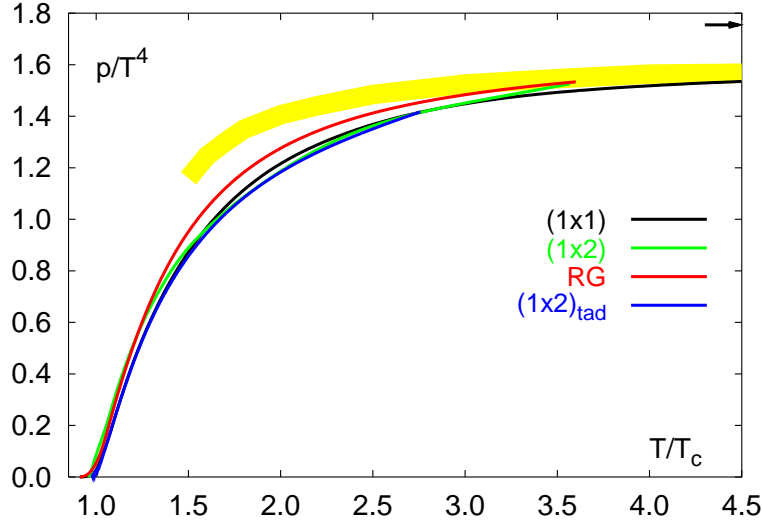


FIGURE 3.1: Pressure of the SU(3) gauge theory. The lines are continuum-extrapolated estimates calculated with different actions [49, 50, 51, 52]. The arrow marks the ideal gas limit. The shaded band shows an approximately self-consistent HTL calculation [60].

factor suppresses glueball contributions to the pressure. It is therefore surprising that the phase transition occurs at such a low $T_c = 270$ MeV because the energy and particle density are comparably low there. Lattice calculations indicate that at finite temperature, the 0^{++} glue ball mass shifts down, but only by about 20% to $m_{GB} = 1.25 \pm 0.1$ GeV for $0.8 T_c < T < T_c$ [54], which is still large compared to T_c . The phase transition is then probably triggered by an increasing number of excited glue ball states as T grows, not by the increasing density of a single particle species, rendering an attempt to describe the phase transition in terms of the lightest degree of freedom only, the mentioned 0^{++} glue ball, futile.

Literally on the other side, the energy density reaches about 85% of its ideal gas value at $2 T_c$ and stays roughly at this value up to $5 T_c$. This fact is naturally explained in a quasiparticle picture where the gluons acquire a thermal mass $\sim g(T)T$ with $g(T)$ running logarithmically (see below). Two things are worth emphasising: first, the gluon plasma deviates significantly from an ideal gas for all temperatures of interest, and second, the thermodynamics shows a smooth behaviour, there are no wiggles or peaks present.

3.1.2 Dynamical quarks

Over the last few years, various lattice calculations of the pressure with different numbers of quark flavours N_f have been performed. In the following we focus on results of the Bielefeld group [55] where a rotationally improved staggered action on a $16^3 \times 4$ lattice was used. There, the N_τ -dependence was found to be small, in contrast to standard staggered fermion actions which show substantially larger cut-off effects [56]. Lattice calculations were performed for two and three flavour QCD with quarks of mass $m_q/T = 0.4$, and for three flavours with two light quarks ($m_q/T = 0.4$) and an additional heavier quark ($m_s/T = 1.0$). From the experience in the pure gauge

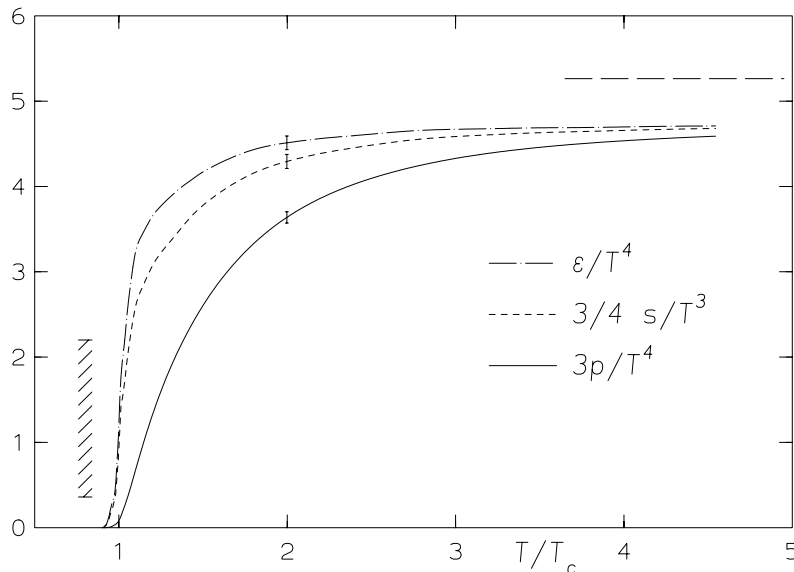


FIGURE 3.2: Normalised energy density, entropy density and pressure of SU(3) gauge theory as a function of T/T_c , extrapolated to the continuum limit [50]. The dashed band indicates the size of the latent heat $\Delta\epsilon$. The dashed line marks the ideal gas limit, and the error bars at $2 T_c$ are a measure for the statistical and systematic uncertainties.

sector, it has been estimated that the continuum EOS lies about 10-20% above the data computed on finite lattices.

Figure 3.3 displays the lattice pressure, normalised to the Stefan-Boltzmann ideal gas value, for the pure gauge system and for systems with 2, 2+1 and 3 quark flavours. A striking feature is that, within the errors arising from the cut-off dependence, the QCD EOS shows a remarkable flavour *independence* when plotted against T/T_c . This picture suggests that the flavour dependence is well approximated by a term reminiscent of an ideal gas,

$$p(T, N_f) \simeq \left(16 + \frac{21}{2} N_f\right) \frac{\pi^2}{90} \tilde{p}(T/T_c) \quad (3.2)$$

with a universal function $\tilde{p}(T/T_c)$. Since T_c changes with the number of degrees of freedom present in the thermal system and therefore with N_f , cf. (2.51), (2.52) and (2.53), \tilde{p} is also implicitly N_f -dependent. Scaling against T/T_c , however, the shape of \tilde{p} remains almost the same, suggesting that the inclusion of thermally active quarks does not change the underlying mechanism of the phase transition. Note however that, after applying the previously mentioned 10-20% correction to the lattice data, the continuum estimate of the pressure with dynamical quarks becomes closer to the ideal gas limit than in the pure gauge sector.

3.2 Perturbative results

Perturbative results of the QCD equation of state are available up to order $\mathcal{O}(g^5)$. However, for temperatures of interest in the experimentally accessible region, the strong coupling constant is presumably large: at $T = 3 T_c$, $g(T) \simeq 2$ from eq.(2.36). The perturbative expansion in powers of g shows bad convergence already for much smaller

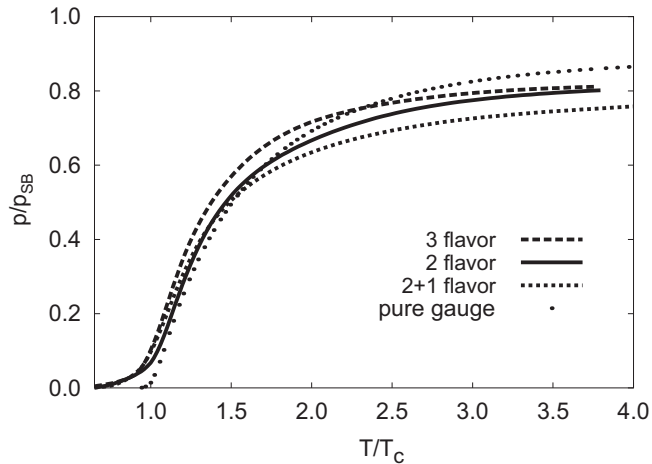


FIGURE 3.3: The pressure, normalised to the Stefan-Boltzmann ideal gas value, for the continuum-extrapolated pure gauge system and for systems with 2, 2+1 and 3 flavours on a $16^3 \times 4$ lattice, obtained with a p4-improved staggered fermion action. The continuum limit is estimated to lie about 10-20% above the curves shown (figure adapted from [55]).

values of the coupling, as apparent from the expression for $F(T)$ in pure SU(3) gauge theory [57]:

$$\frac{F(T)}{F_0} = 1 - 0.095g^2 + 0.121g^3 + [0.212 - 0.086 \log(1/g)]g^4 - 0.082g^5. \quad (3.3)$$

Here, $F_0 = -16(\pi^2/90)T^4$ is the ideal gas value. With quarks, the resulting series behaves similarly. Hence, if g is $\mathcal{O}(1)$, the series oscillates wildly and even overshoots the ideal gas limit at order g^3 and g^4 . In order to get a convergent series, the temperature has to be asymptotically high, $T \gtrsim 10^{10} T_c$, which clearly is far beyond any practical purposes. Furthermore, the more powers of g are included, the more sensitive $F(T)$ becomes on the renormalisation point of $\alpha_s(\mu)$, which is the wrong trend. Even higher orders in g cannot improve the convergence because it is believed from power-counting arguments that the g^5 term is the last one accessible in perturbation theory. At four-loop order, infrared singularities appear that can be removed by the introduction of a chromomagnetic screening mass which, however, gives contributions to $\mathcal{O}(g^6)$ from diagrams with an arbitrary number of loops [58]. Bare perturbation series is clearly inadequate to describe the lattice results. However, the series in (3.3) is not the power series in α_s known from zero temperature perturbation theory; collective medium effects lead to the appearance of non-analytic terms of the form $\alpha_s^{n/2}$ and $\alpha_s^2 \log \alpha_s$. Therefore, the expansion point of perturbation theory should not be a bare particle, but a dressed quasiparticle taking into account the medium from the onset; of course, the resulting series in g has then to be treated self-consistently.

Such a quasiparticle description of QCD thermodynamics has been derived in a more or less rigorous treatment using resummed, approximately self-consistent HTL perturbation theory [59, 60, 12]. Employing the full HTL spectral representations (B.17) and (B.32), the resulting EOS can be matched to lattice data down to temperatures $T \gtrsim 3 T_c$, see the shaded band in figure 3.1. In interpreting these results, however, one has to keep in mind three points: first, the structure of the curve is, since there is no scale around but Λ_{QCD} , entirely governed by $\alpha_s(T)$; all the resummation does is

to fix the normalisation. The range of applicability of the method is therefore closely related to the behaviour of the running coupling that can close to T_c substantially deviate from the naive perturbative form (cf. figure 2.4). Second, the non-perturbative resummation method used to evaluate the pressure, the “ Φ -derivable” approximation, is tailored to the problem, it is not possible to extend it to the calculation of other important quantities such as the screening mass or dilepton rates. Finally, the influence of higher order terms has not yet been clarified due to the complexity of the calculations, leaving the question for the convergence of the series open. Even leaving aside these points, it is at least safe to say that there exists no perturbative description of the EOS for temperatures $T_c < T < 3 T_c$ which is exactly the region where the fireball created in heavy-ion collisions at SPS and RHIC lives. In order to get a quantitative description of URHIC and the signals for the QGP, a more phenomenological *ansatz* seems mandatory today. We believe that one should try to collect all facts that are known about the phase transition (most prominently, these facts will come from the lattice) and try to construct simple, yet reasonable models consistent with these data. Applying these models in different situations will then show their limitations and successes.

3.3 Gluonic quasiparticles

3.3.1 Basic quasiparticle model

In this section, we consider an $SU(N_c)$ gluon plasma ($N_c = 3$) at finite temperature. The use of a quasiparticle model in QCD is based on the observation that in a strongly interacting system, the complex dynamics often rearranges itself in such a way that gross features of the physics can be described in terms of appropriate effective degrees of freedom. From asymptotic freedom, we expect that at very high temperatures the plasma consists of quasifree gluons. As long as the spectral function of the thermal excitations at lower temperatures resembles qualitatively this asymptotic form, a gluonic quasiparticle description is expected to be applicable. The dispersion equation for transverse gluons reads $\omega^2 - k^2 - \Pi_T^*(\omega, k) = 0$. Here, $k = |\vec{k}|$, and Π_T^* is the transverse part of the thermal gluon self-energy. If, for thermal momenta $\omega, k \sim T$, the momentum-dependence of Π_T^* is weak and its imaginary part small, gluon quasiparticles will propagate mainly on-shell with the dispersion relation

$$\omega_k^2 \simeq k^2 + m_g^2(T), \quad (3.4)$$

where $m_g(T)$ acts as an effective mass generated dynamically by the interaction of the gluons with the heat bath background. Since the existence of a preferred frame of reference breaks Lorentz invariance, new partonic excitations, longitudinal gluonic plasmons, are also present in the plasma. However, their spectral strengths (B.19) are exponentially suppressed in the HTL approximation for hard momenta and large temperatures, so gluons are expected to retain their $\nu_g = 2(N_c^2 - 1)$ degrees of freedom despite their masses. A vanishing longitudinal propagator in Coulomb gauge at non-zero momentum $k \gtrsim 1.5 T$ was also found in lattice calculations [61].

For homogeneous systems of large volume V , described by a Hamiltonian H and a conserved charge number operator Q , the standard definitions of the pressure p , the energy density ϵ and the number density n become

$$p(T, \mu) = \frac{T}{V} \log \text{Tr} \left[e^{-\beta(H - \mu Q)} \right] = \frac{T}{V} \log \mathcal{Z}(T, \mu, V), \quad (3.5)$$

$$\epsilon(T, \mu) = \frac{1}{V} \frac{1}{\mathcal{Z}} \text{Tr} \left[H e^{-\beta(H - \mu Q)} \right] \quad \text{and} \quad (3.6)$$

$$n(T, \mu) = \frac{1}{V} \frac{1}{\mathcal{Z}} \text{Tr} \left[Q e^{-\beta(H - \mu Q)} \right]. \quad (3.7)$$

The Gibbs-Duhem relation connects p , ϵ and n with the entropy density s :

$$\epsilon = sT + \mu n - p. \quad (3.8)$$

Furthermore, s and n can be derived from p via

$$s = \left. \frac{\partial p}{\partial T} \right|_{\mu} \quad (3.9)$$

and

$$n = \left. \frac{\partial p}{\partial \mu} \right|_T. \quad (3.10)$$

If the system is an ideal gas,

$$H^{\text{id}} = \sum_{j=0}^d \sum_k \omega_k a_{k,j}^{\dagger} a_{k,j} + E_0, \quad (3.11)$$

where E_0 is the (unobservable) zero-point energy and is usually subtracted of. The index j labels internal degrees of freedom (spin, colour, flavour...), and $a_{k,j}^{\dagger}$ and $a_{k,j}$ are the creation and annihilation operators, respectively, for states with quantum numbers $[j]$ and three-momentum k .

Let us now assume for the moment that the total effect of the strong interactions is subsumed in the thermal mass $m_g(T)$ and that the gluonic quasiparticles are non-interacting otherwise, hence constitute an ideal gas. In order to maintain thermodynamical consistency, however, pressure and energy are not given by their ideal gas expressions anymore. Since the Hamiltonian becomes medium-dependent via the dispersion relation $\omega_k(T)$, eqs.(3.8) and (3.9) are not valid anymore because of the additional $\partial m_g(T)/\partial T$ terms. In more general terms, let $H_{\text{eff}}[\mathcal{F}_i]$ be a Hamiltonian that depends on the n phenomenological functions $\mathcal{F}_i = \mathcal{F}_i(T, \mu)$ ($i = 1..n$) [44] that encode the medium, e.g. $\mathcal{F}_1 = m_g(T)$ (later on, we will introduce a second function $\mathcal{F}_2 = C(T)$). In order to fulfill the identities (3.8), (3.9) and (3.10), we require the stationarity condition

$$\left. \frac{\partial p}{\partial \mathcal{F}_i} \right|_{T, \mu, \mathcal{F}_{j \neq i}} = 0. \quad (3.12)$$

With a medium-dependent dispersion relation, the ideal gas Hamiltonian takes the form

$$H_{\text{eff}}^{\text{id}} = \sum_{j=0}^d \sum_k \omega_k[\mathcal{F}_i] a_{k,j}^{\dagger} a_{k,j} + E_0[\mathcal{F}_i]. \quad (3.13)$$

Now E_0 depends functionally on the \mathcal{F}_i and is (up to a constant) entirely determined by them, so it cannot be subtracted anymore because it contains the external parameters T and μ . Since it represents the energy of the system in the absence of any quasiparticle excitations, $E_0[\mathcal{F}_i]$ can be interpreted as the thermal ground state (vacuum) energy. Note that, because $a_{k,j}^{\dagger} a_{k,j} = n_{k,j}$ counts the number of degrees of freedom in the state $\{[j], k\}$, a special extension of (3.13) would be

$$H_{\text{eff}}^{\text{id}} = \sum_{i=0}^d \sum_k \omega_k[\mathcal{F}_1] n_{k,j}[\mathcal{F}_2] + E_0[\mathcal{F}_1, \mathcal{F}_2] + \bar{H} \quad (3.14)$$

in a theory where the number of quantum field theory degrees of freedom statistically depends, via \mathcal{F}_2 , on temperature. The second Hamiltonian \bar{H} should then represent an effective theory for the ‘bound’ states. Eq.(3.14), which we will put to use below, is the most general expression for an ideal gas.

Returning to the present framework of a gluon gas of quasiparticles with a medium-dependent dispersion relation, the explicit expression for the pressure reads

$$p(T) = \frac{\nu_g}{6\pi^2} \int_0^\infty dk f_B(\omega_k) \frac{k^4}{\omega_k} - B(T), \quad (3.15)$$

where $\nu_g = 16$ is the gluon degeneracy factor and $\omega_k = \sqrt{k^2 + m_g^2(T)}$. The energy density ϵ and the entropy density s take the forms

$$\epsilon(T) = \frac{\nu_g}{2\pi^2} \int_0^\infty dk k^2 f_B(\omega_k) \omega_k + B(T) \quad (3.16)$$

and

$$s(T) = \frac{\nu_g}{2\pi^2 T} \int_0^\infty dk k^2 f_B(\omega_k) \frac{\frac{4}{3}k^2 + m_g^2(T)}{\omega_k}. \quad (3.17)$$

The function $B(T)$ is the ground state energy density

$$B(T) = \frac{1}{V} E_0[m_g(T)],$$

its explicit expression follows (up to a constant) from

$$\left. \frac{\partial p(T, m_g)}{\partial m_g} \right|_T = 0.$$

Note that the entropy density, as a measure of phase space occupation, and the number density are unaffected by $B(T)$.

3.3.2 Thermal masses: Debye vs. Asymptotic

It is obvious that with the pressure given by the lattice, one can always construct a curve $m_g(T)$ to reproduce $p(T)$. The question arises whether the resulting expression for $m_g(T)$ looks reasonable. Previous phenomenological quasiparticle models [45, 46, 47] started from the HTL expression for the asymptotic mass m_∞ , eq.(B.14),

$$m_g(T) = \sqrt{\frac{N_c}{6}} \tilde{g}(T) T, \quad (3.18)$$

to model the thermal gluon mass¹. Phenomenology enters in the effective coupling constant $\tilde{g}(T)$, modelled after the running coupling (2.36), with the two fit parameters T_s and λ :

$$\tilde{g}^2(T) = \frac{48\pi^2}{11N_c \log\left(\frac{\lambda}{T_c} [T + T_s]\right)}. \quad (3.19)$$

¹In the following, we refer to the quasiparticle model with the gluon mass defined by eqs.(3.18) and (3.19) as the *PQP (phenomenological quasiparticle) model*.

By identifying the Landau pole of the effective coupling with a temperature close to T_c , the effective gluon mass (3.18) becomes very heavy in the vicinity of the phase transition, and s , p and ϵ drop abruptly to almost zero. The model can be oppugned in two points.

First, numerical simulations suggest that the deconfinement transition in Yang-Mills theories is second order for $N_c = 2$ [62] and, as mentioned, weakly first order for the physical case $N_c = 3$ [33]. From the general theory of critical phenomena, it is expected that the correlation length $\xi(T)$, which is proportional to the inverse of the gluonic screening Debye mass m_D , grows when T_c is approached from above. The Debye mass m_D measures the exponential spatial decay of the static gluon field correlator

$$\langle A_0^a(\vec{r}) A_0^b(0) \rangle_\beta \propto \delta^{ab} \exp(-m_D(T)r)/r. \quad (3.20)$$

For three colours, the mass gap does not vanish at T_c , so $\xi(T_c)$ remains large, but finite. This behaviour is indeed seen in lattice calculations [63]: m_D drops by a factor of ten when going down from $2 T_c$ to T_c (see figure 3.4). In HTL perturbation theory, $m_D(T)$ and $m_\infty(T)$ are connected by the simple relation, cf. eq.(B.14):

$$m_D = \sqrt{2} m_\infty.$$

A scenario with heavy masses m_g would then imply *small* correlation lengths close to T_c . It is therefore not clear how a decreasing gluonic Debye mass can be matched to *heavy, non-interacting* quasiparticles (an attempt to describe the Debye mass semi-classically by integrating over the quasiparticles was made in [45]). Of course, in a more general non-perturbative framework, m_g and m_D , although both arise from the same polarisation tensor, will not be related *a priori* by a simple constant, as in eq.(B.14). In fact, this relation already breaks down in HTL perturbation theory when next-to-leading order corrections to m_∞ and m_D are included: whereas the asymptotic thermal mass m_∞ starts to exhibit non-localities [60] due to the structure of the effective Lagrangian (2.27), the Debye mass m_D becomes infrared-sensitive to the intrinsically non-perturbative magnetic mass $g^2 T$ [64], leading to the appearance of a $g^2 \log(1/g)$ term (see the detailed discussion in section 6.2).

Second, the quasiparticle masses at T_c become really large: $m_g(T_c) \simeq 1.2$ GeV with the parameters of ref.[45], which is already the mass of the lightest glue ball state at T_c [54] that consists of *two* 'constituent' gluons. Within a scenario of heavy 'constituent' masses at T_c , the formation of bound states at the confinement transition would then imply extremely large binding energies.

3.3.3 Deconfinement and the quasiparticle model

We will argue that these inconsistencies of the PGP can be traced back to the fact that the picture of a non-interacting gas is not appropriate close to T_c because the driving force of the transition, the confinement process, is not taken into account. The physical picture is the following: below T_c , the relevant degrees of freedom in a pure SU(3) gauge theory are heavy, colour singlet glueballs. Approaching T_c , deconfinement sets in and the gluons are liberated, followed by a sudden increase in entropy and energy density, as seen on the lattice. Conversely, when approaching the phase transition from above, the decrease in the thermodynamic quantities is not caused by masses becoming heavier and heavier, instead the number of thermally active degrees of freedom is reduced due to the onset of confinement. As T comes closer to T_c , an

increasing number of gluons gets trapped in glue balls which *disappear* from the thermal spectrum: since $m_{GB}(T_c) \simeq 1.2$ GeV and $T_c \sim 270$ MeV, glue balls are simply too heavy to become thermally excited in the temperature range under consideration (up to about $5 T_c$). The fact that below T_c , the contribution of glue balls to ϵ , p and s is negligible supports this line of reasoning. The important fact is the following: while the confinement mechanism as such is still not understood, it is not necessary to know it in detail since we consider a *statistical* system. All confinement does on a *large* scale is to cut down the number of thermally active gluons as the temperature is lowered. The question remains whether this effect of confinement can be reconciled somehow with the quasiparticle picture. We will show in the following that it is indeed possible in a simple, phenomenological way if we allow for an effective, temperature-dependent number of degrees of freedom $\nu_g(T)$.

Let us assume that the thermal gluon mass $m_g(T)$ does not increase as T_c is approached, but instead follows roughly the behaviour of the Debye mass, i.e. it decreases. Its detailed T -dependence is not important for the discussion at the moment, but it will be examined in more detail in the next section. Consider now the entropy of a gas of massive gluons along eq.(3.17) with such a dropping effective gluon mass. The result for $s(T)$ will clearly overshoot the lattice entropy because light masses near T_c lead to an increase in $s(T)$. However, since the entropy is a measure for the number of active degrees of freedom, the difference may be accounted for by the aforementioned confinement process as it develops when the temperature is lowered toward T_c . This effect can be included in the quasiparticle picture by modifying the number of effective degrees of freedom by a temperature-dependent *confinement factor* $C(T)$:

$$\nu_g \rightarrow C(T) \nu_g. \quad (3.21)$$

As shown above, the effective Hamiltonian then takes its most general form for an ideal gas as

$$H_{\text{eff}}^{\text{id}} = \sum_{i=0}^d \sum_k \omega_k[m_g(T)] n_{k,j}[C(T)] + E_0[m_g(T), C(T)] + \bar{H}_{GB}(T). \quad (3.22)$$

Here, the unspecified function $\bar{H}_{GB}(T)$ includes in principle the dynamics of the glue balls that is negligible for $T \lesssim m_{GB}$. From the stationarity conditions

$$\left. \frac{\partial p}{\partial m_g} \right|_T = 0 \quad \text{and} \quad \left. \frac{\partial p}{\partial C} \right|_T = 0$$

the function $B(T)$ depends on $m_g(T)$ and $C(T)$ through

$$\begin{aligned} B(T) &= B_1(T) + B_2(T) + B_0, \quad \text{where} & (3.23) \\ B_1(T) &= \frac{\nu_g}{6\pi^2} \int_{T_c}^T d\tau \frac{dC(\tau)}{d\tau} \int_0^\infty dk f_B(\omega_k) \frac{k^4}{\omega_k} \quad \text{and} \\ B_2(T) &= -\frac{\nu_g}{4\pi^2} \int_{T_c}^T d\tau C(\tau) \frac{dm_g^2(\tau)}{d\tau} \int_0^\infty dk f_B(\omega_k) \frac{k^2}{\omega_k}. \end{aligned}$$

Setting $C(T) = 1$ in B_2 and $B_1 = 0$, one recovers the PQP model expression for $B(T)$. The integration constant B_0 is chosen such that the gluonic pressure equals the very small glue ball pressure p_{GB} (which is taken from the lattice) at T_c , according

to Gibbs' condition $p_{\text{gluon}} = p_{GB}$. With (3.23), the modification (3.21) leads to the following expressions which replace eqs.(3.15 - 3.17):

$$p(T) = \frac{\nu_g}{6\pi^2} \int_0^\infty dk [C(T)f_B(\omega_k)] \frac{k^4}{\omega_k} - B(T), \quad (3.24)$$

$$\epsilon(T) = \frac{\nu_g}{2\pi^2} \int_0^\infty dk k^2 [C(T)f_B(\omega_k)] \omega_k + B(T) \quad (3.25)$$

and

$$s(T) = \frac{\nu_g}{2\pi^2 T} \int_0^\infty dk k^2 [C(T)f_B(\omega_k)] \frac{\frac{4}{3}k^2 + m_g^2(T)}{\omega_k}. \quad (3.26)$$

In essence, the factor $C(T)$ represents a statistical parametrisation of confinement. It might as well functionally depend not only on the temperature T , but also on energy ω_k and momentum k . For now, our choice in (3.21) is the simplest possibility for $C(T)$, but it has the advantage that it allows quantitative calculations the results of which will *a posteriori* justify our *ansatz*. The explicit temperature dependence of $C(T)$ can be obtained simply as the ratio of the lattice entropy and the entropy (3.26) calculated with a dropping input gluon mass $m_g(T)$. Qualitatively, we expect $C(T \gg T_c) \approx 1$ at high temperatures where the deviation from the Stefan-Boltzmann limit of ϵ , s and p , as seen on the lattice, is caused solely by the thermal masses $m_g(T)$ (and can be accounted for perturbatively). As the phase transition is approached from above, the number of thermally active degrees of freedom decreases and consequently, $C(T)$ becomes less than one. Finally, the entropy below T_c is small, but non-zero, and we can estimate $C(T_c) \sim 0.2$ from lattice data. We would also expect that $C(T)$ is a smooth, monotonously increasing function with T , roughly following the behaviour of the entropy density.

3.3.4 Thermal masses close to T_c

We must now specify our input thermal quasiparticle mass $m_g(T)$ in eqs.(3.24 - 3.26). As mentioned earlier, $m_g(T)$ is to be identified with the transverse part $\Pi_T^*(\omega, k; T)$ of the gluon polarization tensor at $\omega, k \sim T$ (see eq.(3.4)). Evaluating $m_g(T)$ requires a detailed non-perturbative analysis of the gluonic two-point correlation function which lattice calculations could, in principle, provide. In practice this information does not (yet) exist, so we have to rely on a model.

Suppose we still keep the basic form of eq.(3.18),

$$m_g(T) = G(T)T, \quad (3.27)$$

but assume that the dimensionless effective coupling $G(T)$ shows approximate critical behaviour at T close to T_c , similar to the result found in $\lambda\phi^4$ theory (figure 2.4):

$$G(T) \simeq G_0 \left(1 - \frac{T_c}{T}\right)^\beta, \quad (3.28)$$

with some characteristic exponent β and a constant G_0 . The assumption (3.28) implies that the thermal mass behaves as $m_g(T) \sim (T - T_c)^\beta$ close to T_c . Asymptotically at $T \gg T_c$, $G(T)$ should match the HTL perturbative form as in (3.18). In practice

we can choose this matching point, for instance, at $T_m = 3 T_c$. This fixes $G_0 \simeq \sqrt{N_c/6} g(T_m) \simeq 1.3$. A similar value for T_m below which an explicit HTL resummation is expected to fail, was obtained in ref.[65], see also figure 3.1.

The quantity for which lattice information *does* exist is the Debye screening mass $m_D(T)$ that is related to the longitudinal part $\Pi_L^*(\omega, k; T)$ of the polarization tensor. When defined as $m_D^2 = \Pi_L^*(0, k^2 = -m_D^2)$ [64], the result turns out to be gauge-independent for a wide class of gauges to arbitrary order in perturbation theory [66] (unlike the situation for $\omega = 0, k \rightarrow 0$ where Π_L^* is not gauge-invariant at next-to-leading order). While there is no *a priori* reason why m_g and m_D should still be related non-perturbatively as they are in perturbation theory (cf. eq.(B.14)), it is nevertheless instructive to recall what is known about the temperature dependence of the Debye screening mass above T_c . Explicit values for m_D have been extracted from lattice calculations of (colour-averaged) heavy quark potentials $V(R, T)$ [63] by the *ansatz*

$$\frac{V(R, T)}{T} \propto \frac{e^{-\mu(T)R}}{(RT)^d}. \quad (3.29)$$

Perturbation theory predicts $d = 2$ and $\mu(T) = 2m_D(T)$. As elucidated in [63], the potential may be better reproduced in terms of a mixture of one- and two-gluon exchange since the observed behaviour close to T_c favours values of $d \sim 1.5$ in eq.(3.29). It is now interesting to observe that the lattice result for $\mu(T)$ can be parametrised very well by

$$\mu(T) \simeq \text{const.} \cdot T \left([1 + \delta] - \frac{T_c}{T} \right)^\beta \quad (3.30)$$

with $\beta \simeq 0.1$ and a small gap at $T = T_c$ introduced by $\delta \sim 10^{-6}$. The form of eq.(3.30) is indeed reminiscent of approximate critical behaviour and *opposite* to the perturbative expectation, showing once more that perturbation theory has little predictive power near T_c . A non-perturbative analytical calculation of $m_D(T)$ by coupling the gluon to the finite-temperature gluon condensate [67] is also in good qualitative agreement with eq.(3.30), supporting the picture of a dropping Debye mass. Remember that the same behaviour is also seen in the TRG analysis of $\lambda\phi^4$ theory, cf. figure 2.3.

Let us then *assume* that the proportionality (B.14) between the screening mass m_D and the thermal gluon mass m_g remains at least qualitatively valid in the vicinity of the phase transition, i.e. that the exponent β in the characteristic $(1 - T_c/T)^\beta$ behaviour of both m_D and m_g is roughly the same. As it turns out, this is not a serious assumption: we have checked that, as long as $m_g(T)$ and $m_D(T)$ just have similar trends in their T -evolution close to T_c , our results are not sensitive to the detailed quantitative behaviour of the quasiparticle mass.

Guided by these considerations, the thermal gluon mass m_g is thus parametrised as

$$m_g(T) = G_0 T \left([1 + \delta] - \frac{T_c}{T} \right)^\beta. \quad (3.31)$$

where we allow for a small mass gap at $T = T_c$, as indicated by the lattice results for $m_D(T)$ [63]. The small correction $\delta \ll 1$ encodes this deviation. Finally, G_0 is determined by the asymptotic value of the thermal mass, chosen such that the lattice mass and the HTL perturbative result from [45] coincide at $T \approx 3 T_c$, as mentioned above. In order to account for uncertainties and the approximate nature of relation (3.31), we have investigated a range of values for G_0 , δ and β which can be found in

	G_0	δ	β	C_0	δ_c	β_c
Set A	1.35	10^{-5}	0.2	1.24	0.0029	0.34
Set B	1.30	10^{-6}	0.1	1.25	0.0026	0.31
Set C	1.30	10^{-7}	0.05	1.27	0.0021	0.30

TABLE 3.1: Parametrisations for the thermal gluon mass $m_g(T)/T$ and the corresponding confinement factor $C(T)$.

table 3.1. The upper limit of the range is labelled Set A, an intermediate parameter set Set B and the lower limit Set C. Its plots and the lattice data points for $m_D(T)$ are displayed in figure 3.4.

A *decreasing* effective coupling strength $G(T)$ as T_c is approached from above, seems at first sight counterintuitive: One would expect that, at a scale $T \sim \Lambda_{\text{QCD}}$, ‘infrared slavery’ sets in, accompanied by an *increasing* QCD coupling g . However, it should be borne in mind that this expectation is based on a perturbative result extrapolated to large couplings, neglecting non-perturbative effects. As seen in chapter 2.4.2, close to T_c the coupling can indeed show critical behaviour (if the transition is second or weakly first order). A heuristic argument to make the dropping effective coupling plausible in QCD goes as follows. Since we are in a strong coupling regime, the interactions between gluons cannot be described in terms of single gluon exchange, instead they are dominated by (non-perturbative) multi-gluon dynamics. As the temperature is lowered, more and more gluons become confined and form *heavy* glue balls, as outlined earlier. The effective glue ball exchange interaction between gluons reduces approximately to a local four-point interaction proportional to $1/m_{GB}^2$. The total interaction can be interpreted as a superposition of multi-gluon and (weak) glue ball exchange. Obviously, the more glue balls are formed, the weaker becomes this interaction. The coupling $G(T)$ in eqs.(3.28) and (3.31) reflects an interaction between bare gluons from the heat bath on length scales $1/m_{GB}$ and larger that turns these bare gluons into massive, weakly interacting quasiparticles on length scales of order $1/T$. From dimensional arguments (the only other mass scale in the system is the temperature), we may estimate $G(T_c) = \mathcal{O}(T_c/m_{GB} \sim 0.2)$, which is in agreement with our parametrisation of $G(T)$.

3.3.5 Results for SU(3) gauge theory

Now that the temperature behaviour of $m_g(T)$ is given, we can explicitly calculate the entropy density (3.26). Dividing the lattice entropy density by the result of this calculation, we obtain the T -dependence of the confinement factor $C(T)$. A very good fit of the resulting curves again exhibits an approximate critical power-law behaviour:

$$C(T) = C_0 \left(\left[1 + \delta_c \right] - \frac{T_c}{T} \right)^{\beta_c}, \quad (3.32)$$

which is a non-trivial result. The corresponding parameters of $C(T)$ for the different mass parametrisations, sets A, B and C of (3.31), can also be found in table 3.1. Their plots are shown in figure 3.5. $C(T)$ is obviously only weakly sensitive to variations of the mass parameters within a broad band, so the further discussion will be based on Set B. In the following, the quasiparticle model with the gluon mass (3.31) and the

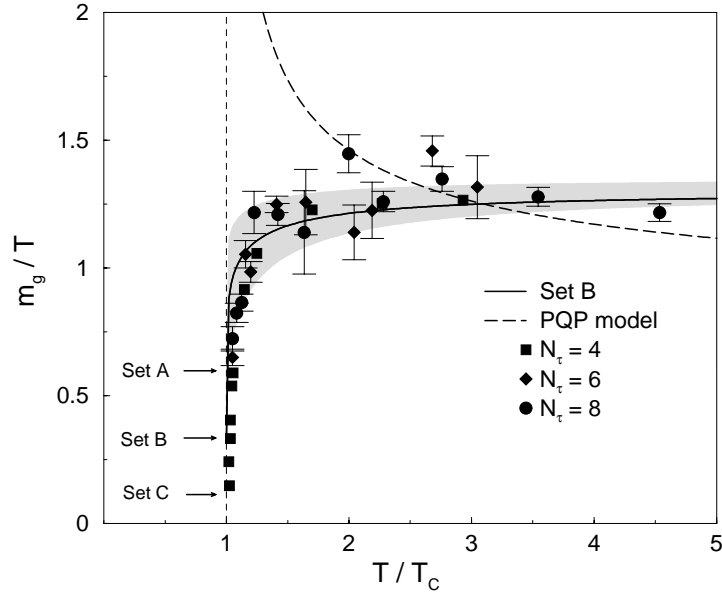


FIGURE 3.4: The thermal gluon mass m_g/T . The grey band shows the parameter range of table 3.1 for eq.(3.31). Set A marks the upper limit and set C the lower, the intermediate set B is displayed as a solid line. The arrows indicate the mass gap $m_g(T_c)/T_c$ of the different sets at the critical temperature. Symbols display $\mu(T)/2$ of eq.(3.29), with $d = 1.5$ fixed, for lattice configurations of different temporal extent N_τ [63]. For comparison the PQP perturbative mass m_g/T of eq.(3.18) is also plotted (dashed line), using the parameters of ref.[45].

confinement factor (3.32) is referred to as 'confinement model'. For the integration constant B_0 appearing in eq.(3.23) we find $0.30 T_c^4 \sim (200 \text{ MeV})^4$. This value is about a factor of 2 larger than in the PQP model and remarkably close to the value of the bag constant at $T = 0$, a welcome feature. As mentioned, we expect the confinement effect to be negligible for $T \gtrsim 3 T_c$ where the HTL quasiparticle model sets in. From there on, $C(T) \rightarrow 1$. The actual deviation of $C(T)$ from 1 for large temperatures has two reasons: first, even in the PQP model a gluon degeneracy of $\nu_g = 16$ does not describe the data, instead a value larger by about 10% is necessary to account for residual sub-leading effects not captured by the model. Second, the behaviour of the gluon mass for larger T is certainly oversimplified since the parametrisation $m_g \propto (T - T_c)^\beta$ is expected to be valid only in the vicinity of T_c . Its value overestimates the HTL perturbative result for $T \geq 3 T_c$ by some 5%, hence the thermodynamical potentials are slightly smaller than in the PQP model. One should instead apply a smooth interpolation between the HTL perturbative mass and the $m_g(T)$ we used for temperatures close to T_c . This would in turn yield a more complicated expression for $C(T)$, but it is in principle straightforward.

In figure 3.6 we compare results of the confinement model to continuum extrapolated SU(3) lattice data [50]. Obviously, the thermodynamic quantities are very well described even close to T_c with our simple and economic parametrisation. The slight deviations in the region $\sim 5 T_c$ arise from our over-simplified functional form of $C(T)$ in that region. We want to stress again that the entropy density is, by construction, *always* fitted.

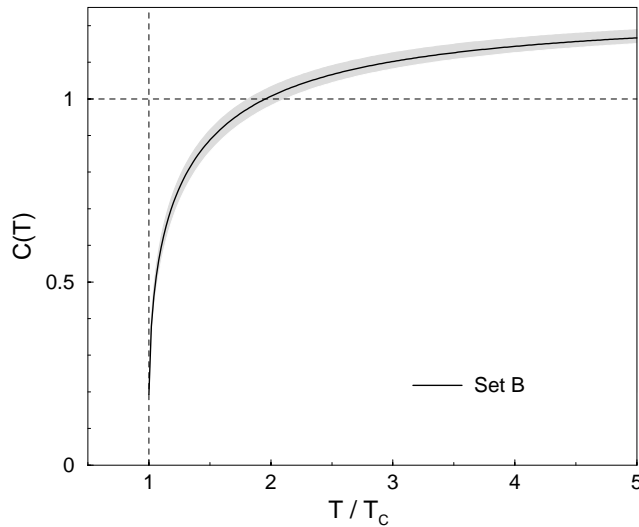


FIGURE 3.5: The confinement factor $C(T)$ as a function of temperature. The grey band shows the range for the corresponding mass parametrisations of table 3.1. The solid line is obtained from set B.

A quantity that is sensitive to the finer details of the model is the trace of the energy-momentum tensor, $T^\mu_\mu = \epsilon - 3p$, which is compared to data from a $32^3 \times 8$ lattice in figure 3.7. The so-called interaction measure

$$\Delta(T) = (\epsilon - 3p)/T^4 \quad (3.33)$$

is connected, via the QCD trace anomaly, to the temperature dependent gluon condensate:

$$T^4 \Delta(T) = \langle \mathcal{G}^2 \rangle_{T=0} - \langle \mathcal{G}^2 \rangle_T. \quad (3.34)$$

Here [50, 68],

$$\langle \mathcal{G}^2 \rangle_T = \frac{11\alpha_s}{8\pi} \langle \mathcal{G}_{\mu\nu}^a{}^2 \rangle_T \quad (3.35)$$

and $\langle \mathcal{G}^2 \rangle_{T=0}$ as in eq.(2.13). Again, excellent agreement over the whole temperature range is observed. The confinement model is even capable of describing the lattice data in the temperature region between T_c and $1.2 T_c$, where the PQP model significantly underestimates the data.

Finally, figure 3.8 shows the function $B(T)$ as a function of temperature. Although the setup of the confinement model is quite different from the PQP model, the shape of this function remains roughly the same. Note, however, that the B_2 term exhibits a completely different temperature behaviour than in the PQP model: it is monotonously decreasing and negative from T_c on. The B_1 term is vital to reproduce the necessary peak structure. The maximal value of $B(T)$ is a factor of ~ 1.6 larger than in the PQP model, but it also becomes negative for larger temperatures, with its zero T_0 slightly shifted from $T_0 \sim 2 T_c$ to $T_0 \sim 2.2 T_c$. An intriguing observation is that its shape now closely resembles the temperature dependence of the spacelike plaquette expectation value Δ_σ . The space- and timelike plaquettes, Δ_σ and Δ_τ , are related to the interaction measure (3.33) by $\Delta = \Delta_\sigma + \Delta_\tau$ and can be expressed in terms of the

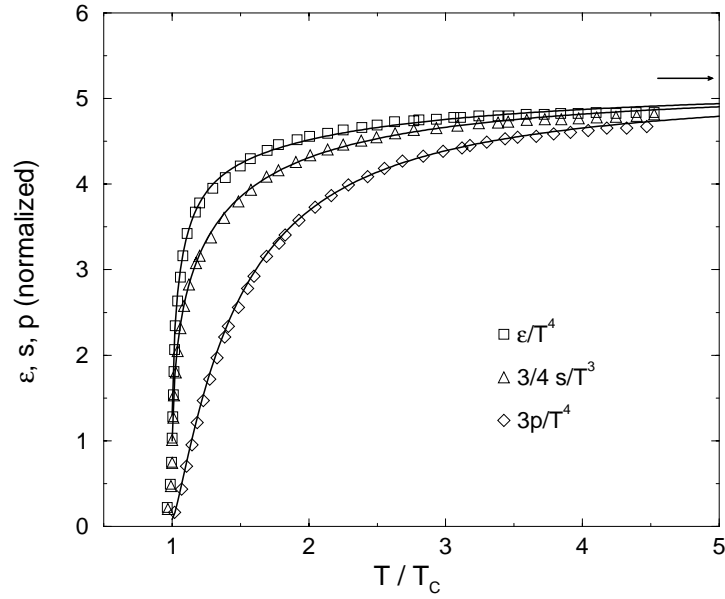


FIGURE 3.6: The normalised energy density $\bar{\epsilon} = \epsilon/T^4$, entropy density $\bar{s} = 0.75 s/T^3$ and pressure $\bar{p} = 3p/T^4$ of our model (solid lines) compared to continuum extrapolated SU(3) lattice data (symbols) [50]. The size of the symbols reflects the lattice uncertainties. The arrow indicates the ideal gas limit for massless gluons.

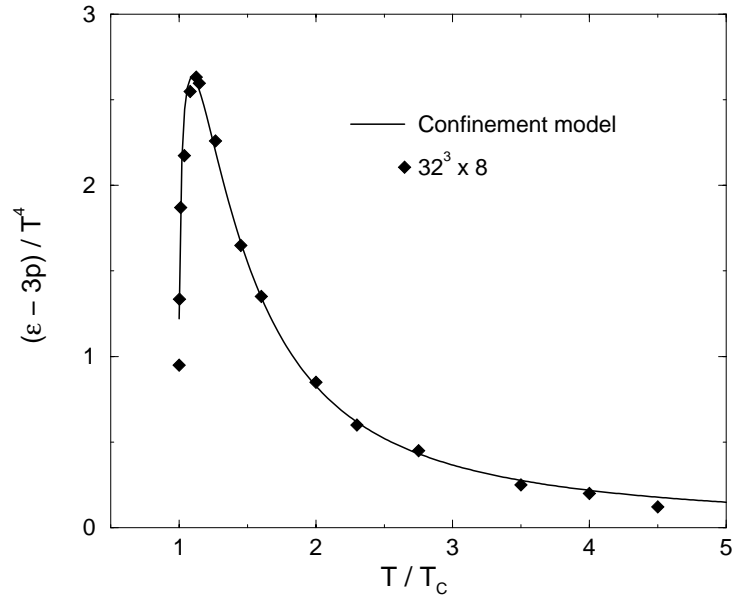


FIGURE 3.7: The interaction measure $\Delta = (\epsilon - 3p)/T^4$ of the confinement model (solid line) versus results (symbols) from a $32^3 \times 8$ lattice. The data symbols already represent the continuum interpolated values [50].

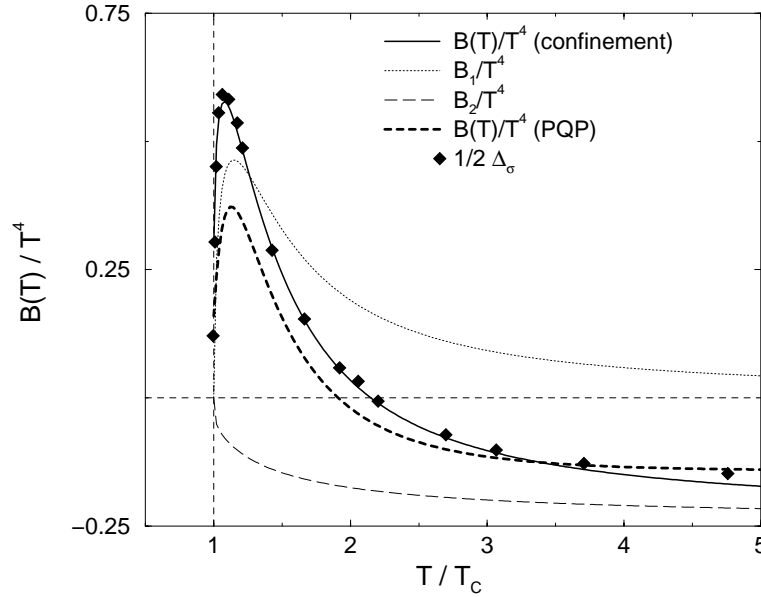


FIGURE 3.8: The function $B(T)$ and its components B_1 and B_2 , defined in eq.(3.23). Also shown is $B(T)$ in the PQP model. Symbols display the spacelike plaquette expectation value $\frac{1}{2}\Delta_\sigma$ taken from the lattice calculation of ref.[50].

thermal chromomagnetic and chromoelectric condensates $\langle \mathbf{B}^2 \rangle_T$ and $\langle \mathbf{E}^2 \rangle_T$ as

$$\begin{aligned} \frac{\alpha_s}{\pi} \langle \mathbf{B}^2 \rangle_T &= -\frac{4}{11} T^4 \Delta_\sigma + \frac{2}{11} \langle \mathcal{G}^2 \rangle_{T=0} \quad \text{and} \\ \frac{\alpha_s}{\pi} \langle \mathbf{E}^2 \rangle_T &= \frac{4}{11} T^4 \Delta_\tau - \frac{2}{11} \langle \mathcal{G}^2 \rangle_{T=0}. \end{aligned} \quad (3.36)$$

What we find in fact is $B(T) = \frac{1}{2}\Delta_\sigma(T)T^4$ (see figure 3.8). This relation between $B(T)$ and $\langle \mathbf{B}^2 \rangle_T$ may be accidental, but it may also hint at a deeper connection between $B(T)$ as a carrier of non-perturbative effects, and the magnetic condensate. After all, $B(T)$ represents the thermal energy of the (non-trivial) Yang-Mills vacuum. In this context it is important to note that this (possible) identification is not caused by thermodynamical self-consistency (otherwise the PQP model should show exactly the same behaviour), but really probes the underlying model. That we find empirically a physical interpretation of $B(T)$ that is not present in other models strongly supports our set up.

3.4 Unquenching the quarks

The extension of the mechanism presented in the last section to systems with dynamical quarks is not straightforward since no concise continuum extrapolation of the QCD EOS with realistic quark masses exists to date. Nevertheless, it is still possible to construct a model of the EOS with 'unquenched' quarks, using some reasonable arguments based on the available lattice data. Recall that, following the argumentation of section 3.1.2, the confinement mechanism itself seems to be only weakly flavour-dependent. Furthermore, there exists evidence that the theory in the limit $N_c \rightarrow \infty$, with $g^2 N_c$ fixed, is quite similar to the $N_c = 3$ gauge theory. Since quark loops are

non-leading $\mathcal{O}(1/N_c)$ contributions to the physics, they will not influence the confinement/deconfinement phase transition within, say, 10%. Finally, as outlined in section 2.4.3, lattice results on the order of the phase transition in full QCD indicate that the transition is first order in the case of three light, degenerate quark flavours and most likely second order for two flavours. If the world as we know it is close to the two flavour world (i.e. if the strange quark mass is so heavy that it does not alter the phase transition qualitatively), we can still assume a 'dropping mass' scenario.

3.4.1 Thermal masses

No lattice data on thermal masses with dynamical quarks are available. We thus construct effective masses for quarks and gluons by assuming that the N_c - and N_f -dependence of m_g and m_q are both given by the HTL asymptotic limit. For the thermal gluon mass, following (B.9), we employ the *ansatz*:

$$\frac{m_g(T)}{T} = \sqrt{\frac{N_c}{6} + \frac{N_f}{12}} \tilde{G}(T, N_c, N_f) \quad (3.37)$$

with the effective coupling

$$\tilde{G}(T, N_c, N_f) = \frac{\tilde{G}_0}{\sqrt{11N_c - 2N_f}} \left([1 + \delta] - \frac{T_c}{T} \right)^\beta. \quad (3.38)$$

\tilde{G}_0 , δ and β are taken to be universal. Setting $\tilde{G}_0 = 9.4$, $\delta = 10^{-6}$ and $\beta = 0.1$, the gluon and quark masses coincide with the two flavour HTL masses at $T \simeq 3 T_c$, using the parameters of ref.[89]. The thermal quark mass becomes [89]

$$\frac{m_q(T)}{T} = \sqrt{\left(\frac{m_{q,0}}{T} + \sqrt{\frac{N_c^2 - 1}{16N_c}} \tilde{G}(T) \right)^2 + \frac{N_c^2 - 1}{16N_c} \tilde{G}(T)^2} \quad (3.39)$$

with the zero-temperature bare quark mass $m_{q,0}$.

In [72], a non-perturbative dispersion equation for a thermal quark interacting with the gluon condensate has been calculated, and it has been found that the effective quark mass is given by $m_q \simeq 1.15 T$ in the temperature range between $1.1 T_c$ and $4 T_c$. Eq.(3.39) is within 10% in agreement with this result. Nevertheless, very close to T_c the parametrisation (3.39) may be too simple: if the expected chiral phase transition is second order (or weakly first order), fermions may decouple in the vicinity of the phase transition because they have no Matsubara zero modes, and the transition dynamics would be dominated by the bosonic gluons only. In this case gluon masses should become independent of N_f . However, as in the pure gluon sector, the results are stable against small variations of the mass parametrisations, and as long as no further information is available, eqs.(3.39) and (3.37) may be taken as an educated guess.

We now proceed as follows: First, we assume that the continuum limit of the pressure can be obtained from the $N_\tau = 4$ lattice data by applying a 10% correction, i.e. $p_{\text{cont}} \simeq 1.1 p_{\text{lat}}$. Second, using Occam's razor we employ a *universal* confinement function $C(T)$ for both quarks and gluons, motivated by eq.(3.2). The extension of eq.(3.24) to systems including quark flavours is straightforward:

$$p(T) = \frac{\nu_g}{6\pi^2} \int_0^\infty dk [C(T) f_B(\omega_k^g)] \frac{k^4}{\omega_k^g} + \sum_{i=1}^{N_f} \frac{2N_c}{3\pi^2} \int_0^\infty dk [C(T) f_D(\omega_k^i)] \frac{k^4}{\omega_k^i} - B(T). \quad (3.40)$$

	C_0	δ_c	β_c
2 flavours	1.25	0.02	0.28
2+1 flavours	1.16	0.02	0.29
3 flavours	1.03	0.02	0.2
gluon	1.25	0.0026	0.31

TABLE 3.2: Parametrisations of eq.(3.32) for the confinement function $C(T)$ in the presence of dynamical quark flavours. For comparison, the corresponding values of the pure gauge system (set B) are also shown.

Here $\omega_k^g = \sqrt{k^2 + m_g^2(T)}$ as before. The quark energy is $\omega_k^i = \sqrt{k^2 + m_i^2(T)}$ for each quark flavour $q = i$, and $m_q(T)$ is given by eq.(3.39) with the bare quark masses $m_{q,0}$. The function $B(T)$, the entropy density $s(T)$ and the energy density $\epsilon(T)$ follow analogously. If the confinement model is applicable, we should expect that the parameters of $C(T)$ in eq.(3.32), as shown in table 3.1 for the gluonic calculations, are similar in the presence of quarks. We start therefore with the gluon values for C_0 , δ_c and β_c and vary them slightly until good agreement with the lattice pressure is obtained. To account for the temperature-dependent *bare* masses used specifically in the lattice calculations, the quark masses $m_{q,0}$ in eq.(3.39) are set to $m_{q,0} = 0.4 T$ (light quarks) and $m_{s,0} = 1.0 T$ (heavy quark). Figure 3.9 shows the results for 2 and 2+1 flavours, the corresponding values for the parameters of $C(T)$ can be found in table 3.2. We observe that indeed, the confinement factor $C(T)$ does not differ much from the pure gluonic case. The factor B_0 is set to $1.4 T_c^4 \simeq (180 \text{ MeV})^4$. The larger value for δ_c is explained by noting that, for $T < T_c$, many light quark-antiquark composites (pions, kaons etc.) are present. They contribute sizably to the entropy in the hadronic phase. Accordingly, $C(T_c)$ is larger than in the pure gluon case, hence δ_c has to increase.

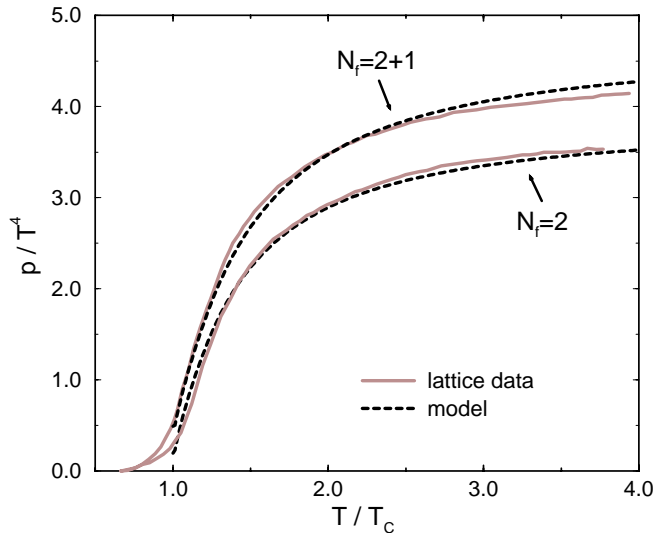


FIGURE 3.9: The rescaled lattice pressure $p_{\text{cont}} \simeq 1.1 p_{\text{lat}}$ (grey lines) for 2 and 2+1 flavours and the pressure obtained from the confinement quasiparticle model with running bare quark masses (dashed lines). Values for the parameters of $C(T)$ are shown in table 3.2.

3.4.2 Physical quark masses

Pressure, energy and entropy density for physical quark masses are finally obtained by setting $m_{q,0}$ in eq.(3.39) to the real-world values $m_{u,d} \simeq 0$ and $m_s \simeq 170$ MeV. This procedure assumes that $C(T)$ is independent of $m_{q,0}$ which is not clear. In present lattice simulations, the pions are too heavy, $m_\pi^{\text{lat}} \geq 450$ MeV, therefore their contribution to $s(T)$ or $p(T)$ is strongly Boltzmann suppressed. Since

$$\frac{e^{-m_\pi^{\text{lat}}/T_c}}{e^{-m_\pi^{\text{phys}}/T_c}} \approx \frac{1}{7},$$

future computations with lighter, more realistic pion masses are expected to find a substantially larger pressure and entropy in the hadronic phase below T_c . On the other hand, the pion- or quark mass dependence of T_c , eq.(2.54), is very moderate, indicating that the confinement mechanism is insensitive to $m_{q,0}$. With this *caveat*, we assume for now that $C(T)$ does not depend on $m_{q,0}$. Figure 3.10 shows a prediction of $\epsilon(T)$, $s(T)$ and $p(T)$ for massless two flavour QCD. Reassuringly, the pressure of the confinement model is well within the narrow estimate for the continuum EOS of ref.[30] for $T > 2 T_c$ that was released *after* our prediction. In contrast to the pure gluon EOS, we observe that the energy and entropy are close to the ideal gas limit already at $T = 3 T_c$. However, it has to be borne in mind that their normalization is set by C_0 which in turn depends on the continuum estimate of the $N_\tau = 4$ lattice data. More reliable estimates for the continuum pressure are needed to confirm this behaviour. It is also worthwhile noting that, going from temperature-dependent bare masses (as used in the lattice simulations) to the chiral limit, the corresponding change of the pressure in the confinement model is stronger than expected from an ideal Fermi gas. It rises by about 7% whereas for an ideal gas with quark mass $m_q/T = 0.4$ the difference would be only about 3.5% (for $N_f = 2$).

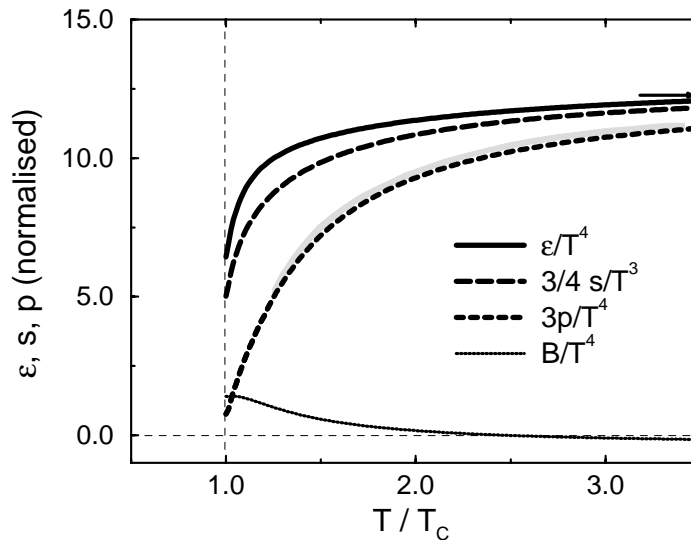


FIGURE 3.10: Pressure, energy and entropy density for two light quark flavours in the confinement model. The arrow indicates the ideal gas limit. The grey band is an estimate of the continuum EOS for massless two flavour QCD, based on an extrapolation of lattice results [30].

In figure 3.11, we plot the energy density for three light quark flavours on a $16^3 \times 4$ lattice [73] and as obtained in the confinement model. We mention that these lattice data are not as well understood as the pressure. In particular, a contribution to ϵ/T^4 proportional to the bare quark mass that vanishes in the chiral limit has been omitted by hand. In addition, there is no estimate of the continuum limit of these lattice data, hence our normalisation, set by C_0 in eq.(3.32), is substantially smaller than in previous cases. Apart from that, the data are very well reproduced down to T_c .

Finally, the most important result of this chapter is displayed in figure 3.12: the calculated pressure, energy and entropy density for “the real world”, a system with two light quark flavours ($m_{q,0} = 0$) and a heavier strange quark ($m_{s,0} \simeq 170$ MeV). Here, the approach to the Stefan-Boltzmann limit is obviously slower than in the two flavour case because of the mass suppression of the third, heavier flavour. N_f in eqs.(3.37), (3.38) and (3.39) was set to 2.3. For comparison, also shown are continuum estimates of lattice data for dynamical staggered fermions with masses $m_{u,0} = m_{d,0} \sim 65$ MeV and $m_{s,0} \sim 135$ MeV [74]. Since the explicit bare mass dependence of the pressure in our model is quite moderate², these data provide another check of our model. Again, the data have been released after our calculations and show very nice agreement even close to T_c . The results for $\epsilon(T)$ and $p(T)$ are also consistent, for $T > 2 T_c$, with an EOS obtained in the PQP model [75]. Closer to T_c , the confinement model predicts a stronger decrease of the energy density, though. Again, $B(T)$ resembles the shape of the corresponding function in the PQP model. However its zero, T_0 , is considerably shifted, from $T_0 \sim 1.7 T_c$ to $T_0 \sim 2.7 T_c$.

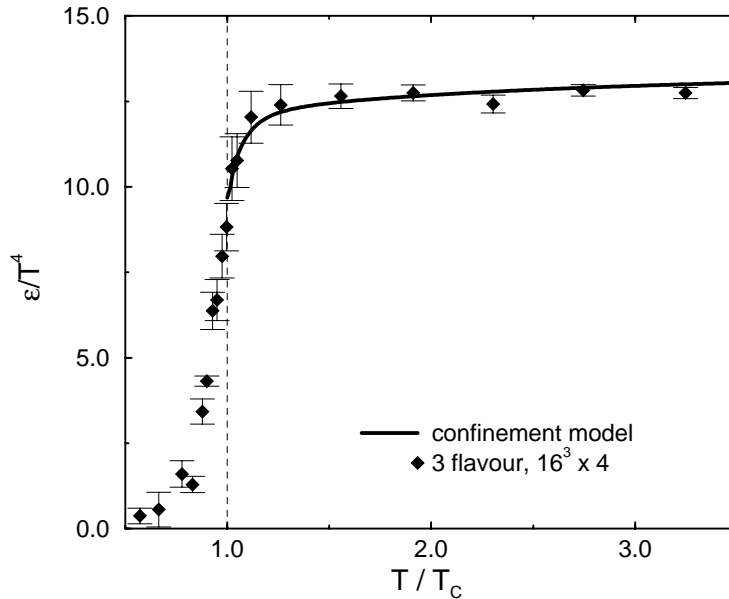


FIGURE 3.11: Energy density estimate in the chiral limit for three quark flavours on a $16^3 \times 4$ lattice [73] (data points) and as obtained in the confinement model (solid line).

²The corresponding curves of the confinement model with the lattice quark masses quoted in the text differ by less than 5% of the ones shown in figure 3.12.

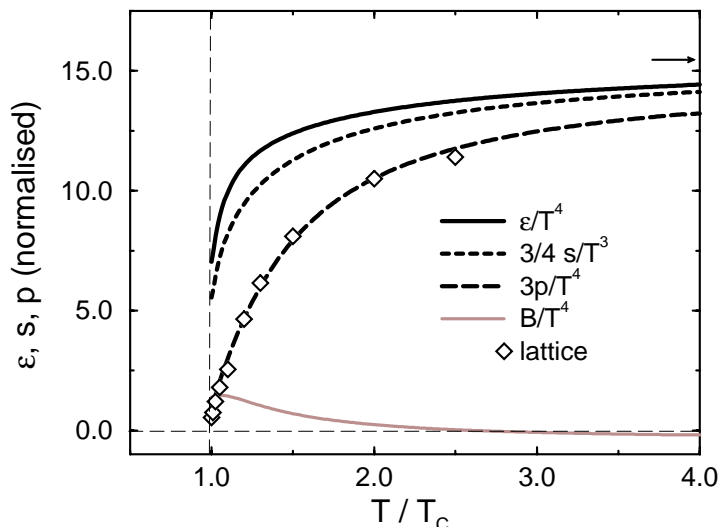


FIGURE 3.12: Pressure, energy and entropy density for two light quark flavours ($m_{u,d} = 0$) and a heavier strange quark ($m_s \simeq 170$ MeV) in the confinement model. The arrow indicates the ideal gas limit of massless three-flavour QCD, the crosses are continuum estimates of lattice data for two light and one heavy quark flavour [74] (see text for further details).

3.4.3 Comparison with other work

There have been several attempts in the literature to describe the phase transition within a more microscopical approach, and we briefly discuss three recent ones, restricting ourselves to the pure SU(3) glue theory. In [69], an evaporation model of the gluon condensate was set up. There, the thermodynamics below T_c is governed by a dilaton Lagrangian that mimics the gluon condensate. Gluons are 'frozen' inside the condensate, and the dilaton excitations are the heavy glueballs. Crossing the critical temperature, the gluons evaporate (deconfine) and interact only perturbatively thereafter. With basically two fit parameters, a critical temperature of $T_c = 290$ MeV can be calculated by minimising the thermodynamical potential, and pressure and energy density are reasonably well described. The fact that the gluon condensate is still present and large at high temperature (see figure 3.7), however, poses some conceptual difficulties, as well as the assumption that the dilaton field is treated in the mean-field approximation which may be more justified for large N_c where the transition becomes strongly first order.

Ref.[70] starts from an interaction between colour charges in a plasma that is mediated by strings. The modified energy density takes the form $\Delta\epsilon = n\sigma\langle l \rangle$, where n is the string density (neglecting spatial correlations), σ the string tension appearing in eq.(2.11) and $\langle l \rangle$ is the average string length. Using a density-dependent mean field spectrum, a dispersion relation for gluons of the form $\omega_k = k + \frac{2}{3}\sigma n^{-1/3}$ can be constructed that gives qualitative agreement of pressure and energy density with the lattice data of figure 3.2. It is then intuitively clear that, approaching T_c from above, gluons become confined, so the average string length has to increase. The term $n^{-1/3} \sim \langle l \rangle$ then acts like an effective, increasing mass, and the model becomes comparable in spirit to the PQP models discussed above. Taking $\langle l \rangle \sim 1$ fm at T_c , one finds $\omega_k(T_c) = k + \mathcal{O}(500$ MeV). Again, the model only parametrises the complicated

QCD dynamics, this time by the strings that are assumed to be non-interacting among themselves.

The QGP has also been described in terms of a condensate of Z_3 Wilson lines [71]. Using as effective degrees of freedom the order parameter of the transition, the spatially averaged gauge-invariant Polyakov loop (2.47), a mean-field potential $V(\langle L \rangle) = -1/2m^2\langle L \rangle^2 + \lambda/4\langle L \rangle^4$ is constructed to obtain the expected behaviour of the pressure close to T_c ,

$$p(T) \sim \left(1 - \frac{T_c}{T}\right)^\gamma T^4.$$

Note that the form of the potential $V(\langle L \rangle)$ for $N_c = 2$ is nothing than the $\lambda\phi^4$ system with SSB considered in section 2.4.2, with interchanged limits: the $\lambda\phi^4$ system condenses at low temperatures whereas the gauge theory develops a non-vanishing VEV at high temperatures, eq.(2.50). With standard mean-field arguments, a number of lattice data can be described. This *ansatz* is presumably closest to our philosophy because it tries to include the anticipated critical behaviour close to T_c from the onset. Furthermore, it makes a number of predictions that are testable on the lattice, most importantly how the phase transition properties change when varying the number of colours.

To conclude, all available models that try to describe the deconfinement phase transition at least semi-quantitatively are phenomenological to date; they parametrise in one way or the other the non-perturbative gluon dynamics and have a more or less large number of fit parameters. Since that situation does not change when dynamical quarks are included, we believe that it is at this stage not possible to calculate QGP signals from first principles. Instead, phenomenological models that cover as much physics as is known should be used wherever possible.

3.5 Finite quark chemical potential

As we have discussed in section 2.4.4, first lattice calculations at finite quark chemical potential μ indicate that for $\mu < 200$ MeV, the physics of the phase transition does not change qualitatively. Since the chemical freeze-out at SPS occurs at about $\mu_{f.o.} \simeq 100$ MeV [41] and at RHIC at $\mu_{f.o.} \simeq 15$ MeV [42], a description of the QGP phase in terms of the same degrees of freedom as at $\mu = 0$ is possible for these experimentally accessible ranges of μ . We will therefore briefly outline in this section the extension of the confinement model to finite, yet small chemical potential, i.e. $\mu/T \lesssim 1$. We compare to lattice data, where appropriate, and briefly dwell on the phenomenological implications of our results. A much more detailed discussion of this issue can be found in the diploma thesis of Michael Thaler [76].

3.5.1 The equation of state

In this section, we will assume flavour symmetry to lighten the notation. At finite μ , the quark contribution to the pressure is modified from the second term in eq.(3.40) to:

$$p(T, \mu) = \frac{N_f N_c}{3\pi^2} \int_0^\infty dk \frac{k^4}{\omega_k} C(T, \mu) [f_D^+(\omega_k) + f_D^-(\omega_k)] - B(T, \mu). \quad (3.41)$$

$f_D^+(\omega_k)$ and $f_D^-(\omega_k)$ stand for the Fermi-Dirac distribution functions for particles and antiparticles, respectively:

$$f_D^\pm(\omega_k) = [\exp(\beta\{\omega_k \mp \mu\}) + 1]^{-1}, \quad (3.42)$$

with the usual energy $\omega_k = \sqrt{k^2 + m(T, \mu, m_q)^2}$. Energy and entropy density follow accordingly. The net particle density associated with the conserved charge Q is derived from (3.10) as

$$n_q(T, \mu) = \frac{N_f N_c}{2\pi^2} \int_0^\infty dk k^2 C(T, \mu) [f_D^+(\omega_k) - f_D^-(\omega_k)], \quad (3.43)$$

which is obviously zero for $\mu = 0$. Since pressure, energy density, particle density and the entropy density are connected by the extended Gibbs-Duhem relation (3.8), we obtain $B(T, \mu)$ from the same stationarity condition (3.12) as at $\mu = 0$. The main difference is that the functions $\mathcal{F}_i(T, \mu)$ now depend on *two* external parameters, so

$$0 = \left. \frac{\partial p}{\partial m} \right|_{T, \mu} = \frac{\partial p}{\partial T} \left[\frac{\partial m}{\partial T} \right]^{-1} + \frac{\partial p}{\partial \mu} \left[\frac{\partial m}{\partial \mu} \right]^{-1}.$$

A similar equation exists for $\partial p / \partial C$, leading to the following equation for $B(T, \mu)$:

$$\begin{aligned} & \frac{\partial B(T, \mu)}{\partial T} + \frac{\mu}{T} \frac{\partial B(T, \mu)}{\partial \mu} = \\ & - \frac{N_c N_f}{2\pi^2} \int_0^\infty dk [f_D^+(\omega_k) + f_D^-(\omega_k)] C(T, \mu) \frac{k^2}{\omega_k} \left[\frac{\partial m^2(T, \mu)}{\partial T} + \frac{\mu}{T} \frac{\partial m^2(T, \mu)}{\partial \mu} \right] \\ & + \frac{N_c N_f}{3\pi^2} \int_0^\infty dk [f_D^+(\omega_k) + f_D^-(\omega_k)] \frac{k^4}{\omega_k} \left[\frac{\partial C(T, \mu)}{\partial T} + \frac{\mu}{T} \frac{\partial C(T, \mu)}{\partial \mu} \right]. \end{aligned} \quad (3.44)$$

This is a partial differential equation of the type

$$x \frac{\partial f(x, y)}{\partial x} + y \frac{\partial f(x, y)}{\partial y} = \mathcal{I}(x, y) \quad (3.45)$$

that has the general solution

$$f(x, y) = \int^x dt \mathcal{I}\left(t, \frac{y}{t}\right) + \mathcal{H}\left(\frac{y}{x}\right). \quad (3.46)$$

Here, $\mathcal{H}(y/x)$ is a solution of the homogeneous equation. Returning to our case, $\mathcal{H}(\mu/T)$ becomes an arbitrary function of the ratio μ/T that has to be fixed by boundary conditions. In section 3.4, the functional form of $B(T, 0)$ has been derived. For $\mu \rightarrow 0$, $\mathcal{H}(\mu/T)$ does not depend on T anymore and therefore has to be identified with the integration constant B_0 in eq.(3.23). $\mathcal{H}(\mu/T)$ surely is a continuous function for $T > T_c$, so for small μ/T , it has to be close to B_0 . Taylor expanding, the first derivative vanishes, as in (2.55), and the series starts only at order $(\mu/T)^2$. For our purposes, we therefore identify $\mathcal{H}(\mu/T)$ with a constant B_0 for all μ under consideration. Assembling all pieces, the final result reads

$$B(T, \mu) = B_0 - \frac{N_c N_f}{2\pi^2} \int_0^\infty dk \int_{T_c}^T d\tau C [f_D^+(\omega_k) + f_D^-(\omega_k)]$$

$$\begin{aligned}
 & \times \frac{k^2}{\omega_k} \left[\frac{\partial m^2}{\partial \tau} + \frac{\mu}{T} \frac{\partial m^2}{\partial (\frac{\mu}{T} \tau)} \right] + \frac{N_c N_f}{3\pi^2} \int_0^\infty dk \int_{T_c}^T d\tau [f_D^+(\omega_k) + f_D^-(\omega_k)] \\
 & \times \frac{k^4}{\omega_k} \left[\frac{\partial C}{\partial \tau} + \frac{\mu}{T} \frac{\partial C}{\partial (\frac{\mu}{T} \tau)} \right], \tag{3.47}
 \end{aligned}$$

where the explicit τ -dependence in $C(\tau, \mu/T \tau)$, $m(\tau, \mu/T \tau)$ and $\omega_k(\tau, \mu/T \tau)$ has been suppressed for the sake of lucidity. In the following, we will assume that $C(T, \mu)$ does not depend on μ . Also \tilde{G} is taken to be eq.(3.38), with no μ -modifications, since T is still the largest scale. The chemical potential appears only in the effective mass (3.39), where we replace $\tilde{G}(T)T \rightarrow [1 + \mu^2/(\pi^2 T^2)]\tilde{G}(T)T$, in accordance with the HTL results (B.25) and (B.26).

How reasonable these assumptions are, can be tested against a lattice calculation of the pressure at T_c and small μ [40]. There, the quantity $\Delta\bar{p} = [p(T_c, \mu) - p(T_c, 0)]/T^4$ was evaluated for two flavours with a bare quark mass of $0.1 T_c$. The chemical potential was chosen to be that at RHIC, $\mu = \mu_{\text{RHIC}} = 0.1 T_c \simeq 17$ MeV, and the pressure at finite μ was calculated using a Taylor expansion about $\mu = 0$, similar to eq.(2.55) (in fact, the expansion coefficient $\partial^2 p / \partial \mu^2|_{\mu=0}$ is just the quark number susceptibility that we will discuss in the next section). As in section 3.4, the measured value of $\Delta\bar{p} = 0.0034$ has to be continuum-extrapolated, so we take again $\Delta\bar{p}_{\text{cont}} \simeq 1.1 \Delta\bar{p}_{\text{lat}}$. The final value of $\Delta\bar{p}_{\text{cont}} = 0.00374$ compares rather favourably with the prediction from our model, where $\Delta\bar{p} = 0.0040$, using eq.(3.41). Since $B(T, \mu)$ reduces to B_0 at T_c , all B -dependence cancels in $\Delta\bar{p}$, and the comparison directly tests the ideal gas *ansatz*. Note that $\bar{p}(T_c, 0) = p(T_c, 0)/T^4$ is about 0.5, so the influence of the chemical potential μ_{RHIC} is a very small effect on the 1% level. Consequently, since at RHIC – and even at SPS – the ratio μ/T will be always small for all reachable values of T (as we derive in the next chapter), the influence of μ on the parton equation of state can be safely neglected in the treatment of URHIC. The bare quark mass dependence, however, is not that well described within our model, as explored in more detail in [76].

Figure 3.13 shows the ratio of $p_q(T, \mu)$ over $p_q(T, \mu = 0)$ as a function of chemical potential μ and temperature T , calculated in the confinement model and excluding the gluon contributions. The dependence on μ is rather weak, as mentioned above, and most pronounced at small temperatures and large μ . In the fugacity approximation, eq.(3.41) can be re-written as

$$p_q(T, \mu)_{\text{fug}} \approx \frac{1}{2} [\exp(\mu/T) + \exp(-\mu/T)] [p_q(T) - B_q(T)],$$

where $p_q(T)$ and $B_q(T)$ are the corresponding functions in the absence of μ and gluons. For $\mu/T_c = 1$, $p_q(T_c, \mu)_{\text{fug}} \approx 1.5 p_q(T_c)$, which already gives almost the value shown in figure 3.13. The most drastic effect of the chemical potential hence comes from the modification of the distribution function.

The existence of quark quasiparticle structures even close to T_c is also evident from figure 3.14. There, first lattice results [83] on the net quark density $n_q(T, \mu)$ for 2+1 flavours are compared with our calculation, using eq.(3.43) with $C(T, \mu) = C(T)$. Obviously, the shape of the lattice data is well described by our model even for μ as large as 70 MeV, whereas the normalisation is off by $\sim 10 - 20\%$. Since the data points have been normalised to the $T \rightarrow \infty$ limit, this lattice continuum extrapolation has to

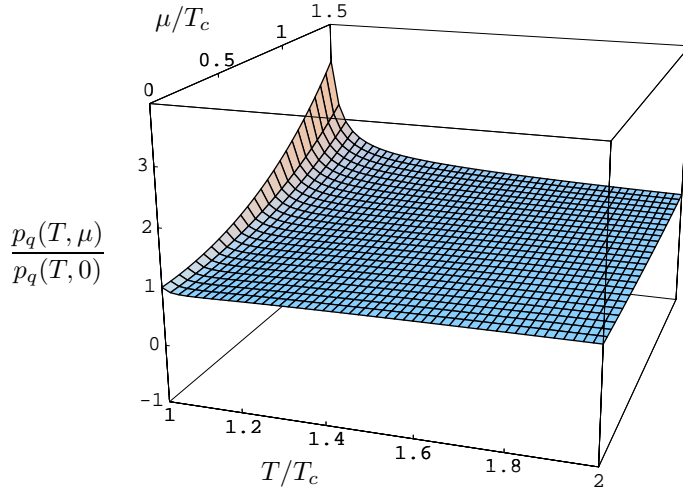


FIGURE 3.13: The ratio $p_q(T, \mu)/p_q(T, 0)$ in the confinement model for $N_f = 2$ (excluding gluons) as a function of quark chemical potential μ/T_c and temperature T/T_c .

be still regarded as preliminary, though. The peak in n_q/T^3 at $T \simeq 1.2 T_c$ arises very naturally in a quasiparticle description, because, in the fugacity approximation,

$$n_q(T, \mu) \simeq \frac{1}{2} [\exp(\mu/T) - \exp(-\mu/T)] n_q^{\text{tot}}(T) = \sinh(\mu/T) n_q^{\text{tot}}(T). \quad (3.48)$$

Here, $n_q^{\text{tot}}(T)$ is the *total* quark density at zero chemical potential, defined in eq.(5.13). Now n_q^{tot} is an increasing function of T and $\sinh(\mu/T)$ is decreasing, at fixed μ . Their product hence exhibits a peak structure that is a strong indicator of the validity of the quark quasiparticle concept even close to T_c .

3.5.2 Quark number susceptibilities

Let Q be the conserved number operator associated with a given particle species and μ its corresponding chemical potential. The mean square deviation of Q is then given by

$$\langle \delta Q^2 \rangle \equiv \langle Q^2 \rangle - \langle Q \rangle^2 = T \frac{\partial \langle Q \rangle}{\partial \mu}. \quad (3.49)$$

The quark number susceptibility (QNS) χ measures the response of the net quark number density $n(T, \mu)_i = \langle Q_i \rangle$ of flavour i to an infinitesimal variation of the chemical potential μ_j :

$$\chi_{ij} = \frac{\partial n_i}{\partial \mu_j} = \frac{\partial^2 p}{\partial \mu_j \partial \mu_i} \quad (3.50)$$

and is related to the fluctuations by $\langle \delta Q^2 \rangle = VT\chi$. For an ideal gas with a single flavour, $\chi_0 = N_c T^2/3$. Since fluctuations of conserved particle numbers or charges may in principle discriminate the QGP against the hadronic phase in ultra-relativistic heavy-ion collisions [77, 78], χ is an interesting quantity for event-by-event fluctuation physics. Moreover, χ can be computed on the lattice for $\mu = 0$ [79] and allows first steps in the $T - \mu$ plane, as the second derivative in the Taylor expansion of $p(T, \mu)$ in small μ . Here, it is used as an independent check of the confinement model that makes predictions for χ without any adjustments.

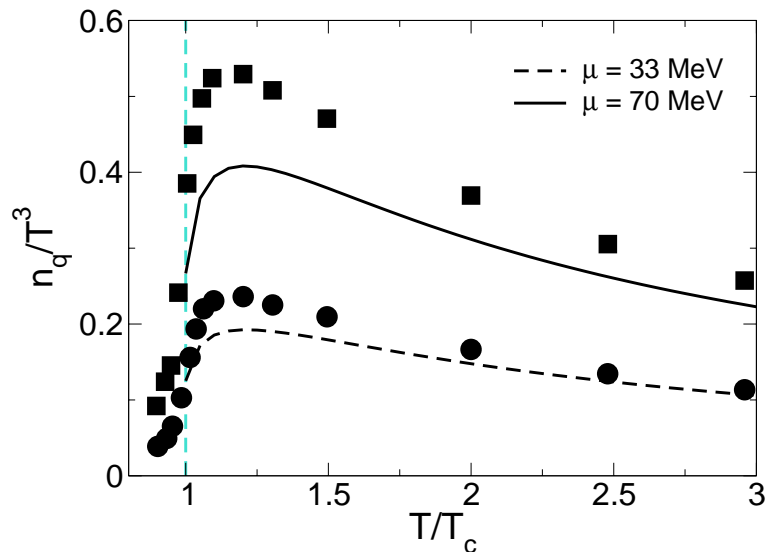


FIGURE 3.14: Net quark density $n_q(T, \mu)/T^3$ for 2+1 flavours as a function of T/T_c . The data points are continuum estimates of a lattice calculation for dynamical staggered fermions with masses $m_{u,0} = m_{d,0} \sim 65$ MeV and $m_{s,0} \sim 135$ MeV [83]. The dashed ($\mu = 33$ MeV) and solid ($\mu = 70$ MeV) line show the corresponding results from the confinement model, using eq.(3.43) with $C(T, \mu) = C(T)$.

The off-diagonal QNS χ_{ud} have been measured on the lattice and were found to be compatible with zero for $1.3 T_c < T < 3.5 T_c$ within errors of $10^{-7} T^2$ [80]. In the confinement model, χ_{ud} vanishes by construction because different flavours do not talk to each other, so our scenario of non-interacting quasiparticles seems to be supported by these lattice results. In contrast, HTL resummed perturbation theory finds a value of $\chi_{ud}^{\text{HTL}}(3 T_c) = \mathcal{O}(10^{-4} T^2)$ [81], which is an unresolved issue at the moment.

In ordinary perturbation theory, the diagonal QNS $\chi \equiv \chi_{ii}$ is presently known to order $g^4 \log(1/g)$ [82]. While the lattice data approach the ideal gas limit from below with increasing temperature and lie about 20% below the ideal gas limit at about $4 T_c$ [79], the perturbative result starts above the ideal gas limit and decreases logarithmically with increasing T . Again, bare perturbation theory fails badly to even capture the trend of the lattice results. In the confinement model, the quark number density $n(T, \mu)$ is defined in eq.(3.43). Since the parametrisation of n is fixed by construction of the quasiparticle model, we can give a parameter-free prediction of χ , again under the assumption that $C(T, \mu)$ does not depend strongly on μ . The QNS for the physical case of two light and one heavy flavour is shown in figure 3.15 and compared with estimates of the continuum limit of the lattice data [79] (see [76] for more details). We observe good agreement with the (coarse) lattice data. The slight overshooting for $T > 3 T_c$ arises from our insufficient parametrisation of $C(T)$ in that region. Of course, more data points with higher statistics and a concise continuum-extrapolation are needed for definite conclusions, but it is encouraging that the confinement model seems to work well even when extended to finite chemical potential.

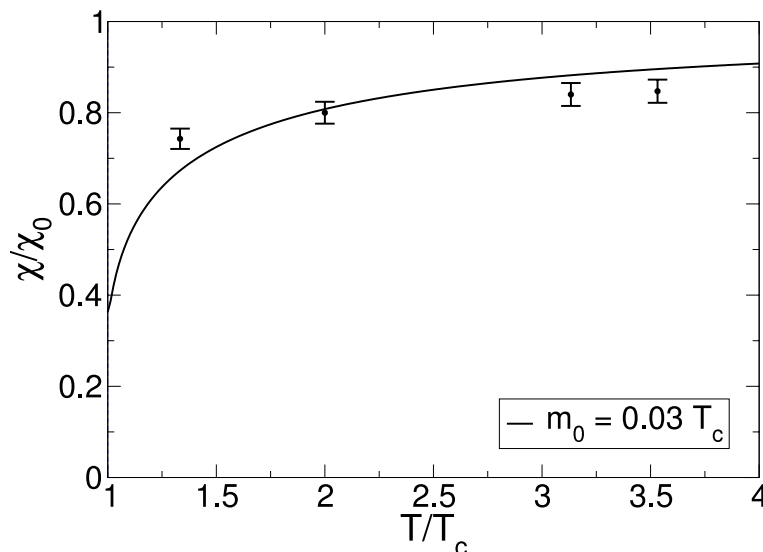


FIGURE 3.15: The ratio $\chi(T)/\chi_0$ in the confinement model for two light flavours ($m_u = m_d = 0.03 T_c$) and a heavy flavour ($m_s = T_c$) as a function of T/T_c . The data points are continuum-extrapolated estimates of the lattice data simulated in [79].

3.6 Intermediate summary

In this chapter, we have constructed a novel quasiparticle description of the QCD EOS in the temperature region $T_c < T \lesssim 3 T_c$ where current heavy-ion experiments operate. Our main improvement, as compared to previous work, is the schematic inclusion of confinement that has so far not been taken into account, but should dominate the dynamics that close to T_c . Since confinement simply reduces the number of thermally active degrees of freedom in a statistical sense, this non-perturbative behaviour is incorporated in a model of quasifree, massive quasiparticles by a modification of the particle distribution functions with a confinement factor $C(T)$. This method corresponds to the maximal extension of any ideal gas model. Our model parametrises the continuum-extrapolated lattice data in a simple and economic fashion, and the interaction measure $\Delta(T)$ is even better reproduced than in previous phenomenological models. The true challenge of the model, however, lies in confronting it with independent lattice data that are not governed by thermodynamic consistency. As a first intriguing check, a possible physical connection of the thermal energy of the Yang-Mills vacuum, $B(T)$, with the chromomagnetic condensate $\langle \mathbf{B}^2 \rangle_T$ has been observed – a feature that is not presented in the PGP models and strongly supports our setup.

For systems with dynamical quarks, sufficiently precise lattice data are not yet available. With reasonable assumptions, we can nevertheless extend the model and find that for $N_f = 2$ and $N_f = 2 + 1$ the pressure of our confinement model is well within narrow lattice estimates for the continuum EOS released after our predictions. Of course, future simulations with higher statistics and smaller quark masses are needed to refine the model. The extension of the confinement model to small quark chemical potential has also proven to be successful. First lattice calculations of the net quark density at finite μ are well described by simple quark quasiparticle structures even close to T_c . Our value for $p(T_c, \mu_{\text{RHIC}})$, with $\mu_{\text{RHIC}} \simeq 17$ MeV, is within 10% in accord with

a recent lattice calculation and differs only by about 1% from the value at zero chemical potential. Since at RHIC and even at SPS the ratio μ/T is small for all reachable values of T , the influence of μ on the parton equation of state can be safely neglected in the treatment of URHIC. In addition, the lattice results on the off-diagonal quark number susceptibilities (that directly measure the interactions) support our picture of a quasifree QGP in the vicinity of the phase transition. We also managed to describe, without any parameter adjustments, the diagonal quark number susceptibility for two light and a heavy quark, where it should be kept in mind that the lattice data are still quite coarse and carry large error bars, though.

To conclude, the thermal quasiparticle-plus-confinement model successfully describes and predicts a variety of lattice data, both in the pure glue sector and for QCD with dynamical quarks. It incorporates the main physics near the phase transition in a schematic, yet thermodynamically consistent way. We believe it to be a reasonable representation of the QGP and use it extensively in the next two chapters, both in the construction of a fireball and in the calculation of QGP signatures.

4 Dilepton Rates

In this chapter, we utilise the quasiparticle formalism developed in chapter 3 in two ways: to describe the dynamics of a URHIC, a fireball model reminiscent of hydrodynamics is set up. Assuming isentropic expansion, the EOS of the system will link initial and final states of the collision. The EOS in the QGP phase for physical values of the quark masses is taken from our quasiparticle setup, figure 3.12, whereas in the hadronic phase a smooth interpolation to a hadronic resonance gas is applied. This procedure results for the first time in a thermodynamically self-consistent description of a fireball evolution in accordance with lattice results.

Once the space-time arena is set up, dilepton rates are put into it. Above T_c , we consistently employ the quasiparticle picture. Special emphasis is put on the suppression of thermally active partonic degrees of freedom as the critical temperature is approached from above. For the hadronic phase, we calculate the dependence of the photon spectral function (that enters the dilepton rate) on temperature and baryon density using Vector Meson Dominance combined with Chiral Dynamics. The main part of this chapter has been published in [84].

4.1 Dileptons from a fireball

The lepton pair emission rate from a hot domain populated by particles in thermal equilibrium at temperature T is proportional to the imaginary part of the spin-averaged, photon self-energy, with these particles as intermediate states. The thermally excited particles annihilate to yield a time-like virtual photon with four-momentum q which decays subsequently into a lepton-antilepton pair.

The differential pair production rate is given by

$$\frac{dN}{d^4x d^4q} = \frac{\alpha^2}{\pi^3 q^2} \frac{1}{e^{\beta q^0} - 1} \text{Im} \bar{\Pi}(q, T) = \frac{\alpha^2}{12\pi^4} \frac{R(q, T)}{e^{\beta q^0} - 1}, \quad (4.1)$$

where the electromagnetic coupling $\alpha = e^2/4\pi$, and we have neglected the lepton masses. We have defined $\bar{\Pi}(q) = -\Pi^\mu_\mu/3$ and introduce the averaged photon spectral function

$$R(q, T) = \frac{12\pi}{q^2} \text{Im} \bar{\Pi}(q, T).$$

Here Π^μ_μ denotes the trace over the thermal photon self-energy which is equivalent to the thermal current-current correlation function

$$\Pi_{\mu\nu}(q, T) = i \int d^4x e^{iqx} \langle \mathcal{T} j_\mu(x) j_\nu(0) \rangle_\beta, \quad (4.2)$$

where j_μ is the electromagnetic current. Eq.(4.1) is valid to order α in the electromagnetic interaction and to all orders in the strong interaction.

The differential rate of eq.(4.1) is integrated over the space-time history of the collision to compare the calculated dilepton rates with the CERES/NA45 data [85] taken in Pb-Au collisions at 160 AGeV (corresponding to a c.m. energy of $\sqrt{s} \sim 17$ AGeV) and 40 AGeV ($\sqrt{s} \sim 8$ AGeV). The CERES experiment is a fixed-target experiment. In the lab frame, the CERES detector covers the limited rapidity interval $\eta = 2.1 - 2.65$, i.e. $\Delta\eta = 0.55$. We integrate the calculated rates over the transverse momentum p_T and average over η , given that $d^4p = Mp_T dM d\eta dp_T d\theta$. The formula for the space-time- and p -integrated dilepton rates hence becomes

$$\frac{d^2N}{dM d\eta} = \frac{2\pi M}{\Delta\eta} \int_0^{\tau_f} d\tau \int d\eta V(\eta, T(\tau)) \int_0^\infty dp_T p_T \frac{dN(T(\tau), M, \eta, p_T)}{d^4x d^4p} \mathcal{A}(M, \eta, p_T), \quad (4.3)$$

where τ_f is the freeze-out proper time of the collision, $V(\eta, T(\tau))$ describes the proper time evolution of volume elements moving at different rapidities and the function $\mathcal{A}(M, \eta, p_T)$ accounts for the experimental acceptance cuts specific to the detector. At the CERES experiment, each electron/positron track is required to have a transverse momentum $p_T > 0.2$ GeV, to fall into the rapidity interval $2.1 < \eta < 2.65$ in the lab frame and to have a pair opening angle $\Theta_{ee} > 35$ mrad. Eq.(4.3) is then convoluted with the finite energy resolution of the detector. Finally, for comparison with the CERES data, the resulting rate is divided by $dN_{ch}/d\eta$, the rapidity density of charged particles.

RHIC operates as a collider experiment, so in this case the fireball is centered around $\eta = 0$. Here, the PHENIX detector acceptance can be schematically modelled by requiring that each electron/positron track falls in the rapidity interval $-0.35 < \eta < 0.35$, has transverse momentum $p_T > 0.2$ GeV and a pair opening angle of $\Theta_{e\bar{e}} > 35$ mrad. At present, an abundance of data on Au-Au collisions at $\sqrt{s} = 130$ AGeV have already been analysed, and first data of the run at the higher energy $\sqrt{s} = 200$ AGeV are available.

4.2 Calculation of the photon spectral function

Since the initial temperature of the fireball is well above T_c for all beam energies considered here (as we will explicitly show later), we need to calculate the photon spectral function $R(q, T)$ that enters (4.1) in both the hadronic and partonic phase. In the following, we fix T_c to be 170 MeV from eq.(2.52), as appropriate for two light thermally active flavours. The strange quark mass is too heavy to shift T_c down to the critical temperature for three massless flavours.

4.2.1 The quark-gluon phase

As long as the thermodynamically active degrees of freedom are quarks and gluons, the timelike photon couples to the continuum of thermally excited $q\bar{q}$ states and subsequently converts into a charged lepton pair. The calculation of the photon spectral function at the one-loop level is performed using standard thermal field theory methods. The well-known leading-order result for bare quarks and gluons as degrees of freedom separates, for a virtual photon with four-momentum $q = (q^0, \vec{q})$, into the vacuum part and a temperature-dependent piece:

$$\text{Im}\bar{\Pi}(q^0, \vec{q}, T) = \text{Im}\bar{\Pi}(q^2, T = 0) [1 + \mathcal{J}(q^0, \vec{q}; T)], \quad (4.4)$$

where

$$\text{Im}\bar{\Pi}(q^2, T=0) = -3 \frac{q^2}{12\pi} \sum_{f=u,d,s} \theta(q^2 - 4m_f^2) e_f^2 \left(1 + \frac{2m_f^2}{q^2}\right) \sqrt{1 - \frac{4m_f^2}{q^2}} \quad (4.5)$$

and

$$\mathcal{J}(q^0, \vec{q}; T) = 2 \left[\frac{T}{|\vec{q}|} \frac{1}{\sqrt{1 - \frac{4m_f^2}{q^2}}} \log \left(\frac{f_D \left(\frac{q_0}{2} - \frac{|\vec{q}|}{2} \sqrt{1 - \frac{4m_f^2}{q^2}} \right)}{f_D \left(\frac{q_0}{2} + \frac{|\vec{q}|}{2} \sqrt{1 - \frac{4m_f^2}{q^2}} \right)} \right) - 1 \right]. \quad (4.6)$$

Here, e_f is the quark electric charge and m_f the quark mass of flavour f . This result, however, holds only up to perturbative higher order corrections in g that take into account collective plasma effects. Here, contributions from soft gluons lead to strong modifications. The corresponding two- and three-loop contributions show no clear convergence [86, 87] even at very high temperatures, similar to the case of the perturbative free energy of the QGP, eq.(3.3). Since the thermodynamic properties of the QGP are well reproduced by a gas of quasiparticles, as outlined in the last chapter, we assume that a quark quasiparticle couples to a photon in the same way as a bare quark (a form factor representing the 'cloud' of the quasiparticle could in principle also be included, but in absence of information about the detailed quasiparticle structure we ignore this point). For a gas of non-interacting quasiparticles, the one-loop result for $\text{Im}\bar{\Pi}$ is already almost sufficient: all higher order QCD effects manifest in the thermal quasiparticle masses $m_q(T)$, the function $B(T)$ and the confinement factor $C(T)$. Incorporation of the first two features in the calculation is straightforward. The bare quark masses in eqs.(4.5) and (4.6) simply have to be replaced by the T -dependent quasiparticle masses for each flavour, see eq.(3.39). The thermal vacuum energy $B(T)$ does not contribute to the dilepton rate.

The naive replacement $f_D \rightarrow C(T)f_D$ is, however, not permitted in eq.(4.6). Since any modification of the free particle distribution functions leads to non-equilibrium field theory, products of delta functions (pinch singularities) may arise in loop calculations. Therefore, the quasiparticle model as it stands cannot be used in expressions derived from perturbative thermal field theory. Recalling the physical interpretation of the confinement factor $C(T)$, we can use the expression for the dilepton rate, eq.(4.1), instead. The mechanism for dilepton production at tree-level is the annihilation of a $q\bar{q}$ pair into a virtual photon where the quark lines are multiplied by the distributions $f_D(\omega_k)$, giving the probability of finding a quark or an antiquark in the hot medium. This also becomes clear when we look at the limit $\vec{q} \rightarrow 0$ of eq.(4.4). Then,

$$\text{Im}\bar{\Pi}(q^0, T) = \text{Im}\bar{\Pi}(q^0, T=0)[1 - 2f_D(q^0/2)], \quad (4.7)$$

and the temperature enters only in the Pauli-blocking of the quarks propagating in the loop. Now, from eq.(4.1)

$$\frac{dN}{d^4x d^4q} \sim f_B(q^0) \text{Im}\bar{\Pi}(q, T). \quad (4.8)$$

Combining the different thermal occupation factors, we end up with the well-known result

$$\frac{dN}{d^4x d^4q} \sim [f_D(q^0/2)]^2, \quad (4.9)$$

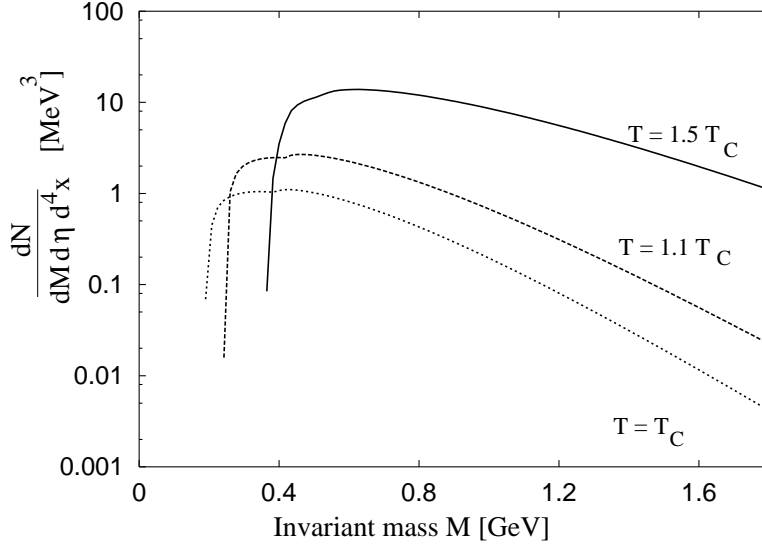


FIGURE 4.1: Dilepton rates originating from the QGP phase in the quasiparticle model for different temperatures.

so the differential dilepton rate is proportional to the probability of finding a quark q times the probability of finding an antiquark \bar{q} with the correct momentum, as anticipated¹. The incorporation of the confinement factor is now obvious: since it reduces the number of thermally active degrees of freedom, it also reduces the dilepton rate by a factor of $C(T)^2$.

In summary, eq.(4.1) can be used to calculate the dilepton rate originating from a hot QGP phase, provided an overall factor $C(T)^2$ is applied to account for the reduced probabilities, and the bare masses m_f in the one-loop expression (4.4) are replaced by the T -dependent thermal masses (3.39). The role of the factor $C(T)$ is illustrated in figure 4.1, where the differential dilepton rate originating from a hot QGP in the quasiparticle approach is shown for different temperatures. Note that the plotted quantity is independent of the fireball volume, so the resulting differences are only due to the dropping quasiparticle masses and the squared confinement factor $C(T)$, which is responsible for a decrease by more than an order of magnitude at $T \sim T_c$ as compared to the highest temperature shown. One also observes that, as expected, the (negative) slope of the production rate in the region of high invariant mass gets steeper as the temperature decreases. It is important to note that this setup neglects contributions from hadronic degrees of freedom above T_c . As mentioned, quarks and gluons become clustered into hadrons (glue balls, mesons) as the temperature approaches T_c from above. These hadronic excitations are comparatively heavy and thus do not contribute much to the thermodynamics. Since we do not know in detail how the statistical re-arrangement of degrees of freedom occurs, we refrain from including these hadronic sources of dilepton yield above T_c . Our calculation is therefore expected to give a *lower limit* on the leptonic radiation from the QGP phase.

¹We neglect a possible chemical potential for the quarks. For finite μ , the corresponding expression would be $\frac{dN}{d^4x d^4q} \sim f_D([q^0 - \mu]/2) f_D([q^0 + \mu]/2)$.

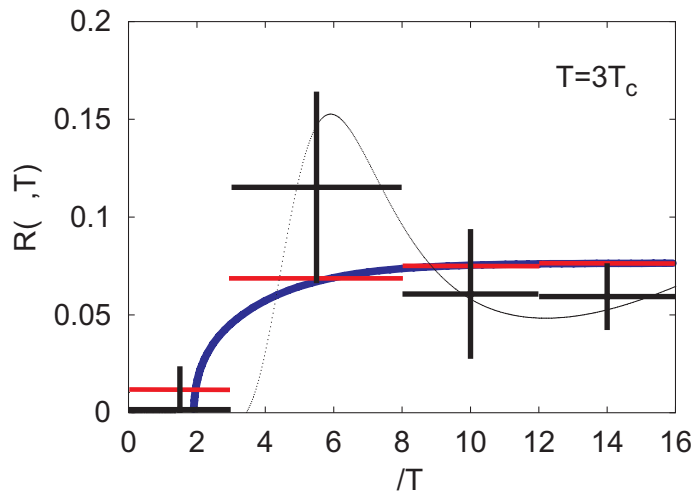


FIGURE 4.2: Lattice data (crosses) [90] on the vector spectral function $R(\omega, \vec{q} = 0; T)$ at $3 T_c$ for $N_f = 2$. The solid line shows our theoretical calculation, deduced from eq.(4.4). The grey horizontal lines denote an average of the theory curve over the energy bins used by the lattice measurements which enables a transparent comparison.

The quasiparticle model does not take into account the collective plasma modes, such as the longitudinal gluonic plasmons and the helicity-flipped quark plasminos. Since their residues (B.19) and (B.34) are exponentially suppressed in the HTL approximation for thermal momenta $k \sim T$, their contributions to the thermodynamical quantities are negligible. However, in the case of soft dilepton production it is well known that these modes lead to sharp, distinct structures in the spectrum, referred to as Van Hove singularities [88]. The plasmino branch has, as visible in figure B.2, a minimum in its dispersion relation at $\vec{k} \neq 0$ (which follows on very general grounds [89], independent of the HTL approximation). This leads to a diverging density of states which, in turn, shows up in the dilepton spectrum as a pronounced peak. Our model cannot exhibit, by construction, such plasmino effects. However, since the peaks are roughly located at $\simeq 2m_q(T)$, where $m_q(T)$ is the thermal mass of the quasiparticles, these Van Hove singularities would be smeared out by the fireball evolution. The thermal mass drops as the temperature goes down, dragging along the peak position with it. Furthermore, since $m_q(T)$ is of the order of the temperature T or smaller in our model, the singularities appear at low invariant mass (< 500 MeV) where they are overwhelmed by the hadronic part of the dilepton production, as we will see later. Therefore the presence of these collective modes would presumably not influence our results for the dilepton rate in the QGP phase.

Our model of the QGP phase also finds preliminary support from a lattice calculation [90] of thermal vector meson correlation functions above T_c in quenched QCD with improved Wilson fermions. Using the maximum entropy method, the vector spectral function was extracted from the corresponding current correlator. Although the statistical uncertainties are still considerable, it is interesting to note that the resulting spectrum resembles the free spectral function, as in our case, and has a gap at low energies given by a thermal mass threshold of $(2 - 3)T$, which is indeed close to $2m_q(T)$, the natural cut-off of the spectrum and, correspondingly, of the thermal dilepton radiation in the confinement model (see figure 4.1). Figure 4.2 compares the lattice data

and our calculated spectrum. Of course, higher statistics and improved actions are mandatory to confirm these observations, but at least it is safe to say at the moment that the full spectral function does not differ by a large factor from its non-interacting counterpart. In the future, lattice calculations at $T = 1.2 T_c$ are also planned. Since this close to T_c our quasiparticle model starts to deviate significantly from the PGP models [45, 46], it might be possible to rule out one or the other model if the lattice data show sufficient statistical significance.

4.2.2 The hadronic phase

Below T_c , the effective degrees of freedom change to colour singlet, bound $q\bar{q}$ or qqq ($\bar{q}q\bar{q}$) states. The photon couples now to the lowest-lying 'dipole' excitations of the vacuum, the hadronic $J^P = 1^-$ states: the ρ , ω and ϕ mesons and multi-pion states carrying the same quantum numbers. The electromagnetic current-current correlation function can be connected to the currents generated by these mesons using an effective Lagrangian which approximates the SU(3) flavour sector of QCD at low energies. The appropriate model for our purposes is the *improved Vector Meson Dominance* model combined with chiral dynamics of pions and kaons as described in [91]. Within this model, the following relation between the imaginary part of the irreducible photon self-energy $\text{Im}\bar{\Pi}$ and the vector meson self-energies $\Pi_V(q)$ in vacuum is derived:

$$\text{Im}\bar{\Pi}(q) = \sum_V \frac{\text{Im}\Pi_V(q)}{g_V^2} |F_V(q)|^2, \quad F_V(q) = \frac{(1 - g/g_V^0) q^2 - m_V^2}{q^2 - m_V^2 + i\text{Im}\Pi_V(q)}, \quad (4.10)$$

where m_V are the (renormalised) vector meson masses, g_V^0 is the γV coupling and g is the vector meson coupling to the pseudoscalar Goldstone bosons π^\pm, π^0 and K^\pm, K^0 . Eq.(4.10) is valid for a virtual photon with vanishing three-momentum \vec{q} . For finite three-momenta there exist two scalar functions $\bar{\Pi}_L$ and $\bar{\Pi}_T$, because the existence of a preferred frame of reference (the heat bath) breaks Lorentz invariance, and one has to properly average over them. However, taking the limit $|\vec{q}| \rightarrow 0$ should be reasonable for our purposes in view of the fact that the c.m. rapidity interval accessible at CERES and RHIC restricts $|\vec{q}|$ on average to only a fraction of the vector meson mass m_V .

Finite temperature modifications of the vector meson self-energies appearing in eq.(4.10) are calculated using thermal Feynman rules. Our explicit calculations for the ρ - and ϕ -meson can be found in ref.[92]. At the one-loop level, the ρ and ϕ are only marginally affected by temperature even close to T_c because of the comparably large pion and kaon masses: $m_\pi \simeq T_c$, $m_K \simeq 3 T_c$. The thermal spectral function of the ω -meson has been discussed by us in detail in [93]. There, the pure in-medium reaction $\omega\pi \rightarrow \pi\pi$ (ω scattering off a thermal pion) was found to cause a considerable broadening of the ω spectral function because at temperatures $T > 60$ MeV, a substantial fraction of pions become excited. The increase of the ω width with temperature is then, not surprisingly, reminiscent of the rate at which the thermal pion density grows. However, because of the additional Bose enhancement of the two final state pions, the scattering rate actually rises even stronger than T^3 . In fact, a good fit over the temperature range considered is

$$\Gamma_{\omega\pi \rightarrow \pi\pi} = \left(\frac{T}{T_s}\right)^5 \text{ MeV} \quad \text{with} \quad T_s = 72.3 \text{ MeV} \simeq \frac{m_\pi}{2}. \quad (4.11)$$

For $T > 120$ MeV, this width becomes larger than the pure decay term $\omega \rightarrow 3\pi$, rising up to about 40 MeV at $T = 150$ MeV. The total decay width $\Gamma_\omega(T)$, as the sum of

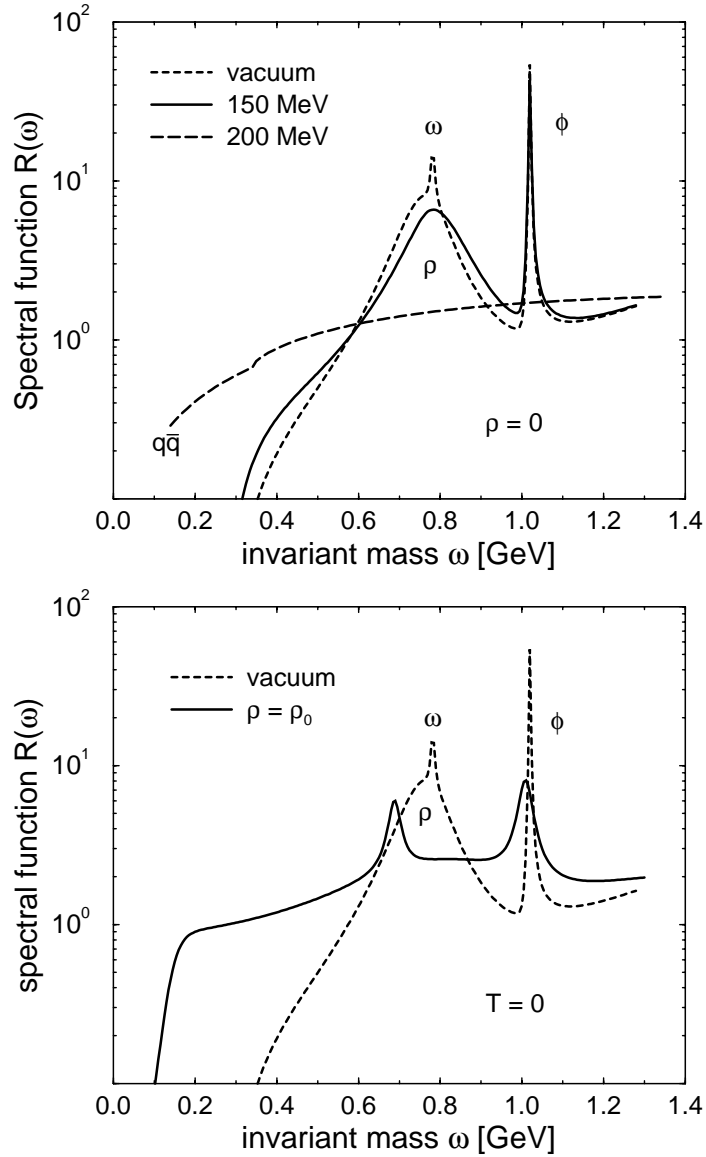


FIGURE 4.3: The photon spectral function $R(\omega) = (12\pi/\omega^2) \text{Im}\bar{\Pi}(\omega)$ at finite temperature and $\rho_B = 0$ (upper panel) and at $T = 0$ and baryon density of normal nuclear matter, $\rho_B = \rho_0 = 0.17 \text{ fm}^{-3}$ (lower panel). For orientation, the $q\bar{q}$ line in the left panel shows the spectral function in the QGP phase with massless u - and d -quarks and $m_s = 150 \text{ MeV}$ for s -quarks, neglecting α_s -corrections.

decay and scattering terms, leads to $\Gamma_\omega(100 \text{ MeV}) \simeq 15 \text{ MeV}$ and $\Gamma_\omega(150 \text{ MeV}) \simeq 55 \text{ MeV} = 8 \Gamma_\omega(0)$.

At higher invariant masses $1 \text{ GeV} < M < 2 \text{ GeV}$, πa_1 annihilation is the dominant source of dileptons [94, 95]. The vacuum vector and axialvector spectral functions become mixed to order T^2 with a strength $T^2/(6f_\pi^2)$ (f_π being the pion decay constant) due to their coupling to the pionic heat bath [96] and should be degenerate at the point

of chiral symmetry restoration. The effect of the a_1 and higher resonances can then be approximately subsumed in a structureless continuum above 1 GeV [97]. We practically implement the πa_1 contribution by adding a flat 2π continuum to the resonance ρ meson spectral function that feeds into the photon spectral function, reminiscent of the perturbative plateau of $q\bar{q}$ annihilation. The corresponding photon spectral function with all three vector meson contributions is displayed in figure 4.3 (upper panel).

There is still considerable stopping of the interpenetrating nuclei at SPS energies, resulting in a net baryon density ρ_B in the central rapidity region. At RHIC, measurements [98, 99] indicate that the proton over antiproton excess is small, implying that the baryons are distributed over a larger rapidity interval. Therefore, finite baryon density effects should not play such an important role at RHIC kinematics. For the evaluation of density effects which are relevant at SPS conditions, we use the results discussed in [100]. There it was shown that, to leading order, Π_V is related to the vector meson - nucleon scattering amplitude T_{VN} :

$$\begin{aligned}\Pi_V(q^0, \vec{q} = 0; \rho_B) &= \Pi_V^{\text{vac}} - \rho_B T_{VN}(q), \text{ where} \\ T_{VN}(q) &= -\frac{i}{3} \int d^4x e^{iqx} \langle N | \mathcal{T} j_\mu(x) j^\mu(0) | N \rangle,\end{aligned}\tag{4.12}$$

with $|N\rangle$ being zero-momentum free nucleon states. The linear density approximation used in (4.12) is expected to be valid for baryon densities ρ_B up to normal nuclear matter. Since the baryon density at SPS at the phase transition is also of the order ρ_0 and decreases thereafter, it is safe to say that eq.(4.12) constitutes a reasonable starting point for calculations. In the following, we assume that the temperature- and density dependences of Π_V factorise, i.e. we replace Π_V^{vac} in eq.(4.12) by the temperature-dependent $\Pi_V(T)$ and leave T_{VN} unaffected. This amounts to neglecting contributions from matrix elements such as $\langle \pi N | \mathcal{T} j_\mu(x) j^\mu(0) | \pi N \rangle$ (nucleon-pion scatterings where the pion comes from the heat bath). Furthermore, this approximation does not take into consideration a possible T -dependent pion or nucleon mass. Some effective models suggest that, near the phase transition, the nucleon mass follows the behaviour of the chiral condensate $\langle \bar{q}q \rangle$ and drops abruptly as the quarks lose their constituent masses. Such modifications of particle properties may have a considerable impact on the spectral functions. However, since the temperature range over which the dropping takes place is narrow, we expect such effects not to leave distinct signals in the dilepton spectra which are only sensitive to the integrated time (and hence temperature) evolution of the system.

The photon spectral function at finite density and zero temperature is depicted in figure 4.3 (lower panel). The interaction with nucleons causes a strong broadening of the ρ meson down to the one pion threshold, leading to a complete dissolution of its quasiparticle peak structure. The modifications of the ω and ϕ meson spectral distributions are more moderate: the ϕ mass stays close to its vacuum value, accompanied by a ninefold increased width, whereas the mass of the ω drops by about 100 MeV at normal nuclear matter density, and its width increases by a factor of about 5. This calculated dropping of the ω mass in a nuclear environment may be observed experimentally in the near future at the HADES spectrometer at GSI. Monte Carlo cascade simulations of π^- Pb reactions at pion beam momenta around 1.3 GeV suggest that the detector resolution will indeed be sufficient to separate the shifted in-medium ω peak from its vacuum counterpart [101], allowing for an independent test of the spectral function at finite density.

To summarise, the most prominent changes of the photon spectral function, when compared to the vacuum case, arise from the broadening of the ρ due to finite baryon density effects and the broadening of the ω due to scattering off thermal pions. The ϕ meson retains its distinct peak structure even under extreme conditions of density and temperature. Very close to T_c , however, these results based on perturbative calculations, are not expected to be reliable. As shown in section 3.5, the influence of a baryon chemical potential on the QGP is negligible in the EOS, both at RHIC and SPS conditions. The same holds for the partonic spectral function since the chemical potential would enter it only logarithmically. As $\mu_B \ll T$, we can therefore safely neglect any chemical potential in the QGP phase in the following.

4.2.3 After freeze-out contributions

At the freeze-out stage, there are still vector mesons present. These will decay with their vacuum properties on their way to the detector and add to the dilepton yield from the previous thermalised phase. The invariant mass region below approximately 400 MeV is mainly filled by the Dalitz decays of the vector mesons. We take these contributions from the experimental analysis of the CERES collaboration for SPS conditions. Since the PHENIX acceptance starts only above 1 GeV, the Dalitz decays do not play a significant role at RHIC.

For the calculation of the direct decay of a vector meson V into a lepton pair we start with the following formula:

$$\frac{dN_V}{dM d\eta} = \frac{1}{\Delta\eta} \frac{\alpha^2}{12\pi^4} R_V(M, T=0) \int_{\tau_f}^{\infty} d\tau V_f \int d^3q \frac{M}{q^0} f_B(q^0, T_f) \exp\left(-\frac{\tau - \tau_f}{\gamma(q)\tau_0^V}\right).$$

Here, T_f and V_f are the fireball temperature and volume, respectively, at freeze-out. After τ_f , the freeze-out time, all medium effects are switched off, so the vacuum photon spectral function $R_V(M, T=0)$ determines the rate. The corresponding momentum distribution is given by the thermal Bose function, evaluated at the freeze-out temperature T_f . However, the *absolute number* N of vector mesons as a function of time is not a constant: since the mesons decay and there is no thermal recombination, N decreases exponentially like $\exp(-(\tau - \tau_f)/(\gamma(q)\tau_0^V))$. The vacuum life time of the vector meson V under consideration is denoted by τ_0^V , and $\gamma(q)$ accounts for time dilatation effects on particles with finite three-momentum:

$$\gamma(q) = \frac{1}{\sqrt{1-v^2}} = \frac{q^0}{M}.$$

After the time integration we end up with:

$$\frac{dN}{dM d\eta} = \frac{1}{\Delta\eta} \frac{\alpha^2}{12\pi^4} \tau_0 R(M, T=0) V_f \int d^3q f_B(q^0, T_f).$$

The averaged space-time four-volume that is available after freeze-out is therefore $V_f \tau_0^V$, as anticipated. The integral over d^3q now yields the freeze-out particle density $n(M) = N(M)/V$ of the virtual photons as a function of invariant mass. Note that the information on the vector mesons remains *entirely* in the photon spectral function. With the factor V_f we obtain the total number of photons at freeze-out. When weighted with $R_V(M)$, this gives the dN/dM distribution for the process meson $\rightarrow \gamma^* \rightarrow e^+e^-$.

We have also checked that a commonly used Breit-Wigner *ansatz* of the form

$$\frac{dN_{e^+e^-}}{dM} = [V_f n(T_f, M)] \xi B_V \frac{M^2 \Gamma_V(M)}{(M^2 - m_V^2)^2 + M^2 \Gamma_V(M)^2} \quad (4.13)$$

yields almost identical results. Here, $\Gamma_V(M)$ stands for the M -dependent decay width, ξ is the normalization factor and B_V the branching ratio for the leptonic decay of the corresponding vector meson.

4.2.4 Drell-Yan and charm contributions

At invariant masses $M > 1$ GeV the Drell-Yan mechanism, i.e., hard quark-antiquark annihilation $q\bar{q} \rightarrow \ell^+\ell^-$ at leading order (LO), constitutes another source of (non-thermal) dileptons. Its differential LO cross section in a nucleus(A_1)-nucleus(A_2) collision reads

$$\frac{d\sigma(A_1 A_2)}{dy dM} = \frac{8\pi\alpha^2}{9 M s} \sum_q e_q^2 \times \quad (4.14)$$

$$\left[(Z_1 f_q^p(x_1) + (A_1 - Z_1) f_q^n(x_1)) (Z_2 f_{\bar{q}}^p(x_2) + (A_2 - Z_2) f_{\bar{q}}^n(x_2)) + (q \leftrightarrow \bar{q}) \right]$$

where \sqrt{s} denotes the c.m. energy of the nucleon-nucleon collision and $x_{1,2} = M/\sqrt{s} \exp(\pm y)$ is the momentum fraction of the beam and target parton respectively.

The Drell-Yan cross section (4.14) is computed using the LO MRST parametrisation [102] for the parton distributions $f_i^p(x, \mu^2)$ evaluated at the hard scale $\mu^2 = M^2$. However, it has been checked that using different LO sets (e.g., CTEQ5L [103] or GRV98LO [104]) affects the results by only 10 % at SPS and 20% at RHIC energies. To account for higher order corrections, we multiply the LO expression (4.14) by a K factor $K = 2$ fitted from pp data [105]. Finally, nuclear effects like shadowing or quark energy loss are expected to suppress the Drell-Yan yield by about 30-50% [106, 107]. Since these effects are still poorly known quantitatively, we neglect them and consider our Drell-Yan rate as an *upper limit* on the actual rate.

Using the Glauber model of multiple independent collisions, the average dilepton multiplicity in a A_1 - A_2 collision at impact parameter b is given by

$$\frac{dN(A_1 A_2)}{dy dM}(b) = T_{A_1 A_2}(b) \times K \frac{d\sigma(A_1 A_2)}{dy dM}, \quad (4.15)$$

with the normalised thickness function

$$T_{AB}(b) = \int d^2s T_A(s) T_B(\tilde{s}), \quad (4.16)$$

where

$$T_A(b) = \int dz \rho_A(z, b) \quad (4.17)$$

is the overlap function as longitudinal integral of the nuclear density ρ_A and $\tilde{s} = |\vec{b} - \vec{s}|$. In eq.(4.15), $T_{A_1 A_2}(b)$ is computed assuming the standard Woods-Saxon nuclear density profile. The Drell-Yan pair multiplicity (4.15) is then averaged for the 30% and 6% most central collisions to be compared with CERES and PHENIX data, respectively. In addition to these centrality cuts, we need to rely on further assumptions to take

properly into account the acceptance of these experiments. Therefore, we shall assume the generic form $d\sigma/dp_{\perp} \propto p_{\perp}/(1 + (p_{\perp}/p_0)^2)^6$ ($p_0 = 3$ GeV) for the p_{\perp} dependence of the DY process [105]. Furthermore, neglecting corrections due to the intrinsic k_{\perp} of the incoming partons, the angular distribution is taken to be $dN/d\Omega \propto 1 + \cos^2 \theta$ where θ is the angle between the lepton and the beam axis.

Another source of dileptons in the high invariant mass region consists of semileptonic decays of charmed mesons. Whereas earlier calculations found a considerable yield from open charm exceeding the thermal radiation [108], the subsequent inclusion of medium effects like energy loss led to a suppression of the dielectron rate and made it comparable to or even lower than the Drell-Yan yield [109, 110]. Since the Drell-Yan contribution plays only a subdominant role in the following, we will not explicitly include the open charm contributions.

4.3 Fireball model

In this section, we set up a fireball model to describe the dynamics of a URHIC after thermalisation of the system has occurred. A much more detailed discussion of the model that covers all the finer details can be found in the dissertation of Thorsten Renk [111].

We assume that the physics of the fireball is the same inside each volume of given proper time τ , thus averaging over spatial inhomogeneities in density and temperature. The volume itself is taken to be an expanding cylinder, in which the volume elements move away from the centre in order to generate the observed flow. There is no global Lorentz frame in which thermodynamics can be applied. As the fireball expands, volume elements away from the centre are moving with large velocities and are subject to time dilatation when seen in the c.m. frame of the collision. We assume a linear rise in rapidity when going from central volume elements to the fireball edge along the beam (z)-axis and the transverse axis. As the velocities along the z -axis are typically large (up to c) as compared to transverse motion (up to $0.55 c$) for SPS and RHIC conditions, we make the simplifying assumption that the proper time is in a one-to-one correspondence to the z -position of a given volume element, thus neglecting the time dilatation caused by transverse motion (this introduces an error on the 5% level). The whole system is assumed to be in local thermal (though not necessarily in chemical) equilibrium at all times, which is supported experimentally by phenomena like elliptic flow [112]. Theoretically, only perturbative estimates are possible, which therefore may only be applicable at LHC or RHIC, but mechanisms like 'bottom-up' thermalisation [113] have been proposed that achieve equilibration on time scales of $1 \text{ fm}/c$. This is also the time scale at SPS for the two colliding nuclei to pass through each other, $\tau \sim 2R_A/\gamma$, with the nuclear radius R_A and the gamma factor $\gamma \sim 10$.

Given this overall framework, the volume expansion of the fireball is governed by the longitudinal growth speed v_z and the transverse expansion speed v_{\perp} at a given proper time. These quantities can be determined at the freeze-out point and correspond to the observed amount of flow. However, flow is measured in the lab frame and needs to be translated into the growth of proper time volume. We employ a detailed analysis of the freeze-out conditions for central Pb+Pb collisions at 160 AGeV [114] to fix the endpoint of the evolution. The initial state is constrained using the overlap geometry of the colliding nuclei. The expansion between initial and freeze-out stages is then required to be in accordance with the EOS for two light quarks and a heavy strange

quark as determined from the quasiparticle model, see figure 3.12. The resulting model serves as the basic setup, its extension to different beam energies and collision centralities is discussed in 4.3.5.

4.3.1 Initial and freeze-out conditions

We use the data set **b1** of [114] as the endpoint of our fireball evolution. The data set has been obtained by a simultaneous fit of the fireball emission function to hadronic m_T spectra and HBT radii, so as to disentangle the contributions from flow and temperature to these quantities. The fireball is characterised by a transverse box-shaped density distribution with a radius $R_B = 12.1$ fm. This corresponds to a root mean square radius of $R_{\text{rms}}^f = 8.55$ fm ($= R_B/\sqrt{2}$). The average transverse expansion velocity is found to be $0.5 c$ and the temperature at freeze-out is $T_f = 100$ MeV. Looking at the longitudinal expansion, a velocity $v_z^f \approx 0.9 c$ at the fireball front is needed in $\pm z$ direction in order to account for the observed shape of dN_{ch}/dy distributions.

The initial conditions in transverse direction can be fixed by the overlap geometry. Here, $R_0 \approx 4.5$ fm and $v_\perp = 0$ for central collisions. The initial longitudinal size of the fireball is related to the amount of stopping of the matter in the collision and the time τ_0 necessary for the formation of a thermalised system. There is no direct information on these two quantities. However, pQCD calculations indicate $\tau_0 \approx 1$ fm/ c for SPS conditions and shorter times at RHIC. The initial longitudinal velocity v_z^i can be inferred from hydrodynamical calculations. Since the initial state in principle determines the final state (once the EOS is known), we can fit this parameter to the observed dN/dy spectra. This procedure points at $v_z^i \approx 0.5 c$. The initial longitudinal size of the system at proper time τ_0 is then calculated by the intercept of $z(t) = v_z^i \cdot t$ with the $\tau = \sqrt{t^2 - z^2} = \tau_0$ line.

4.3.2 Volume evolution

Using the available information on initial and freeze-out conditions and the EOS of the system, we now reconstruct the evolution of the fireball volume in proper time:

(1) The EOS translates into a temperature (and hence τ) dependent acceleration profile $a = \text{const.} \cdot p(T)/\epsilon(T)$ that exhibits a soft transition point at $T = T_c$. The ratio p/ϵ is reminiscent of the behaviour of the speed of sound of the system since $c_s^2 = dp/d\epsilon$, and hence governs the acceleration. Previous approaches [121, 119] only assumed a constant acceleration profile, which is clearly insufficient. Comparing initial and final conditions, we need both longitudinal and transverse acceleration to account for the velocity gain, and we keep the possibility of having two different constants c_\perp and c_z which relate transverse and longitudinal accelerations to p/ϵ . In practice, the temperature evolution with τ is calculated starting with a trial solution and iterating the result to obtain a self-consistent solution.

(2) Starting with an *ansatz* for the radial expansion velocity,

$$v_\perp(\tau) = c_\perp \int_{\tau_0}^{\tau} d\tau' \frac{p(\tau')}{\epsilon(\tau')} \quad (4.18)$$

and

$$R(\tau) = R_0 + c_\perp \int_{\tau_0}^{\tau} \int_{\tau_0}^{\tau'} d\tau' d\tau'' \frac{p(\tau'')}{\epsilon(\tau'')}, \quad (4.19)$$

where R_0 is the initial overlap rms radius of the collision region, we fix the two unknown parameters c_\perp and τ_f by the requirement that $R(\tau_f) = R_{\text{rms}}^f$ and $v_\perp(\tau_f) = v_\perp^f$.

(3) For the longitudinal expansion we follow the motion of the fireball front in the c.m. frame and use the expressions

$$v_z(t) = v_z^i + c_z \int_{t_0}^t dt' \frac{p(t')}{\epsilon(t')} \quad (4.20)$$

and

$$z(t) = z_0 + v_z^i \cdot t + c_z \int_{t_0}^t \int_{t_0}^{t'} dt' dt'' \frac{p(t'')}{\epsilon(t'')}. \quad (4.21)$$

The movement of the fireball front in the c.m. frame can now be translated into the growth of volumes in proper time by finding the intercept of $z(t)$ and $\tau = \text{const.}$ and calculating the pathlength along this curve of fixed proper time. The time t starts running at t_0 such that $z_0 = v_z^i t_0$ is the initial longitudinal extension, v_z^i being the initial longitudinal expansion velocity. The longitudinal position $z(t)$ and t itself define a proper time curve $\tau = \sqrt{t^2 - z^2(t)}$. Solving for $\tilde{t} = t(\tau)$ we can construct $\tilde{z}(\tau) = z(\tilde{t})$. Then the position of the fireball front $z(t)$ in the c.m. frame can be translated into the total longitudinal extension $L(\tau)$ of the cylinder on the curve of constant proper time τ :

$$L(\tau) = \int_{-\tilde{z}(\tau)}^{\tilde{z}(\tau)} ds \sqrt{1 + \frac{|s|}{\sqrt{s^2 + \tau^2}}}, \quad (4.22)$$

the integration accounting for the expansion in both positive and negative z -direction. The parameters c_z and t_f (freeze-out in c.m. frame) are fixed by $v_z(t_f) = v_z^f$ and $z(t_f)$ to lie on the $\tau = \tau_f$ line, with τ_f determined from the radial expansion, as explained above.

The total volume, as a function of proper time, finally reads

$$V(\tau) = L(t(\tau)) [\pi R^2(\tau)]. \quad (4.23)$$

In order to construct a self consistent evolution model, we need to specify the proper ratio $p(T(\tau))/\epsilon(T(\tau))$ corresponding to the volume expansion. The evolution of $T(\tau)$ is dealt with in the next section. For the QGP phase, the ratio is then determined within the quasiparticle model. Unfortunately, no reliable information on p/ϵ is available for the hadronic phase. We can, however, deduce the value of the ratio p/ϵ at both T_c and T_f , and interpolate between these limits. As the lattice indicates neither a sharp drop in ϵ nor in p when approaching T_c from above, it appears reasonable to assume that the p/ϵ ratio stays small in the vicinity of the phase transition even in the hadronic phase. On the other hand, the decoupling of the system at freeze-out implies that interactions between its constituents become unimportant, therefore we recover the ideal gas limit at $T \rightarrow T_f$, where standard thermodynamics predicts $p/\epsilon = 1/3$ (for massless particles). We now interpolate linearly between these two values to cover the temperature region inbetween.

4.3.3 Temperature evolution

The temperature profile $T(t)$ of the fireball is uniquely determined by the assumed condition of isentropic expansion once the volume expansion is known. In order to derive the temperature T at a given time, we calculate the entropy density via

$$s(\tau) = S_0/V(\tau), \quad (4.24)$$

where S_0 is the total entropy of the fireball. The relation between the entropy density s and the fireball temperature T is fixed by the EOS. By inverting this (unique) relation numerically, we finally obtain the temperature profile. As mentioned, the EOS of the QGP phase is taken from figure 3.12. Unfortunately, determining the behaviour of the hadronic phase is not quite as easy for a number of reasons. First, the large bare quark masses employed in lattice calculations lead to pion masses $m_\pi^{\text{lat}} \gtrsim 3 m_\pi^{\text{phys}}$. The resulting thermal suppression of these degrees of freedom causes a considerable discrepancy of the lattice EOS with respect to that of the interacting pion gas or the free hadronic resonance gas. However, since there are indications that the transition is triggered by the increasing number of resonances (and not by the increasing pion density), the effect of the large quark masses might not be as important as it seems at first sight. Second, even the description of the hadronic phase in terms of a non-interacting or perturbatively interacting system is bound to fail near the phase transition. Only in the very final stages, near the freeze-out, interactions cease to be important and we may assume that a non-interacting system describes the situation adequately.

We parametrise our insufficient knowledge close to T_c by interpolating smoothly between two regimes, the QGP quasiparticle result for $T > T_c$ and the non-interacting hadronic resonance gas result for $T < T_f$. Since the transition is likely a smooth crossover for physical quark masses (cf. section 2.4.3), we can safely assume that there are no discontinuities in the EOS. The situation is shown for the RHIC scenario in figure 4.4 and compared to the ideal quark-gluon gas and the hadronic resonance gas approach used in other works (e.g. [115, 116]). Evidently, the deviations in both the quark-gluon phase and the hadronic phase from the ideal gas are large, amounting to a factor of more than two for the entropy density near T_c . Keeping in mind that a smaller entropy density translates into a higher temperature in an isentropic expansion, we conclude that our model predicts a prolonged lifetime of the QGP phase as compared to the ideal gas *ansatz*, whereas the lifetime of the hadronic phase is reduced somewhat.

At SPS, the measured ratio of protons over antiprotons indicates a partial stopping of nucleons during the collision phase, resulting in an excess of quarks over antiquarks in the fireball region [117]. Since baryon number is conserved, this implies the existence of a T -dependent baryochemical potential μ_B , which in turn translates into an approximate fugacity factor $\lambda_B = \exp(\mu_B/T)$ multiplying the entropy density created by baryons. For the thermodynamics of the QGP phase, quark chemical potentials of the order 100 MeV ($\sim \mu_B/3$) play no role, as elaborated on in section 3.5. Furthermore, the thermal yield of pions in the fireball is not enough to account for the observed number of pions. This can be similarly compensated by the introduction of a chemical potential for pions (and kaons), which in turn influences the hadronic EOS.

By imposing entropy and baryon number conservation, the evolution of μ_B can be followed through the fireball expansion. In practice, the evaluation at each T rests on the assumption of the system being an ideal hadronic gas, which we believe is unreasonable near the phase transition. Fortunately, $T_f \simeq 100$ MeV is far enough distant

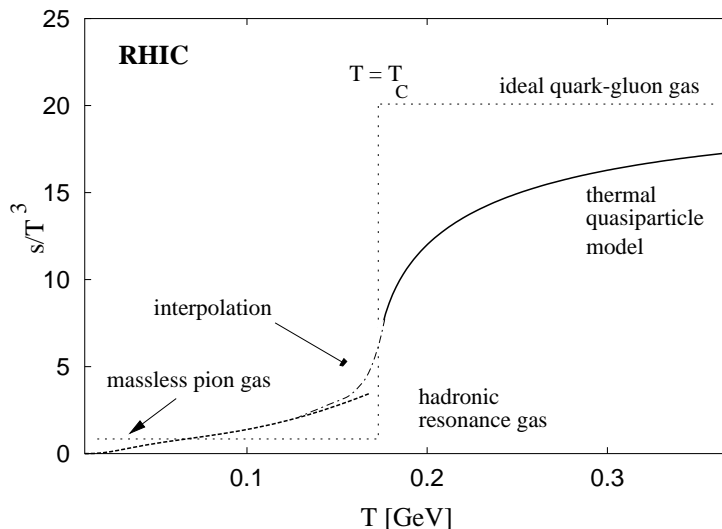


FIGURE 4.4: The temperature dependence of the entropy density $s(T)$ in the RHIC kinematical scenario as compared to the ideal quark-gluon gas and the massless, non-interacting pion gas limit (dotted line). The three relevant regions used in the model calculation are given as ideal hadronic resonance gas (solid line), interpolation (dash-dotted line) and thermal quasiparticle model (dashed line).

from the phase transition, and that is where we fix the entropy. Furthermore, we expect pions to be the dominant thermally active degrees of freedom. We use a pion chemical potential $\mu_\pi(T_f) = 123$ MeV as obtained in [114], which gives the correct total pion multiplicity when evaluated with the fireball freeze-out volume.

Correcting the contributions from the different particle species for the corresponding fugacity factors, we obtain a point of the $s(T)$ curve, $s(T_f)$, where our interpolation starts. This situation is shown in figure 4.5. One observes that, unlike the RHIC scenario, the entropy density under SPS conditions is larger in the range $T_f < T < T_c$, resulting in a faster dropping of temperature during the hadronic expansion phase. Having now specified the relevant part of the EOS of the system, the temperature evolution of the fireball is uniquely determined by the total entropy S_0 and the evolution of the volume $V(\tau)$ with proper time. The total entropy, finally, can be obtained by measuring charged particle multiplicities N^+ and N^- in suitable rapidity bins and calculating

$$D_Q = \frac{N^+ - N^-}{N^+ + N^-}. \quad (4.25)$$

The quantity D_Q stands for the inverse of the specific entropy per net baryon S/B , and the product $D_Q(S/B)$ roughly measures the entropy per pion [118]. For SPS collisions at 160 AGeV, we find $S/B = 26$ for central collisions. For RHIC 6% central Au-Au collisions at 130 AGeV, the specific entropy $S/B = 130$ is substantially higher due to the larger particle multiplicity and the smaller net baryon content in the central region. For beam energies of 200 AGeV that are of interest here, not enough information on dN/dy spectra is available at this moment, so we utilise the predictions from a thermal model calculation [42]. With the ratios $\bar{p}/p = 0.75$, $\bar{p}/\pi^- = 0.09$ and $K^-/\pi^- = 0.15$, we obtain the specific entropy as $S/B \approx 250$, as already estimated (albeit with different parameters) in [119].

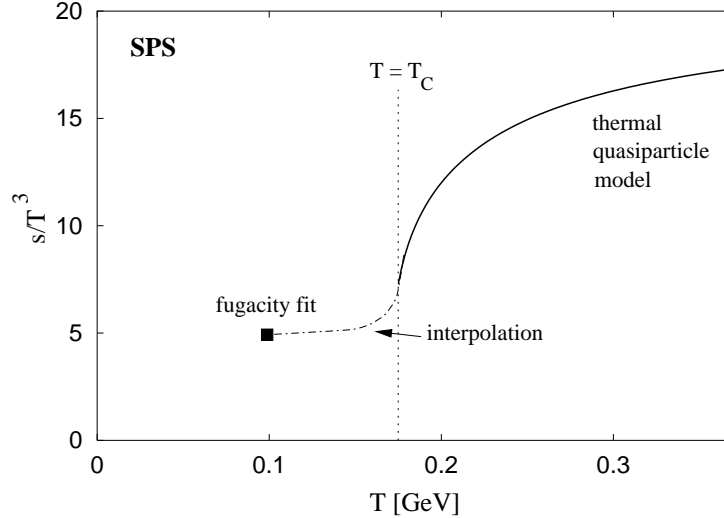


FIGURE 4.5: Temperature dependence of the entropy density for SPS conditions, including the interpolation to the fugacity corrected value at freeze-out. As the entropy density below T_f is irrelevant for the fireball evolution, the interpolation is stopped at this point.

4.3.4 Chemical composition

As already mentioned, the total thermal pion yield of the fireball at freeze-out is not enough to account for the observed number of pions, and a large chemical potential of $\mu_\pi = 123$ MeV has to be used to compensate [114]. The common point of view is that particle numbers are fixed at a chemical freeze-out point [41] and the absence of inelastic reactions then introduces a chemical potential. The statistical model is enormously successful in describing the finally observed ratio as a fit of chemical freeze-out temperature and baryon density, using the free properties of particles. However, as we have shown in section 4.2.2, in-medium modifications of particle masses and widths occur, changing the amount of particle production at the freeze-out temperature. This is not in direct contradiction to the apparent success of the statistical model, as a different set of T and μ might be able to explain the observed ratios once the modifications are taken into account. Furthermore, the absence of all inelastic reactions, leading to decay processes only, is most likely an oversimplification for some particles, e.g. for the $\rho \leftrightarrow \pi\pi$ system. If we knew the particle properties and the particle abundances at hadronisation reliably, the correct way to proceed would be to set up a system of coupled rate equations and follow the various decay and recombination processes to the thermal freeze-out. Unfortunately, theoretically there is no way to assess these properties reliably near the phase transition yet. In the following, we will therefore parametrise the hadrochemistry of the fireball on a phenomenological basis by the following approach: a pion chemical potential is introduced *ad hoc* and fitted at the thermal freeze-out point ($\mu_\pi = 123$ MeV [114]) to the total pion multiplicity. It is assumed to decrease with temperature linearly up to T_c (as also found in [114]) where it vanishes, corresponding to a situation where resonance decays continuously feed pions into the system. All other necessary chemical potentials are adjusted such as to reproduce the observed pion to particle ratios at all times.

4.3.5 Variations with beam energies and centralities

It is mainly the detailed information on the final and initial state which enables us to reconstruct the fireball evolution in the case of the 160 AGeV central collision scenario. Unfortunately, no such detailed analysis is available for the 30% central Pb+Au collision scenario for which dilepton data have been taken. The same holds for the 40 AGeV dilepton data. It is therefore necessary to extend the framework established above to different centralities and beam energies by a suitable re-scaling of key quantities characteristic of the evolution.

First of all, the total entropy deposition in the fireball region must be different when going to more peripheral collisions or lower beam energies. We assume that the entropy per baryon scales with the number of negatively charged hadrons observed in the final state and take the SPS value of $s/\rho_B = 26$ as a baseline. When going to peripheral collisions, we assume that this value is still a good estimate. Here, the total entropy in the system is naturally reduced because the number of nucleons participating in the collision is smaller. Second, the overlap geometry is different in peripheral collisions, resulting in a smaller initial fireball volume. We will neglect details of the transverse geometry and keep parametrising the fireball volume as a cylinder, ignoring all effects of elliptic flow. Its initial transverse area is adjusted to the value of the calculated overlap area, hence the cylinder radius is reduced as compared to central collisions. These approximations should still be valid for not too large impact parameters. Note that the model breaks down anyway for very peripheral events, since the assumption of rapid thermalisation certainly ceases to be valid for system sizes of a couple of nucleons.

The initial velocity v_z^i of the fireball front is an important quantity which must change for more peripheral collisions. As discussed before, $v_z^i \simeq 0.5c$ for central collisions at SPS. On the other hand it is an empirical fact that in pp collisions leading particles loose on average about one unit of rapidity. This is the limit we expect for very peripheral collisions. In order to account for this effect, we assume that the rapidity loss from incoming nuclei to the bulk of the produced matter scales with the number of binary collisions per participant (~ 2.7 for central collisions, 1 for pp) and interpolate linearly between these limits.

For the 40 AGeV data, we take the total entropy to be about half the entropy at 160 AGeV because $N_{\pi^-}^{160} \approx 600$ and $N_{\pi^-}^{40} \approx 310$, cf. eq.(4.25). The initial energy density, estimated by Bjorken's formula from dN/dy at midrapidity, is about 2/3 of the value at 160 AGeV, but still well above the critical energy density required to form a QGP plasma. Looking at the final state of the fireball, HBT analyses of NA49 [120] indicate that the radius parameters are very similar at 40 and 160 AGeV, suggesting that the reaction dynamics do not significantly change in this energy region.

Obviously, altering the initial entropy deposition results in a correspondingly different fireball evolution and in general a different freeze-out state. Freeze-out occurs when the mean free path of particles exceeds the dimensions of the fireball. As pions are the most abundant particle species in the fireball, we assume that the pion density determines the mean free path λ of particles in the medium. The freeze-out condition reads therefore

$$\sigma\lambda\rho_\pi = 1, \tag{4.26}$$

where σ stands for a typical hadronic cross section. As the observed HBT radii for 40 and 160 AGeV appear rather similar, we do not expect the total freeze-out volume to change more than a factor two. This is thermodynamically consistent with fixing the freeze-out temperature $T_f = 100$ MeV for all SPS scenarios. As λ scales $\sim \sqrt[3]{V}$, this is a sensible *ansatz* – the resulting freeze-out pion densities are very similar when looking at (4.26). This is still true if we take modifications of the pion density by a pion chemical potential μ_π into account; about the same value of μ_π is needed in all SPS scenarios to account for the observed total pion yield.

At RHIC, the situation is different since the extension of the model to higher beam energies poses a more difficult task. While a detailed analysis of the freeze-out stage is certainly possible with the amount of data collected by RHIC so far, this task has not been carried out so far. For the time being, we will henceforth aim at a semi-quantitative description of the RHIC physics. Assuming that the entropy per participant scales with the total multiplicity, we can calculate the initial entropy S_0 . The thermalisation time is assumed to decrease from 1 fm/c at SPS to 0.6 fm/c at RHIC, which is a conservative estimate. Furthermore, no large pion chemical potential appears to be necessary to account for the observed total yield and therefore the thermal pion density at a given temperature is lower, leading to a higher freeze-out temperature with (4.26). We find that an expansion scenario with $T_f = 130$ MeV fits both the observed total particle yield and leads to the correct freeze-out pion density.

The freeze-out volume has now to be adjusted accordingly. From dN/dy particle distributions, $y_f \approx 5.5$ and therefore v_z^f can be extracted. Moreover, experimental results indicate that transverse flow and the geometrical freeze-out radius are virtually unchanged from SPS to RHIC energies [120], so we keep these two parameters equal to the SPS case. Finally we adjust v_z^i consistently with the assumed freeze-out temperature.

The fireball evolution is now calculated as described above, using re-scaled total entropy, initial radius, final state longitudinal and transverse flow and freeze-out radius as new inputs. The parameter sets obtained for the different fireball scenarios are summarised in table 4.1. Note that the corresponding times in the c.m. frame can be considerably larger. Especially for RHIC conditions, volume elements travel near the speed of light at the fireball edge and hence live more than four times longer in the c.m. frame than in their own reference frame.

\sqrt{s}	τ_0	τ_c	τ_f	$V_f [10^3 \text{ fm}^3]$	v_\perp^f	v_z^i	v_z^f	s/ρ_B
8.4 (SPS)	1.5	4.0	15.0	7.0	0.36	0.45	0.75	13
17.4 (SPS)	1.0	6.5	16.0	14.4	0.53	0.45	0.9	26
200 (RHIC)	0.6	10.0	18.0	100	0.56	0.9	0.9985	250

TABLE 4.1: Listed are the proper time for the fireball formation τ_0 , the phase transition time τ_c and the freeze-out time τ_f for SPS at 40 and 160 AGeV and RHIC at $\sqrt{s} = 200$ AGeV. All times are given in fm/c. The volume at freeze-out and the flow velocities at rms radius v_\perp^f and maximum longitudinal extension v_z^f are also shown. In order to compare the thermodynamic conditions, we finally provide s/ρ , the entropy per baryon.

4.3.6 Discussion of temperature and volume

The resulting volume evolutions for 40 and 160 AGeV are plotted in figure 4.6. Note that these curves correspond to the volume at proper time τ , which is larger than the geometrical size of the fireball in the c.m. or the lab frame. For RHIC, the curve looks very similar, only the scale on the y -axis changes by a multiplicative factor of about 7. The corresponding temperature evolution is shown in figure 4.7. We observe that the QGP phase lasts about half of the total fireball lifetime for 160 AGeV, and considerably less for 40 AGeV.

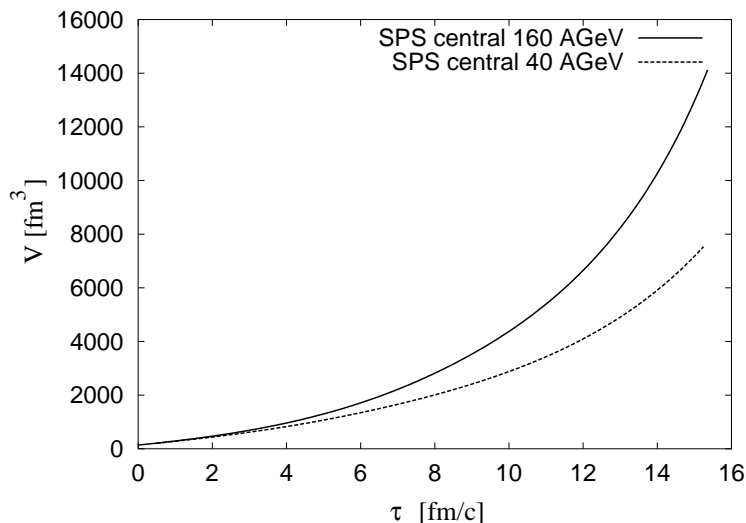


FIGURE 4.6: The volume expansion for SPS conditions. Shown are the curves for 160 AGeV (solid line) and 40 AGeV (dashed line) 5% most central collisions.

Since our setup and results differ in some essential points from previous work [115, 116, 119, 121], we shortly dwell on a discussion of the distinctive features.

In our quasiparticle model there is no mixed phase of coexisting hadronic gas and QGP. Based on the observation that there is *no strong first order* transition visible in the lattice data, the EOS right and left of T_c match smoothly. Inserting the EOS of an ideal quark-gluon gas instead, a large gap in the $s(T)$ diagram is created. The resulting latent heat $(\Delta S)T_c$ generates a mixed phase of considerable duration (5 - 10 fm/c), as found in previous approaches. This large latent heat, however, is in no fashion supported by any recent lattice data and entirely an artifact of the poor approximation of the QGP dynamics by an ideal gas.

By construction of the model, hadronic observables derived from the expanding fireball, e.g. rapidity distributions of charged particles, p_T -spectra, HBT radii and observed particle numbers, are described adequately. This is an important constraint of the model. There is very little freedom left to tune the fireball evolution. The initial temperatures are quite large (~ 300 MeV for SPS central conditions, 420 MeV for RHIC) and are uniquely determined by the total (measured) entropy, the initial volume and our EOS for the quark-gluon phase. To some extent these large values are related to

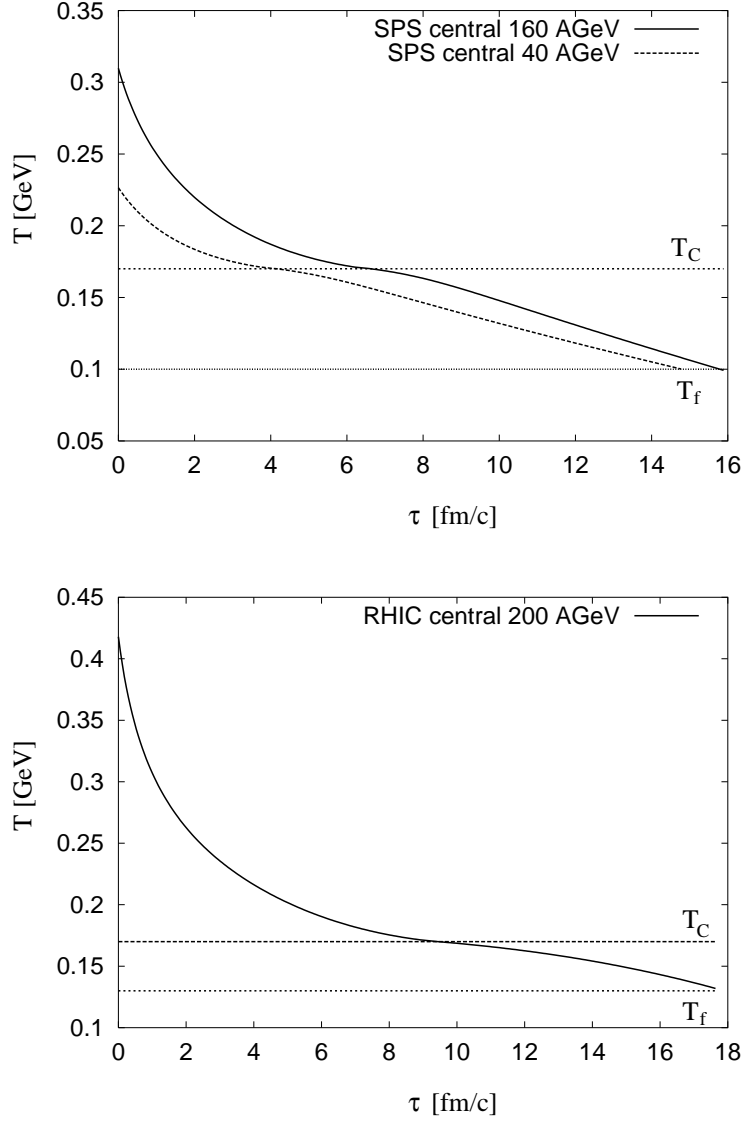


FIGURE 4.7: Time evolution of the temperature for SPS (upper panel) and RHIC (lower panel) conditions as obtained with the fireball model. The critical and freeze-out temperatures are indicated by the horizontal lines.

our choice of the formation time $\tau_0 = 1.0$ fm/c (SPS) and $\tau_0 = 0.6$ fm/c (RHIC) of the thermal system; if τ_0 is increased, the initial temperature decreases correspondingly. However, unlike the results found in [119], we do not observe any strong sensitivity of the dilepton yields to the choice of τ_0 : as the fireball expands, differences in the initial volume become increasingly unimportant. If the total evolution time of the QGP phase is small, these changes may well matter, but since the lifetime of the QGP phase in our model is comparatively large, the possible difference affects only a small fraction of the total lifetime in a region where the fireball volume (and, correspondingly the dilepton yield) is small anyway.

Comparing with the Bjorken estimate of the initial energy density, one should keep in mind that the extrapolation from the final to the initial state is different in the present approach. In the Bjorken scenario, no longitudinal acceleration is present, therefore the mapping of final state rapidity distributions to initial state spatial distributions finds a larger initial volume than our scenario. If we assume no or only small longitudinal acceleration in order to compare the two approaches, we indeed find initial temperatures between 220 and 240 MeV, consistent with the Bjorken estimate. This assumption, however, is incompatible with a freeze-out temperature of 100 MeV and the measured freeze-out geometry.

We also observe a prolonged lifetime of the QGP evolution phase of the fireball as compared to previous results: within our setup, $\tau_{\text{QGP}} \simeq 7$ fm/ c for SPS and $\tau_{\text{QGP}} \simeq 10$ fm/ c for RHIC, whereas the fireball scenario put forward in refs.[119] and [121] finds, using an ideal gas EOS, $\tau_{\text{QGP}} \simeq 1$ fm/ c for SPS and $\tau_{\text{QGP}} \simeq 4$ fm/ c for RHIC, each time accompanied by a mixed phase of duration 3 – 4 fm/ c . This discrepancy is a consequence of our volume evolution and the use of the more realistic EOS of our quasiparticle model, as opposed to that of the ideal quark-gluon gas. Near the phase transition, the entropy density in the quasiparticle model is about a factor two smaller than the one of the ideal quark-gluon gas, and it takes a correspondingly larger volume (and larger evolution time) to reach this entropy density in an isentropic expansion. Furthermore, the use of a realistic acceleration profile slows down the expansion close to T_c , even supporting the longer life time.

4.4 Dilepton invariant mass spectra

Once the time evolution of the fireball is given in terms of the temperature $T(\tau)$, the baryon density $\rho(\tau)$ and the volume $V(\tau)$, and with the knowledge of the photon spectral function, we have all the necessary ingredients to calculate dilepton rates using eq. (4.3). We fold the result with the acceptance of the CERES and the PHENIX detectors, respectively, and average over the rapidity region covered by these two experiments. The so-called 'hadronic cocktail', dileptons produced after freeze-out through various decay processes, with the exception of vector-meson decays, is taken from experimental analyses and subsequently added. This contribution fills the region of very low invariant masses ($M < 150$ MeV). The dilepton yields resulting from direct vector meson decays after freeze-out, as described in section 4.2.3, and the Drell-Yan yield from section 4.2.4 are added to the hadronic cocktail, taking into account the limited kinematic acceptance and energy resolution of the detector.

4.4.1 SPS data at 40 and 160 AGeV

We start with a discussion of the SPS CERES/NA45 experiment, treating 40 AGeV and 160 AGeV data in parallel. The final results for the dilepton invariant mass spectra are shown in figures 4.8 and 4.9. Our calculation reproduces the overall spectrum of the 160 AGeV CERES data quite well. It overestimates the rates somewhat around invariant masses of 200 to 400 MeV and achieves a good description in the region above 400 MeV up to 1.8 GeV. Recall that our QGP model rate constitutes only a lower limit on the actual rate because it neglects the radiation from non-partonic (cluster) degrees of freedom above the critical temperature. Bearing in mind that the region above 1 GeV is mainly populated by dileptons originating from the QGP phase, as evident from the left panel of figure 4.8, there might still be additional radiation close above T_c arising from hadronic clusters embedded in a QGP environment. The Drell-Yan

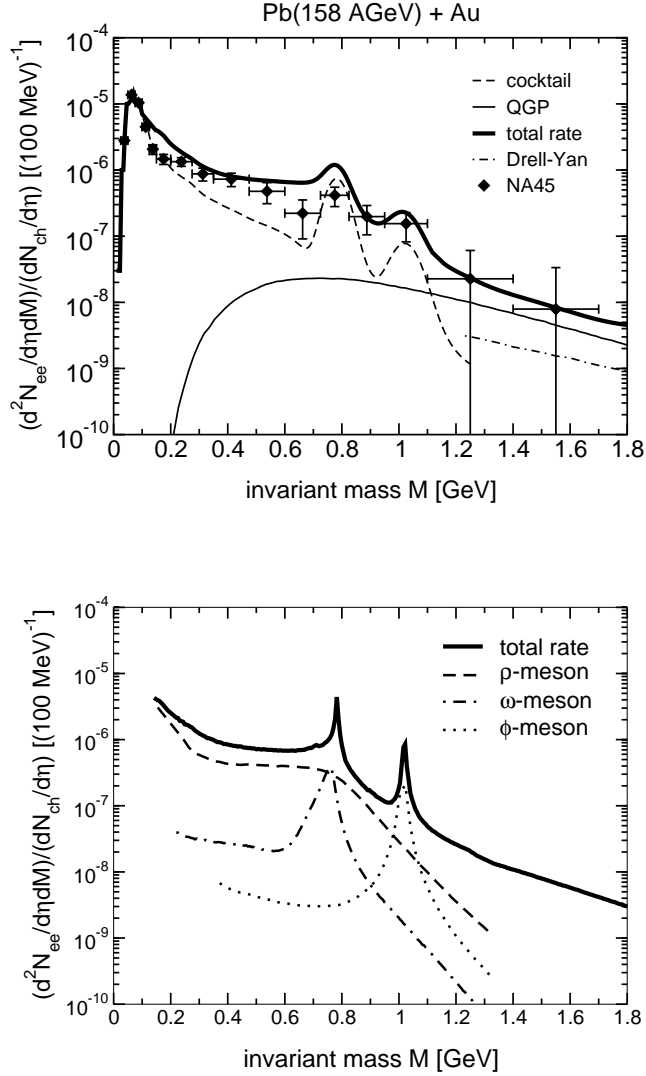


FIGURE 4.8: Upper panel: Dilepton invariant mass spectra, normalised to $dN_{ch}/d\eta = 250$, in units of $(100 \text{ MeV})^{-1}$, for the SPS CERES/NA45 Pb(158 AGeV)+Au experiment [123]. Shown are the data, the total rate, the cocktail contribution including the after freeze-out decays of vector mesons, the QGP contribution and the Drell-Yan yield. Lower panel: Contributions from ρ , ω and ϕ mesons (excluding after freeze-out yield) shown separately, assuming perfect detector resolution.

contribution is non-negligible, but still outshined by the QGP by a factor of 3.

Changes in the spectra of the vector mesons indicate tendencies towards chiral symmetry restoration, so the lower panel of figure 4.8 shows the contributions of ρ , ω and ϕ mesons separately, not including the after freeze-out yield. The ρ meson loses its quasiparticle structure entirely due to strong collision broadening at finite density, and fills the whole low mass region between the two pion threshold and $\sim 800 \text{ MeV}$. The

ω meson, a sharp peak in the vacuum, broadens at finite temperature mainly due to the thermal scattering process $\omega\pi \rightarrow \pi\pi$, cf. eq.(4.11). Furthermore, the mass shift at finite baryon density smears the remaining peak structure considerably. Effectively, the remaining signal arises from the direct decays of ω mesons after freeze-out. The ϕ meson has become a spread-out but still visible resonance structure, showing only moderate broadening at finite temperature and baryon density. It might therefore be a suitable candidate for gauging the strength of vector meson modification.

To test the modelling of the vector meson spectra, we calculate the total number of ω and ϕ mesons, suitably averaged over their medium-induced spread in invariant mass, as

$$\langle N_\omega \rangle = \frac{1}{N_{ch}} \int_{0.65 \text{ GeV}}^{0.9 \text{ GeV}} dM \frac{d^2 N_{\omega \rightarrow ee}}{d\eta dM} = 9 \cdot 10^{-7}$$

and

$$\langle N_\phi \rangle = \frac{1}{N_{ch}} \int_{0.95 \text{ GeV}}^{1.1 \text{ GeV}} dM \frac{d^2 N_{\phi \rightarrow ee}}{d\eta dM} = 1.8 \cdot 10^{-7}.$$

Comparing with numbers from a statistical model calculation, $\langle N_\omega \rangle = 4 \cdot 10^{-7}$ and $\langle N_\phi \rangle = 2.2 \cdot 10^{-7}$ [122], we indeed find reasonable agreement. Note that the relatively large ω meson yield is primarily caused by the pion fugacity factor $[\exp(\mu_\pi/T_f)]^3$ at freeze-out, which reflects the enhanced feeding through the $3\pi \rightarrow \omega$ process. Going from 160 AGeV to 40 AGeV beam energy, analyses of HBT radii and transverse radial flow [120] indicate that the reaction dynamics do not change dramatically, therefore we do not expect drastic differences in the rate. Indeed, the data at 40 AGeV look similar to the 160 AGeV case, and the calculated rate, shown in figure 4.9, also bears this similarity and achieves a good fit without twisting the setup of the model. Since the initial temperature is lower and the QGP phase shorter in the 40 AGeV case, the partonic dilepton contribution is obviously much smaller, but nevertheless still present. Owing to the greater initial baryonic density, the in-medium modifications of the vector mesons become more pronounced, most prominently visible in the ω meson channel. Its downward mass shift drags the peak structure along the time evolution of the fireball, creating a small bump on top of the completely dissolved ρ meson that fills up the low-mass region again. Its yield after freeze-out constitutes a visible signal that may be experimentally observable with suitable energy resolution. The ϕ meson contribution clearly sticks out above the smooth ρ meson 'continuum'. To conclude, we find no distinct differences in our calculation for the two beam energies probing dilepton production at SPS so far, in accord with experimental findings. This indicates that the general setup of our model is fairly robust. Future data at 20 and 80 AGeV will aid to test this statement. The fact that we moderately overestimate the data in the region between 200 and 300 MeV invariant mass is explained as follows. Since this range is dominated by the low-mass behaviour of the ρ meson spectral function at finite density, this behaviour may indicate that the influence of finite three-momentum on the spectra in that very region is non-negligible. Consider the 160 AGeV and 40 AGeV data taken for different transverse momenta $p_T < 500$ MeV and $p_T > 500$ MeV, shown in figures 4.10 and 4.11. We observe that the general shape of the data pattern is well described by the calculation for both p_T regions and both beam energies. However, for the high p_T case, the calculation again overshoots the data in the low mass region whereas this is not so in the low p_T case. This can be traced to the use of the spectral functions for three-momentum equal to zero in order to describe the photon spectral function in the hadronic phase. This approximation is of limited validity at high

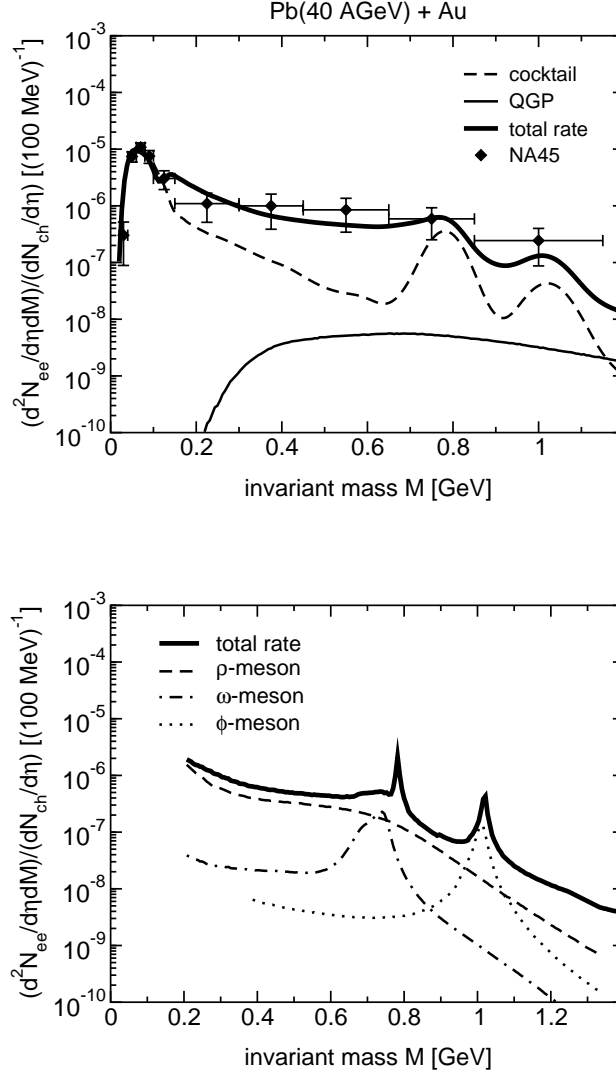


FIGURE 4.9: Upper panel: Dilepton invariant mass spectra, normalised to $dN_{ch}/d\eta = 210$, in units of $(100 \text{ MeV})^{-1}$, for the SPS CERES/NA45 Pb(40 AGeV)+Au experiment [124]. Shown are the preliminary data, the total rate, the cocktail contribution including the after freeze-out decays of vector mesons and the QGP contribution. Lower panel: Contributions from ρ , ω and ϕ mesons (excluding after freeze-out yield) shown separately, assuming perfect detector resolution.

p_T where the spectral function ought to become smaller than in our approximation. Therefore we expect improved agreement with the data for the low invariant mass region both at 40 and 160 AGeV once this effect is taken into account properly (which is, however, not an easy task due to the appearance of higher resonances).

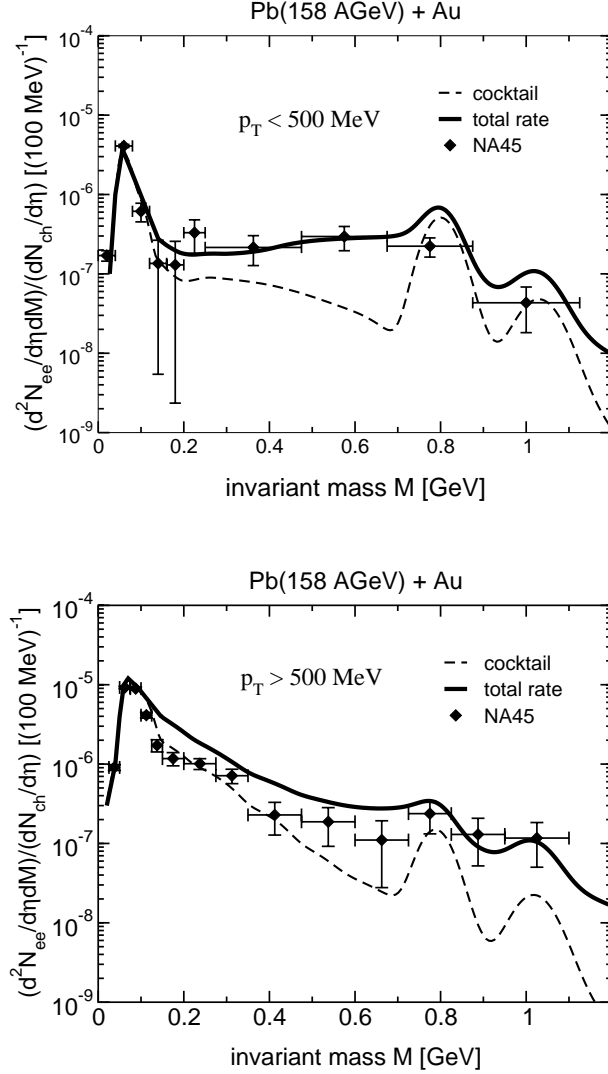


FIGURE 4.10: Upper panel: Dilepton invariant mass spectra for transverse momenta of the e^+e^- pair $p_T < 500$ MeV for the SPS CERES/NA45 Pb(158 AGeV)+Au experiment [123]. Shown are the data, the total rate and the cocktail contribution. Lower panel: Same for $p_T > 500$ MeV.

4.4.2 RHIC at $\sqrt{s} = 200$ AGeV

For the RHIC scenario, thermally generated dileptons are dominant. Measurements of proton ratios at $\sqrt{s} = 130$ AGeV indicate that the central collision region remains almost net-baryon free, compared to SPS energies. Within a statistical thermal model, the particle ratios are accounted for by a small baryon chemical potential of about 50 MeV at chemical freezeout [42]. At 200 AGeV, this value is predicted to be even smaller. Effects of finite baryon density are therefore almost absent and consequently both the ρ and the ϕ meson are expected to show up in the spectrum as pronounced structures, whereas there should be no clear trace of the in-medium ω meson due to its

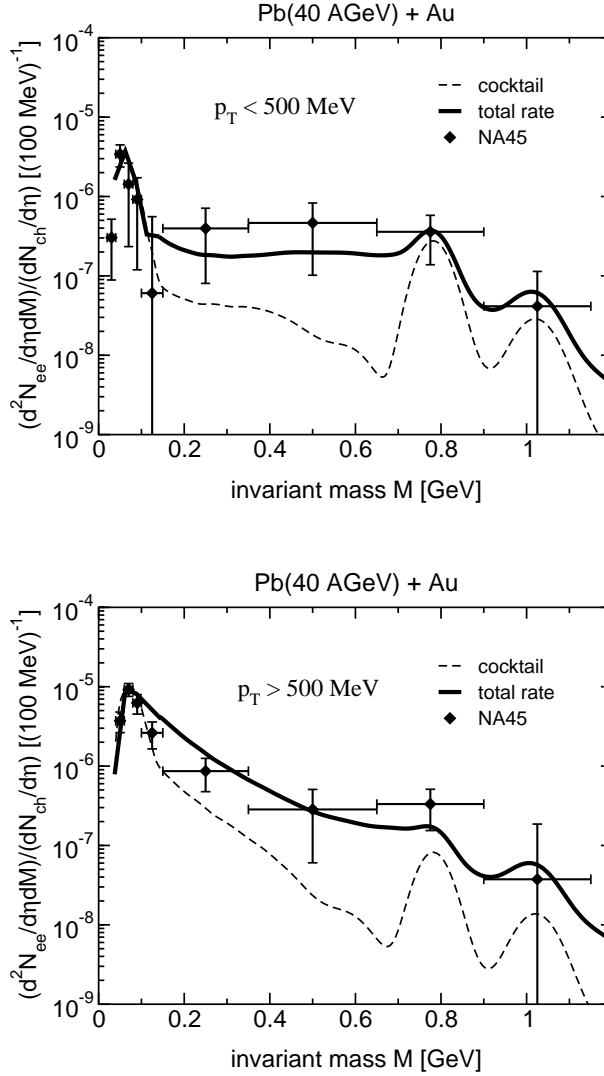


FIGURE 4.11: Upper panel: Dilepton invariant mass spectra for transverse momenta of the e^+e^- pair $p_T < 500$ MeV for the SPS CERES/NA45 Pb(40 AGeV)+Au experiment [125]. Shown are the data, the total rate and the cocktail contribution. Lower panel: Same for $p_T > 500$ MeV.

strong thermal broadening. Contributions from Drell-Yan processes, which dominate in the very high invariant mass region, are an order of magnitude smaller.

The corresponding prediction for the dilepton yield at 200 AGeV, including the schematic acceptance for the PHENIX detector, is shown in figure 4.12. The ω and ϕ meson resonances clearly stick out over the smooth ρ meson and QGP contributions. Although PHENIX will only start to measure at $M \geq 1$ GeV, it may be possible to resolve the ϕ meson peak. However, a significant part of the peak strength is built up by the after freeze-out contributions, making it difficult to disentangle the in-medium

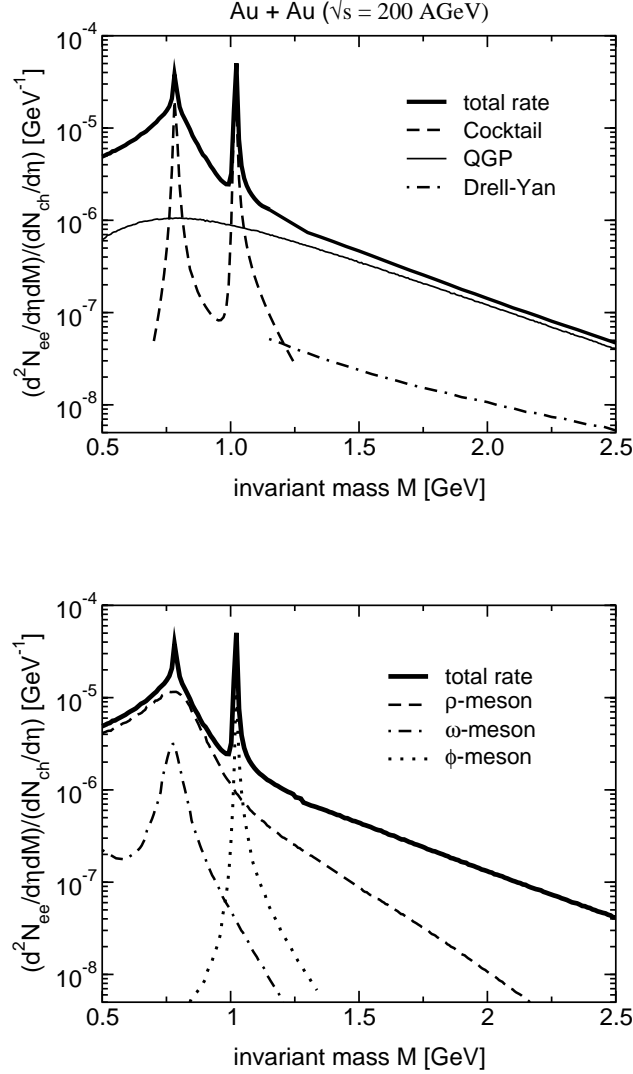


FIGURE 4.12: Upper panel: Dilepton invariant mass spectra, normalised to $dN_{ch}/d\eta = 650$ [126], in units of GeV^{-1} , for the RHIC experiment PHENIX at $\sqrt{s} = 200$ AGeV. Shown are the total rate, the cocktail consisting of the after freeze-out decays of ω and ϕ vector mesons, the QGP contribution and the Drell-Yan yield. Lower panel: Contributions from ρ , ω and ϕ mesons (excluding after freeze-out yield) shown separately.

modifications on the hadrons. For $M \geq 1.3$ GeV, the dilepton spectrum is dominated by thermal QGP radiation, outshining the hard Drell-Yan dilepton yield. Comparing our prediction for PHENIX with the one shown in ref. [119], we find rough agreement of the rate for the low mass region below ~ 1 GeV. Although the dilepton yield from the QGP phase is suppressed in our case by the factor $C(T)^2$ (cf. section 4.2.1), we still find an enhancement of a factor of about 4 in the range $1.3 - 2.5$ GeV over the rate in [119] that employs a (perturbative) chemical undersaturation model in the QGP phase. Owing to the non-perturbative nature of the QGP close to T_c , this model may

not be applicable in that very region. Furthermore, it depends crucially on the value taken for $\alpha_s(T)$. Note that our rate also constitutes only a lower limit there, so that the actual rate may even be larger. High precision data will allow to pin down one or the other model.

4.4.3 Sensitivity to model parameters

We would like to stress that the gross features of our model are set, once the parametrisation of the fireball evolution has been matched to the hadronic observables, and the EOS of both phases has been constructed in accordance with lattice QCD and empirical constraints. The remaining uncertainties, mainly about the initial state of the fireball, the thermal masses of the quasiparticles and the detailed shape of the EOS, do not alter the results substantially; they lead to only moderate or even weak dependence on those parameters. Fine-tuning is still possible, but only within the limits that retain consistency with the overall framework.

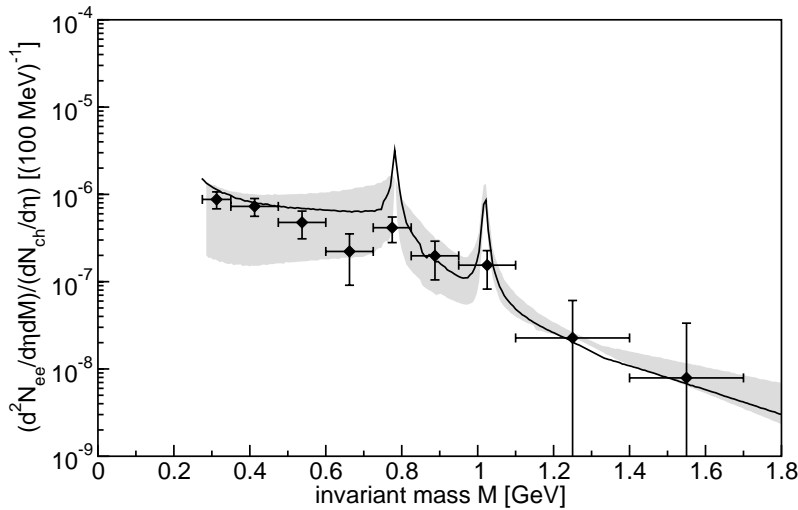


FIGURE 4.13: Dilepton invariant mass spectra for the SPS CERES/NA45 experiment at 160 AGeV. Shown are data (symbols), the total rate introduced in section 4.4.1 (solid line) and a band (shaded) that represents the range in the dilepton yield when varying the parameters τ_0 , v_z^i and T_c . See text for details.

We have investigated the sensitivity of the model to parameter changes in some detail for the SPS scenario at 160 AGeV. In order to get a theoretical 'error band', we have explored the extremes of our parameter ranges, a combination of parameters that yields the largest and the smallest possible QGP contribution. The resulting range is shown in figure 4.13 as a grey band, together with the data points and the curve from the previous section. Regarding the initial conditions, the largest uncertainty comes from the initial fireball formation length z_0 or, equivalently, the time τ_0 . We let it vary from 0.5 fm/c to 2 fm/c, i.e. from fast to slow equilibration. Consider next the initial longitudinal flow velocity v_z^i . A variation of this quantity from 0.3 c to 0.8 c implies a modification of the pressure-driven accelerated motion in order to arrive at the same final velocity of 0.9 c , as determined by the rapidity distributions of the observed hadrons. Strong deviations from $v_z^i \simeq 0.5 c$, however, lead to inconsistent values for the thermal freeze-out temperature T_f . Finally, modifications of the criti-

cal temperature T_c influence mainly the relative weight of the contributions from the QGP phase and the hadronic gas phase to the dilepton yield and hence change the shape of the dilepton spectra. Lattice data on T_c suggest a range from 140 MeV for three massless, thermally active flavours to about 185 MeV for two massless flavours and a realistic pion mass. Due to the self-consistent modelling of the temperature and volume evolution, there is no simple one-to-one correspondence of these parameters to the dilepton yield.

The upper limit of the grey band in figure 4.13 now corresponds to the scenario with a *small* QGP contribution, i.e. small τ_0 , large v_z^i and high T_c . On the other hand, the lower limit includes a *large* QGP contribution with large τ_0 , small v_z^i and low T_c . It is instructive to note that the shape of the spectrum changes only moderately above 1 GeV invariant mass within these extreme parameter variations. The first scenario, however, tends to overestimate the data in the region of the ρ peak, whereas the second scenario does not leave enough time for the hadronic phase to build up the e^+e^- excess in the low-mass region between 200 and 800 MeV, effectively ruling out a large QGP contribution.

4.5 Intermediate summary

As found in previous approaches, the proposed dilepton excess in the intermediate mass region at SPS is unlikely to be a direct signal from the QGP, it can be explained by non-trivial, yet conventional hadronic physics. The experimental resolution in the region where the QGP presumably shines most prominently is unfortunately too coarse at the moment to extract a conclusive result. The situation at RHIC might improve since there is a window above 1 GeV and the region which will be ultimately filled by semileptonic decays of charm mesons, where the QGP radiation will be dominant. Since our approach predicts an enhancement of the radiation by a factor of 4 over the result of [119], it might even be possible to pin down specific models of both the radiation itself and the fireball evolution.

The most important point at this stage is that we have explored the evolution of a fireball through the quark-gluon and hadronic phases using, for the first time, input and constraints from lattice QCD in a thermodynamically self-consistent framework. The use of the quasiparticle model put forward in chapter 3 in the context of heavy-ion collisions has significantly improved the modelling of the fireball, eliminating many free parameters of its evolution in connection with hadronic final-state measurements. It is remarkable that our quasiparticle model is able to reproduce the measured dilepton data without any further modification, despite the suppression of dilepton radiation near the phase transition temperature due to the presence of the factor $C(T)^2$ in eq.(4.1). Note that the dilepton signatures of previous phenomenological quasiparticle models of the QGP would be qualitatively distinct: since there the quasiparticle masses rise as T_c is approached from above, the threshold of dilepton production would shift to invariant masses far above the ϕ meson peak, leaving the low-invariant mass region essentially unpopulated. Detailed knowledge of the slope of the invariant mass spectrum above 1 GeV will also give an indication of the average temperature in the quark-gluon phase, serving as a constraint for the fireball dynamics in the QGP region.

On the hadronic side, high resolution measurements of the invariant mass spectrum around the region of the ω and the ϕ meson mass can reveal information on the average density and temperature in the hadronic phase. The broadening and mass shift

of the ω meson with temperature can serve as a 'thermometer' once the cocktail contribution is reliably assessed. A visible enhancement in the ω region beyond the rate originating from ω meson decays after freeze-out would hint at a temperature which is on average lower than assumed in this model and therefore point to a lower freeze-out temperature or alternative in-medium effects on hadrons. On the other hand, the ϕ meson signal, being nearly unmodified by temperature effects over a comparably long timespan, may be used as a 'standard candle' at RHIC conditions.

Experimental measurements using different nuclear system sizes or different impact parameters can provide different relative weights of QGP and hadronic dilepton radiation to the observed yield. One may thus hope to disentangle these contributions and test the model assumptions above and below the phase transition separately, at least in a qualitative fashion. It is important to note that fireball thermodynamics, as described in this work, leads to temperatures well above T_c for a broad range of initial conditions, making the formation of a QGP unavoidable if one believes in lattice QCD and thermalisation. These regions of high energy density do not necessarily contribute significantly to the dilepton yield, though: low-mass dileptons are more sensitive to aspects of the chiral symmetry restoration, or the duality of hadron and parton spectra close to T_c . On the other hand, high initial temperatures lead to large gluon densities in the first few fm/c of the fireball collision that are a direct signal of deconfinement and predominantly responsible for J/ψ suppression – a topic to which we turn now.

5 J/ψ Suppression

In this chapter, we apply the quasiparticle and fireball models successfully used to describe dilepton data in the previous chapter, to the phenomenology of J/ψ suppression in heavy-ion collisions. Within a kinetic approach, we model the interactions of the J/ψ with the medium in the space-time arena that was set up in chapter 4. Again, the medium above T_c consists of the quasiparticle model of chapter 3 in order to maintain maximal consistency. A more detailed discussion of the whole calculation can be found in [127], we outline here the main trail of thoughts and stress the implications of the quasiparticle model.

5.1 Screening and the J/ψ

A possible dissolution of bound quarkonia states, e.g. J/ψ , was proposed long ago [128] as an experimental signature of the quark-gluon plasma in heavy-ion collisions. Since c and b quarks are comparatively heavy as compared to typical temperature scales ($m_c = 1 - 1.4$ GeV, $m_b = 4 - 4.5$ GeV [4]), they can be treated to a certain extent in a non-relativistic fashion. In particular, the interaction between the heavy c and \bar{c} quark can be modelled by the Cornell potential (2.11) for the lowest lying bound states (J/ψ , ψ'). As temperature rises (but stays below T_c), the parameters of the potential become temperature-dependent:

$$V(r, T) = \sigma(T)r + \frac{\bar{\alpha}(T)}{r} \exp(-m_D(T)r). \quad (5.1)$$

The string tension σ is expected to decrease as T increases, marking the onset of the deconfinement transition, and this is indeed seen in quenched lattice calculations [63]: $\sigma(T_c)/\sigma(0) = 0.12$. Above the deconfinement temperature, the string tension vanishes, and the potential is perturbatively characterised by an exponentially damped Coulomb part because the virtual gluons transmitting the interaction between the quarks acquire a thermal screening mass, the *Debye mass* $m_D(T)$ (B.9). Lattice simulations of the interquark potential (for infinitely heavy, static test quarks) do indeed show that the potential flattens at T increases [73], as apparent from figure 5.1. In chapter 6, we will examine in much more detail the phenomenon of screening.

The very first suggestion to study J/ψ production in heavy-ion collisions was subsequently based on a two-fold observation: First, the initial energy density produced in the collisions is above the critical one that is necessary to produce the QGP. Second, J/ψ is in essence bound by the potential (5.1) which becomes screened in the QGP. J/ψ s produced in the initial stage of the collision will dissolve and their charm quarks end up in pairs of D mesons (open charm). We would therefore expect that the J/ψ production cross section is suppressed in a sufficiently energetic AB collision as compared with extrapolations from proton-proton (pp) collisions. The first systematic signs of suppression [129] were later on explained by more conventional mechanisms [130], already present in proton-nucleus (pA) reactions. Only with the advent of Pb+Pb

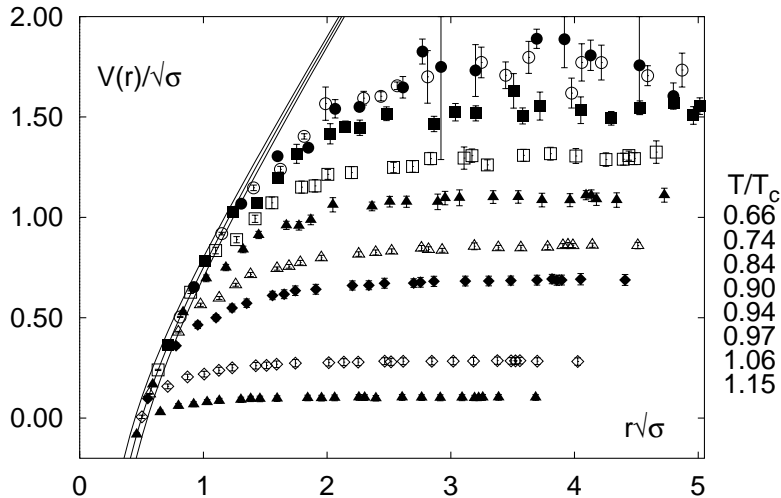


FIGURE 5.1: Temperature dependence of the interquark potential in three-flavour lattice QCD [73]. All quantities are plotted in units of the zero temperature string tension $\sqrt{\sigma} \simeq 420$ MeV. The solid lines mark the zero temperature Cornell potential $V(r) = \bar{\alpha}/r + \sigma r$ with $\bar{\alpha} = 0.25 \pm 0.05$. The potentials have subsequently been normalised at the shortest distance available on the lattice ($rT = 0.25$).

collisions the first signals of anomalous suppression, beyond extrapolations from pA collisions, were seen by the NA50 collaboration at the CERN SPS [131].

However, as in the case of dilepton radiation treated in the last chapter, J/ψ suppression is always folded with the time evolution of the fireball. Since the evolution continues after the plasma undergoes a transition from partonic back to hadronic degrees of freedom, any information on the early stage is then hidden behind distortions from the hadronic phase. While much phenomenology has been developed in order to explain the latest SPS data [132], it is still not clear at the moment whether or not the seen anomalous suppression can be attributed to the presence of a QGP: realistic models can be constructed to incorporate well known nuclear effects such as initial state gluon radiation [133], color excitation [134], initial state parton energy loss [135] and coherence effects [136]. All of these can potentially account for the observed data without the need to invoke a (thermalised) QGP, albeit with a more or less large number of free parameters. Our approach will be different: having already constructed a fireball model that is consistent with a large number of hadronic observables and that has proven to be successful in describing dilepton data, we are now in a position to explore whether the same description is consistent with the observed J/ψ measurements of NA50. The specific time evolution of the medium is hence not constructed or fitted in order to reproduce the desired J/ψ suppression effect. We have to consistently employ the quasiparticle model presented in chapter 3 to describe, within the framework of kinetic theory, the interactions of the J/ψ with the partonic quasiparticles. The result is then tightly constrained, leaving only very limited room for adjusting parameters. In the following, we will not distinguish the different charmonium states (J/ψ and χ_c) which contribute to J/Ψ production from one another, we will simply indicate a charmonium by Ψ unless otherwise stated.

5.2 Initial conditions

5.2.1 Open charm

The production of charmed quarks is commonly described within perturbative QCD. In the following, we restrict ourselves to the leading order treatment presented in [138, 139], with suitable adjustments in order to meet phenomenology. This section bears some similarity with the discussion of the Drell-Yan background for dilepton radiation, section 4.2.4. We consider the leading processes

$$q\bar{q} \rightarrow c\bar{c} \quad \text{and} \quad gg \rightarrow c\bar{c}.$$

In terms of their elementary differential cross sections $d\hat{\sigma}_i/d\hat{t}$, the spectrum of c quarks produced in pp collisions at rapidity y_c and transverse momentum p_T is

$$\frac{d\sigma_{pp}^c}{dy_c dp_T^2} = K \int dy_{\bar{c}} \sum_{i=u,d,s,g} x_1 f_{i/p}(x_1, \mu_c^2) x_2 f_{i/p}(x_2, \mu_c^2) \frac{d\hat{\sigma}_i}{d\hat{t}}, \quad (5.2)$$

where $x_{1,2}$ are the momentum fractions of the partons in the colliding protons. The factorisation scale is taken at $\mu_c = 1.4$ GeV, which is of the order of the c quark mass, and an empirical scaling factor $K = 2$ is used, as in the Drell-Yan case. We employ the GRV94LO parton distributions $f_{i/p}$ [140] and neglect the effect of intrinsic transverse momentum of partons.

To estimate the spectrum of c quarks in AB collisions, the simplest approach is to scale the pp result with the overlap function $T_{AB}(b)$, defined in eq.(4.16). On the other hand, as the collision energy increases, shadowing effects are expected to become important, reducing the total yield [141]. Another correction to be introduced is the Cronin effect on partons' transverse momenta, which results in a broader p_T spectrum of charmed quarks. As in the Drell-Yan case, the quantitative consequences of these nuclear effects are not well under theoretical control, therefore we neglect them for now. The charmed quark spectrum in AB collisions is then computed as

$$\frac{dN_{AB}^c}{dy_c dp_T^2}(b) = \frac{d\sigma_{pp}^c}{dy_c dp_T^2} T_{AB}(b). \quad (5.3)$$

5.2.2 Hidden charm

The description of charmonium production in nuclear collisions is a more complicated task as compared to $c\bar{c}$ production because exclusive production of composite particles in hadronic collisions is basically a non-perturbative process. As above, pp collisions provide the baseline. The Ψ rapidity modulation can be inferred from the relation

$$\frac{d\sigma}{dy} \sim x_1 g(x_1) x_2 g(x_2), \quad (5.4)$$

where $xg(x) \sim (1-x)^5$ is the gluon distribution in the proton and $x_{1,2} = (m_\Psi/\sqrt{s}) \exp(\pm y)$. For the overall normalisation we use the parametrisation for the total charmonium production cross section [142]

$$\sigma_{pp}^\Psi(s) = 2\sigma_0 (1 - m_\Psi/\sqrt{s})^n, \quad (5.5)$$

where $\sigma_0 = 1.28 \mu\text{b}$ and $n = 12$. In addition, we assume a Gaussian form for the p_T -dependent part, with a width parameter $\Lambda = 1$ GeV. Assembling the pieces, the

invariant Ψ spectrum in pp collisions becomes

$$\frac{d\sigma_{pp}^{\Psi}}{dy d^2p_T} = \sigma_{pp}^{\Psi}(s) F(s, y) [(\pi\Lambda^2)^{-1} \exp(-p_T^2/\Lambda^2)], \quad (5.6)$$

where the y -dependent part reads, with eq.(5.4),

$$F(s, y) = C(s) [1 - 2(m_{\Psi}/\sqrt{s}) \cosh y + m_{\Psi}^2/s]^5, \quad (5.7)$$

while $C(s)$ is chosen to satisfy the constraint $\int dy F(s, y) = 1$.

We now consider nuclear effects, starting with proton-nucleus (pA) collisions. It has been shown that the experimental results on charmonium production can be explained using

$$\sigma_{pA}^{\psi} = \sigma_{pp}^{\psi} \int d^2b T_A(b) S_A^{\text{abs}}(b) \quad (5.8)$$

for the total production cross section. $T_A(b)$ stands for the overlap function (4.17), and the factor

$$S_A^{\text{abs}}(b) = \frac{1 - \exp[-\sigma_{\psi N}^{\text{abs}} T_A(b)]}{\sigma_{\psi N}^{\text{abs}} T_A(b)} \quad (5.9)$$

is the survival probability for Ψ to escape the nucleus without being dissociated. It includes the effective absorption cross section $\sigma_{\psi N}^{\text{abs}}$, a quantity of the order of 3 mb for midrapidity Ψ s as measured at $E_{\text{lab}} = 800$ GeV at Fermilab, while it amounts to 5 – 7 mb for midrapidity Ψ s as measured at $E_{\text{lab}} = 158 - 200$ GeV at the SPS. The absorption cross in (5.9) section parametrises various poorly known effects, with varying importance depending on the collision energy. Among these effects are the presence of colour degrees of freedom in the dynamics of colliding nucleons, initial state parton energy loss and coherence length and shadowing effects. A common property of all of the above is the linear dependence on the path length, at least to leading order.

When looking at Ψ production in nucleus-nucleus (AB) collisions, we can estimate the cross section for a given impact parameter by generalising (5.8). The effects of the produced medium will be discussed in the next section, so, neglecting them for the moment, we obtain

$$\frac{dN_{AB}^{\Psi}}{dy d^2p_T}(b) = \frac{d\sigma_{pp}^{\Psi}}{dy d^2p_T} T_{AB}(b) S_{AB}^{\text{nuc}}(b), \quad (5.10)$$

where nuclear effects are included in the generalised suppression function

$$S_{AB}^{\text{nuc}}(b) = T_{AB}^{-1}(b) \int d^2s T_A(s) S_A^{\text{nuc}}(s) T_B(\tilde{s}) S_B^{\text{nuc}}(\tilde{s}). \quad (5.11)$$

Since nuclear effects also depend on energy, we have chosen $\sigma_{\psi N}^0 = 5$ mb at the SPS energy $\sqrt{s_0} = 17.3$ GeV in order to be in agreement with the pA measurement, and assumed the relation

$$\sigma_{\psi N}^{\text{abs}}(s) = \sigma_{\psi N}^0 (s/s_0)^{\lambda} \quad (5.12)$$

with $\lambda = 0.2$ in order to simulate nuclear effects as predicted in [136].

5.3 Thermodynamics of the medium

Having set up the initial conditions for charm and charmonia, we now let them propagate through the medium produced in the collision. Since there exists a sharp separation of scales ($m_c, m_\psi \gg T$), these particles will not thermalise, but they will interact with the medium constituents over the duration of the fireball expansion. Above T_c , we consistently describe the QGP by the quasiparticle model set up in chapter 3, below the critical temperature, we employ, as in section 4.3.3, a hadronic resonance gas description, including all particles up to 1.6 GeV mass while assuming no medium effects on their masses and widths. Although this prescription is oversimplified, we will see that possible corrections bear no effect on the final result.

It is instructive to plot the total particle density as a function of temperature, which, in the QGP phase, takes the form

$$\begin{aligned} n^{\text{tot}}(T) &= n_g^{\text{tot}}(T) + n_q^{\text{tot}}(T) = \\ &= \nu_g \int \frac{d^3k}{(2\pi)^3} [C(T) f_B(\omega_k^g)] + 4N_c \sum_{i=1}^{N_f} \int \frac{d^3k}{(2\pi)^3} [C(T) f_D(\omega_k^i)], \end{aligned} \quad (5.13)$$

with the notation already used in eq.(3.40). In the hadronic phase, a similar density formula applies: In order to smoothly match with the partonic part, the hadronic degrees of freedom have to be switched off at some stage. In chapter 3, this was not taken into account since we only considered the region above T_c . Here, we introduce – mainly for illustrational purposes – a deconfinement factor $D(T)$ analogous in form to that in eq.(3.32) (that replaces $C(T)$ in (5.13)). In this case, the parameters are, however, chosen arbitrarily simply to suppress hadrons above T_c and to avoid an awkward, unphysical jump in the degrees of freedom. Their detailed values play no role in the following.

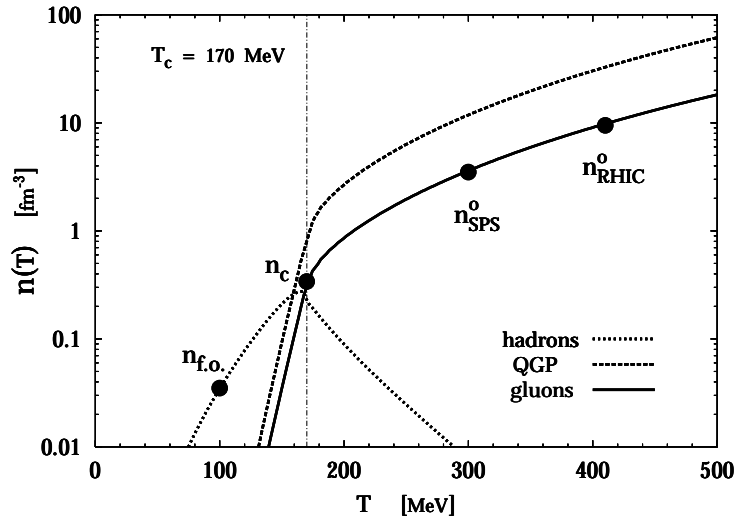


FIGURE 5.2: Expected particle densities as a function of the temperature T in the hadronic and partonic phases. Here, $n_{f.o.}$ denotes the freeze-out density of the fireball, n_c the critical density, n_{SPS}^o the initial quasiparticle gluon density at SPS and n_{RHIC}^o the corresponding value at RHIC. The vertical line indicates the value of the critical temperature $T_c = 170$ MeV.

The total density is shown in figure 5.2, from small temperatures up to $\simeq 500$ MeV, according to eq.(5.13). The confinement factor $C(T)$ accounts for the release of the partonic constituents of the hadrons as T grows. Since it does not jump abruptly to one as T_c is reached, some hadronic clusters and hence non-zero hadron densities persist slightly above the critical temperature. We have indicated the the values of particle densities at the beginning and the end of the time evolution of the fireball. Comparing the numbers involved, it is obvious that the number density in the QGP is always an order of magnitude larger than the hadronic one (note the logarithmic scale). This should be a robust, model-independent statement and has a crucial impact on Ψ evolution in the produced medium.

Having characterised the matter constituting a strongly interacting system in the thermodynamic limit, we take the space-time arena the medium will live in to be the same as in chapter 4: the fireball reaches local thermal (though not necessarily chemical) equilibrium within a time of the order of 1 fm/ c . As outlined in section 4.3, the fireball evolution is fully constrained by data for central collisions at SPS with $E_{\text{lab}} = 158$ AGeV, and we take over these parameters *without further adjustments*. An extension towards different centralities, that is needed for a J/ψ description, and higher beam energies is not on the same firm ground, but the necessary assumptions have been discussed in section 4.3.5, and, again, we will use the same setup having proven to be successful in the case of dilepton radiation. We stress that this fireball model has been fixed by independent observables and ensures accordance with a multitude of hadronic measurements. In contrast with previous approaches, we have therefore eliminated the medium evolution as an adjustable parameter in the Ψ description.

5.4 Charmonium Evolution

5.4.1 Kinetic description of dissociation and formation

We now examine the interaction between Ψ and the produced medium. The natural framework in which to study the time evolution of Ψ is that of kinetic theory. We will make use of a semi-classical treatment, setting up a relativistic Boltzmann equation for the Ψ phase-space distribution $f_\Psi(p, x)$. The collision term, which contains interaction cross sections, provides the interface between charm and the medium. One of the elements of the collision term describes Ψ dissociation, a second piece allows for $c\bar{c}$ coalescence in the QGP. In the partonic phase, the dominating process is $\Psi g \leftrightarrow c\bar{c}$, leading to

$$p^\mu \partial_\mu f_\Psi(p) = \int \frac{d^3k}{(2\pi)^3 E_k} \frac{d^3q_1}{(2\pi)^3 E_1} \frac{d^3q_2}{(2\pi)^3 E_2} \delta^{(4)}(p + k - q_1 - q_2) \times W_{c\bar{c} \leftrightarrow \Psi g} \left[f_c(q_1) f_{\bar{c}}(q_2) - f_\Psi(p) f_g(k) \right], \quad (5.14)$$

which is the Boltzmann equation for f_Ψ , characterised by a collision term containing the interaction probability $W_{c\bar{c} \leftrightarrow \Psi g} = W_{\Psi g \leftrightarrow c\bar{c}}$. We have chosen the kinematics such that p is the Ψ and k the gluon momentum, and q_1 and q_2 are the c and \bar{c} momenta. Making use of the momentum-conserving δ -function, some of the phase space integrals can be eliminated, leading to the intuitive result

$$\left(\partial_t + \vec{v} \cdot \vec{\nabla}_r \right) f_\Psi(\vec{r}, \vec{p}, t) = -\lambda_D(\vec{r}, \vec{p}, t) f_\Psi(\vec{r}, \vec{p}, t) + \lambda_F(\vec{r}, \vec{p}, t). \quad (5.15)$$

The dissociation (loss) term

$$\lambda_D(\vec{r}, \vec{p}, t) = \sum_n \int d^3k \sigma_D^n(s) v_{\text{rel}}(\vec{k}, \vec{p}) f_n(\vec{r}, \vec{k}, t) \quad (5.16)$$

consists of a sum over the various constituents of the medium, each interacting with Ψ with a different dissociation cross section σ_D^n . v_{rel} is the relative velocity between Ψ and constituent n . The formation (gain) term

$$\lambda_F(\vec{r}, \vec{p}, t) = \int d^3q_1 \sigma_F(s) v_{\text{rel}}(\vec{q}_1, \vec{q}_2) f_{\bar{c}}(\vec{r}, \vec{q}_1, t) f_c(\vec{r}, \vec{q}_2, t) \quad (5.17)$$

describes the coalescence process of Ψ formation by c and \bar{c} quarks.

In accordance with the model for the medium, we assume to have a system which expands as function of proper time in a cylindrical volume where densities are uniform. Integrating over Ψ transverse momenta, we can reduce (5.15) to a simpler first order differential equation for the rapidity density of Ψ ,

$$\frac{d}{d\tau} N_{\Psi}^y = - \sum_n \langle\langle \sigma_D^n v_{\text{rel}} \rangle\rangle \rho_n N_{\Psi}^y + \langle\langle \sigma_F v_{\text{rel}} \rangle\rangle \rho_{\bar{c}} N_c^y, \quad (5.18)$$

which now depends on the proper time τ . The double brackets indicate an average over the momenta of the initial particles, except for the last rapidity integral which is left undone. Explicitly,

$$\langle\langle \sigma v_{\text{rel}} \rangle\rangle = \frac{\int d^2p_a^T [f_a(p_a)] \int d^3p_b [\sigma v_{\text{rel}}(p_a, p_b) f_b(p_b)]}{\int d^2p_a^T [f_a(p_a)] \int d^3p_b [f_b(p)]}, \quad (5.19)$$

where p_a and p_b indicate the Ψ and g momenta for dissociation and c and \bar{c} momenta for formation, respectively. We note that leaving the y -integration undone is important since we intend to compute the value of the final Ψ rapidity distribution at midrapidity, and not the whole yield. While the charm density is denoted by $\rho_{\bar{c}} = \rho_c = N_c/V$, the medium constituent's density is always labelled ρ_n .

It is clear that an equation analogous to (5.18) but with opposite sign on the r.h.s. is necessary for charm in order to ensure its conservation as function of time. This means that the initial (constant) total amount of charmed quark pairs is $N_c^0 = N_{\Psi} + N_c$. However, at each rapidity it is a good approximation to assume that the total charm distribution equals the distribution of unbound quarks since $N_c^y = N_{\bar{c}}^y \gg N_{\Psi}^y$, allowing to simplify the rate equation to

$$\frac{d}{d\tau} N_{\Psi}^y(\tau) = -\lambda_D(\tau) N_{\Psi}^y(\tau) + \lambda_F(\tau). \quad (5.20)$$

Within this approximation, the rates take on the form

$$\lambda_D(\tau) = \sum_n \langle\langle \sigma_D^n v_{\text{rel}} \rangle\rangle(\tau) \rho_n(\tau) \quad \text{and} \quad \lambda_F(\tau) = \langle\langle \sigma_F v_{\text{rel}} \rangle\rangle N_c^0 N_c^y / V(\tau), \quad (5.21)$$

where we have written out the explicit time dependence in the various terms. In particular, the process of averaging the dissociation cross section introduces an implicit time dependence because of the temperature dependence in the phase space density

of the medium. On the other hand, since charmed quark distributions are time independent, the formation cross section is so also.

Having reduced the Boltzmann equation to a much simpler one, consistent with the description of the medium as being spatially uniform, we can now directly integrate eq.(5.20) in order to obtain a solution in closed form:

$$N_{\Psi}^y(t) = \left\{ N_{\Psi}^y(0) + \int_{t_0}^t dt' \lambda_F(t') \exp \left[\int_{t_0}^{t'} dt'' \lambda_D(t'') \right] \right\} \exp \left[- \int_{t_0}^t dt' \lambda_D(t') \right]. \quad (5.22)$$

The structure of the solution is quite self-explanatory. Neglecting the Ψ formation process, we obtain the usual exponential suppression, while the formation term becomes important as soon as the number of charmed quarks becomes large. This is expected to be the case when the collision energy increases, and the formation will eventually overwhelm suppression.

It might seem natural at this stage to also incorporate the mentioned Debye screening of the interquark potential, for example by assuming complete J/ψ dissolution above a certain temperature [143, 144]. However, it is not clear what an all-embracing description of the interaction of the J/ψ with the medium should be. In a sense, screening arises from the interaction of the virtual gluons that bind the J/ψ with the gluons of the environment. After all, such a process can also be viewed as scattering of the J/ψ , that fluctuates into a $c\bar{c}$ pair and non-perturbative multi-gluon exchanges, off the thermalised gluons. Taking into account both screening and kinetic scattering can amount to a certain degree to double counting. Disentangling the effects even qualitatively, however, is a highly non-trivial task. At this stage, we might argue that screening, as inferred from the lattice, is a purely static concept. Since the produced J/ψ s are not produced at rest with respect to the medium, a kinetic description seems to be appropriate within the present context.

5.4.2 Cross sections for dissociation and formation

In this section we discuss how open and hidden charm states will interact with the different degrees of freedom of the produced medium (quarks and gluons at the beginning, hadrons later), considering both dissociation and formation. These cross sections are the last missing ingredient in (5.22). Starting with the QGP, to lowest order one might expect that the two processes illustrated in figure 5.3 are contributing to Ψ dissociation. However, a quark can interact with the Ψ only via gluon exchange. Within the spirit of the quasiparticle model, the process labelled (b) in the figure is effectively already included in the definition of the temperature dependent gluon mass (remember that the quasiparticles are non-interacting among themselves on thermal length scales). Computing both contributions would cause an erroneous double counting. In other words, Ψ s only see quasiparticle gluons in the plasma. This is basically the same reasoning used in chapter 4.2.1 to calculate partonic dilepton rates, and to stay consistent, we employ it also in the present context.

Concentrating now on the process labelled (a) in figure 5.3, we come to the problem of computing a cross section involving a relativistic bound state, which is non-trivial. In the present case we can argue that the $c\bar{c}$ system is to a first approximation non-relativistic, greatly simplifying the treatment. As put forward originally by Bhanot and Peskin [145, 146], the lowest lying levels of a quarkonium can be described by

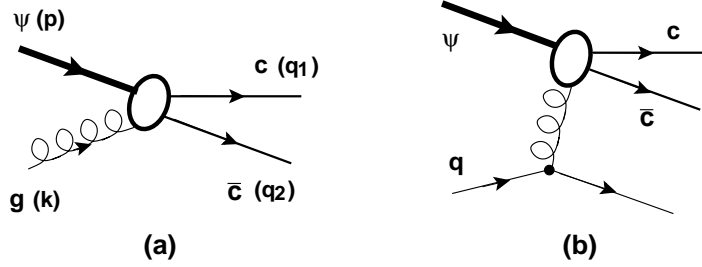


FIGURE 5.3: Diagrams contributing to lowest order to Ψ dissociation. The process involving a gluon quasiparticle (a) exhausts the amplitude since it already takes into account the one involving a quark quasiparticle (b).

the Coulomb part of the interquark potential (2.11), which is justified to some extent by the magnitude of the heavy quark mass. Then, using operator product expansion techniques or more recent non-relativistic factorisation techniques [147], it is possible to obtain the analytic expression

$$\sigma_D(\omega) = \frac{2\pi}{3} \left(\frac{32}{N_c} \right)^2 \frac{1}{\mu^{3/2} \epsilon^{1/2}} \frac{(\omega/\epsilon - 1)^{3/2}}{(\omega/\epsilon)^5} \quad (5.23)$$

for the gluon dissociation process of a heavy quarkonium. It is a function of the gluon energy ω in the rest frame of the quarkonium and contains the threshold energy ϵ and the mass scale μ , related to the heavy quark mass. The threshold energy is connected to the binding energy ϵ_0 by $\epsilon = \epsilon_0 + \epsilon_0^2/(2m_\Psi)$. In the following, the binding energy is taken to be $\epsilon_0 = 780$ MeV and the mass parameter is $\mu_c = 1.95$ GeV, as chosen in [146] to fit the mass values of the first two levels (J/ψ and ψ') of the charmonium system.

We now consider the possibility of $c\bar{c}$ coalescence in the QGP, a method for Ψ formation which has been recently considered by a number of authors [148]. The number of charmed quarks produced in a AB collision can be large, and the chance that a c and a \bar{c} quark find each other close in phase space can therefore become significant. Since charm quarks do not thermalise, they can be considered free streaming after production, which leads to a one-to-one correspondence of space-time and ordinary rapidity. Their interaction probability is then mainly determined by the width of the Ψ wave function in momentum space. This has not been taken into account consistently yet. For the moment, we take as an upper limit on the correlation interval the rapidity spread of the fireball immediately after thermalisation, when all hard processes should have ceased to be effective. Using the cross section calculated above for the Ψ dissociation cross section by gluons, we can apply detailed balance to the reaction $\Psi g \leftrightarrow c\bar{c}$. In the zero momentum frame, flux factors are identical for the direct and reverse processes, and simple kinematics yield the relation

$$\sigma_F(s) = \sigma_D(s) \frac{4}{3} \frac{(s - m_\Psi^2)^2}{s(s - 4m_c^2)}. \quad (5.24)$$

In the latter equation the factor $4/3$ arises by counting the number of degrees of freedom (spin and colour factors) in the two different channels.

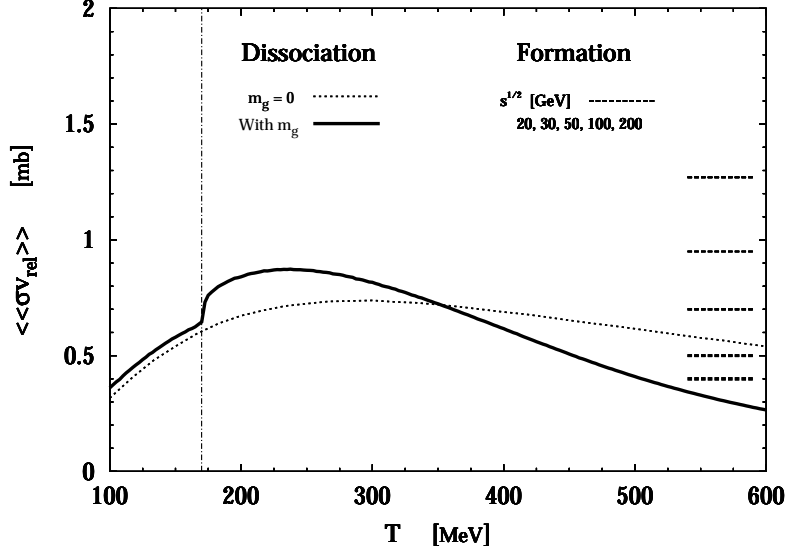


FIGURE 5.4: Dissociation and formation cross sections after averaging with momentum distributions according to eq.(5.19). These are used to construct the solution to the kinetic equation as given by (5.22).

Coming now to the case of hadronic dissociation, we could, in principle, use one of the many approaches which have been developed [142, 149]. However, since typical hadronic cross sections are comparable in magnitude [142, 149]. However, since typical hadronic cross sections are comparable in magnitude with the partonic ones calculated above, the effect of hadronic dissociation becomes negligible because of the much smaller particle number densities in the confined phase. Unless the cross sections become anomalously large, the density that enters the dissociation term (5.21) will be at least an order of magnitude smaller than that during the partonic phase, as evident from figure 5.2 (note the logarithmic scale). Henceforth, since the hadronic phase exists only at moderately low number densities, it has no bearing on Ψ evolution.

Having discussed how formation and dissociation are realised in terms of cross sections, we now average them with the distributions of the colliding particles, according to eq.(5.19). The results are collected in figure 5.4. Some characteristic features arise: first of all, the magnitude of the dissociation cross section, plotted as a thick continuous line, is close to 1 mb in the temperature range $200 < T < 300$, relevant at SPS energy. Above 300 MeV the cross section starts decreasing, since the average relative momenta between Ψ s and gluons are growing. For comparison the result obtained with a gluon mass $m_g = 0$ is plotted as a thin dotted line. As one observes, the mass of gluon quasiparticles helps overcoming the dissociation threshold, providing a slightly larger magnitude for the cross section. On the right side of figure 5.4 horizontal dashed lines are plotted. They indicate the values of the averaged formation cross section (that are temperature independent). From thin to thick (top to bottom) they correspond to growing center of mass energy $\sqrt{s} = 20$ (SPS), 30, 50, 100, 200 (RHIC) GeV of the heavy ion collision.

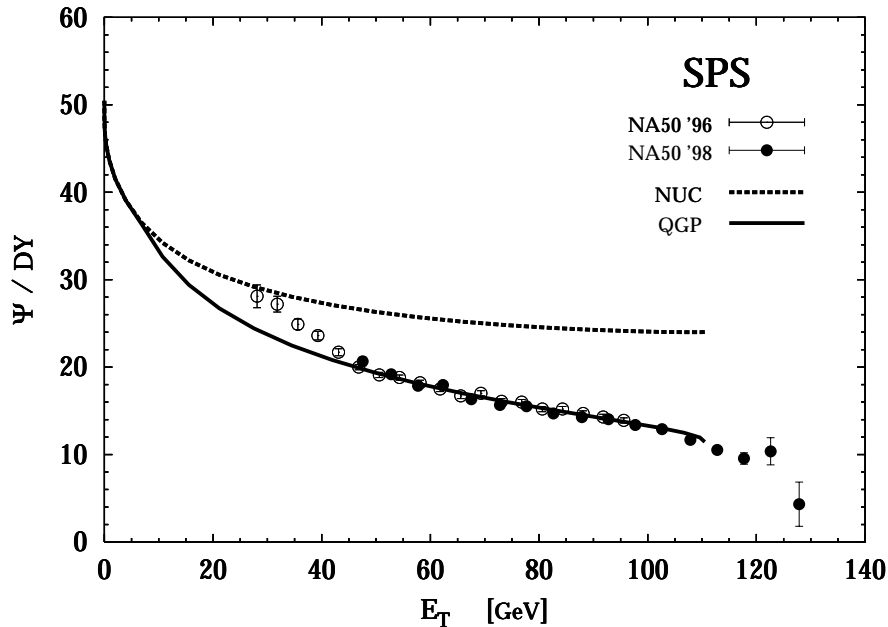


FIGURE 5.5: Result at SPS energy for the ratio Ψ/DY as function of the transverse energy. The dashed curve includes only nuclear effects, while the full line is the complete result including gluon dissociation (and negligible formation).

5.4.3 Results

Assembling all elements of the calculation as discussed in the previous sections, we now make contact with experiment. We start from the case of Pb+Pb collision at $\sqrt{s} = 17.4$ GeV ($E_{\text{lab}} = 158$ GeV) and use the solution of the kinetic equation given in (5.22), converting the impact parameter dependence of the solution into a dependence on the total transverse energy E_T . In this way we arrive at the results plotted in figure 5.5. The agreement with data is quite remarkable and deserves some detailed comments. Apparently, all curves end at $E_T \simeq 110$ GeV, which corresponds to zero impact parameter, $b = 0$. To go beyond this point it is necessary to include effects of fluctuations, which are quite straightforward to address [151]. Second, the result shows that formation at this energy is totally negligible, while suppression is caused exclusively by collision with quasiparticle gluons.

It is worth stressing again that a purely hadronic dissociation of Ψ is ruled out. This is not a consequence of small cross sections, but rather of a hadronic number density that is more than an order of magnitude lower than the partonic one. At T_c we find $n_h \simeq 0.5 \text{ fm}^{-3}$, at freeze-out the density goes down another order of magnitude to 0.05 fm^{-3} , as visible in figure 5.2. Apparently, the model fails to describe the data in the region $E_T = 10 - 50$ GeV. Since this energy range corresponds to very peripheral collisions, it is clear that the assumption of (rapid) thermalisation that lies at the heart of our model is not valid anymore for system sizes of a few nucleons only. As soon as the system size becomes large enough to justify a thermal description, we indeed find very nice agreement with the data, stressing again that we did not tune the fireball or a cross section to arrive at the shown curves.

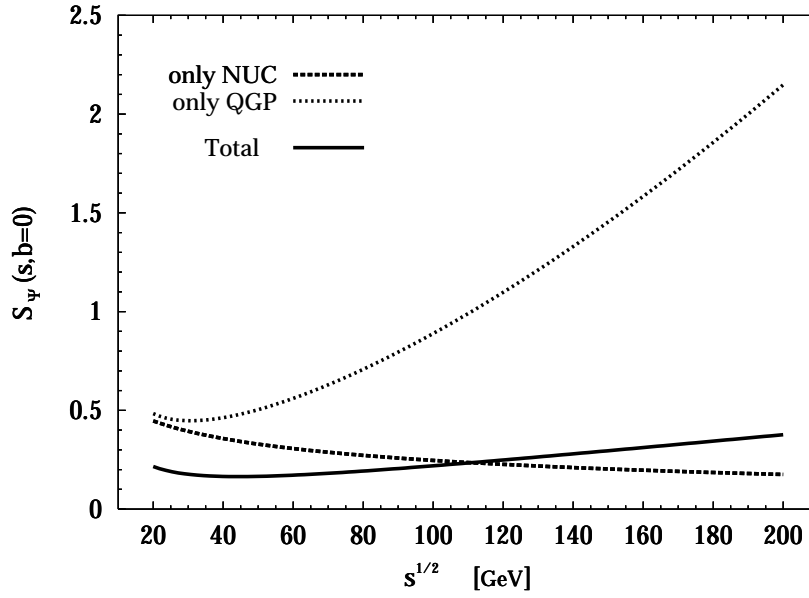


FIGURE 5.6: Suppression factor S for Ψ as function of the collision energy. The dashed curve indicates suppression due to nuclear effects alone, the dotted line shows the effect of the QGP with enhancement ($S_\Psi > 1$) starting at $\sqrt{s} > 100$ GeV. The continuous line is the full result. Since nuclear suppression is much stronger than formation, the net effect is still $S < 1$.

As we now increase the collision energy, staying at $b = 0$, we observe an interesting feature. Since the amount of charmed quarks grows substantially with increasing beam energy, we expect that the formation of Ψ s via $c\bar{c}$ coalescence will eventually exceed the primordial production. Indications of the onset of this mechanism clearly appear in our calculations: figure 5.6 shows a rise of the amount of secondary Ψ s (dotted curve). On the other hand, nuclear effects at high energy will further reduce the amount of primordial Ψ s as compared to the SPS case. The net effect is a slowly rising suppression function $S(\sqrt{s})$, but even at RHIC energy $S(200 \text{ AGeV}) < 1$.

We can also examine the centrality dependence of the suppression for central RHIC collisions. For this purpose we plot in figure 5.7 the suppression factor

$$S_\Psi(b) = \frac{N_\Psi^y(b)|_{AB}}{T_{AB}(b) N_\Psi^y|_{pp}} \quad (5.25)$$

as function of the number of participants. It clearly becomes 1 for very peripheral collisions, steeply drops due to dissociation in the QGP and starts rising again for sufficiently central events because of $c\bar{c}$ coalescence. In accord with figure 5.6, we do not find a net enhancement of Ψ , but this result needs to be confirmed by more accurate calculations since the RHIC fireball is presently not characterised by the same data quality as the SPS one. In addition, shadowing effects might be more pronounced, modifying the initial conditions for the rate equations (initial number of charm), which in turn influences the coalescence rate. It is encouraging, though, that first results of the PHENIX experiment at RHIC indicate no net enhancement, either [152].

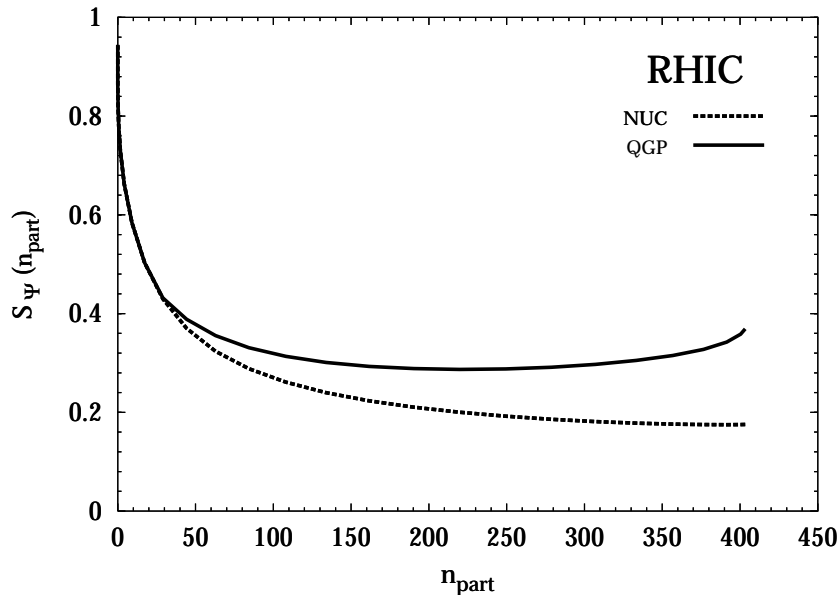


FIGURE 5.7: Survival probability of Ψ at full RHIC energy as a function of centrality by means of the number of participants. The dashed curve includes only nuclear effects, while the full line is the complete result including gluon dissociation and $c\bar{c}$ coalescence.

5.5 Intermediate summary

In this chapter, we have calculated Ψ production from an expanding fireball over a wide range of centralities and beam energies, from SPS in Pb(158 AGeV)+Pb collisions to RHIC at $\sqrt{s} = 200$ AGeV. Consistently employing the confinement quasiparticle developed in chapter 3 and the fireball of chapter 4, we set up a Boltzmann equation with a collision term containing both gain and loss terms. At SPS energy, we were able to describe the suppression data very well, without the need to invoke hadronic comovers. These results support the hypothesis that the QGP is actually already produced in Pb+Pb collisions at the CERN/SPS. It is important to note that, within our outlined approach, a purely hadronic framework would not be successful in describing existing data, as in the dilepton case. Moreover, since the hadronic phase exists only at moderately low number densities, it has no bearing on Ψ evolution. We also considered extrapolations up to RHIC energies where, despite the more extreme conditions as compared to SPS, a sizable fraction of Ψ still survives. Although a clear trend towards more copious Ψ production in AB collisions was found, no significant net enhancement is present in the end, which seems to be in accord with first RHIC data. We stress once more that, in contrast to previous approaches, we have eliminated the medium evolution as an adjustable parameter in the Ψ description by fixing it to hadronic observables and lattice data.

Despite the success of the model, several improvements are desirable. For instance, we have neglected the effect of the static Debye screening in Ψ binding. A treatment of both this feature and collisions, as discussed here, would be a further significant step forward in understanding charmonium properties in hot and dense matter. Moreover, a more constrained description of the expanding fireball at RHIC is needed that is feasible with improved data (analysis). Finally, more has to be done to describe

the initial conditions for charm and Ψ evolution, taking into account the details of produced spectra and providing a better description of nuclear effects.

6 Screening at Finite Temperature

In the last chapters, we have successfully applied the confinement quasiparticle model to the description of two QGP signatures, and all observations are consistent with the formation of a QGP in URHIC. To round off this work, we now shift our scope away from experiments towards a more conceptual problem: asymptotic freedom lies at the heart of the QGP, as mentioned several times, but it has never been explicitly derived at high temperature in a concise manner. This final chapter will deal with the calculation of a running coupling constant at very high temperatures in QCD (and also in QED), ultimately justifying the phenomenological *ansatz* of Collins and Perry [1] put forward in 1975. Instead of a loop expansion, we evaluate the energy shift of the vacuum to leading order in the coupling constant after applying an external (chromo)magnetic field H , extending the approach of [153, 154] to finite temperature. From that, we extract an effective, temperature- and scale-dependent coupling constant $\alpha_{\text{eff}}(H, T)$. QCD with a magnetic background field at finite temperature has been studied in a number of works [155]. In contrast to previous approaches, we lay out a less technical calculation of charge screening without reference to propagators or self-energies, resorting to entities that have an immediate physical interpretation (energy densities and susceptibilities). We also explain how the HTL results can be recovered from our approach. Eventually, instead of applying the somewhat opaque and heavy machinery of Bessel and hypergeometric functions, as commonly done, we use simple integral expansion techniques to obtain a transparent result where explicitly all contributions to order g^2 are contained in. The main parts of this chapter have been published in [156].

6.1 Thermal screening

In quantum field theory, fluctuations of the vacuum give rise to the production of pair quanta which tend to screen (or antiscreen) the charge of a heavy test particle. If one perturbatively calculates the non-relativistic potential $V(r)$ between two unlike static charges, say, in QED, the usual Coulomb-like behaviour is modified by the photon self-energy $\Pi(K^2)$ such that

$$V(r) = \int \frac{d^3k}{(2\pi)^3} e^{i\vec{k}\cdot\vec{r}} \frac{-e^2}{k^2 + \Pi(K^2 = -k^2)}, \quad (6.1)$$

where $k = |\vec{k}|$ and $K = (k^0, \vec{k})$. Inserting the text-book result for $\Pi(K^2)$ [157] and expanding for small distances $k^2 \gg m_e^2$, the quantum fluctuations lead to an effective coupling constant

$$\alpha_{\text{eff}}(k) = \frac{\alpha}{1 - \frac{\alpha}{3\pi} \log\left(\frac{k^2}{\Lambda^2}\right)}, \quad (6.2)$$

where $\Lambda = \exp(5/3)m_e$ is a scale related to the electron mass m_e . This is, of course, the familiar result of the running coupling in QED which is commonly obtained using renormalisation group methods. In [153, 154], it has been shown that the running of a

coupling constant at $T = 0$ can be understood in physical terms by the polarisability of the vacuum. The effects of quantum fluctuations can be incorporated to a certain extent in a scale dependent dielectric permittivity ϵ that defines an effective charge

$$\alpha_{\text{eff}} = \frac{\alpha}{\epsilon}. \quad (6.3)$$

In vacuum, Lorentz invariance dictates that

$$\mu\epsilon = 1, \quad (6.4)$$

where μ is the magnetic permeability. Calculating $\mu(k)$ at the momentum scale k and extracting the leading logarithmic contribution, one finally recovers the familiar expressions for the running couplings in QED, eq.(6.2), and QCD, eq.(2.10), as we will recapitulate in section 6.3. Then, asymptotic freedom can be interpreted in terms of a paramagnetic ground state.

Perturbatively, the quantity that enters the Fourier transform of the potential at finite temperature is the static limit of the longitudinal gauge boson self-energy $\Pi_L(k^0, k; T)$ [8]:

$$V(r, T) = \int \frac{d^3k}{(2\pi)^3} e^{i\vec{k}\cdot\vec{r}} \frac{-e^2}{k^2 + \Pi_L(0, k; T)}. \quad (6.5)$$

Equivalently, one can define a dielectric permittivity by [158]

$$\epsilon(k, T) = 1 + \frac{\Pi_L(0, k, T)}{k^2}. \quad (6.6)$$

The perturbative one-loop thermal contribution to Π_L has been calculated long ago as [159]:

$$\Pi_L(0, k, T) = \frac{e^2 T^2}{3} \equiv (m_D^e)^2 \quad \text{for QED}, \quad (6.7)$$

and

$$\Pi_L(0, k, T) = \left(N_c + \frac{N_f}{2} \right) \frac{g^2 T^2}{3} \equiv (m_D^c)^2 \quad \text{for QCD}, \quad (6.8)$$

which defines screening masses m_D that also follow from eq.(B.7). Since the static limits of the self-energies are momentum-independent, the poles of the expression in (6.5) are simply the gauge invariant Debye masses m_D defined in eqs.(6.7) and (6.8) and lead to an exponential damping of the potential $V(r) \sim \exp(-m_D r)/r$, as already mentioned in chapter 5. In particular, this form of Π_L has the consequence that gluons *screen* the strong interaction, in contrast to the zero temperature case, over long distances. However, the formula for the running QCD coupling constant (2.36), commonly used in thermal perturbative calculations, assumes that typical momentum transfers are of the order of the temperature, hence

$$\alpha_s(T) \sim \frac{1}{\beta_0 \log(T)}. \quad (6.9)$$

In this expression, gluons therefore retain their *antiscreening* property, reflecting the ultraviolet sector of the theory. The transition to Debye screening is not obvious.

6.2 The Debye mass on the lattice

In abelian theories like QED, the concept of the Debye mass is well understood: since the electromagnetic current j_μ^{em} is a gauge-invariant quantity, the Debye mass can be

extracted from the two-point correlation function of j_0^{em} , i.e. from $\Pi_{00} = \Pi_L$ (see above). This is not the case in QCD, which makes the very definition of a Debye mass conceptually difficult. Due to the nonlinear coupling of the gluons, relation (6.6) remains valid only within certain gauges (like the temporal axial gauge) [9]. Finally, the presence of massless gluons in non-abelian theories prevents a perturbative evaluation of the Debye mass beyond next-to-leading (NLO) order [160]:

$$m_D^{(2)}(T) = m_D^{(1)} + \frac{N_c g^2 T}{4\pi} \log\left(\frac{m_D^{(1)}}{g^2 T}\right) + \mathcal{C}_N g^2 T, \quad (6.10)$$

with the leading order (LO) result $m_D^{(1)}$ given by (6.8). Here, the coefficient \mathcal{C}_N is a non-perturbative number that depends on N_c only. It arises from the *ad hoc* removal of infrared loop singularities that are associated with the masslessness of magnetic gluons. In perturbation theory, the static limit of the transverse self-energy Π_T vanishes, as apparent from eq.(B.8), and this feature is expected to persist even after resummation. Hence the perturbative screening mass $m_M(T)$ is identically zero, which makes certain loop integrals, together with the infrared behaviour of the Bose distribution function, diverge.

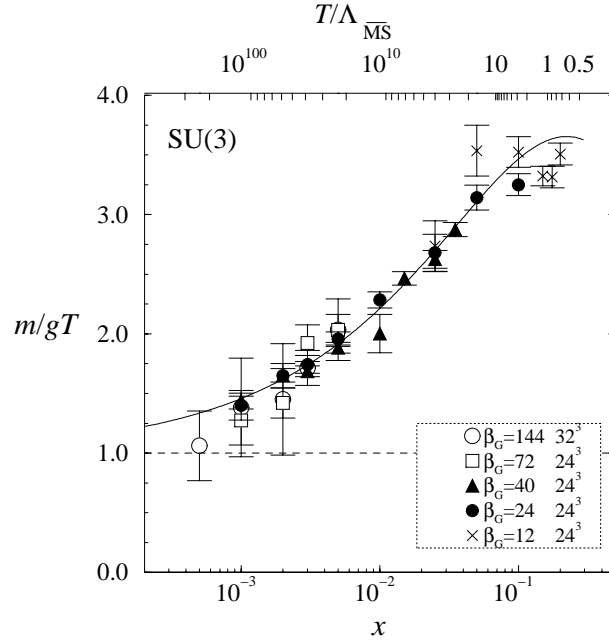


FIGURE 6.1: The gauge-invariant ratio $m_D^{\text{lat}}/(gT)$ for SU(3) [162] as a function of $T/\Lambda_{\overline{MS}} \simeq T/T_c$ (upper x -axis). m_D^{lat} is the Debye mass measured on lattices with varying lattice spacing $\beta_G \sim 1/a$ and spatial extent, gT the LO perturbative result.

However, there are arguments that the magnetic gluons acquire a screening mass m_M non-perturbatively. Non-abelian gauge theories allow for monopole-like magnetic field configurations not accessible in an expansion in g . Thermally excited monopole-antimonopole pairs will therefore screen magnetostatic fields, as electric charges screen electrostatic fields. From dimensional arguments it is expected that m_M is proportional to the mass gap in three-dimensional Yang-Mills theories and thus of the form $m_M = \mathcal{C}' g^2 T$ [161]. This reasoning also finds support from the lattice, as we will show

below. Using that magnetic mass as an infrared regulator, eq.(6.10) can be obtained at the expense of introducing the unknown, non-perturbative constant \mathcal{C}' that is related in a unique fashion to \mathcal{C}_N . Clearly, close to T_c we do not believe eq.(6.10) to be a good representation of the Debye mass since the coupling constant is large and critical behaviour is dominant, cf. section 3.3.4. Only for some $T \gg T_c$ the coupling will become sufficiently small.

In ref.[162], a Debye mass was extracted from the large distance exponential fall-off of correlators of gauge-invariant operators $\mathcal{O}(t, \vec{x})$

$$\langle \mathcal{O}(\tau, \vec{x}) \mathcal{O}(\tau, 0) \rangle \sim |\vec{x}|^\beta \exp(-m_D(T)|\vec{x}|).$$

This correlator was subsequently evaluated with Monte Carlo methods in a dimensionally reduced 3D effective theory, put on a lattice. Figure 6.1 shows the result for $N_c = 3$ and $N_f = 0$. The LO perturbative¹ result is $m_D^{(1)}(T) = g(T)T$, which is obviously only valid for ridiculously high temperatures $T \gtrsim 10^{100} T_c$. Below that temperature (which is anyway far above the Planck scale), the measured mass is much larger, by a factor 2 – 3, which can be traced back to the large non-perturbative correction in (6.10): here, $\mathcal{C}_3 = 2.46 \pm 0.15$. In the range $T_c < T \lesssim 100 T_c$, the measured Debye mass m_D^{lat} stays rather constant at $\approx 3.3m_D^{(1)}(T)$.

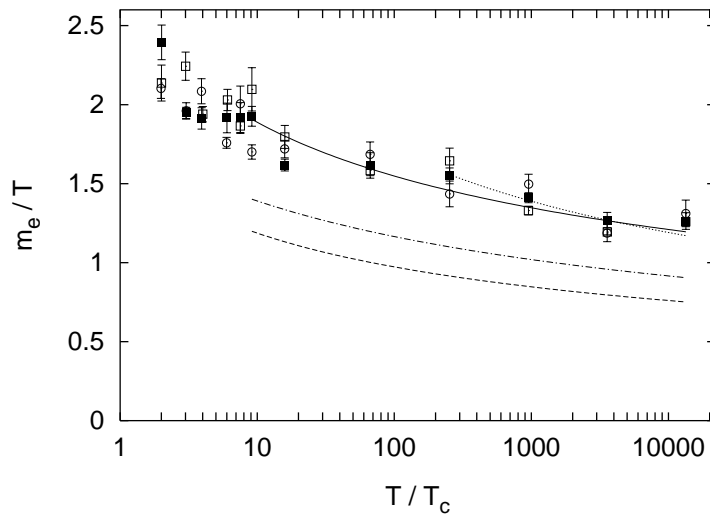


FIGURE 6.2: Electric screening mass (m_e) over temperature in SU(2) as a function of T/T_c [163]. The different data points correspond to various lattice sizes and lattice actions. The dashed line shows the LO result $\sqrt{2/3}g(T)T$, the dot-dashed line the NLO result (6.10), with $m_M(T)$ (or equivalently \mathcal{C}_2) determined within the same simulation.

In ref.[163], the finite temperature gluon propagator was calculated in SU(2) lattice gauge theory, using standard Wilson and improved Symanzik actions. From the long-distance behaviour of correlation functions of temporal and spatial components of the gauge fields electric and magnetic screening masses were extracted, cf. eq.(3.20). The result for m_D^{lat} is displayed as the data points in figure 6.2. As above, the measured

¹Here and in the following, the perturbative $g(T)$ is usually derived from the zero temperature running coupling constant (2.10), $\alpha_s(\mu)$, taking as the scale μ the lowest non-vanishing bosonic Matsubara frequency $2\pi T$.

value is again larger than the LO perturbative result $m_D^{(1)}(T) = \sqrt{2/3}g(T)T$ (dashed line) for temperatures up to $10^4 T_c$, this time by about 60%. Even the NLO result (dot-dashed line), although an improvement, still falls short of describing the lattice data.

Apparently, the temperature dependence of the Debye mass is nevertheless well described by a term of the form $\mathcal{C}g(T)T$. In figure 6.3, fits of the constant \mathcal{C} have been performed, and the data are very well described by $m_D^{\text{lat}}(T) \simeq \sqrt{1.7}g(T)T \approx 1.6 m_D^{(1)}$. Extractions of the Debye mass from Polyakov loop correlators (which are related to the interquark potential via eq.(2.49)) find similar values for $m_D^{\text{lat}}(T)$, so this result seems to be rather robust. In addition, figure 6.3 also shows that the magnetic screening mass is indeed non-vanishing and can be well parametrised by $m_M^{\text{lat}}(T) \simeq 0.5g^2(T)T$ (i.e. $\mathcal{C}' \simeq 0.5$), confirming the functional g^2 -dependence put forward above.

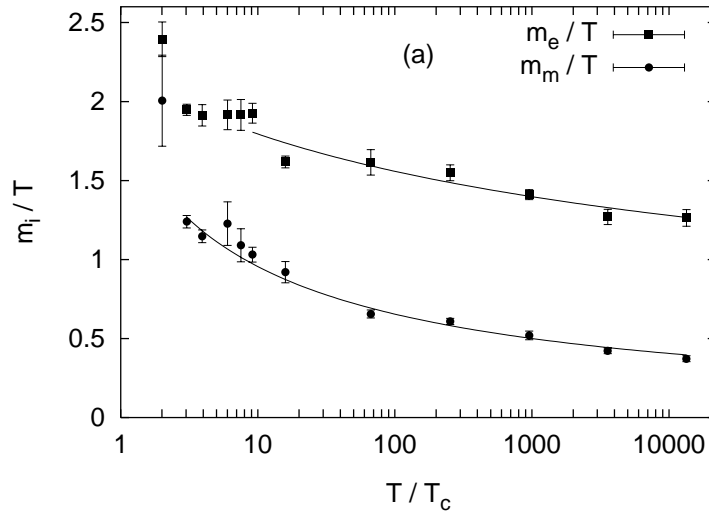


FIGURE 6.3: Electric (m_e) and magnetic (m_m) screening mass over temperature in SU(2) as a function of T/T_c [163]. The simulation was performed on a large lattice of size $32^2 \times 64 \times 8$ with the standard Wilson action. The solid lines show the fits leading to $m_e \simeq \sqrt{1.7}g(T)T$ and $m_m \simeq 0.5g^2(T)T$.

Summarising, all available lattice data seem to suggest that the Debye screening mass runs logarithmically with temperature, $m_D = \mathcal{C}g(T)T$, as expected from asymptotic freedom. However, the numerical coefficient \mathcal{C} does not agree at all with perturbative expectations for $T \lesssim 10^{10}T_c$. The NLO correction (and especially its non-perturbative component arising from the magnetic screening mass) seems to be large, which is not surprising in light of the fact that the coupling $g(T)$ is still of the order of one for all temperatures of interest.

It is nevertheless remarkable that these lattice calculations indicate a clear logarithmic running of $g(T)$ over large distances. So far, this feature has only been motivated phenomenologically [1], but not derived within a consistent theoretical framework. From a conceptual point of view, it is of utmost importance to confirm that assumption (because asymptotic freedom lies at the heart of the QGP), even if its application may not be that useful in actual calculations. In the rest of the final chapter of this thesis,

we present a calculation of the effective running coupling at high temperatures and long wavelengths, not relying on a Feynman graph expansion, that will exactly take us there.

6.3 The zero temperature case

In this section, we define our notation and briefly review the calculation of refs.[153, 154]. To obtain a scale-dependent magnetic permeability $\mu(H)$, let us look at the change in the energy E of the vacuum when an external magnetic field H is applied:

$$\Delta E = -\frac{1}{2} [4\pi\chi(H)] V H^2 - E_{\text{vac}}, \quad (6.11)$$

where $\mu(H) = 1 + 4\pi\chi(H)$, and $\chi(H)$ is the field-dependent magnetic susceptibility. The expression for the energy in the presence of the field H is completely general since all scales that characterise the “medium” (e.g. $\Lambda_{\text{QCD}}, m_e$) can be combined with H such as to end up in $\chi(H)$. In particular, linear response theory would yield an H -independent susceptibility, whereas in the mean field approximation a $\chi(H)$ may be derived from the implicit equation

$$H_{\text{eff}} = H + 4\pi\chi(H_{\text{eff}})H, \quad (6.12)$$

introducing the effective, local field H_{eff} as the sum of the external and the locally induced field. As soon as the energies at $H = 0$ and finite H are known to some approximation, a field-, or equivalently, scale-dependent $\mu(H)$ can be extracted. Later, the external field $2eH$ is identified with the scale K^2 at which the physical process is probed.

For charged scalar fields, the general expression for the energy spectrum of a single Fourier mode reads

$$E_{n,k}^{\pm} = \omega_k \left(n_k^{\pm} + \frac{1}{2} \right), \quad (6.13)$$

distinguishing between particles (+) and antiparticles (-). The dispersion relation $\omega_k = k$ follows from the positive energy solution of the Klein-Gordon equation for massless, non-interacting particles. At $T = 0$, the occupation number n_k^{\pm} for the ground state is zero. Summing over particle and antiparticle states, we recover the familiar divergent zero-point vacuum energy $E_0 = \sum_k \omega_k$. For massless spin- $\frac{1}{2}$ fermions, the energy without an external field becomes

$$E_0^f = -2 \sum_k \omega_k. \quad (6.14)$$

The factor 2 arises from the spin summation, the factor -1 stems from the anti-commutation relation fermionic annihilation and creation operators obey. In the presence of the magnetic field H , we substitute $\partial_\mu \rightarrow D_\mu = \partial_\mu - igqA_\mu$, where q is the charge of the (anti)particle in units of the coupling g . Choosing the orientation of the H -field along the z -axis, we construct a vector potential as $A_\mu = (0, 0, x_1 H, 0)$. This choice for A_μ obeys $\partial_\mu A^\mu = 0$. In the following, we treat QED and QCD in parallel and define $e = qg$. We have to solve for the energy spectrum of $i\mathcal{D}\psi(x) = 0$, which is basically a relativistic version of the Landau theory for the diamagnetic properties of an electron gas. The solution for the energy of a single Fourier mode becomes

$$\bar{\omega}_{n,k_3,s_3} = \sqrt{k_3^2 + 2eH(n + 1/2 + s_3)}. \quad (6.15)$$

In addition, the x_1 space variable is shifted by $-k_2/(eH)$. Note that the energy depends only on two quantum numbers. The third is “hidden” in the mentioned x_1 shift. Here $s_3 = \pm\frac{1}{2}$, the z -component of the spin. The Hs_3 term clearly shows the coupling of the spin to the external field, and hence, if the spin of the fermion is antiparallel to the H -field, the energy is lowered. For QCD, there is also an implicit sum over the colour charges q hidden in $e = gq$. Finally, for a vector gauge boson the H -independent energy is the same as for a scalar field, except that there is an additional factor of 2 counting the transverse spin degrees of freedom:

$$E_0^g = 2 \sum_k \omega_k. \quad (6.16)$$

The sum over colour degrees of freedom yields an additional multiplicative factor of $N_c^2 - 1$. In presence of the magnetic field that couples to the gauge boson (hence QED is not relevant here), we separate the field A_μ into the classical background part A_μ^b and the fluctuating quantum part A_μ^q . The equations of motion become $D_\mu \mathcal{G}^{\mu\nu} = 0$, where $\mathcal{G}^{\mu\nu}$ is the gluon field strength tensor (2.2). With a suitable choice of background gauge,

$$\partial^\mu A_\mu^q + [A_\mu^b, A^{\mu,q}] = 0, \quad (6.17)$$

the energy for the two physical degrees of freedom of A_μ can be written as

$$\bar{\omega}_{n,k_3,s_3} = \sqrt{k_3^2 + 2eH(n + 1/2 + s_3)}, \quad (6.18)$$

the same as in the fermionic case, but now with $s_3 = \pm 1$. Again, summation over the colour charges is implicitly assumed.

We want to extract the leading $\log(H)$ contribution to the energy shift induced by the external field. With the total spin s of the particle considered and $i = f, g$:

$$\Delta E^i = (-1)^{2s} \left(\sum_{n,k_2,k_3,s_3} \bar{\omega}_{n,k_3,s_3}^i - \sum_{k_1,k_2,k_3,s_3} \omega_k \right), \quad \text{where} \quad (6.19)$$

$$\bar{\omega}_{n,k_3,s_3}^i = \sqrt{k_3^2 + 2eH(n + 1/2 + s_3)}. \quad (6.20)$$

Introducing a quantisation volume $V = L^3$, we replace the sum over k_2 and k_3 by an integral weighted with the density of states. Taking into account that the x_1 variable was shifted, k_2 is restricted to $0 \leq k_2 \leq LeH$. Then,

$$\sum_{k_2,k_3} \rightarrow \frac{L}{2\pi} \int dk_3 \frac{L}{2\pi} (eH \cdot L) = \frac{V}{4\pi^2} (eH) \int dk_3. \quad (6.21)$$

To regularise the divergence, we will use a UV cut-off Λ such that $0 \leq n \leq \frac{\Lambda^2}{2eH} = n_\Lambda$ and $k_3^2 \leq \Lambda^2$. The first idea would be to replace the sum over n by an integral. However, if we perform the shift $n' = 2eHn$, we find that the integral would be independent of H to leading order. That is, we would have recovered the vacuum result, in the absence of the field H , that has to be subtracted anyway in the end. So what we need is the *correction* to the replacement of a sum with an integral. Such a correction term suitable for our case here is provided by a specific Euler sum rule

$$\sum_{n=n_1}^{n_2} f(n + 1/2) = \int_{n_1}^{n_2} f(x) dx - \frac{1}{24} f'(x) \Big|_{n_1}^{n_2}.$$

We may now re-define the energy shift as

$$\Delta E^i = (-1)^{2s} \sum_{s_3} \left\{ \sum_{n=0}^{n_\Lambda} f(n+1/2+s_3) - \int_0^{n_\Lambda} dn f(n+1/2+s_3) \right\},$$

where

$$f(x) = \frac{V}{2\pi^2} (eH) \int_0^\Lambda dk_3 \sqrt{k_3^2 + 2eHx}.$$

Since we are not interested in the soft modes of the order of eH (the leading logarithmic behaviour is dominated by the UV behaviour of the theory), we split the sum into two pieces ($N \ll n_\Lambda$)

$$\sum_{n=0}^{n_\Lambda} = \sum_{n=0}^N + \sum_{n=N}^{n_\Lambda}.$$

Let us treat s_3 formally as a continuous variable. Taylor expanding in s_3 (since $n \geq N \gg s_3$), we are left with

$$\begin{aligned} \Delta E^i &= (-1)^{2s} \sum_{s_3} \sum_{n=N}^{n_\Lambda} \left(f(n+1/2) - s_3 f'(n+1/2) + \frac{s_3^2}{2} f''(n+1/2) + \dots \right) \\ &+ \Phi(eH, N). \end{aligned} \quad (6.22)$$

Now $\Phi(eH, N)$, which represents the contributions from soft modes only, does not depend on Λ . It is thus proportional to $(eH)^2$ for dimensional reasons, a small non-leading logarithmic contribution, and may be safely neglected. The linear term in s_3 vanishes upon summation, and re-substituting $e = gq$, we find

$$\Delta E^i = -\frac{1}{2} V (gH)^2 \left[\frac{q^2 (-1)^{2s}}{2\pi^2} \sum_{s_3} \left(\frac{s_3^2}{2} - \frac{1}{24} \right) \log \left(\frac{\Lambda^2}{2eH} \right) \right]. \quad (6.23)$$

The sum over a $SU(N_c)$ multiplet of the squared charges q^2 is $N_f/2$ for the fundamental representation (N_f quark flavours) and $N_c/2$ for the adjoint representation (the gluons) [154]. For QCD, the susceptibility therefore becomes

$$4\pi\chi \rightarrow -g^2 \frac{11N_c - 2N_f}{48\pi^2} \log \left(\frac{2eH}{\Lambda^2} \right), \quad (6.24)$$

which reproduces the leading expression obtained by renormalisation group calculations, eq.(2.10), if we identify $2eH = K^2$. Note that the combination eH is a renormalisation group invariant (otherwise also the covariant derivative (2.3) would be non-invariant, which would render gauge invariance a mess) and Lorentz invariant since $\mathcal{G}_{\mu\nu} \mathcal{G}^{\mu\nu} = H^2$. For QED, the sum over the charge(s) is simply 1, so we obtain

$$4\pi\chi \rightarrow + \frac{e^2}{12\pi^2} \log \left(\frac{2eH}{\Lambda^2} \right),$$

again in accordance with the renormalisation group result, eq.(6.2). Having outlined the calculation of [153, 154], we now switch on temperature.

6.4 The temperature-dependent part

At finite temperature T , the occupation number n_k^\pm appearing in eq.(6.13) does not vanish anymore for the thermal ground state, instead $n_k = (\exp(\beta\omega_k) - 1)^{-1} = f_B$, the

usual Bose-Einstein distribution function. For fermions, $n_k = (\exp(\beta\omega_k) + 1)^{-1} = f_D$, the Fermi-Dirac distribution function. Thus, when summing over the infinitely many degrees of freedom, we find for the total vacuum energy² of a charged scalar field

$$E_0^s = \sum_k \omega_k (1 + 2f_B(\omega_k)). \quad (6.25)$$

The result clearly separates into the divergent ground state energy already treated and a finite, T -dependent part. In the case of a finite magnetic field H , the higher energy modes (6.20) are occupied with their respective thermal probabilities, and we can write ($i = f, g$):

$$\Delta E^i = E^i - E_0^i, \quad (6.26)$$

$$E^i = \sum_{n,k_2,k_3,s_3} \bar{\omega}_{n,k_3,s_3}^i \left[(-1)^{2s} + \frac{2}{\exp(\beta\bar{\omega}_{n,k_2,s_3}^i) - (-1)^{2s}} \right], \quad (6.27)$$

$$E_0^i = \sum_{k_1,k_2,k_3,s_3} \omega_k \left[(-1)^{2s} + \frac{2}{\exp(\beta\omega_k) - (-1)^{2s}} \right]. \quad (6.28)$$

Again, we need to extract the leading thermal contribution to $\mu(k)$. However, at finite temperature, relation (6.4) does not hold any more. One could imagine to continue with

$$\mu(k)\epsilon(k) = n(k)^2, \quad (6.29)$$

where $n(k)$ is the momentum-dependent index of refraction. This quantity is related to the photon or gluon phase velocity by $v_p = 1/n$, and v_p could be extracted from the (full) dispersion relation of the corresponding gauge boson since $v_p = \omega_k/k$. However, eq.(6.29) holds only for "on-shell" propagating gauge bosons. Since Lorenz invariance is formally broken by the presence of the heat bath, μ and ϵ become functions of k^0 and k , and eq.(6.29) reads, more explicitly, $\mu(\omega_k, k)\epsilon(\omega_k, k) = n(k)^2$. Using the explicit expressions for $\mu(\omega, k)$ and $\epsilon(\omega, k)$ as listed e.g. in [158], and the dispersion relation for the gluons, one indeed recovers in HTL perturbation theory this identity.

Here, however, we consider an off-shell external field, so a relation between $\mu(0, k)$ and $\epsilon(0, k)$ is required that can be obtained by the following argument: the total energy density of the system can be written as the sum of the field and the induced medium energy density:

$$\mathcal{E}_{\text{tot}} = \frac{1}{2}H^2 + \frac{1}{V} \sum_i \Delta E^i. \quad (6.30)$$

With the effective local field H_{eff} defined in (6.12), we rewrite \mathcal{E} as

$$\mathcal{E}_{\text{tot}} = \frac{1}{2}H_{\text{eff}}^2 = \frac{1}{2} \frac{(eH)^2}{e_{\text{eff}}^2}.$$

In the last step we made use of the fact that eH has to be a renormalisation group invariant, so $eH = e_{\text{eff}}H_{\text{eff}}$. The effective coupling constant is now defined by [154, 155]

$$\frac{1}{e_{\text{eff}}^2} \equiv 2 \frac{\partial \mathcal{E}_{\text{tot}}}{\partial (eH)^2} = \frac{1}{e^2} [1 - 4\pi\chi(2eH, T)],$$

²A short note on notation: in the following, we will split the total energy in two pieces: $E^i = E_{\text{vac}}^i + E_{\text{th}}^i(T)$. E_{vac}^i is referred to as the temperature-independent "ground state energy", whereas $E_{\text{th}}^i(T)$ will be called "thermal vacuum energy". That notation is not entirely satisfactory since the vacuum is not empty anymore at finite temperature, it is filled by thermal excitations. "Vacuum" means in this context absence of external particles.

using (6.11) and (6.30), similar to the $T = 0$ case. Replacing $2eH$ by k^2 , as at $T = 0$, our master formula hence reads

$$\alpha_{\text{eff}}(k, T) = \frac{\alpha}{\epsilon(k, T)} = \frac{\alpha}{1 - 4\pi\chi(k, T)}. \quad (6.31)$$

The thermal piece of eq.(6.27) can be compactly re-written as

$$\begin{aligned} \frac{E_{th}(T, b, s, s_3)}{VT^4} &= \\ &= \frac{b}{2\pi^2} \sum_{s_3} \sum_{n=0}^{\infty} \int_0^{\infty} dx \frac{\sqrt{x^2 + b(n + 1/2 + s_3)}}{\exp\left(\sqrt{x^2 + b(n + 1/2 + s_3)}\right) - (-1)^{2s}}, \end{aligned} \quad (6.32)$$

where x is dimensionless and

$$b = \frac{2eH}{T^2}$$

is a measure for the ratio of quantum and thermal effects. We consider the high-temperature limit $b \ll 1$ in the rest of the chapter.

6.4.1 A first (incomplete) approximation

The sum appearing in expression (6.32) obviously cannot be evaluated exactly. It is instructive to work out the first intuitive approximation to the sum although we will show in the next section that it is too crude.

Consider the fermionic part. Note that the factor $b(n + 1/2 + s_3)$ plays the role of a mass term in the integral in eq.(6.32), so the contribution of the terms in the sum becomes exponentially suppressed as n increases. In contrast to the $T = 0$ case we are therefore interested in the behaviour of the sum at *small* n where the s_3 spin component is not negligible. Thus we cannot apply a Taylor expansion in s_3 , as done in (6.22), but need an exact summation over s_3 . Isolating then the lowest lying Landau mode (LLL) $n = 0, s_3 = -1/2$ and combining the remaining expressions into a single sum, we find

$$\frac{E^f}{VT^4} \equiv \tilde{E}^f = \frac{b}{24} + \frac{b}{\pi^2} \sum_{n=0}^{\infty} \int_0^{\infty} dx \frac{\sqrt{x^2 + b(n+1)}}{\exp\left(\sqrt{x^2 + b(n+1)}\right) + 1}. \quad (6.33)$$

Since $b \ll 1$, the terms in the sum vary slowly with n , so we can again try to trade the sum for an integral over n :

$$\tilde{E}^f = \frac{b}{24} + \frac{2}{\pi^2} \int_0^{\infty} dr \frac{r^2 \sqrt{r^2 + b}}{\exp\left(\sqrt{r^2 + b}\right) + 1}. \quad (6.34)$$

Furthermore neglecting terms of order b in the integral, we obtain

$$E_{(0)}^f = -\frac{1}{2} V H^2 \left[-\frac{(m_D^e)^2}{2eH} \right] + \frac{7}{4} \frac{\pi^2}{15} VT^4 \quad (6.35)$$

for QED with the HTL Debye mass defined in eq.(6.7). These approximations amount to ignoring $\mathcal{O}(e)$ corrections to the single Landau levels and the density of states. The second term in (6.35) is simply the energy $E_0^f(T)$ of a thermally excited, noninteracting massless fermion-antifermion pair, i.e. the thermal energy of the *unperturbed* vacuum

that has to be subtracted anyway, cf. eq.(6.26). That this term arises from the calculation is non-trivial, but absolutely necessary for consistency. We have therefore recovered within our simple framework the perturbative one-loop HTL result from the LLL contribution to the energy of the magnetically perturbed thermal vacuum. The energy difference that enters in (6.11) already yields $4\pi\chi(H, T)$ as the expression in square brackets, and the effective coupling constant reads, following eq.(6.31),

$$\alpha_{\text{eff}}(k, T) = \frac{\alpha}{\epsilon(k, T)} = \frac{\alpha}{1 + \frac{(m_D^\epsilon)^2}{k^2}},$$

as within HTL perturbation theory, cf. (6.6).

For QCD with N_f flavours, we obtain

$$E_{(0)}^f = -\frac{1}{2}VH^2 \left[-\frac{m_{D,f}^2}{2eH} \right] + N_f \frac{7\pi^2}{60} VT^4 \quad (6.36)$$

with the fermionic part of the squared QCD Debye mass (6.8), $m_{D,f}^2 = N_f/6 g^2 T^2$. For the total evaluation of the QCD susceptibility, we need to add the contribution from the gauge bosons. At zero temperature, contributions from “unphysical” gluon states in the calculation of the energy spectrum, eq.(6.18), are exactly cancelled by Fadeev-Popov ghost contributions within the background gauge condition used here. Since we only consider excitations of energy levels that were evaluated at $T = 0$, no ambiguity in counting degrees of freedom arises at finite T and we still work only with physical gluon degrees of freedom with two polarisation states. We proceed in close analogy to the fermionic case: first, we sum over $s_3 = \pm 1$. A subtlety arises since the combination $n = 0$ and $s_3 = -1$ in eq.(6.32), defining the gluonic LLL, gives a negative value under the square root for small x . We will discard this contribution of the LLL in this section³, arguing that an energy difference should be a physical, real quantity with no imaginary part. In section 6.5, we investigate in detail what happens when the LLL is included, and it will turn out that the final result depends crucially on the very nature of the LLL. For now, the sum over n in (6.32) for $s_3 = -1$ starts only at $n = 1$. Isolating again the *new* LLL ($n = 1, s_3 = -1$) contribution to the sum, we are left with

$$\begin{aligned} \frac{E^g}{VT^4} &\equiv \tilde{E}^g = \frac{b}{2\pi^2} \int_0^\infty dx \frac{\sqrt{x^2 + b/2}}{\exp\left(\sqrt{x^2 + b/2}\right) - 1} \\ &+ \frac{b}{\pi^2} \sum_{n=0}^\infty \int_0^\infty dx \frac{\sqrt{x^2 + b(n+3/2)}}{\exp\left(\sqrt{x^2 + b(n+3/2)}\right) - 1}. \end{aligned} \quad (6.37)$$

Replacing the sum by an integration, setting $b = 0$ in the integrals and summing over colour, the result becomes

$$E_{(0)}^g = -\frac{1}{2}VH^2 \left[-\frac{m_{D,g}^2}{2eH} \right] + 2(N_c^2 - 1) \frac{\pi^2}{15} VT^4. \quad (6.38)$$

Again, the last term is the thermal energy $E_0^g(T)$ of the unperturbed $SU(N_c)$ gluon vacuum. The expression in square brackets exactly corresponds to the gluonic part of

³The imaginary part of the LLL is, of course, also present at $T = 0$, and we will discuss its implications in more detail in section 6.5. It played no role in section 6.3, though, because only the behaviour of the series at large n was of importance there.

the squared QCD Debye mass, $m_{D,g}^2 = N_c/3 g^2 T^2$. Putting all pieces together, the effective coupling becomes

$$\alpha_{s,\text{eff}}(k, T) = \frac{\alpha_s}{1 + \frac{(m_D^c)^2}{k^2}},$$

very similar to the QED case. In our model, the HTL (chromo)electric Debye masses therefore appear as the LLL contribution to the energy difference that arises when one probes the thermal vacuum by a (chromo)magnetic field. It is worth noting that, in this approximation, the alignment of an external field always *increases* the thermal energy of the vacuum, regardless of the non-abelian structure of the theory. Therefore $\chi(k, T)$ is always negative and we conclude, using eq.(6.31), that the static potential would become screened by both fermions and by gauge bosons.

6.4.2 A better approximation

However, additional contributions to eqs.(6.35), (6.36) and (6.38) of the *same order in* e^2 arise from two sources. First, the expansion of the integrals (6.34) and (6.37) in b is similar to the high temperature expansion of loop integrals with massive particles in the small quantity m_0/T . Appendix C contains the relevant formulae. Second, the correction to the replacement of the sum by an integral yields terms to order b and b^2 that are provided by the Euler-MacLaurin formula

$$\sum_{n=0}^N f(n) = \int_0^N f(x) dx + \frac{1}{2} [f(N) + f(0)] + \frac{1}{12} [f'(N) - f'(0)] + \dots, \quad (6.39)$$

where the dots denote terms with higher derivatives in $f(n)$. For our purposes, eq.(6.39), taking $N \rightarrow \infty$, is sufficient, as long as $f(x) \in \mathcal{C}^2$ for $x \in [0, N]$. When calculating the thermal contribution to the vacuum energy, we include these correction terms to the integral in the following and expand all integrals in the small parameter b , using the relations presented in appendix C. The summation of all terms to order e^2 then alters the results in (6.36) and (6.38) *qualitatively*. We stress again that, using (6.39), *all* contributions to order e^2 are summed up.

6.4.3 Results for QED

For fermions, we start with eq.(6.33). Defining $\delta^2 = b$, we obtain to order δ^4

$$\begin{aligned} \tilde{E}_{(1)}^f &= \frac{\delta^2}{24} + \frac{2}{\pi^2} \int_0^\infty dr \frac{r^2 \sqrt{r^2 + \delta^2}}{\exp(\sqrt{r^2 + \delta^2}) + 1} + \frac{\delta^2}{2\pi^2} \int_0^\infty dr \frac{\sqrt{r^2 + \delta^2}}{\exp(\sqrt{r^2 + \delta^2}) + 1} \\ &- \frac{\delta^4}{24\pi^2} \int_0^\infty dx \left\{ \frac{1}{\sqrt{x^2 + \delta^2}} - \frac{1}{1 + \exp(-\sqrt{x^2 + \delta^2})} \right\} \frac{1}{\exp(\sqrt{x^2 + \delta^2}) + 1}. \end{aligned} \quad (6.40)$$

Using the functions $f_i(y)$ and $g^+(y)$ defined in appendix C, we re-write

$$\tilde{E}_{(1)}^f = \frac{\delta^2}{24} + \frac{2}{\pi^2} f_5(\delta) + \frac{5\delta^2}{2\pi^2} f_3(\delta) + \frac{\delta^4}{2\pi^2} f_1(\delta) - \frac{\delta^4}{24\pi^2} g^+(\delta). \quad (6.41)$$

Expanding in δ and keeping all terms up to $\mathcal{O}(\delta^4)$, surprisingly all terms of order δ^2 *cancel*, and we are left with

$$\tilde{E}_{(1)}^f = \frac{7\pi^2}{60} + \frac{\delta^4}{96\pi^2} \log(\mathcal{A}_f \delta^2) \quad (6.42)$$

with $\gamma = 0.5772\dots$, the Euler-Mascheroni constant, and the constant $\mathcal{A}_f = \exp(2\gamma - 1)/\pi^2 \simeq 0.12$. The first term is the well-known thermal vacuum energy in the absence of the field H . Since $\delta^2 \ll 1$, the alignment of a magnetic field hence *decreases* the energy of the vacuum at finite temperature, in contrast to the result of the previous section. The susceptibility in QED therefore becomes

$$4\pi\chi(H, T) = -\frac{\alpha}{3\pi} \log\left(\mathcal{A}_f \frac{2eH}{T^2}\right). \quad (6.43)$$

Note that the pre-factor of the logarithm is the same as in the zero-temperature case! Including this pure quantum correction for the QED running coupling, eq.(6.2), all field dependence drops out, and we finally obtain with (6.31)

$$\alpha_{\text{eff}}(k, T) = \frac{\alpha}{1 - \frac{\alpha}{3\pi} \log\left(\frac{T^2}{\Lambda_T^2}\right)} \quad \text{with } \Lambda_T = m_e \frac{e^{\gamma+7/6}}{\pi} \simeq \frac{\Lambda}{3}, \quad (6.44)$$

which is valid to order e^2 and for momenta

$$m_e \ll k \ll T. \quad (6.45)$$

Using the zero-temperature coupling $\alpha_{\text{eff}}(k)$ from eq.(6.2), the effective coupling can, to this order, be rewritten as

$$\alpha_{\text{eff}}(k, T) = \alpha_{\text{eff}}(T) = \alpha_{\text{eff}}(\langle k \rangle \simeq 3 T). \quad (6.46)$$

So the common practice used in perturbation theory to simply take the running of the coupling at zero temperature and set as the scale the thermally averaged momentum scale $\langle k \rangle \simeq 3 T$ does indeed find support from our calculation for QED. Alternatively, one may also take for the relevant energy scale the lowest non-vanishing Matsubara frequency, which becomes πT for fermions.

6.4.4 Results for QCD

For QCD, the fermionic contribution takes a form similar to the QED result,

$$4\pi\chi(H, T)_q = -\frac{g^2 N_f}{24\pi^2} \log\left(\mathcal{A}_f \frac{2eH}{T^2}\right). \quad (6.47)$$

Note that the pre-factor of the logarithm is again the same as at zero temperature. The calculation of the gluonic part of χ runs along the same lines outlined above. Starting with eq.(6.37) and setting $\delta^2 = b/2$, we obtain by use of the functions $h_i(y)$ and $g^-(y)$

$$\begin{aligned} \tilde{E}^g &= \frac{2}{\pi^2} h_5(\sqrt{3}\delta) + \frac{\delta^2}{\pi^2} [7h_3(\sqrt{3}\delta) + h_3(\delta)] \\ &+ \frac{\delta^4}{\pi^2} \left[h_1(\delta) + 3h_1(\sqrt{3}\delta) - \frac{1}{6} g^-(\sqrt{3}\delta) \right]. \end{aligned} \quad (6.48)$$

Expanding, we find that all terms of order δ^3 cancel and the result becomes

$$\tilde{E}^g = \frac{2\pi^2}{15} - \frac{b}{12} - \frac{5b^2}{128\pi^2} \log(\mathcal{A}_g b), \quad (6.49)$$

with the constant $\mathcal{A}_g = \exp(2\gamma - 13/10 + 11/5 \log 3)/(32\pi^2) \simeq 0.03$. Similar to the fermionic part, the alignment of a chromomagnetic field hence always *lowers* the energy

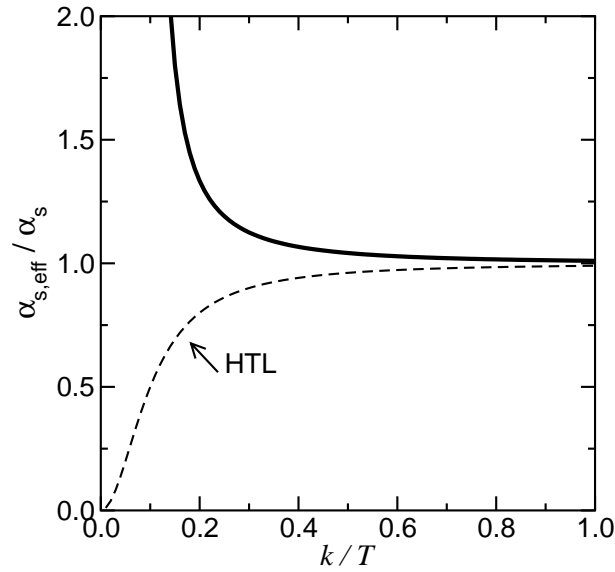


FIGURE 6.4: The ratio $\alpha_{s,\text{eff}}/\alpha_s$ of eq.(6.51) as a function of k/T for a coupling $g = 0.1$ and $N_f = 0$ (solid line). For comparison, the corresponding ratio in the HTL calculation, using the Debye mass of eq.(6.8), is also plotted (dashed line).

of the gluonic vacuum, however, this time the difference goes linearly in b and not only logarithmically. Finally summing over colour, the gluonic susceptibility reads

$$4\pi\chi(H, T)_g = \frac{N_c g^2 T^2}{3 \ 2eH} + 5N_c \frac{g^2}{48\pi^2} \log\left(\mathcal{A}_g \frac{2eH}{T^2}\right). \quad (6.50)$$

In this expression the sign is reversed as compared to eq.(6.47), and $4\pi\chi$ is always positive. The total thermal result for QCD, excluding the $T = 0$ contribution, becomes

$$\alpha_{s,\text{eff}}(k, T) = \frac{\alpha_s}{1 - \alpha_s \frac{4\pi N_c T^2}{3 k^2} - \frac{\alpha_s}{12\pi} \left[5N_c \log\left(\frac{\mathcal{A}_g k^2}{T^2}\right) - 2N_f \log\left(\frac{\mathcal{A}_f k^2}{T^2}\right) \right]}. \quad (6.51)$$

Since the gluon contribution dominates by far over the logarithmic fermionic, there is *antiscreening* at high temperature and long distances. This result is in contrast to expectation and lattice results on the interquark potential, cf. figure 5.1. Extrapolating eq.(6.51) beyond the kinematical region $g \ll k/T \ll 1$ where our approximations are valid, a Landau pole appears in the infrared region $k/T \simeq g$. Figure 6.4 shows the ratio $\alpha_{s,\text{eff}}/\alpha_s$ as a function of k/T for a weak coupling $g = 0.1$, compared to the HTL result. A similar behaviour is also found in more sophisticated renormalisation group analyses of the running coupling at finite temperature (see, e.g., [164, 165, 166]). We note that these results compare quite well with the numerical solutions obtained in ref.[165]. Since eq.(6.51) depends only on the dimensionless quantity k/T , taking the limit $T \rightarrow \infty$ at large k is in a sense equivalent to probing the infrared region $k \rightarrow 0$ at smaller T , indicating that non-perturbative, soft physics might play a role even at high T . It is, however, important to keep in mind that these results were obtained neglecting the gluonic LLL because of its imaginary part. In the next section, we will include this mode consistently which will change the results.

6.5 The gluonic lowest Landau level

The calculation of $\Delta E_g(T)$ in (6.32) involves a sum over all Landau levels

$$\bar{\omega}_{n,k_3} = \sqrt{k_3^2 + 2eH(n + 1/2 \pm 1)},$$

weighted by the corresponding thermal occupation probabilities. As is well-known, the LLL with $n = 0$ and $s_3 = -1$ acquires an imaginary part for small k_3 already at zero temperature [167, 168]. This tachyonic instability signals that the constant field H will decay to some new, unspecified vacuum state, maybe accompanied by the formation of a chromomagnetic condensate. In previous approaches, this feature persisted even at high temperatures [169], despite asymptotic freedom, but could be avoided by the ad hoc introduction of some thermal electric [170] or magnetic gluon screening mass [171]. The influence of the LLL on the high-temperature physics was at best inconclusive. In section 6.4.4, we have therefore discarded the contribution of the LLL. Now we will include the explicit expression for the LLL, which reads, with $\delta^2 = eH/T^2$,

$$E_{\text{LLL}} = VT^4 \left(\frac{\delta^2}{\pi^2} \int_0^\infty dx \frac{\sqrt{x^2 - \delta^2}}{\exp(\sqrt{x^2 - \delta^2}) - 1} \right). \quad (6.52)$$

An expansion of the integral in small δ (though not a power series) for positive $x^2 + \delta^2$ exists (see appendix C) as

$$\int_0^\infty dx \frac{\sqrt{x^2 + \delta^2}}{\exp(\sqrt{x^2 + \delta^2}) - 1} = \frac{\pi^2}{6} + \frac{\delta^2}{4} \left[\log\left(\frac{\delta}{4\pi}\right) + \gamma + \frac{1}{2} \right] + \mathcal{O}(\delta^6). \quad (6.53)$$

Since only $\delta = 0$ is a non-regular point in (6.52), we can analytically continue the expansion to imaginary values of δ . To obtain its sign, we have to pick the correct Riemann sheet of the square root function. With the usual Feynman ϵ -prescription, as applied at $T = 0$ [168], $\delta^2 \rightarrow \delta^2 - i\epsilon$, which leads to $\sqrt{-\delta^2} \rightarrow -i\sqrt{\delta^2}$. As outlined in the appendix, all higher order terms left out in (6.53) involve x -integrals over functions of the form

$$\frac{\sqrt{x^2 + \delta^2}}{x^2 + \delta^2 + (2\pi n)^2}, \quad \text{with } n \in \mathbb{N} \setminus \{0\}.$$

As long as $|\delta| < 2\pi$, no poles appear, and the only branch cut comes from the square root we have dealt with above. In our case, there is henceforth just an imaginary part of E_{LLL} arising from the complex logarithm:

$$E_{\text{LLL}} \simeq VT^4 \left\{ \frac{\delta^2}{6} - \frac{\delta^4}{8\pi^2} \left[\log\left(\frac{\delta^2}{16\pi^2}\right) + 2\gamma + 1 \right] + i \left(\frac{\delta^4}{8\pi} \right) \right\}.$$

Despite the width of the unstable mode being small, $\text{Im}E_{\text{LLL}}/\text{Re}E_{\text{LLL}} = \mathcal{O}(\delta^2) \ll 1$, the positive sign of the imaginary part would indicate a blow-up of the LLL configuration, not a decay, which is unphysical. However, when re-writing δ , the imaginary part

$$\text{Im}E_{\text{LLL}} = \text{Im}[\Delta E_{\text{th}}(T)] = +V \frac{(eH)^2}{8\pi} \quad (6.54)$$

turns out to be *independent* of temperature. At zero temperature, the imaginary part of the energy difference is calculated to be $\text{Im}[\Delta E_{\text{vac}}] = -V(eH)^2/(8\pi)$ [168], which is exactly the opposite of (6.54). Taking both contributions into account, the total imaginary part of the energy difference hence *vanishes*, which renders the

high temperature vacuum stable. This result has been long sought after, but previous approaches [169, 172] always found a remaining imaginary part of the form $\text{Im}[\Delta E_{\text{th}}(T)] = -VT^4[\delta^3/(2\pi)]$. All contributions of order δ^3 in $\Delta E(T)$ always cancel, however, within our approach when all contributions of order g^2 are consistently taken into account. In addition, whereas the squared sum of the charges $e = gq$ (that is responsible for the factors $g^2 N_c/2$ and $g^2 N_f/2$ in eq.(6.24) and the following) does not depend on the direction of the external field in colour space, terms not quadratic in the coupling, like $\delta^3 \sim e^{3/2}$, are not group-invariant and do depend on the specific colour choice of the magnetic field [155], a result that is probably unphysical.

Combining now the real part of E_{LLL} with the sum over all higher lying Landau modes, eq.(6.49), we find that the troublesome $-\delta^2/6$ term is *exactly* cancelled by $\text{Re}E_{\text{LLL}}$ which henceforth eliminates the Landau pole in the infrared. Furthermore, the logarithms combine such as to yield, after summing over the colour charges q^2 ,

$$\Delta E_g = -\frac{1}{2}VH^2 \left[g^2 \frac{11N_c}{48\pi^2} \log \left(\bar{\mathcal{A}}_g \frac{2eH}{T^2} \right) \right]$$

with $\bar{\mathcal{A}}_g = \exp(2\gamma + \log 3 - 1/22)/(32\pi^2) \simeq 0.03$. The expression in square brackets already stands for $4\pi\chi_g(T, H)$. Together with the quark contribution $\chi_q(T, H)$ of eq.(6.47),

$$4\pi\chi(T, H) = g^2 \frac{11N_c}{48\pi^2} \log \left(\bar{\mathcal{A}}_g \frac{2eH}{T^2} \right) - g^2 \frac{2N_f}{48\pi^2} \log \left(\mathcal{A}_f \frac{2eH}{T^2} \right),$$

which looks deceptively similar to the running coupling at $T = 0$. Indeed, taking into account the one-loop zero temperature QCD susceptibility (6.24), we arrive at

$$\alpha_s^{\text{eff}}(T, \Lambda) = \frac{\alpha_s(\Lambda)}{1 + \frac{\alpha_s(\Lambda)}{12\pi} \left[11N_c \log \left(\frac{[\bar{\mathcal{A}}_g 2\pi T]^2}{\Lambda^2} \right) - 2N_f \log \left(\frac{[\mathcal{A}_f \pi T]^2}{\Lambda^2} \right) \right]}, \quad (6.55)$$

with $\bar{\mathcal{A}}_g = \exp(-\gamma - 1/2 \log(3/8) + 1/44) \approx 0.938$ and $\bar{\mathcal{A}}_f = \exp(-\gamma + 1/2) \approx 0.926$. This expression looks very similar to what was found in the QED case (6.46): all field (or momentum) dependence in α_s^{eff} has dropped out. It is just the one-loop running coupling constant at zero temperature, where the loop particles carry some average thermal momentum $\langle k \rangle = \mathcal{O}(T)$, as originally put forward in [1]. However, we are now in a position to refine that result: coming from the lowest Matsubara frequencies, quarks propagating in a thermal loop should have πT as momentum, whereas the lowest non-vanishing bosonic frequency is $2\pi T$ – and these values are indeed very close to the numbers appearing in the logarithms of (6.55) in front of T .

6.6 Intermediate summary

We have therefore been able to show for the first time in a self-contained calculation that, for long wavelength modes, the running coupling at finite temperature becomes very simple, as has been expected for long on a phenomenological basis [1]: it follows from the zero temperature renormalisation group equations, with the momentum scale replaced by a suitable thermal scale that seems to follow from the lowest, non-zero Matsubara frequencies and is then, of course, different for quarks and gluons. This distinction of thermal momentum scales for fermions and bosons in the effective coupling is also a new outcome of our calculation. All collective medium effects over large distances $R \gg 1/T$ can therefore be subsumed in a running coupling strength that does not depend on R .

This result implies that there is no need for the commonly proposed hierarchy of scales $T \gg gT \gg g^2T \gg \dots$ since thermal physics becomes scale-independent at large distances. It might therefore be sufficient at one-loop order to calculate the physics at the hard scale T only and incorporate all soft physics of order gT and smaller into a running thermal coupling constant, without the need for HTL resummation. This line of reasoning is supported by the fact that we have recovered the HTL results for the effective coupling in a cruder approximation to ΔE_{th} , neglecting $\mathcal{O}(g)$ corrections to the single Landau levels and the density of states. The partial resummation of hard modes only seems to be insufficient and does not capture all effects to a given order in g .

7 Summary and Conclusions

*“Where shall I begin, please your Majesty”, she asked.
“Begin at the beginning”, the King said, gravely,
“and go on ’till you come to the end: then begin again.”*

LEWIS CARROLL, ALICE’S ADVENTURES IN WONDERLAND

In chapters 2 and 3, we have given an up-to-date overview of the thermodynamics of QCD, referring mainly to latest lattice data. Since QCD is expected to undergo a transition from a hadronic to a partonic phase at a critical temperature $T_c = \mathcal{O}(200 \text{ MeV})$, the possibility of creating a hot system in that temperature regime in heavy-ion experiments has triggered much experimental and theoretical activity in recent years. By now a multitude of data has been accumulated, but we are still far away from a consistent, reliable theoretical interpretation of these data. This is due mainly to two reasons: first, QCD thermodynamics at high temperatures is an intriguing subject. Superficially simple and analytically tractable, it shows an unexpected level of complexity when explored in more detail, as we have exemplarily demonstrated by the equation of state and the Debye screening mass. Second, the heavy-ion collision itself is a very complicated process involving poorly known strong interaction physics. As a consequence, previous work has mainly focused on interpreting one piece of data within a specific approach and a certain number of fit parameters. The main goal of this thesis was to explore to what extent the formation of a QGP can be inferred from current data – within a unified description, taking into account as much information as is available. In view of the complications mentioned above, our work is primarily phenomenological (and hence not the last step, merely a beginning). However, since we tried to take into consideration as many constraints as possible in the construction of our model, we significantly improved over previous approaches.

The actual work can be divided in three pieces: (1) specification of the hot medium, (2) construction of the fireball and (3) calculation of signatures. Following the discussions of chapter 2, we have constructed in chapter 3 a novel quasiparticle description of the QCD EOS in the temperature region $T_c < T \lesssim 3 T_c$, based on a model of quasifree, massive partons. The thermal coupling was taken to exhibit critical behaviour. For the first time, we have schematically included confinement by a modification of the particle distribution functions and achieved a simple, thermodynamically consistent and economic parametrisation of continuum-extrapolated lattice data for the EOS of SU(3) gauge theory. The lattice data basically constituted the only input of the model, the rest followed from there. Empirically, a connection of the thermal energy of the Yang-Mills vacuum, $B(T)$, with the chromomagnetic condensate $\langle \mathbf{B}^2 \rangle_T$ was found, a feature not present in previous models. Since this identification is not based on ther-

modynamic consistency (i.e. not stringent within the framework), but specific to our model, it strongly supports our setup of the QGP.

Next, we have carefully investigated the currently available lattice data on QCD with dynamical quarks and subsequently extended the confinement model to $N_f \neq 0$ by a number of sensible arguments. Our predictions for $N_f = 2$ and $N_f = 2 + 1$ were confirmed by more recent preliminary continuum extrapolations of lattice data. The extension of the quasiparticle-plus-confinement model to small quark chemical potential ($\mu \lesssim T$) was straightforward, parameter-free and proved to be feasible: the value for $p(T_c, \mu_* = 0.1 T_c)$ is within 10% of a recent lattice calculation. Our model is also capable of describing the first lattice results on the net quark density $n_q(T, \mu)$. This supports the validity of our quasiparticle description even close to T_c . In addition, lattice results on the off-diagonal quark number susceptibilities (which directly measure the interactions) support our picture of a quasifree QGP in the vicinity of the phase transition. We also managed to describe, without any parameter adjustments, lattice data on the diagonal quark number susceptibility for two light quarks and a heavy quark, albeit with the *caveat* that these data are not yet very well understood. All in all, the quasiparticle confinement model successfully describes and predicts a variety of lattice data and seems to be a reasonable representation of the QGP equation of state.

The function $C(T)$, introduced in section 3.3.3, parametrises our ignorance about details of the confinement mechanism. It would be desirable to connect this macroscopic quantity with microscopic, first-principle QCD dynamics, preferably starting in the gluon sector. The connection of $B(T)$ to the chromomagnetic condensate seems to imply that magnetic monopoles indeed play an important role in QCD thermodynamics close to T_c and provides a starting point for further investigations and more refined model building. A comparison of $B(T)$ with lattice data for the spacelike plaquette Δ_σ in the presence of quarks will shed more light on such conjectures.

In the shorter run, it should be possible to extend the model self-consistently to larger values of the quark chemical potential μ using Maxwell relations. So far, we have neglected any μ -dependence in the confinement function $C(T)$ and the coupling $g(T)$. To improve on that issue, the partial differential flow equations for $C(T, \mu)$ and $g(T, \mu)$ that follow from the stationarity condition (3.12) should be solved numerically, with appropriate boundary conditions. The confinement model can then give results on, e.g., $p(T, \mu)$ close to the transition line even for $\mu \gg T$ – as long as the phase structure of QCD does not change qualitatively.

Regarding the second step of the program outlined above, a fireball model reminiscent of hydrodynamics has been developed in chapter 4 for CERN/SPS Pb(160 AGeV)+Au and Pb(40 AGeV)+Au collisions and RHIC Au+Au collisions at $\sqrt{s} = 200$ AGeV. In this model, we have assumed that thermalisation constitutes a valid concept for the description of the produced medium in an URHIC, which allowed us to use the aforementioned quasiparticle interpretation of the QGP. Using entropy conservation, the EOS of the system links the initial and final states of the collision and accordingly constrains its evolution inbetween. The EOS in the QGP phase for physical values of the quark masses was taken from the quasiparticle-plus-confinement model, whereas in the hadronic phase a smooth interpolation to a hadronic resonance gas was applied. The final state was chosen such as to comply with a large number of hadronic measurements (particle abundances, rapidity and p_T -spectra, HBT radii), the initial

state follows from geometrical overlap considerations and the measured entropy per baryon. A novel feature of our approach was the modelling of the volume evolution by a time-dependent acceleration profile proportional to the ratio p/ϵ that naturally incorporates the soft point in the EOS at T_c . No more input was required, all other characteristics (initial temperature and energy density, particle densities, temperature and volume profile, duration of QGP phase, freeze-out volume etc) follow from there. This procedure resulted, for the first time, in a thermodynamically self-consistent description of a fireball evolution in accordance with a multitude of lattice results and hadronic final-state measurements. With initial temperatures well above T_c (420 MeV at central $\sqrt{s} = 200$ AGeV, 310 MeV at central $\sqrt{s} = 17.4$ AGeV and still 230 MeV at $\sqrt{s} = 8.4$ AGeV), the present scenario supports the hypothesis that the quark-gluon phase is actually reached, at a transient stage, in current heavy-ion experiments. The life time of the QGP, $\tau_{\text{QGP}} = 4 - 10$ fm/c, is sizable compared to the total life time of the fireball which lies in the range $14 - 18$ fm/c, and larger than predicted in previous approaches – a consequence of our realistic EOS and acceleration profile. The relative weight of the QGP with respect to the subsequent hadronic phase decreases, of course, with decreasing c.m. energy. With such a large QGP life time, we next explored if the QGP leaves any distinct traces in experimental data and focussed on two observables that are sensitive to different stages of the fireball expansion: dilepton radiation at low invariant masses and J/ψ suppression. The fireball setup was kept fixed with no extra adjustable parameter.

Chapter 4 featured the calculation of dilepton rates where experimental data exist for SPS Pb(160 AGeV)+Au and Pb(40 AGeV)+Au. Above T_c , we have calculated the photon spectral function (that enters the rate) within the quasiparticle model to one-loop order, i.e. $q\bar{q} \rightarrow \gamma^* \rightarrow e^+e^-$. Gross features of the confinement process have been taken into account by a suppression of dilepton radiation near the phase transition by a factor $C(T)^2$. The first preliminary lattice calculations of the vector spectral function have now indeed confirmed – on a qualitative basis – our calculation. Below T_c , the dominant contributions to dilepton radiation are pion and kaon annihilation processes that are enhanced by the formation of intermediate vector mesons, e.g. $\pi\pi \rightarrow \rho \rightarrow \gamma^*$, $\pi\pi\pi \rightarrow \omega \rightarrow \gamma^*$ or $K\bar{K} \rightarrow \phi \rightarrow \gamma^*$. These processes have been evaluated at finite temperature and baryon density using Vector Meson Dominance combined with Chiral Dynamics, utilising results of earlier calculations. At the phase transition, this perturbative hadronic description cannot be applied, but no better information exists to date.

Folding the spectral function with the fireball evolution, we have achieved a good description of the SPS CERES/NA45 data at the two mentioned beam energies, both for the total rate and in the p_T -separated bins. A slight overshooting at very low invariant masses $M < 200$ MeV could be traced back to the behaviour of the rho meson spectral function at large three-momentum where its approximation by the zero momentum spectrum clearly breaks down. As found in previous approaches, the proposed dilepton excess in the low mass region at SPS is not a direct signal from the QGP, it can be explained by non-trivial, yet conventional hadronic physics, mainly collisional broadening of the rho meson. The apparent duality of the hadron and parton spectra can, however, be regarded as a precursor of chiral symmetry restoration accompanying the deconfinement process: close to the transition, it will not be possible to disentangle a very broad rho meson from a continuous, perturbative $q\bar{q}$ spectrum. So in that sense, the dilepton rate is not an indicator of the QGP itself, but rather an indicator of the phase transition and the associated symmetry restoration.

The experimental resolution in the region where the QGP would presumably shine most prominently is unfortunately too coarse at the moment to extract a conclusive result. The situation at RHIC, where no data exist yet, might improve: there is a window above 1 GeV and the region which will ultimately be filled by semileptonic decays of charm mesons, where the QGP radiation will radiate dominantly, and RHIC will cover that energy range. The QGP shows up in an indirect and subtle way in the SPS dilepton rate, though, because a purely hadronic framework would not be successful in describing the data within our outlined approach. The relative strength of hadronic contributions to the high mass region and the low mass region is quite different as compared to those of the QGP. Purely hadronic scenarios which are able to account for the low mass region would necessarily fail in the high mass region and vice versa.

Further improvement on the theory side is not straightforward at this stage. The future clearly requires reliable calculations of both hadronic and partonic sources of lepton radiation, reducing the model dependence in the hadronic sector and improving convergence of the rate in the partonic sector. Due to the highly non-perturbative nature of the transition, this can quite possibly only be achieved by lattice calculations of the vector (photon) spectral function. Since the spectrum is a dynamical quantity, lattice theorists presently have, however, to rely on indirect means to extract it (such as the maximum entropy method), which in turn introduces additional uncertainties. The resolution and background estimates of current dilepton experiments are still insufficient to distinguish between models for in-medium modifications of hadrons. The general fireball set up, as it stands, must be improved by introducing a more sophisticated spatial profile, taking into account radial inhomogeneities (to account for elliptic flow) or more realistic longitudinal baryon rapidity distributions (to improve the RHIC fireball). Detailed comparisons with more involved hydrodynamical calculations must be performed. We believe that the fireball modelling should advance on all sides more or less equally. Fixing one particular item on a 10% level will do no good if another item is still allowed to vary by 50% (if both have comparable influence on data). Improvement on the three-momentum behaviour of the rho meson spectral function, for example, as mentioned above, seems therefore not to be a very pressing issue at the moment.

In chapter 5, we have applied the quasiparticle and fireball models, successfully used to describe dilepton data in chapter 4, to the phenomenology of charmonium Ψ (J/ψ and χ_c) suppression in heavy-ion collisions. We solved a Boltzmann equation with a collision term containing both gain and loss terms, representing Ψ formation due to coalescence of c and \bar{c} quarks and Ψ dissociation due to collisions with gluon quasiparticles, respectively. The elementary process $\Psi g \rightarrow c\bar{c}$ was modelled by a simplified dissociation cross section which considered Ψ as a Coulomb bound state, the corresponding back reaction $c\bar{c} \rightarrow \Psi g$ was obtained by detailed balance. For SPS Pb(158 AGeV)+Pb collisions, we were able to describe the NA50 suppression data very well as a function of centrality, without additional new ingredients. Coalescence was found to play no role at SPS energies. Since the hadronic phase exists only at moderately low number densities, it has no bearing on the Ψ evolution and cannot explain the present data without introducing anomalously large cross sections. The partonic interaction cross section, as calculated, is comparable with common hadronic ones, therefore it is solely the large gluon density (that follows uniquely from the confinement model) in the initial stage of the fireball evolution that is responsible for the suppression – a direct signal of the deconfinement process. We also considered extrapolations up

to RHIC energies where, despite the more extreme conditions as compared to SPS, a sizable fraction of Ψ still survives. Although a clear trend towards more copious Ψ production was found, no significant net enhancement is present in the end. This tendency is confirmed by first preliminary results from the PHENIX experiment. Several improvements of our approach are possible: as in the dilepton case, a more constrained description of the expanding fireball at RHIC conditions is needed. Only then our estimates can be regarded as predictions. The initial conditions for charm and Ψ evolution should take into account the details of the produced spectra and provide a better incorporation of the (at this stage poorly known) nuclear effects.

To summarise the data-driven part of this work:

- Under the assumption of thermalisation, it is likely that the QGP has been produced, at a transient stage, in current heavy-ion collisions at CERN/SPS and RHIC.
- Data of low mass dilepton emission (which are sensitive to the *late* stage) and charmonium suppression (which are sensitive to the *early* stage) are successfully and consistently described by the quasiparticle model including thermodynamic aspects of confinement, in combination with a fireball fixed by freeze-out hadron observables only.
- The tendency towards chiral symmetry restoration shows up in the dilepton data through the flattened hadronic spectral function. The deconfinement process is responsible for J/ψ suppression.
- The QGP does not, as initially anticipated, leave extremely pronounced signatures in data, it rather shows up in subtle ways: a purely hadronic description cannot reproduce these data without introducing anomalous modifications of standard physics.

Two further immediate tests of our model are feasible: first, data on direct (real) photons exist from the WA98 collaboration at CERN/SPS in the region $1 \text{ GeV} < p_T < 4 \text{ GeV}$. The calculation of a direct photon rate from the confinement model (that will involve interactions among the quasiparticles) can be performed because a clear separation of thermal, $T = \mathcal{O}(200 \text{ MeV})$, and photon, $p_T = \mathcal{O}(2 \text{ GeV})$, scales exists. Second, jet quenching will be a prominent candidate for probing the QGP at RHIC. Energy loss of high-energetic particles is largely governed by partonic particle densities we can provide a reliable expression for. In both calculations, the fireball has to be the same as in the dilepton case, to obtain maximal consistency.

Chapter 6, finally, still dealt with QCD phenomenology, albeit in a more conceptual fashion. Asymptotic freedom lies at the heart of the QGP, but its explicit perturbative derivation, e.g. within finite temperature renormalisation group equations, has proven unexpectedly subtle, even for small couplings, and has not been achieved so far in a concise manner. Although the temperature region with $g \ll 1$ is of no relevance to current and future experiments, it is remarkable that lattice calculations of the Debye mass do indeed indicate a clear logarithmic running of $g(T)$ at high temperatures and long distances, as we have discussed in detail in section 6.2. We evaluated the energy shift of the vacuum to leading order in the small coupling constant after applying an external (chromo)magnetic field H , extending the approach of refs. [153, 154] to finite temperature. From the result, we extracted an effective, temperature- and scale-dependent coupling constant $\alpha^{\text{eff}}(H, T)$ for QED and QCD.

In a first approximation, neglecting $\mathcal{O}(g)$ corrections to the single Landau levels and the density of states, we are able to recover the HTL results for the effective coupling in a transparent way. This has not been achieved by previous approaches. In what followed, we showed explicitly that the partial resummation of hard modes only is insufficient and that it does not capture all important effects. Taking into account all contributions to order g^2 , we demonstrated for the first time in a self-contained calculation that, for long wavelength modes, the running coupling at finite temperature indeed becomes very simple: taken together with its zero temperature counterpart, it does not depend on the external scale H anymore and follows from the zero temperature renormalisation group equations, with the momentum scale replaced by a suitable thermal scale that seems to follow from the lowest, non-zero Matsubara frequencies and is then, of course, different for quarks and gluons. This distinction of thermal momentum scales for fermions and bosons in the effective coupling is another new outcome of our calculation. The same formal result $\alpha^{\text{eff}} = \alpha(\langle k \rangle \simeq \pi T)$ was also found in QED, supporting the setup of the calculation. All collective medium effects over large distances $R \gg 1/T$ can therefore be subsumed in a running coupling constant that does not depend on R .

The inclusion of the lowest lying Landau mode (LLL) turned out to be crucial in the calculation. When it is neglected, an unphysical Landau pole appears at small k/T . The failure of various thermal renormalisation group approaches to obtain the correct running of the coupling may have its root there. In addition, the thermal imaginary part of the LLL exactly cancels its well-known zero temperature counterpart within our approach and removes the former instability of the vacuum, a welcome feature. QCD thermodynamics at high temperatures and large distances seems indeed to be simple, purely perturbative and asymptotically free, which perfectly closes the circle with eq.(1.1).

To draw a final conclusion, it is worthwhile to go back to the quotation at the beginning of this chapter: the advice of the king is certainly apt not only for Alice, but also for heavy-ion theorists. URHIC physics is a growing field – not only in numbers of people working on it, but also in understanding. It is still far from maturity. Whereas there is mostly general consensus about the orders of magnitude involved, more specific predictions often differ by vast amounts. In view of this, it is necessary to really begin at the beginning: gather everything that is known, build a consistent model and pin down all assumptions. From there on, go right through to the end and try to describe as much experimental data as possible. It is of no use to stop somewhere inbetween after having successfully fitted one single observable. At the end, check where the model works and where it fails. Go back to the beginning, try to improve on the weak points and iterate the process. Ultimately, a consistent picture of the elusive quark-gluon plasma will hopefully emerge.

A Thermal Spectral Functions

Here we list some general properties of the spectral function [8]. For a bosonic Heisenberg field operator $\phi(x^\mu)$, the thermal propagator is defined by

$$iD(x) = \theta(x^0)\langle\phi(x)\phi(0)\rangle_\beta + \theta(-x^0)\langle\phi(0)\phi(x)\rangle_\beta = \quad (\text{A.1})$$

$$= \theta(x^0)D^>(x) + \theta(-x^0)D^<(x). \quad (\text{A.2})$$

The argumentation for fermionic fields runs similar, taking into account their Grassmann nature. The *spectral function* is derived from the field commutator as

$$\rho(x) = \langle[\phi(x), \phi(0)]\rangle_\beta = D^>(x) - D^<(x). \quad (\text{A.3})$$

The *retarded* and *advanced* propagators follow as

$$iD_R(x) = \theta(x^0)\rho(x) = \theta(x^0)(D^>(x) - D^<(x)), \quad (\text{A.4})$$

$$iD_A(x) = -\theta(-x^0)\rho(x). \quad (\text{A.5})$$

In equilibrium, $D^>$ and $D^<$ are not independent, but connected by the Kubo-Martin-Schwinger (KMS) relation. In Fourier space,

$$D^>(k) = D^<(-k) = e^{\beta k^0} D^<(k). \quad (\text{A.6})$$

Hence,

$$D^>(k) = \rho(k)[1 + f_B(k^0)], \quad (\text{A.7})$$

$$D^<(k) = \rho(k)f_B(k^0), \quad (\text{A.8})$$

and the full thermal propagator – both in the imaginary- and the real-time formalism – can be reconstructed once $\rho(k)$ is known. From the analytical properties of the Feynman propagator follows that the spectral function in an interacting theory can be derived from its imaginary part

$$\rho(k) = -2 \operatorname{sgn}(k^0) \operatorname{Im} D_F(k, T). \quad (\text{A.9})$$

Assuming a Schwinger-Dyson ansatz for the full Feynman propagator,

$$D_F(k) = \frac{1}{k^2 - m^2 - \Pi(k, T) + i\epsilon} \quad (\text{A.10})$$

with the Feynman self-energy $\Pi(k, T)$, the (real) spectral density reads

$$\rho(k) = -2 \operatorname{sgn}(k^0) \frac{\operatorname{Im}\Pi(k, T)}{[k^2 - m^2 - \operatorname{Re}\Pi(k, T)]^2 + [\operatorname{Im}\Pi(k, T)]^2}, \quad (\text{A.11})$$

a Breit-Wigner shape in the time-like region $k^2 > 0$. If $\operatorname{Im}\Pi$ is non-vanishing for space-like k^2 , a continuum contribution – usually associated with damping processes – is also part of the spectrum. The spectral function therefore contains information on

the fundamental excitations and their particle properties (pole mass, damping width). If the imaginary part is small, $\rho(k)$ defines a sharply peaked quasiparticle structure. Especially, for $\text{Im}\Pi \rightarrow 0$,

$$\rho(k) = 2\pi \text{sgn}(k^0)\delta(k^2 - m^2 - \text{Re}\Pi(k, T)). \quad (\text{A.12})$$

If, in addition, $\text{Re}\Pi$ is only weakly momentum-dependent, the effect of the medium on the propagating particle is mainly a thermal mass shift. The temperature-independent spectral function for a free field theory follows immediately as

$$\rho(k)_{\text{free}} = 2\pi \text{sgn}(k^0)\delta(k^2 - m^2).$$

More explicitly, eq.(A.12) can be recast as a sum of in-medium particle ($k^0 > 0$) and antiparticle ($k^0 < 0$) contributions:

$$\rho(k) = 2\pi [Z_+(k)\delta(k^0 - \omega(k, T)) - Z_-(k)\delta(k^0 + \omega(k, T))], \quad (\text{A.13})$$

where $\omega(k, T)$ are the solutions of the implicit equation

$$D_F^{-1}(k^0 = \omega, \vec{k}, T) = 0, \quad (\text{A.14})$$

and define the *dispersion relation* of the medium-modified particles. The *residues* Z_{\pm} gauge the strength of the pole excitations by

$$Z_{\pm} = \left[\frac{\partial D_F^{-1}(k^0, \vec{k}, T)}{\partial k^0} \Big|_{k^0 = \pm\omega} \right]^{-1}. \quad (\text{A.15})$$

At vanishing temperature, the imaginary part of the self-energy is connected with the physical decay rate of the particle. Put in a heat bath, particles will acquire a finite thermal damping width by their interactions with the medium. However, since a system in thermal equilibrium does not change anymore as time passes, the interpretation of the damping width is different now – otherwise the medium would dissolve. Using the Kobes-Semenoff cutting rules for bosons, the imaginary part of the self-energy is related to the creation rate $\Gamma^<$ and decay rate $\Gamma^>$ by

$$\text{Im}\Pi(k, T) = -k^0 (\Gamma^>(k, T) - \Gamma^<(k, T)).$$

In thermal equilibrium, $\Gamma^>$ and $\Gamma^<$ are connected by the KMS-relation: $\Gamma^> = e^{\beta k^0} \Gamma^<$. The recombination of particles encoded in $\Gamma^<$ is a pure plasma effect and therefore vanishes as $T \rightarrow 0$. If the plasma is weakly disturbed out of equilibrium, i.e. if the perturbed momentum distribution of the particles deviates only slightly from the Bose-Einstein distribution, it can be shown by a Boltzmann-like equation that $\Gamma = \Gamma^> - \Gamma^<$ describes the inverse timescale $1/\tau$ at which the system approaches its equilibrium state. Then, the damping rate γ of a particle becomes

$$\gamma(k, T) = -\frac{\text{Im}\Pi(k, T)}{2|k^0|}. \quad (\text{A.16})$$

B Hard Thermal Loop Self-Energies

This chapter summarises results on the Hard Thermal Loop (HTL) self-energies that are referred to throughout the main text. We focus mainly on non-abelian gauge theories with N_c colours and N_f flavours, but quote the corresponding expressions for QED where necessary.

B.1 Gauge boson HTL self-energies

For gauge bosons, the self-energy $\Pi^{\mu\nu}(k) = (g^{\mu\nu} - k^\mu k^\nu / k^2) \bar{\Pi}(k^2)$ is transverse at zero temperature due to current conservation. At finite temperature or baryon density, Lorentz invariance is formally broken by the existence of a preferred frame of reference, namely the rest frame of the heat bath or matter, respectively. A Lorentz-invariant framework can be recovered by introducing the four-velocity of the matter u^μ which becomes $(1, \vec{0})$ in its rest frame. Now $\Pi_{\mu\nu}(k)$ acquires a longitudinal component

$$\Pi_{\mu\nu}(k; T) = -P_{\mu\nu}^T(k, u) \Pi_T(k, u; T) - P_{\mu\nu}^L(k, u) \Pi_L(k, u; T).$$

Factors of k^0 appearing in the distribution functions which explicitly break Lorentz invariance are now substituted by factors of $w = k_\mu u^\mu$. The generalisation of the three-momentum is $\bar{k} = \sqrt{w^2 - k^2}$ which reduces to $|\vec{k}|$ in the rest frame.

The two independent projection tensors are

$$P_{\mu\nu}^T = g_{\mu\nu} - \frac{k_\mu k_\nu}{k^2} + \frac{k^2}{\bar{k}^2} \tilde{u}_\mu \tilde{u}_\nu, \quad (\text{B.1})$$

$$P_{\mu\nu}^L = -\frac{k^2}{\bar{k}^2} \tilde{u}_\mu \tilde{u}_\nu, \quad (\text{B.2})$$

where $\tilde{u}_\mu = u_\mu - w k_\mu / k^2$. The two scalar invariants are given by

$$\Pi_T(k, u) = \frac{1}{2} \left(\Pi^\mu_\mu + \frac{k^2}{\bar{k}^2} u^\mu u^\nu \Pi_{\mu\nu} \right), \quad (\text{B.3})$$

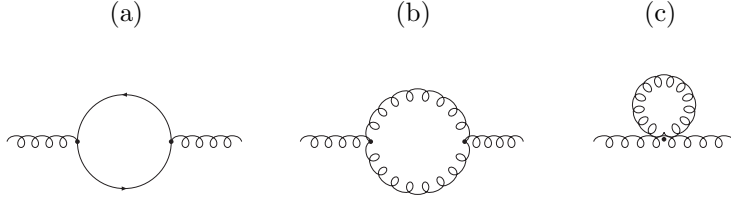
$$\Pi_L(k, u) = -\frac{k^2}{\bar{k}^2} u^\mu u^\nu \Pi_{\mu\nu}. \quad (\text{B.4})$$

The same procedure is applied to obtain the free gauge boson propagator which has the general structure

$$D_{\mu\nu}^F = P_{\mu\nu}^T D_T^F + P_{\mu\nu}^L D_L^F + \frac{i\xi}{k^2} \frac{k_\mu k_\nu}{k^2}, \quad (\text{B.5})$$

ξ being the gauge parameter. Resumming the self-energies by use of a Dyson equations hence modifies the transverse and longitudinal components of the propagators, and the free propagators $D_{L,T}^F$ are replaced by

$$iD_T(k) = \frac{1}{k^2 - \Pi_T(k, T)} \quad \text{and} \quad iD_L(k) = \frac{1}{k^2 - \Pi_L(k, T)}. \quad (\text{B.6})$$



The gluon self-energy

The self-energy can be calculated to one-loop order under the assumption of soft external momentum $k^0, |\vec{k}| \ll T$ (see diagrams (a), (b) and (c)), and the leading HTL terms are given by the expressions

$$\Pi_L(k^0, \vec{k}) = m_D^2 \left[1 - \frac{k^0}{2|\vec{k}|} \log \left(\frac{k^0 + |\vec{k}|}{k^0 - |\vec{k}|} \right) \right], \quad (\text{B.7})$$

$$\Pi_T(k^0, \vec{k}) = \frac{1}{2} \left[m_D^2 + \frac{(k^0)^2 - |\vec{k}|^2}{|\vec{k}|^2} \Pi_L \right]. \quad (\text{B.8})$$

where

$$m_D^2 \equiv \left(N_c + \frac{N_f}{2} \right) \frac{g^2 T^2}{3} \quad (\text{B.9})$$

is the *Debye screening mass* in the presence of N_f massless flavours. If the flavours carry conserved charges,

$$m_D^2 \rightarrow m_D^2 + \sum_f \frac{g^2 \mu_f^2}{2\pi^2} \quad (\text{B.10})$$

with the chemical potentials μ_f . Amazingly, the result in QED – which consists only of diagram (a), the electron loop – has exactly the same structure with the only modification

$$m_D^2 \rightarrow \frac{e^2 T^2}{3}, \quad (\text{B.11})$$

where e stands for the electromagnetic coupling.

The poles of the longitudinal and transverse propagators in (B.6) yield the dispersion law for travelling waves in the plasma, using (A.14),

$$\omega_{L,T}^2 = \vec{k}^2 + \text{Re}\Pi_{L,T}(\omega_{L,T}, \vec{k}). \quad (\text{B.12})$$

The numerical solution for $D_T^{-1} = 0$ and $D_L^{-1} = 0$ is shown in figure (B.1). The transverse mode describes the propagation of the zero-temperature gluons, modified by the medium. Indeed, for $|\vec{k}| \gg m_D$, the transverse dispersion relation becomes that of a massive free particle with a T -dependent mass,

$$\omega_T^2 \simeq \vec{k}^2 + m_\infty^2, \quad (\text{B.13})$$

where we defined the *asymptotic mass* m_∞ by

$$m_\infty = \frac{m_D}{\sqrt{2}}. \quad (\text{B.14})$$

Since the mass is generated dynamically, gauge invariance is not violated.

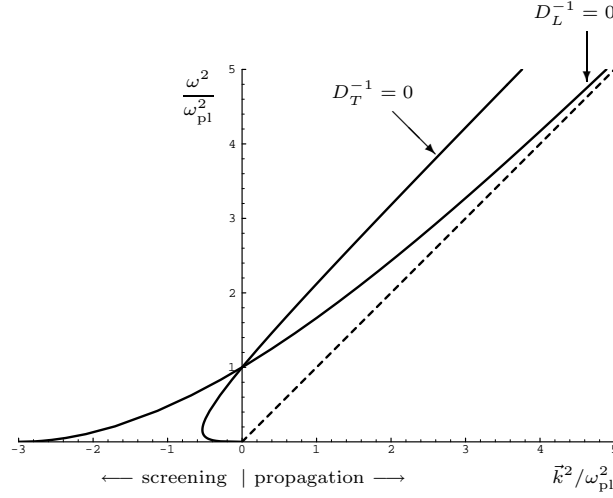


FIGURE B.1: The location of the zeros of D_T^{-1} (spatially transverse gauge bosons) and of D_L^{-1} (longitudinal plasmons) in quadratic scales such as to show propagating modes and screening phenomena on one plot. The dashed line shows the dispersion relation of a free massless boson. Figure and caption adapted from [173].

The longitudinal excitation is a pure collective plasma effect, commonly dubbed plasmon, and approaches the free dispersion relation exponentially since, for $|\vec{k}| \gg m_D$,

$$\omega_L \simeq |\vec{k}| \left[1 + 2 \exp\left(-\frac{\vec{k}^2 + m_\infty^2}{m_\infty^2}\right) \right]. \quad (\text{B.15})$$

Both modes start for $\vec{k} = 0$ from a common, non-zero $\omega(0)$, the *plasma frequency*

$$\omega_{\text{pl}} = \frac{m_D}{\sqrt{3}}. \quad (\text{B.16})$$

The region $\omega < \omega_{\text{pl}}$ gives information about the screening of the chromomagnetic and chromoelectric fields. In particular, the static limit $\omega = 0$ yields an inverse screening length of m_D for the electrostatic mode, arising from the longitudinal mode, whereas the magnetostatic mode remains unscreened: $m_M = 0$.

The spectral function takes the form

$$\rho_{L,T}(k) = 2\pi Z_{L,T}(k) \{ \delta(k^0 - \omega_{L,T}) - \delta(k^0 + \omega_{L,T}) \} + \beta_{L,T}(k). \quad (\text{B.17})$$

As elucidated in appendix A, the spectrum of the medium-modified particles consists therefore of quasiparticle modes with vanishing damping width (since the time-like imaginary part is zero at this loop order¹), and a continuum contribution $\beta_{L,T}$ that is only present for space-like momenta $k^2 < 0$. It gives rise to a large imaginary part below the light cone that is interpreted as Landau damping, the scattering of hard loop particles off soft gauge bosons. It is important to note that for hard external momenta, $k^0, |\vec{k}| \geq \mathcal{O}(T)$, (B.7) and (B.8) are not valid anymore, except for $|k^2| \ll T^2$. However, the poles of the HTL propagators D_L and D_T exactly lie in that region, hence they

¹This can be naturally interpreted in QED as the infinitely strong Pauli blocking of the thermal loop particles. For a virtual photon at rest, $\text{Im}\Pi(k^0, T) = \text{Im}\Pi(k^0, T=0)[1 - 2f_D(k^0/2)]$ from the cutting rules, and in the HTL approximation $f_D(k^0/2) \simeq 1/2 - \mathcal{O}(k^0/T)$.

still yield the correct leading order behaviour of the quasiparticle modes even for hard momenta.

The residues Z read for large momenta $|\vec{k}|$

$$Z_T(k) \simeq \frac{1}{2|\vec{k}|} \quad \text{and} \quad (\text{B.18})$$

$$Z_L(k) \simeq \frac{2|\vec{k}|}{m_\infty^2} \exp\left(-\frac{\vec{k}^2 + m_\infty^2}{m_\infty^2}\right). \quad (\text{B.19})$$

Since the longitudinal mode is a collective effect, its contribution is only important for small $|\vec{k}|$, for large momenta the mode decouples with exponentially vanishing pole strength. The transverse residue approaches the $T = 0$ result. Hence, physics that is dominated by hard thermal modes may be describable in terms of in-medium versions of the physical transverse gauge bosons only.

The time-like damping width

$$\gamma(\vec{k}, T)_{L,T} = -\frac{1}{2\omega_{L,T}} \text{Im}\Pi_{L,T}(\omega_{L,T}, \vec{k}, T) \quad (\text{B.20})$$

becomes non-zero only at order $g(gT)$ in the HTL calculation. For an excitation at rest, $\Pi_L = \Pi_T$, and the gauge-independent result reads, for $N_f = 0$,

$$\gamma \simeq 0.09 N_c g^2 T. \quad (\text{B.21})$$

The ratio of the damping width of the gauge boson over its mass determines the range of validity of the quasiparticle picture of the plasma. For pure glue theory, $\gamma/\omega_{\text{pl}} \simeq 0.5g$ for SU(3). Realistic values for g in a QGP are of the order 1, so the damping is non-negligible, but nevertheless does not invalidate the picture of an identifiable quasiparticle pole, at least to leading order.

B.2 Fermion HTL self-energies

The self-energy for massless fermions at finite temperature has the general form

$$\Sigma(k^0, \vec{k}) = a(k)\gamma^0 + b(k)[\hat{\vec{k}} \cdot \vec{\gamma}], \quad (\text{B.22})$$

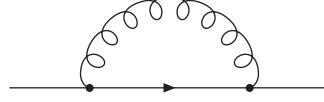
where a and b are c -functions and $\hat{\vec{k}} = \vec{k}/|\vec{k}|$. In the one-loop HTL approximation,

$$a(k) = \frac{m_f^2}{2|\vec{k}|} \log\left(\frac{k^0 + |\vec{k}|}{k^0 - |\vec{k}|}\right), \quad (\text{B.23})$$

$$b(k) = \frac{1}{|\vec{k}|} [m_f^2 - k^0 a(k)] \quad (\text{B.24})$$

with the thermal fermion mass

$$m_f^2 \equiv \frac{N_c^2 - 1}{16N_c} g^2 T^2. \quad (\text{B.25})$$



The fermion self-energy

At finite μ_f ,

$$T^2 \rightarrow T^2 + \frac{\mu_f^2}{\pi^2}. \quad (\text{B.26})$$

As in the gauge boson case (B.9), all T - and μ -dependence is subsumed in the thermal mass (B.25). Again, the QED result has the same structure with

$$m_f^2 \rightarrow \frac{e^2 T^2}{8}. \quad (\text{B.27})$$

The fermion propagator can be decomposed in the form

$$S(k) = \frac{1}{2} \Delta_+ \left(\gamma^0 + \hat{k} \cdot \vec{\gamma} \right) + \frac{1}{2} \Delta_- \left(\gamma^0 - \hat{k} \cdot \vec{\gamma} \right), \quad (\text{B.28})$$

with $\Delta_{\pm} = -(k^0 \mp \{|\vec{k}| + \Sigma_{\pm}\})^{-1}$ and $\Sigma_{\pm} = b \pm a$. The subscripts (+) and (-) refer to quasiparticles with positive and negative ratio χ of helicity over chirality, respectively. At $T = 0$, the theory is chirally invariant in the limit of vanishing fermion masses, and fermions with positive energy have $\chi = +1$. The other solution $\chi = -1$ that emerges at finite T constitutes a purely collective mode, the plasmino.

As in the previous section, the in-medium version of the physical $T = 0$ mode resembles a free massive particle for large momenta $|\vec{k}| \gg m_f$,

$$\omega_{\pm}^2 \simeq \vec{k}^2 + \hat{m}_{\infty}^2 \quad (\text{B.29})$$

with the fermionic asymptotic mass

$$\hat{m}_{\infty} = \sqrt{2} m_f. \quad (\text{B.30})$$

The collective plasma mode approaches the lightcone exponentially fast since

$$\omega_- \simeq |\vec{k}| + \frac{2|\vec{k}|}{g} \exp\left(-\frac{2\vec{k}^2}{m_f^2}\right). \quad (\text{B.31})$$

Calculating the spectral function yields

$$\rho_{\pm}(k) = 2\pi [Z_{\pm}(k) \delta(k^0 - \omega_{\pm}) + Z_{\mp}(k) \delta(k^0 + \omega_{\mp})] + \hat{\beta}_{\pm}(k), \quad (\text{B.32})$$

very similar to the gauge boson case. The continuum $\hat{\beta}_{\pm}$, again, contributes only below the light cone as Landau damping. The residues for large momenta take the form

$$Z_+(k) \simeq 1 + \frac{2|\vec{k}|^2}{m_f^2} \left[1 - \log\left(\frac{2|\vec{k}|^2}{m_f^2}\right) \right] \quad \text{and} \quad (\text{B.33})$$

$$Z_-(k) \simeq \frac{2|\vec{k}|^2}{gm_f^2} \exp\left(-\frac{2|\vec{k}|^2}{m_f^2}\right), \quad (\text{B.34})$$

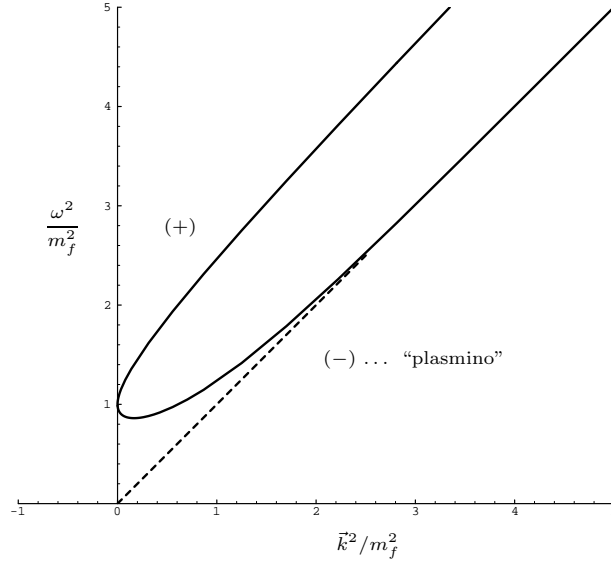


FIGURE B.2: The location of the zeros of Δ_{\pm}^{-1} in the HTL approximation in quadratic scales. The dashed line shows the dispersion relation of a free massless fermion. Figure and caption adapted from [173].

indicating that for $|\vec{k}| \gg m_f$, the collective mode decouples, like the plasmon. The (+) mode rapidly moves towards the free particle residue, and the only effect of the heat bath is the dynamical generation of a thermal mass that does not break chiral symmetry.

For smaller momenta, a minimum occurs in the (-) dispersion relation at $|\vec{k}|/m_f \simeq 0.4$. This is not a relict of the HTL approximation, but can be traced back to the generic form of the fermionic self-energy, eq.(B.22) and hence is expected to occur – though not necessarily at the same position – in any evaluation of Σ [89]. The feature of a vanishing group velocity at finite \vec{k} causes the Van Hove singularities that lead to distinct peaks in dilepton rates.

C Integral Expansions

Here we present the formulas used to evaluate the δ -dependent integrals appearing in eqs.(6.48) and (6.41). Fermionic integrals of the form

$$f_n(y) = \int_0^\infty dx \frac{x^{n-1}}{\sqrt{x^2 + y^2}} \frac{1}{\exp(\sqrt{x^2 + y^2}) + 1}$$

can be expanded for small y (note our slightly different convention compared to [9]). Using the identity

$$\frac{1}{e^z + 1} = \frac{1}{2} - \sum_{n=-\infty}^{\infty} \frac{z}{z^2 + (2n+1)^2\pi^2}$$

and multiplying each term by $x^{-\epsilon}$, a series expansion of the integral is obtained. The potentially diverging terms can be evaluated within dimensional regularisation, and after integrating term by term and letting $\epsilon \rightarrow 0$ at the end, one obtains

$$f_1(y) = -\frac{1}{2} \left[\log\left(\frac{y}{\pi}\right) + \gamma \right] + \dots, \quad (\text{C.1})$$

$$f_3(y) = \frac{\pi^2}{12} + \frac{y^2}{4} \left[\log\left(\frac{y}{\pi}\right) + \gamma - \frac{1}{2} \right] + \dots \quad \text{and} \quad (\text{C.2})$$

$$f_5(y) = \frac{7\pi^4}{120} - \frac{\pi^2}{8}y^2 - \frac{3}{16}y^4 \left[\log\left(\frac{y}{\pi}\right) + \gamma - \frac{3}{4} \right] + \dots, \quad (\text{C.3})$$

where $\gamma = 0.5772\dots$ is the Euler-Mascheroni constant. For bosons,

$$h_n(y) = \int_0^\infty dx \frac{x^{n-1}}{\sqrt{x^2 + y^2}} \frac{1}{\exp(\sqrt{x^2 + y^2}) - 1}.$$

With the corresponding identity

$$\frac{1}{e^z - 1} = \frac{1}{z} - \frac{1}{2} + 2 \sum_{n=1}^{\infty} \frac{z}{z^2 + (2\pi n)^2},$$

the bosonic expansions read

$$h_1(y) = \frac{\pi}{2y} + \frac{1}{2} \left[\log\left(\frac{y}{4\pi}\right) + \gamma \right] + \dots, \quad (\text{C.4})$$

$$h_3(y) = \frac{\pi^2}{6} - \frac{\pi}{2}y - \frac{y^2}{4} \left[\log\left(\frac{y}{4\pi}\right) + \gamma - \frac{1}{2} \right] + \dots \quad \text{and} \quad (\text{C.5})$$

$$h_5(y) = \frac{\pi^4}{15} - \frac{\pi^2}{4}y^2 + \frac{\pi}{2}y^3 + \frac{3}{16}y^4 \left[\log\left(\frac{y}{4\pi}\right) + \gamma - \frac{3}{4} \right] + \dots \quad (\text{C.6})$$

For the evaluation of derivative terms, we need the leading $\log(y)$ behaviour of integrals such as

$$\begin{aligned} g^\pm(y) &= g_1^\pm(y) + g_2^\pm(y) = \\ &= \int_0^\infty dx \left(\frac{1}{\sqrt{x^2 + y^2}} - \frac{1}{1 \pm \exp(-\sqrt{x^2 + y^2})} \right) \frac{1}{\exp(\sqrt{x^2 + y^2}) \pm 1}. \end{aligned} \quad (\text{C.7})$$

The expansion of the first term in brackets, g_1^\pm , is known since $g_1^+ = f_1$ and $g_1^- = h_1$. For the evaluation of the second a trick is convenient. Introduce a parameter α to write

$$g_2^\pm(y; \alpha) = - \int_0^\infty dx \frac{\exp(\alpha\sqrt{x^2 + y^2})}{(\exp(\alpha\sqrt{x^2 + y^2}) \pm 1)^2}. \quad (\text{C.8})$$

Obviously, $g_2^\pm(y; 1)$ is the sought quantity. Now $g_2^\pm(y; \alpha)$ can also be written as

$$\frac{\partial}{\partial \alpha} \left[\int_0^\infty dx \frac{1}{\sqrt{x^2 + y^2}} \frac{1}{\exp(\alpha\sqrt{x^2 + y^2}) \pm 1} \right] = \frac{d}{d\alpha} g_1^\pm(\alpha y). \quad (\text{C.9})$$

Expanding eq.(C.8) for small y hence yields

$$g_2^-(y; \alpha) = -\frac{1}{\alpha^2} \frac{\pi}{2y} + \frac{1}{2\alpha} + \dots \quad \text{for bosons and} \quad (\text{C.10})$$

$$g_2^+(y; \alpha) = -\frac{1}{2\alpha} + \dots \quad \text{for fermions.} \quad (\text{C.11})$$

Setting $\alpha = 1$ and putting the pieces together, the leading-log behaviour of eq.(C.7) is

$$g^+(y) = -\frac{1}{2} \left[\log\left(\frac{y}{\pi}\right) + \gamma + 1 \right] + \dots \quad \text{for fermions and} \quad (\text{C.12})$$

$$g^-(y) = +\frac{1}{2} \left[\log\left(\frac{y}{4\pi}\right) + \gamma + 1 \right] + \dots \quad \text{for bosons.} \quad (\text{C.13})$$

List of Figures

1.1	A sketch of the phase diagram of QCD in the $T - \mu_B$ plane	9
2.1	The one-loop running coupling $g(T)$ as a function of T/T_c	23
2.2	Ratio of expectation values v_β/v_0 as a function of T/T_c	25
2.3	Ratio of m_β^2/m_0^2 as a function of T/T_c	26
2.4	Ratio of λ_β/λ_0 as a function of T/T_c	27
2.5	Polyakov loop expectation value, chiral condensate and the associated susceptibilities	29
2.6	The finite temperature phase diagram of QCD as a function of the light and heavy quark masses	30
2.7	The lattice $T - \mu$ phase diagram by Fodor and Katz	32
2.8	The lattice $T - \mu$ phase diagram by Allton et al.	33
3.1	Pressure of the SU(3) gauge theory	36
3.2	Equation of state of SU(3) gauge theory as a function of T/T_c	37
3.3	The pressure for the pure gauge system and for systems with 2, 2+1 and 3 flavours	38
3.4	The thermal gluon mass m_g/T	47
3.5	The confinement factor $C(T)$ as a function of T/T_c	48
3.6	Equation of state of the confinement model	49
3.7	The interaction measure Δ	49
3.8	The function $B(T)$ and its components B_1 and B_2	50
3.9	The rescaled lattice pressure $p_{\text{cont}} \simeq 1.1 p_{\text{lat}}$	52
3.10	Equation of state for two light flavours	53
3.11	Energy density estimate for three light flavours	54
3.12	Equation of state for two light quarks and a heavy strange quark	55
3.13	The ratio $p_q(T, \mu)/p_q(T, 0)$ in the confinement model	59
3.14	Net quark density $n_q(T, \mu)/T^3$ as a function of T/T_c	60
3.15	The ratio $\chi(T)/\chi_0$ in the confinement model	61
4.1	Dilepton rates in the quasiparticle model for different temperatures	66
4.2	The vector spectral function at $3 T_c$	67
4.3	The photon spectral function at finite temperature and baryon density	69
4.4	Entropy density in the RHIC kinematical scenario	77
4.5	Entropy density for SPS conditions, including fugacity corrections	78
4.6	Volume expansion for SPS conditions	81
4.7	Time evolution of the temperature at SPS and RHIC	82
4.8	Dilepton invariant mass spectra for SP Pb(158 AGeV)+Au	84
4.9	Dilepton invariant mass spectra for SPS Pb(40 AGeV)+Au	86
4.10	p_T -binned dilepton spectra for SPS Pb(158 AGeV)+Au	87
4.11	p_T -binned dilepton spectra for SPS Pb(40 AGeV)+Au	88
4.12	Dilepton invariant mass spectra for RHIC Au+Au at $\sqrt{s} = 200$ AGeV.	89
4.13	Dilepton spectra, varying the parameters τ_0 , v_z^i and T_c	90

5.1	Temperature dependence of the interquark potential in lattice QCD . . .	94
5.2	Particle densities as a function of temperature in the hadronic and partonic phases	97
5.3	Diagrams contributing to lowest order to Ψ dissociation	101
5.4	Dissociation and formation cross sections after averaging with momentum distributions	102
5.5	Ratio Ψ/DY as function of the transverse energy at SPS	103
5.6	Suppression factor S for Ψ as function of the collision energy	104
5.7	Survival probability of Ψ at RHIC as a function of centrality	105
6.1	The gauge-invariant ratio $m_D^{\text{lat}}/(gT)$ for SU(3)	109
6.2	Electric screening mass over temperature in SU(2)	110
6.3	Electric and magnetic screening mass over temperature in SU(2)	111
6.4	The ratio $\alpha_{s,\text{eff}}/\alpha_s$ of eq.(6.51) as a function of k/T	120
B.1	Dispersion relation for gauge bosons	135
B.2	Dispersion relation for fermions	138

Bibliography

- [1] J. C. Collins and M. J. Perry, Phys. Rev. Lett. **34** (1975) 1353.
- [2] P. Braun-Munzinger and J. Stachel, J. Phys. **G28** (2002) 1971.
- [3] D. K. Srivastava and B. Sinha, Phys. Rev. **C64** (2001) 034902.
- [4] Review of Particle Physics, Particle Data Group, Eur. Phys. **J C3** (1998) 1.
- [5] A. Di Giacomo, Nucl. Phys. **B** (Proc. Suppl.) **108** (2002) 21.
- [6] M.A. Shifman, A.I. Vainshtein and V.I. Zakharov, Nucl. Phys. **B147** (1979) 385.
- [7] M. Gell-Mann, R. Oakes and B. Renner, Phys. Rev. **175** (1968) 2195.
- [8] M. Le Bellac, *Thermal Field Theory*, Cambridge University Press, Cambridge, England, 1996.
- [9] J. I. Kapusta, *Finite-temperature field theory*, Cambridge University Press, Cambridge, England, 1989.
- [10] R. D. Pisarski, Phys. Rev. Lett. **63** (1989) 1129.
- [11] E. Braaten and R. D. Pisarski, Phys. Rev. **D45** (1992) 1827.
- [12] J.-P. Blaizot and E. Iancu, Phys. Rept. 359 (2002) 355.
- [13] For lectures on lattice QCD, see e.g. F. Karsch, hep-lat/0106019; G. Münster and M. Walzl, hep-lat/0012005; R. Gupta, hep-lat/9807028.
- [14] K. Symanzik, Nucl. Phys. **B226** (1983) 187; *ibid.* 205.
- [15] M. Alford, W. Dimm, G. P. Lepage, G. Hockney and P. B. Mackenzie, Nucl. Phys. **B** (Proc. Suppl.) **42** (1995) 787.
- [16] D. B. Kaplan, Phys. Lett. **B288** (1992) 342.
- [17] K. G. Wilson, Phys. Rev. **D10** (1974) 2445.
- [18] J. Kogut and L. Susskind, Phys. Rev. **D11** (1975) 395.
- [19] M. D’Attanasio and M. Pietroni, Nucl. Phys. **B472** (1996) 711.
- [20] M. D’Attanasio and M. Pietroni, Nucl. Phys. **B498** (1997) 443.
- [21] B. Bergerhoff, J. Manus and J. Reingruber, Phys. Rev. **D61** (2000) 125005.
- [22] B. Bergerhoff, Phys. Lett. **B437** (1998) 381.
- [23] B. Bergerhoff and J. Reingruber, Phys. Rev. **D60** (1999) 105036.
- [24] B. Bergerhoff and J. Reingruber, Phys. Lett. **B488** (2000) 435.

- [25] M. Pietroni, Phys. Rev. Lett. **81** (1998) 2424.
- [26] J.R. Espinosa, M. Quiros and F. Zwirner, Phys. Lett. **B291** (1992) 115.
- [27] P. Elmfors, Z. Phys. **C56** (1992) 601.
- [28] N. Tetradis and C. Wetterich, Nucl. Phys. **B398** (1993) 659.
- [29] M. Stephanov, K. Rajagopal and E. Shuryak, Phys. Rev. **D60** (1999) 114028.
- [30] F. Karsch, lectures given at *40th Internationale Universitätswochen für Theoretische Physik: Ddense Matter (IUKT 40)*, Schladming, Styria, Austria, 3-10 Mar 2001.
- [31] R. D. Pisarski and F. Wilczek, Phys. Rev. **D29** (1984) 338.
- [32] E. Laermann, Nucl. Phys. **B** (Proc. Suppl.) **63A** (1998) 114.
- [33] B. Svetitsky and L. G. Yaffe, Nucl. Phys. **B210** (1982) 423.
- [34] F. Karsch and L. Lütgemeier, Nucl. Phys. **B550** (1999) 449.
- [35] F. Karsch, E. Laermann and A. Peikert, Nucl. Phys. **B605** (2001) 579.
- [36] F. K. Brown, Phys. Rev. Lett. **65** (1990) 2491; S. Aoki et al., Nucl. Phys. **B** (Proc. Suppl.) **73** (1999) 459.
- [37] K. Rajagopal and F. Wilczek, *At the frontier of particle physics, vol. 3*, edited by M. Shifman, World Scientific 2001, p. 2061; hep-ph/0011333.
- [38] I. M. Barbour et al., Nucl. Phys. **B** (Proc. Suppl.) **60A** (1998) 220.
- [39] Z. Fodor and S. D. Katz, Phys. Lett. **B534** (2002) 87.
- [40] C. R. Allton et al., hep-lat/0204010.
- [41] P. Braun-Munzinger, I. Heppe and J. Stachel, Phys. Lett. **B465** (1999) 15.
- [42] P. Braun-Munzinger, D. Magestro, K. Redlich and J. Stachel, Phys. Lett. **B518** (2001) 41.
- [43] P. de Forcrand and O. Philipsen, hep-lat/0205016.
- [44] M. I. Gorenstein and S. N. Yang, Phys. Rev. **D52** (1995) 5206.
- [45] A. Peshier, B. Kämpfer, O. P. Pavlenko and G. Soff, Phys. Rev. **D54** (1996) 2399.
- [46] P. Levai and U. Heinz, Phys. Rev. **C57** (1998) 1879.
- [47] A. Peshier, B. Kämpfer and G. Soff, Phys. Rev. **C61** (2000) 045203.
- [48] R. A. Schneider and W. Weise, Phys. Rev. **C64** (2001) 055201.
- [49] G. Boyd et al., Phys. Rev. Lett. **75** (1995) 4169.
- [50] G. Boyd et al., Nucl. Phys. **B469** (1996) 419.
- [51] M. Okamoto et al. (CP-PACS Collaboration), Phys. Rev. **D60** (1999) 094510.
- [52] B. Beinlich et al., Eur. Phys. J. **C6** (1999) 133.
- [53] H. Forkel, Phys. Rev. **D64** (2001) 034015.

-
- [54] N. Ishii, H. Suganuma and H. Matsufuru, Nucl. Phys. **B** (Proc. Suppl.) **106** (2002) 516.
- [55] F. Karsch, A. Peikert and E. Laermann, Phys. Lett. **B478** (2000) 447.
- [56] J. Engels et al., Phys. Lett. **B396** (1997) 210; A. Ali Khan (CP-PACS collaboration), Phys. Rev. **D64** (2001) 074510.
- [57] C. Zhai and B. Kastening, Phys. Rev. **D52** (1995) 7232.
- [58] A. Linde, Phys. Lett. **B96** (1980) 289.
- [59] J. O. Andersen, E. Braaten and M. Strickland, Phys. Rev. Lett. **83** (1999) 2139; Phys. Rev. **D61** (2000) 014017; *ibid.* 074016.
- [60] J.-P. Blaizot, E. Iancu and A. K. Rebhan, Phys. Rev. Lett. **83** (1999) 2906; Phys. Lett. **B470** (1999) 181; Phys. Rev. **D63** (2001) 065003.
- [61] P. Petreczky, F. Karsch, E. Laermann, S. Stickan and I. Wetzorke, Nucl. Phys. (Proc. Suppl.) **106** (2002) 513.
- [62] F. Karsch, talk given at the *Enrico Fermi International School of Physics*, Varenna, Italy, Jun 26 - Jul 6, 1984.
- [63] O. Kaczmarek, F. Karsch, E. Laermann and M. Lütgemeier, Phys. Rev. **D62** (2000) 034021.
- [64] A. K. Rebhan, Phys. Rev. **D48** (1993) R3967.
- [65] A. Peshier, Phys. Rev. **D63** (2001) 105004.
- [66] R. Kobe, G. Kunstatter and A. K. Rebhan, Phys. Rev. Lett. **64** (1990) 2992; Nucl. Phys. **B355** (1991) 1.
- [67] I. Schmidt and J.-J. Yang, Phys. Lett. **B468** (1999) 138.
- [68] H. Leutwyler, proceedings of the Conference *QCD - 20 years later*, edited by P.M. Zerwas and H.A. Kastrup, World Scientific 1993, p. 693.
- [69] A. Drago and M. Gibilisco, hep-ph/0112282.
- [70] T. S. Biro, A. A. Shanenko and V. D. Toneev, nucl-th/0102027.
- [71] R. D. Pisarski, Phys. Rev. **D62** (2000) 111501.
- [72] A. Schäfer and M. Thoma, Phys. Lett. **B451** (1999) 195.
- [73] F. Karsch, Nucl. Phys. **A698** (2002) 199.
- [74] Z. Fodor, S. D. Katz and K. K. Szabo, hep-lat/0208078.
- [75] A. Peshier, talk given at *5th International Workshop on Thermal Field Theories and Their Applications*, Regensburg, Germany, 10-14 Aug 1998; hep-ph/9809379.
- [76] M. Thaler, diploma thesis, Technische Universität München, Germany, 2002.
- [77] M. Asakawa, U. W. Heinz and B. Müller, Phys. Rev. Lett. **85** (2000) 2072.
- [78] S. Jeon and V. Koch, Phys. Rev. Lett. **85** (2000) 2076.
- [79] R. V. Gavai and S. Gupta, Phys. Rev. **D65** (2002) 094515.

- [80] R. V. Gavai, S. Gupta and P. Majumdar, Phys. Rev. **D65** (2002) 054506.
- [81] J. P. Blaizot, E. Iancu and A. Rebhan, Phys. Lett. **B523** (2001) 143.
- [82] T. Toimela, Int. J. Theor. Phys. **24** (1985) 901.
- [83] Z. Fodor, plenary talk given at Quark Matter 2002, Nantes, France, 18-24 July 2002, hep-lat/0209101.
- [84] T. Renk, R. A. Schneider and W. Weise, Phys. Rev. **C66** (2002) 014902.
- [85] G. Agakichiev et al. (CERES collaboration), Phys. Rev. Lett. **75** (1995) 1272; G. Agakichiev et al. (CERES collaboration), Phys. Lett. **B422** (1998) 405.
- [86] P. Aurenche, F. Gelis, R. Kobes and H. Zaraket, Phys. Rev. **D58** (1998) 085003.
- [87] P. Aurenche, F. Gelis and H. Zaraket, Phys. Rev. **D61** (2000) 116001.
- [88] E. Braaten, R. D. Pisarski and T. C. Yuan, Phys. Rev. Lett. **64** (1990) 224.
- [89] A. Peshier and M. H. Thoma, Phys. Rev. Lett. **84** (2000) 841.
- [90] F. Karsch, E. Laermann, P. Petreczky, S. Stickan and I. Wetzorke, Phys. Lett. **B530** (2002) 147.
- [91] F. Klingl, N. Kaiser and W. Weise, Z. Phys. **A356** (1996) 193.
- [92] R. A. Schneider and W. Weise, Eur. Phys. J. **A9** (2000) 357.
- [93] R. A. Schneider and W. Weise, Phys. Lett. **B515** (2001) 89.
- [94] C. Song, C. M. Ko and C. Gale, Phys. Rev. **D50** (1994) R1827.
- [95] G. Q. Li and C. Gale, Nucl. Phys. **A638** (1998) 491.
- [96] V. L. Eletsky and B. L. Ioffe, Phys. Rev. **D47** (1993) 3083; V. L. Eletsky and B. L. Ioffe, Phys. Rev. **D51** (1995) 2371.
- [97] M. Urban, M. Buballa and J. Wambach, Phys. Rev. Lett. **88** (2002) 042002; E. Marco, R. Hofmann and W. Weise, Phys. Lett. **B530** (2002) 88.
- [98] W. A. Zajc et al. (PHENIX Collaboration), Nucl. Phys. **A698** (2002) 39.
- [99] PHOBOS Collaboration, Phys. Rev. Lett. **87** (2001) 102301.
- [100] F. Klingl, N. Kaiser and W. Weise, Nucl. Phys. **A624** (1997) 527.
- [101] W. Schön, R. A. Schneider and W. Weise, in preparation.
- [102] A. D. Martin, R. G. Roberts, W. J. Stirling and R. S. Thorne, Phys. Lett. **B531** (2002) 216.
- [103] H. L. Lai et al. (CTEQ), Eur. Phys. J. **C12** (2000) 375.
- [104] M. Glück, E. Reya, and A. Vogt, Eur. Phys. J. **C5** (1998) 461.
- [105] P. L. McGaughey et al. (E772), Phys. Rev. **D50** (1994) 3038.
- [106] K. J. Eskola, V. J. Kolhinen and C. A. Salgado, Eur. Phys. J. **C9** (1999) 61.
- [107] F. Arleo, Phys. Lett. **B532** (2002) 231.

-
- [108] S. Gavin, P. L. McGaughey, P. V. Ruuskanen and R. Vogt, Phys. Rev. **C54** (1996) 2606.
- [109] E. Shuryak, Phys. Rev. **C55** (1997) 961.
- [110] Z. Lin, R. Vogt and X.-N. Wang, Phys. Rev. **C57** (1998) 899.
- [111] T. Renk, PhD thesis, Technische Universität München, Germany, 2002.
- [112] U. W. Heinz and S. M. H. Wong, Phys. Rev. **C66** (2002) 014907.
- [113] R. Baier, A. H. Mueller, D. Schiff and D.T. Son, Phys. Lett. **B502** (2001) 51.
- [114] B. Tomasik, U. A. Wiedemann and U. W. Heinz, nucl-th/9907096.
- [115] J. Sollfrank, P. Huovinen, M. Kataja, P. V. Ruuskanen, M. Prakash and R. Venugopalan, Phys. Rev. **C55** (1997) 392.
- [116] C. M. Hung and E. Shuryak, Phys. Rev. **C57** (1998) 1891.
- [117] B. Jacak (NA44 Collaboration), in *Hot and Dense Nuclear Matter*, edited by W. Greiner, H. Stöcker and A. Gallmann, Plenum, New York, 1994, p. 607.
- [118] J. Letessier, A. Tounsi, U. Heinz, J. Sollfrank and J. Rafelski, Phys. Rev. **D51** (1995) 3408.
- [119] R. Rapp, Phys. Rev. **C63** (2001) 054907.
- [120] S. Y. Panitkin, Nucl. Phys. **A698** (2002) 323.
- [121] R. Rapp and J. Wambach, Eur. Phys. J. **A6** (1999) 415.
- [122] H. J. Specht, private communication.
- [123] B. Lenkeit et al. (CERES Collaboration), Nucl. Phys. **A661** (1999) 23.
- [124] S. Damjanovic (CERES collaboration), proceedings of the *Fourth International Conference on Physics and Astrophysics of Quark Gluon Plasma*, Jaipur, 2001; nucl-ex/0111009.
- [125] S. Damjanovic, private communication.
- [126] PHOBOS Collaboration, Phys. Rev. Lett. **88** (2002) 022302.
- [127] A. Polleri, T. Renk, R. A. Schneider and W. Weise, in preparation.
- [128] T. Matsui and H. Satz, Phys. Lett. **B178** (1986) 416.
- [129] C. Baglin et al. (NA38 Collaboration), Phys. Lett. **B220** (1989) 471; Phys. Lett. **B255** (1991) 459.
- [130] C. Gerschel and J. Hüfner, Phys. Lett. **B207** (1988) 253; Z. Phys. **C56** (1992) 171.
- [131] M. C. Abreu et al. (NA50 Collaboration), Phys. Lett. **B410** (1997) 327.
- [132] M. C. Abreu et al. (NA50 Collaboration), Phys. Lett. **B477** (2000) 28.
- [133] J. Hüfner and B. Z. Kopeliovich, Phys. Lett. **B445** (1998) 223.
- [134] J. Hüfner, B. Z. Kopeliovich and A. Polleri, Eur. Phys. J. **A11** (2001) 457.

- [135] B. Z. Kopeliovich and F. Niedermayer, JINR-E2-84-834, available as scanned preprint on the KEK database, unpublished.
- [136] B. Kopeliovich, A. Tarasov and J. Hüfner, Nucl. Phys. **A696** (2001) 669.
- [137] D. Kharzeev, C. Lourenco, M. Nardi and H. Satz, Z. Phys. **C74** (1997) 307.
- [138] R. K. Ellis, *Lectures given at 17th SLAC Summer Inst.*, Stanford, California, USA, 10-21 Jul, 1989.
- [139] R. V. Gavai et al., Int. J. Mod. Phys. **A10** (1995) 2999.
- [140] M. Glück, E. Reya and A. Vogt, Z. Phys. **C53** (1992) 127.
- [141] B. Z. Kopeliovich and A. V. Tarasov, hep-ph/0205151.
- [142] R. Vogt, Phys. Rept. **310** (1999) 197.
- [143] S. Digal, P. Petreczky and H. Satz, Phys. Lett. **B514** (2001) 57; Phys. Rev. **D64** (2001) 094015.
- [144] C. Y. Wong, Phys. Rev. **C65** (2002) 034902.
- [145] M. E. Peskin, Nucl. Phys. **B156** (1979) 365.
- [146] G. Bhanot and M. E. Peskin, Nucl. Phys. **B156** (1979) 391.
- [147] Y. Oh, S. Kim and S. H. Lee, Phys. Rev. **C65** (2002) 067901.
- [148] P. Braun-Munzinger and J. Stachel, Phys. Lett. **B490** (2000) 196; R. L. Thews, M. Schroedter and J. Rafelski, Phys. Rev. **C63** (2001) 054905; M. I. Gorenstein et al., Phys. Lett. **B524** (2002) 265.
- [149] C. Gerschel and J. Hüfner, Ann. Rev. Nucl. Part. Sci. **49** (1999) 255; H. Satz, Rep. Prog. Phys. **63** (2000) 1511.
- [150] L. P. Csernai and J. I. Kapusta, Phys. Rept. **131** (1986) 223.
- [151] A. Capella, E. G. Ferreira and A. B. Kaidalov, Phys. Rev. Lett. **85** (2000) 2080; J. P. Blaizot, M. Dinh and J. Y. Ollitrault, Phys. Rev. Lett. **85** (2000) 4012; J. Hüfner, B. Z. Kopeliovich and A. Polleri, nucl-th/0012003.
- [152] T. Frawley, talk given at *16th International Conference on Ultrarelativistic Nucleus-Nucleus Collisions (QM2002)*, Nantes, France, 18-24 Jul 2002.
- [153] N. K. Nielsen, Am. J. Phys. **49** (1981) 1171.
- [154] J. L. Petersen, proceedings of the *1997 European Summer School of High-Energy Physics*, edited by N. Ellis and M. Neubert, CERN Report 98-03.
- [155] D. Persson, Annals Phys. **252** (1996) 33, and references therein.
- [156] R. A. Schneider, Phys. Rev. **D66** (2002) 036003; R. A. Schneider, hep-ph/0210281.
- [157] M. Peskin and D. Schroeder, *An Introduction to Quantum Field Theory*, Addison-Wesley Publishing Company, Reading, USA, 1995.
- [158] H. A. Weldon, Phys. Rev. **D26** (1982) 1394.
- [159] E. V. Shuryak, Sov. Phys. JETP **47** (1978) 212.

-
- [160] A. K. Rebhan, Nucl. Phys. **B430** (1994) 319.
- [161] D. Gross, R. Pisarski and L. Yaffe, Rev. Mod. Phys. **53** (1981) 43.
- [162] K. Kajantie, M. Laine, J. Peisa, A. Rajantie, K. Rummukainen and M. Shaposhnikov, Phys. Rev. Lett. **79** (1997) 3130.
- [163] U. M. Heller, F. Karsch and J. Rank, Phys. Rev. **D57** (1998) 1438.
- [164] M.A. van Eijck, C.R. Stephens, C.G. van Weert, Mod. Phys. Lett. **A9** (1994) 309.
- [165] P. Elmfors and R. Kobes, Phys. Rev. **D51** (1995) 774.
- [166] K. Sasaki, Phys. Lett. **B369** (1996), 117; Nucl. Phys. **B472** (1996) 271.
- [167] G. K. Savvidy, Phys. Lett. **B71** (1977) 131.
- [168] N. K. Nielsen and P. Olesen, Nucl. Phys. **B144** (1978) 376.
- [169] M. Ninomiya and N. Sakai, Nucl. Phys. **B190** (1981) 316.
- [170] K. Enqvist and P. Olesen, Phys. Lett. **B329** (1994) 195.
- [171] P. Elmfors and D. Persson, Nucl. Phys. **B538** (1999) 309.
- [172] D. Persson, Annals Phys. **252** (1996) 33.
- [173] A. Rebhan, lectures given at *Cargese Summer School on QCD Perspectives on Hot and Dense Matter*, Cargese, France, 6-18 Aug 2001.

Acknowledgements

I would like to thank all people who contributed – in one way or the other – to the success of this work.

First of all, I am indebted to Prof. Dr. Wolfram Weise for his permanent interest in the ongoing work, his trust and his virtually unlimited support and motivation. The last two years were intense and challenging, but the reward is a truly unique PhD that would not have been possible elsewhere.

I am also grateful to

- Thorsten Renk: member of the Italy Fellowship, partner in lively discussions about physics and life in general and connoisseur ("I've got two beans..."). The night in Bielefeld's Irish Karaoke pub will never be forgotten.
- my colleagues Thomas Schwarz, Stefan Fritsch and Michael Thaler for physics talk, advice on running Lopster, the "occasional" frag sessions, Münster and a very comfortable working atmosphere,
- all other members of the T39 group for advice, help and humour,
- the people and staff at the ECT* in Trento, especially Rachel.

Obviously, the support from people outside the university is always important – and sometimes vital. So I will not finish without roaring a loud *Thank you to*

- my friends Alex and Gustav. It is good to know you.
- my band members Zyna, Marc, "Fingerfly" Tobi and Till. Without you, life would be dull and gray. May your glasses never be empty.
- my parents who supported me all these years.

Get me a little oblivion for all the things undone.